CIVIL ENGINEERING STUDIES
Illinois Center for Transportation Series No. 13-027
UILU-ENG-2013-2028
ISSN: 0197-9191

EFFECTS OF A NONUNIFORM SUBGRADE SUPPORT ON THE RESPONSES OF CONCRETE PAVEMENT

Prepared By
Alexander S. Brand
Jeffery R. Roesler
Hemant L. Chavan
University of Illinois at Urbana-Champaign

Francisco Evangelista Jr.
University of Brasilia, Brazil

Research Report No. ICT-13-027

Illinois Center for Transportation

September 2013

Technical Report Documentation Page

1. Report No.	2. Government Accession No.	3. Recipient's Catalog No.
ICT-13-027		

4. Title and Subtitle

Effects of a Nonuniform Subgrade Support on the Responses of Concrete Pavement

5. Report Date
September 2013

6. Performing Organization Code

7. Author(s)
Alexander S. Brand, Jeffery R. Roesler, Hemant L. Chavan, and Francisco Evangelista Jr.

8. Performing Organization Report No.
ICT-13-027
UILU-ENG-2013-2028

9. Performing Organization Name and Address

Department of Civil and Environmental Engineering
University of Illinois at Urbana-Champaign
205 N. Mathews Ave, MC 250
Urbana, IL 61801

10. Work Unit (TRAIS)

11. Contract or Grant No.

12. Sponsoring Agency Name and Address

Iowa State University
2711 South Loop Drive
Suite 4700
Ames, IA 50010

13. Type of Report and Period Covered

14. Sponsoring Agency Code

15. Supplementary Notes

16. Abstract

Intelligent compaction is gaining attention for its ability to spatially map the compaction effort of a pavement support layer, and it has also been shown to be able to detect areas of nonuniform compaction, which raises the issue of what the effects of a nonuniform support condition are on the stresses and deflections in a rigid pavement. This study considered multiple nonuniform support conditions, including theoretically generated and predetermined and randomly assigned from measured field data. The slabs and nonuniform support conditions were modeled using two-dimensional and three-dimensional finite element methods with input variables being axle type, curling, and lateral and longitudinal axle movements. Overall the study found that certain nonuniform support conditions and axle positions can significantly increase the peak tensile stress in the slab over even uniform soft support. In particular, a single slab with soft longitudinal edge support and a slab with “randomly” assigned nonuniformities were critical cases that increased the peak slab tensile stresses. When the slab was modeled with preexisting through-length surface cracks, it was found that the nonuniform soft edges support conditions would result in unstable crack growth based on the significant increase in the stress intensity factor. When modeling a set of concrete slabs over a nonuniform support based on field data, the peak tensile stresses were increased relative to a uniform support based on the location of the wheel load relative to the nonuniformity and also based on the adjacent differences in nonuniform soil stiffness. The field data was also statistically reassigned by normal and beta distributions to predefined area sizes, which demonstrated that with a normal distribution, the probability of low k-values along the pavement edge increased thereby raising the probability of higher peak tensile stresses. Overall, certain nonuniform support of concrete slabs can produce much higher tensile stresses than a uniform support condition, particularly when considering different loading positions and curling conditions, soft support along the pavement edge, and preexisting cracks.

17. Key Words	18. Distribution Statement
Concrete pavement, nonuniform support, intelligent compaction, finite element, cracks, subgrade support	No restrictions. This document is available to the public through the National Technical Information Service, Springfield, Virginia 22161.

19. Security Classif. (of this report)	20. Security Classif. (of this page)	21. No. of Pages	22. Price
Unclassified	Unclassified		

ACKNOWLEDGMENT

Acknowledgment is given to the Federal Highway Administration and Iowa State University for funding this project as part of DTFH61-06-H-00011 Work Plan 18, with particular thanks for the collaboration with Professor David J. White and Dr. Pavana Vennapusa at Iowa State University. Additionally, the researchers would like to acknowledge Applied Research Associates for the use of the ISLAB2000 software.

TABLE OF CONTENTS

CHAPTER 1 INTRODUCTION AND LITERATURE REVIEW

The use of intelligent compaction (IC) technologies has been gaining interest for its capability of spatially mapping the compaction of a given pavement layer. IC rollers can adjust drum parameters in an attempt to produce a uniformly compacted layer. In order to assess the need for IC and how IC should be implemented, engineers need to know what level of nonuniformity is not acceptable and will lead to reduced pavement performance over the assumed design life. The objective of this report is to demonstrate what type of nonuniform support condition will have a significant effect on concrete slabs through both theoretical analyses and field data collection.

1.1 Intelligent Compaction

Typically, IC technology works to uniformly compact a material in a layer, such as a soil subgrade or subbase, by adjusting the amplitude, frequency, or other roller drum characteristics (Van Hampton 2009). One recent report noted that there is need for construction specifications in order to incorporate IC technology (Mooney et al. 2010). Currently, state agencies in Colorado, Florida, Iowa, Michigan, Minnesota, Texas, and Wisconsin are investigating the possibility of implementing IC technology (FHWA 2011).

One significant advantage of IC technologies is that they can map the uniformity of the pavement layers by immediately locating soft, weak, or nonuniform areas (Petersen 2005, Hossain et al. 2006, Petersen and Peterson 2006, White et al. 2006, Mooney and Rinehart 2007, White et al. 2007, Sebesta et al. 2009). It is crucial to locate these areas of nonuniformities since they have been demonstrated to cause stress concentrations in the stabilized pavement layers, which could potentially result in premature distresses and failures (White et al. 2005). With current construction and earthwork handling processes, it has been shown, using IC roller measurements, that there exists a spatial anisotropy in soil stiffness (Facas et al. 2010).

In addition to subgrade layers being compacted with IC technology, the compaction of surface layers (particularly asphalt) can also be measured by IC technology. Xu et al. (2012) located areas of nonuniformity in a hot-mixed asphalt surface course compacted with IC technology, and additional analysis demonstrated that the nonuniformities would result in a reduced predicted pavement fatigue life (relative to the predicted performance of an assumed uniformly compacted layer).

1.2 Nonuniform Support

The analysis of a concrete slab with nonuniform support was perhaps first considered in the late 1950s. Leonards and Harr (1959) developed equations to analyze a concrete slab that was experiencing loss of support because of slab curling. Richart and Zia (1962) analyzed an infinite slab with an elastic support spanning a circular void. Hudson and Matlock (1966) considered a finite sized concrete slab under center, edge, and corner loading and inserted a circular void under each load and found that the loss of support under the load greatly increased the slab deflections.

Later work at the University of Illinois considered the effects of nonuniform material properties. Levey (1968) and Levey and Barenberg (1970) developed a two-layer system that

had variable material moduli modeled by discrete elements that were connected by springs of variable stiffness. Each layer had a fixed mean modulus and the variability was based on a selected standard deviation. A statistical process was developed to randomly assign the elastic modulus of the top layer in the finite element program based on a normal distribution of the expected values of these properties. The authors found that the responses were affected by the statistical changes in material moduli of adjacent elements, and they also noted that a larger area with slightly less than average modulus had a greater effect on the slab responses than a small area with larger difference in modulus.

Barenberg et al. (1976) applied the same statistical process developed previously (Levey 1968, Levey and Barenberg 1970) to spatially assign paving material properties such as soil stiffness and concrete elastic modulus values to specific user-defined areas with the aim of analyzing pavement systems having nonuniform material properties. A finite element model for analysis of two-layered slabs on a Winkler foundation was selected to analyze stresses, strains, and deflections. These critical slab responses were completed for several load locations (edge and corner). The critical strain results showed that location of the critical strain did not always occur under the loading position, which validates the presence of corner breaks because of edge loading. The authors reported an overall low sensitivity of the pavement responses to the varying subgrade stiffness (range of 11-197 psi/in) with a constant slab elastic modulus. For example, for a coefficient of variation (COV) of 30% in the k-value assignment, an increase of approximately 11% and 2% in tensile strain was observed from the uniform support (single k-value) to the worst-case k-value distribution for edge and corner loadings, respectively. The best and worst support conditions were created by placing the strongest and weakest 4 ft^2 area of k-values around the critical load location. The responses of varying the slab elastic modulus under a uniform k-value support condition were more critical. For a 30% COV in data set of slab elastic modulus assignment, an increase of approximately 25% and 38% in strain was observed from the best condition to the worst for edge and corner loading cases, respectively. The authors noted that application of moving load over a nonuniform pavement system along with increasing the size of nonuniform area would develop a better understanding of critical responses.

As part of a larger study, White et al. (2005) assessed the effect of a nonuniform subgrade support on critical pavement responses for long term pavement performance. A spatial grid pattern of the subgrade engineering properties was developed based on in situ field tests from 12 sites. The influence of spatial variability of the subgrade on the pavement was analyzed using the two-dimensional finite element program ISLAB2000. The results of the analysis showed that the maximum principal stresses and deflections were reduced in the pavement under a uniform subgrade, thereby increasing the fatigue life of the slab. The nonuniform support condition resulted in a decrease in the predicted fatigue life of the pavement versus the assumed uniform support in nearly all cases tested. This limited study demonstrated the possibility that subgrade nonuniformity can lead to a reduced fatigue life.

CHAPTER 2 TWO-DIMENSIONAL FINITE ELEMENT ANALYSIS OF A SLAB WITH PREDETERMINED NONUNIFORM SUBGRADE SUPPORT

Based on the findings by Barenberg et al. (1976) and White et al. (2005) that variability in the subgrade k-value can affect the concrete slab responses, the first section of the study was aimed at determining the effects of various designed nonuniformities on the concrete slab maximum tensile stresses. A total of 12 subgrade cases were considered, ten of which had some degree of nonuniformity that was predetermined. These subgrade cases were not based on field conditions, since it was initially desired to determine the effects of various extreme nonuniform cases. For the analysis, a two-dimensional finite element analysis was conducted using the program ISLAB2000, Version 2.0, provided by Applied Research Associates.

2.1 Factorial Study Design and Inputs

In this analysis, a single slab was considered without restraint and without load transfer. The slab was modeled to be directly on the subgrade. The fixed inputs for all simulations are shown in Table 1. The variables that were changed are shown in Table 2. The 12 subgrade cases are depicted in Figure 1. In this factorial analysis, the following variables were changed: subgrade support condition (Figure 1), axle type on the slab, axle location (movement of the axle along the slab), axle offset from the edge of the slab, and temperature differential (curling).

Table 1. Fixed Finite Element Analysis Inputs

Slab Size	144 by 180 in
Slab Thickness	8 in
Elastic Modulus	4.00×10^6 psi
Poisson Ratio	0.15
Coefficient of Thermal Expansion	5.50×10^{-6}/°F
Unit Weight	0.087 pci
Tire Pressure	90 psi
Tire Contact Aspect Ratio (b/a)	1
Element Mesh Size	2 x 2 in
Wheel Spacing	96 in
Axle Spacing (Tandem Axle)	48 in
Axle Spacing (Steer-Drive Axle)	48 and 96 in

Table 2. Input Variables in the Finite Element Analysis

Subgrade Cases	Two uniform and ten with various nonuniform support conditions (Soft = 50 or Stiff = 500 psi/in)
Axle Configurations (Loads)	Single (18 kip), Tandem (36 kip), Steer-Drive (54 kip)
Axle Location	10-in increments from transverse edge to mid-slab edge
Wheel Offset	Edge (0 in offset) and Wheelpath (19 in offset)
Temperature Differential	-20, 0, 20 °F (linear profile)

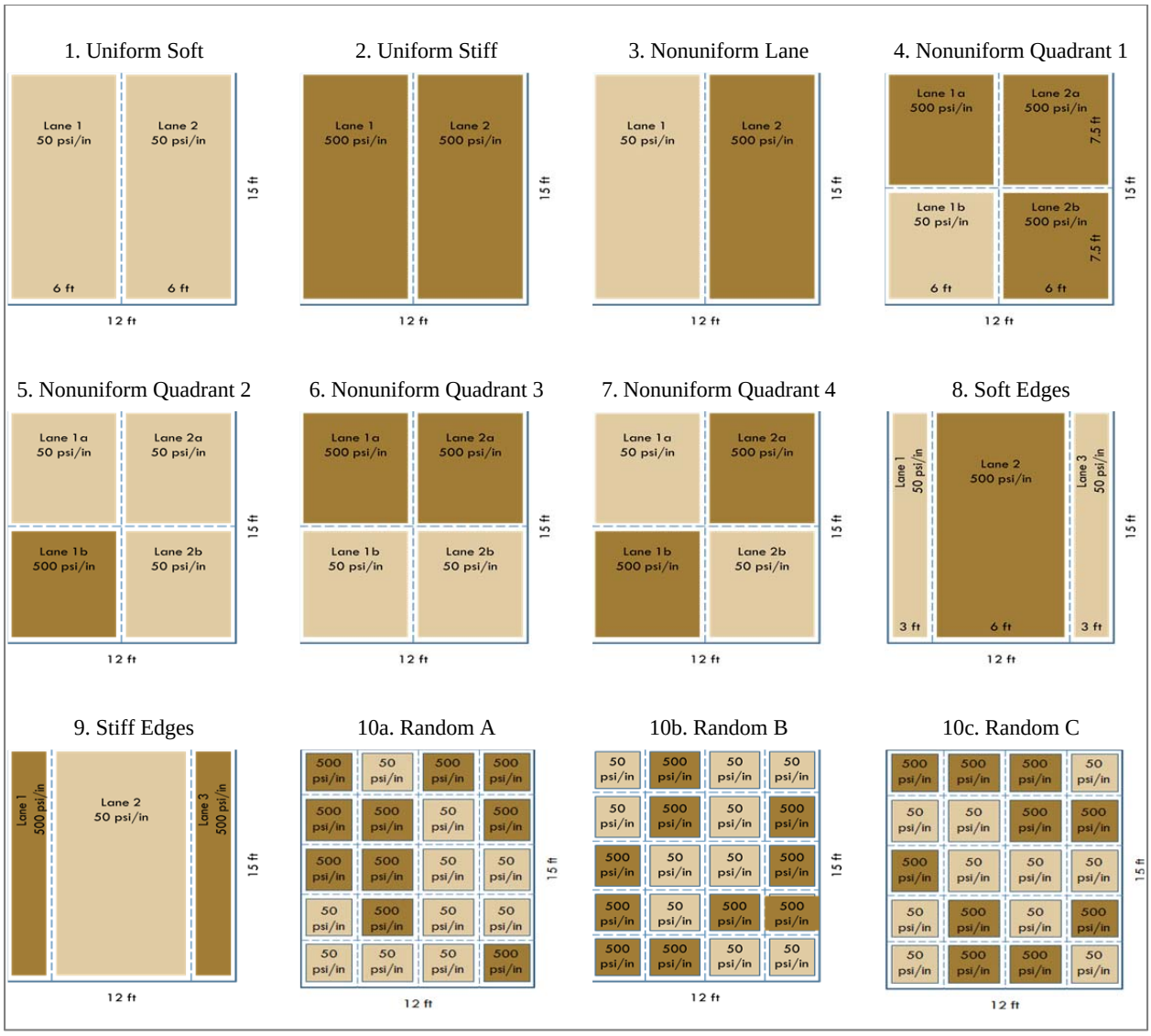

Figure 1. The twelve predetermined nonuniform cases considered in this analysis.

The 12 subgrade support conditions presented in Figure 1 were all predetermined to vary in k-value from soft (50 psi/in) to stiff (500 psi/in) to simulate an extreme variation. Of the 12 cases, two are of a uniform k-value to be referenced to as the control cases (Cases 1 and 2). Case 3 has two 6-ft-wide lanes of differing soft and stiff k-values. The quadrant cases (Cases 4, 5, 6, and 7) were split into four areas, each measuring 6 x 7.5 ft, which were then assigned either soft or stiff k-values. The edge cases (Cases 8 and 9) each have 3-ft-wide longitudinal edges of a different k-value to the center 6 ft of the subgrade. The “random” cases (Cases 10a, 10b, and 10c) were predetermined to have 20 areas of a set size (3 x 3 ft), which were then “randomly” assigned a uniform soft or stiff k-value such that there were ten total areas each of soft and stiff k-values.

Three axle types were considered for the analysis: single, tandem, and steer-drive. Each axle was designed to bear 18 kips, so each individual wheel carries 9 kips. With a tire pressure of 90 psi, each wheel is therefore modeled as a square load measuring 10 in square. The

wheels on a given axle were spaced 96 in apart (see Figure 2). For the tandem axle, two single axles were spaced 48 in apart. The steer-drive axle essentially consisted of a tandem axle with another single axle spaced 96 in away.

The initial loading position for the axles was at the transverse slab edge (which means that the center of the axle was 5 in offset from the edge). The center of the axle (which was the rear axle for tandem and steer-drive) was then moved in 10-in increments along the slab up to the mid-slab edge (90 in).

Two wheel offsets were also considered: edge and wheelpath. For edge loading, the axle was moved along the longitudinal edge. For wheelpath loading, the axle was offset 19 in from the longitudinal edge (see Figure 2). This offset was selected so that the axle would be exactly centered on the slab.

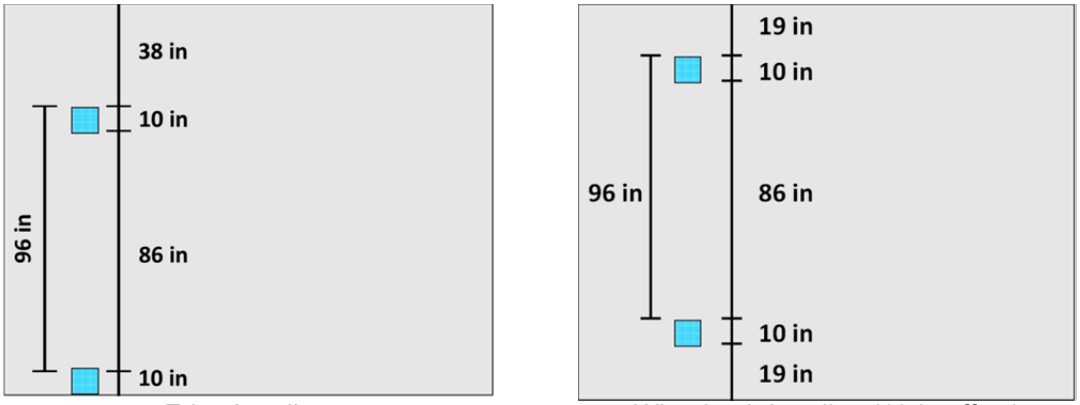

Edge Loading Wheelpath Loading (19-in offset)

Figure 2. The geometry of the lateral wheel position offsets.

The final variable was the linear temperature differential. This was varied to determine the effect of the combination of nonuniform support with slab curling on the slab responses. Three linear differentials were considered: 0, -20, and +20°F. With a negative differential, a slab curls upward, and with a positive differential, the slab curls downward.

The two-dimensional finite element program ISLAB2000 uses plate bending elements to idealize the behavior of the concrete slab, and the subgrade was modeled as a Winkler foundation. The slab was placed directly on top of the subgrade with no frictional interaction (full slip condition), but the slab was allowed to separate under temperature loading. The subsequent finite element analyses resulted in a total of 1,800 finite element runs. For each axle position, the maximum principal stress (tensile), tensile stress spatial location (x,y,z), and maximum deflection were recorded.

2.2 Slab Response Results: No Temperature Differential

2.2.1 Edge Loading

For the single axle edge loading cases (Figure 3 and Figure 4), the highest tensile stresses occurred in the random Case 10a (441 psi) followed closely by the uniform soft Case 1 (434 psi). This result suggested that the random nonuniformity would be more severe than a uniform low strength (soft) subgrade. However, Case 10b random support conditions shown in Figure 3 and Figure 4 resulted in much lower stresses than Case 10a and had higher stresses

at the transverse edge versus the mid-slab longitudinal edge. Analyzing Case 10c demonstrated that the random cases can be unpredictable and were very dependent on the location of the nonuniformity and axle position. For example, in Case 10a, part of the axle is on a soft subgrade while the other part is on a stiff soil near the mid-slab edge, which is different for Cases 10b and 10c. In Cases 8 (soft edges) and 10b, the largest stress experienced occurred at the transverse edge while in Cases 1, 10a, and 5, the largest stress occurred near or at the mid-slab edge. Case 2 with uniform high soil stiffness appeared to be the exception where the stress at the transverse edge was similar to the stress at the mid-slab edge.

In all single axle edge loading cases, the largest deflection occurred at the transverse edge (i.e., the corner loading condition). The largest deflections for all cases was experienced by Case 1, which is to be expected since it had the weakest subgrade while Cases 2 and 9 had the lowest deflections with the stiffest edge support condition.

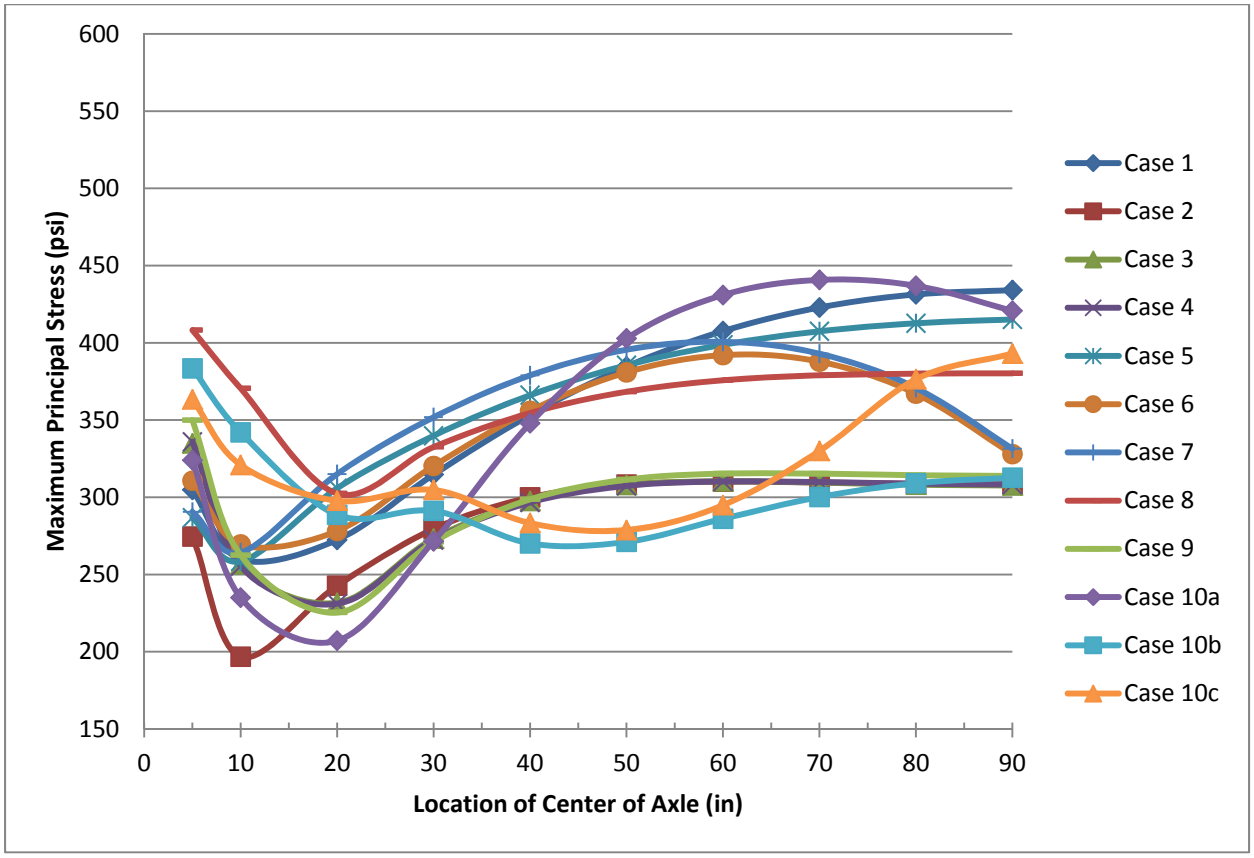

Figure 3. Maximum principal stress values for each single axle position and subgrade condition for no temperature differential and edge loading.

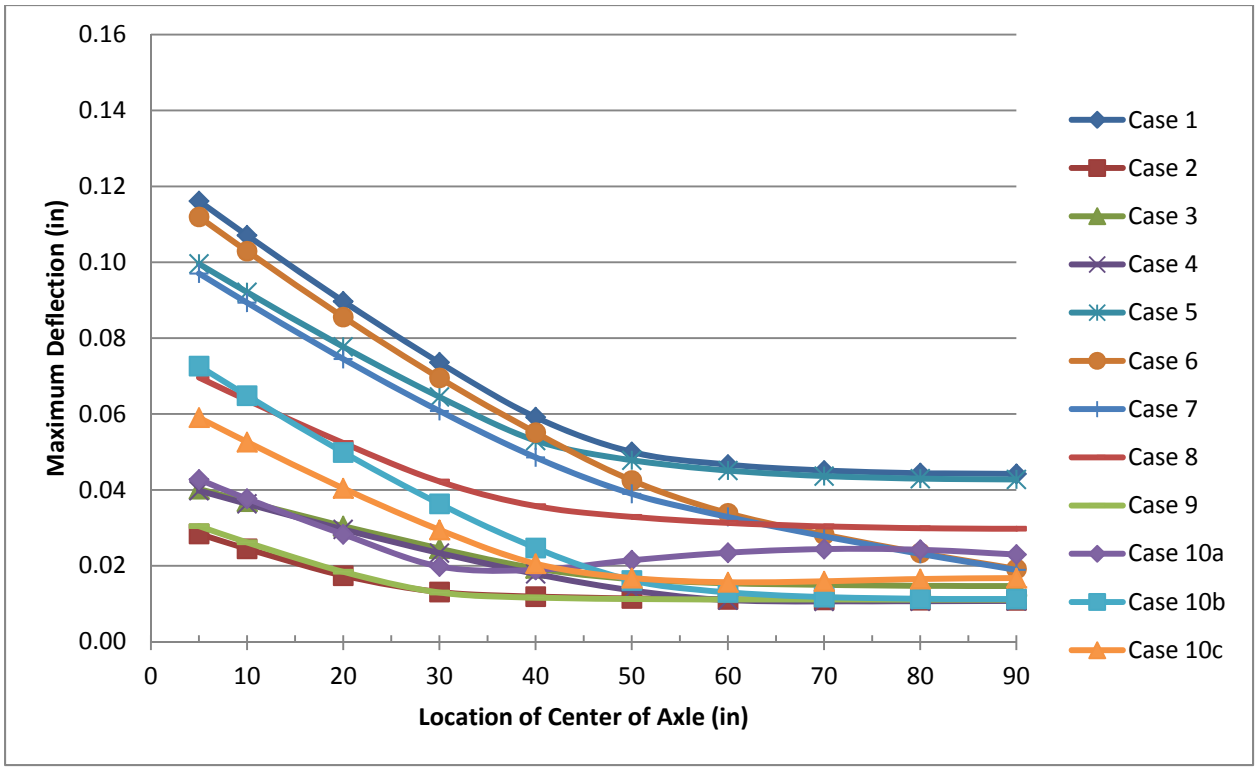

Figure 4. Maximum deflection values for each single axle position and subgrade condition for no temperature differential and edge loading.

For the tandem axle edge loading cases, Case 8 (soft edges) produced the highest tensile stress (550 psi), as shown in Figure 5, on the top of the slab when the tandem axle was located at the transverse edge load position. Case 10a (random) resulted in the second highest stress (450 psi), which occurred near the mid-slab load position at the bottom of the slab. The uniform support (Case 1) condition of 50 psi/in also produced 411 psi near the mid-slab loading position. The lowest tensile stresses occured with Case 2 (uniform stiff) and Case 10b (random). The random nonuniform cases (Cases 10a, 10b, and 10c) had a wide range of tensile stresses, depending on the axle position relative to the local slab support conditions.

The deflections caused by tandem axles were higher than single axle deflections, with the maximum deflections occurring in Case 1 (uniform soft) and Case 6 (quadrant) for the transverse edge loading while Case 1 (uniform soft) and Case 5 (quadrant) produced the largest deflection at the mid-slab edge loading (see Figure 6). The lowest deflections occurred again under the cases with the greatest support stiffness (i.e., Cases 2 and 9 at the transverse edge and Case 4 near the mid-slab edge).

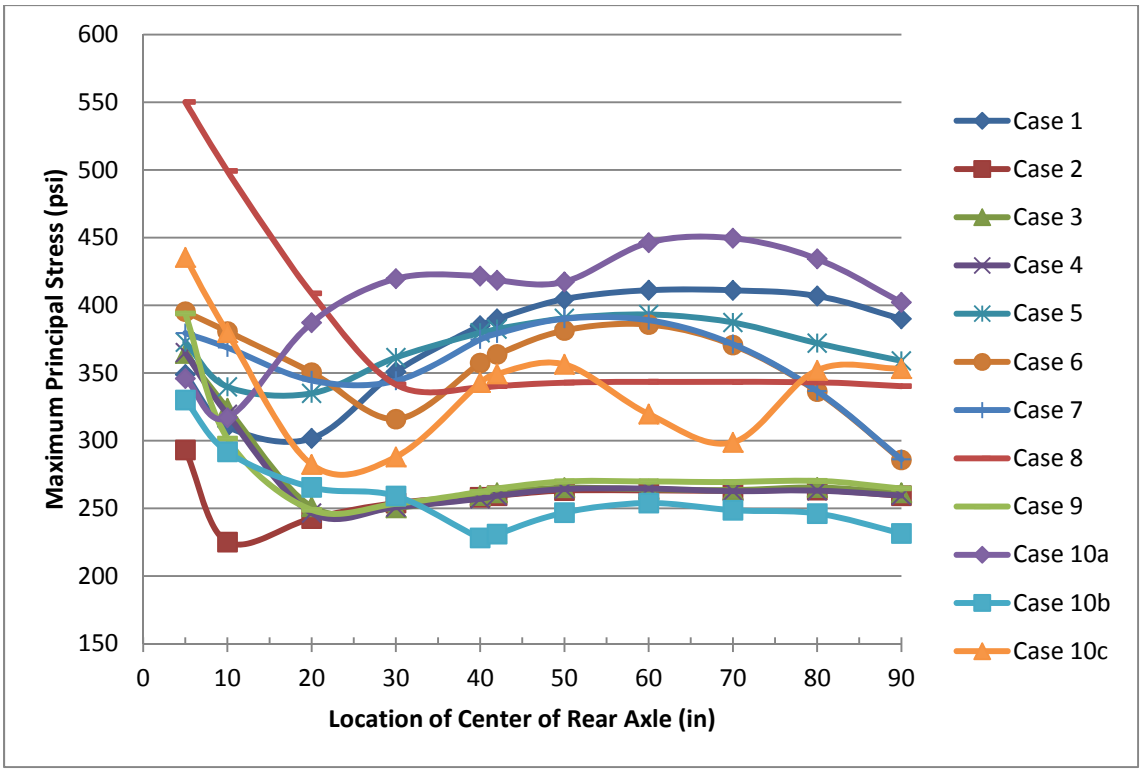

Figure 5. Maximum principal stress values for each tandem axle position and subgrade condition for no temperature differential and edge loading.

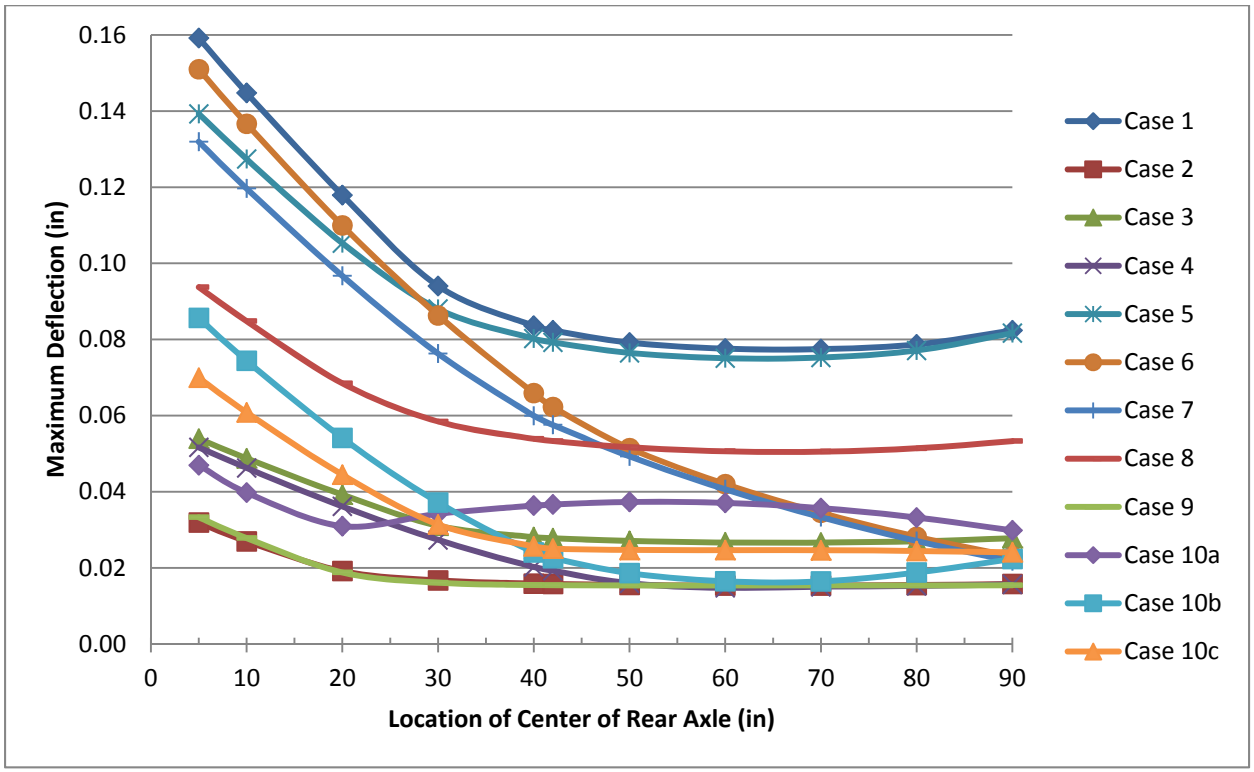

Figure 6. Maximum deflection values for each tandem axle position and subgrade condition for no temperature differential and edge loading.

The edge loading cases for the steer-drive axle (54-kip total weight) were reported only for the first four longitudinal positions after which the result would be the same as the tandem axle configuration since the front axle leaves the slab. For many cases the higher loading resulted in higher stresses (see Figure 7 and Figure 8). For all Cases except 3 and 4, the stresses caused by the steer-drive configuration were higher at the transverse edge compared to the tandem axle. As for the stresses at the last steer-drive loading location (just before the front axles leave the slab), for all Cases except 1, 5, and 10a, the stresses caused by the steer-drive were higher than from the tandem axle. The most extreme stress difference was 36%, but the average stress difference was 7%.

Compared to the tandem axle deflections, the deflections for the steer-drive configuration were lower at the transverse edge for all cases except Case 8. At the last steer-drive loading location (just before the front axle leaves the slab), the deflections were lower for only Cases 4, 6, 7, and 10a. The deflections for all cases differed least at and near the transverse edge and differed the most at the last steer-drive loading location. The greatest deflection difference was 44%, but the average difference was only 7.5%.

As in the tandem axle cases, Case 8 had the greatest tensile stress (568 psi) near the transverse edge position on the top of the slab and it was the maximum tensile stress of all positions for all axle configurations. As with the single and tandem instances, Case 2 had the lowest stresses and deflections with a uniform stiff soil under the slab. Case 10a did not have the highest tensile stress of the random nonuniform cases, but rather Cases 10b and 10c had higher stresses at certain axle positions. This result for the three axle configurations demonstrated that the maximum responses are a function of area of nonuniform support, axle configuration, and loading position on the slab. Overall, the deflections increased because of the steer-drive axle loads compared to the tandem axle. The deflection results were similar to those of the tandem findings: Cases 1, 6, and 5 had the highest overall deflections, cases with low subgrade stiffness along the longitudinal edge, while Cases 2 and 9 had the lowest deflections with high support stiffness along the edge.

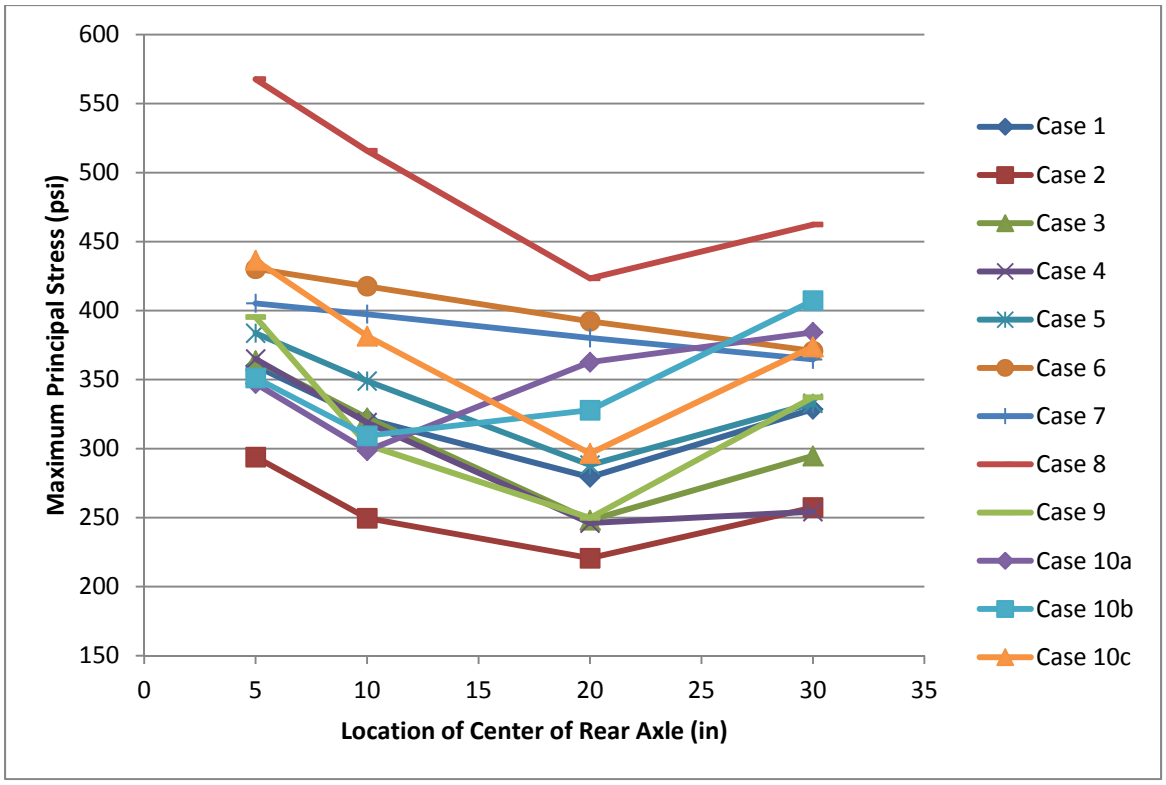

Figure 7. Maximum principal stress values for each steer-drive axle configuration position and subgrade condition for no temperature differential and edge loading.

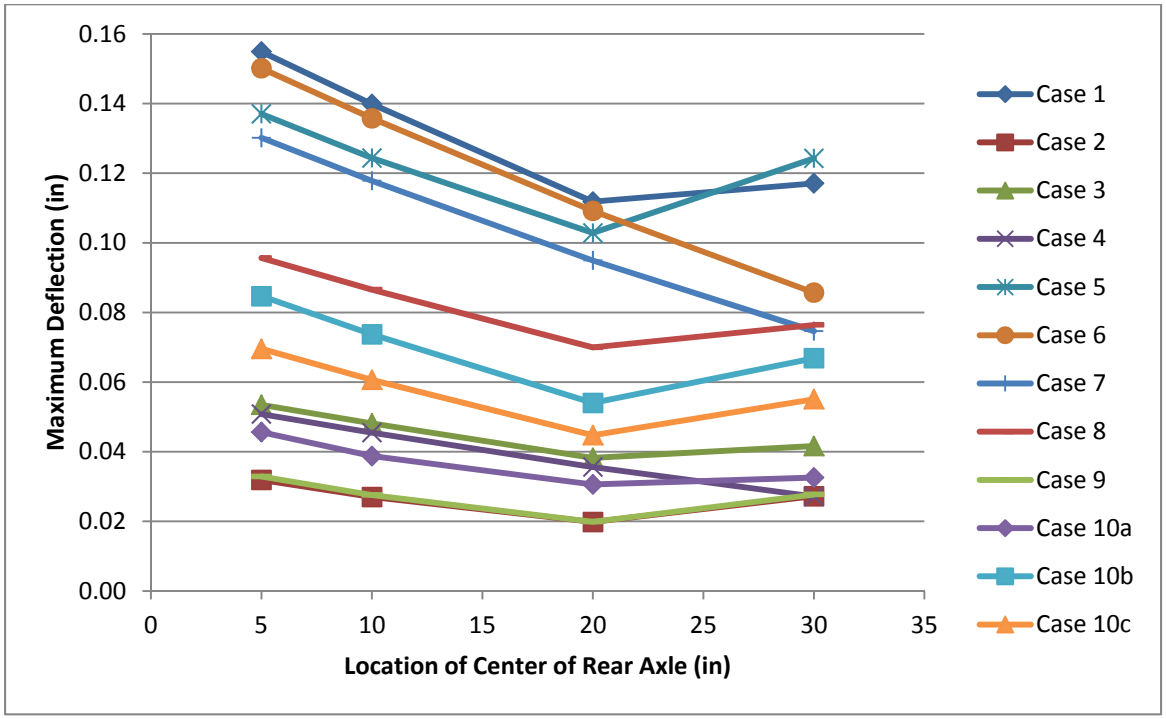

Figure 8. Maximum deflection values for each steer-drive axle configuration position and subgrade condition for no temperature differential and edge loading.

2.2.2 Wheelpath Loading

Overall, the tensile stresses in the slab when the axles were laterally offset 19 in from the edge (which is assumed wheelpath) were significantly lower than the edge-loaded cases. For the single axle wheelpath loading, Cases 1 and 10a had the largest stresses near the mid-slab longitudinal edge, but Cases 3, 4, 5, 7, 8, and 10b produced the maximum tensile stresses (~315 psi, as shown in Figure 9) at the transverse edge load position. These cases have a nonuniform support condition with areas of low soil stiffness near the transverse edge. Cases 2 and 9 had the lowest tensile stresses for the single axle wheelpath loading because of the nonuniform areas near the edge with high soil stiffness. As seen in Figure 10, Cases 1 and 6 had the greatest deflections, which occurred at the transverse edge load position while Cases 3 and 5 produced the largest deflections at the mid-slab longitudinal edge. Large deflections occurred when the axle was placed over areas of low stiffness soil.

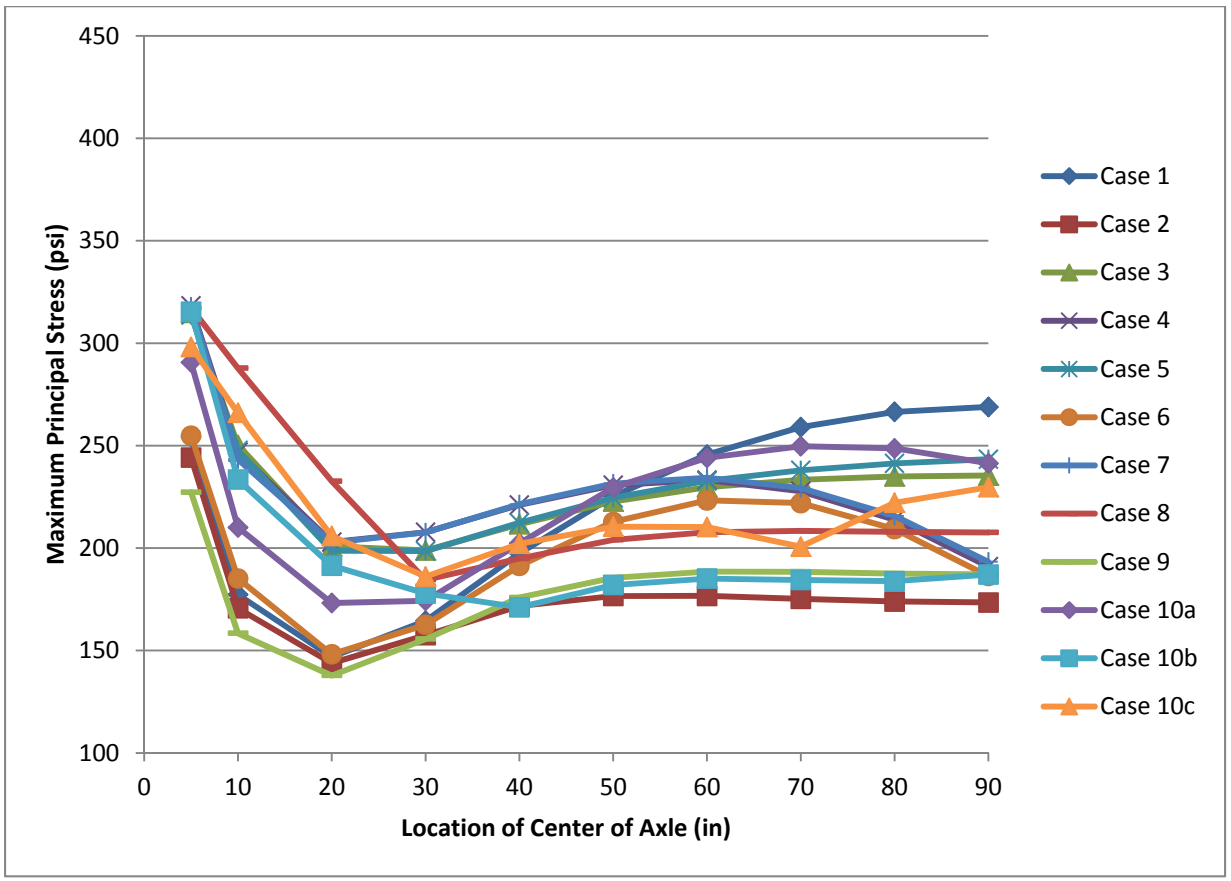

Figure 9. Maximum principal stress values for each single axle longitudinal position and subgrade condition for no temperature differential and wheelpath loading.

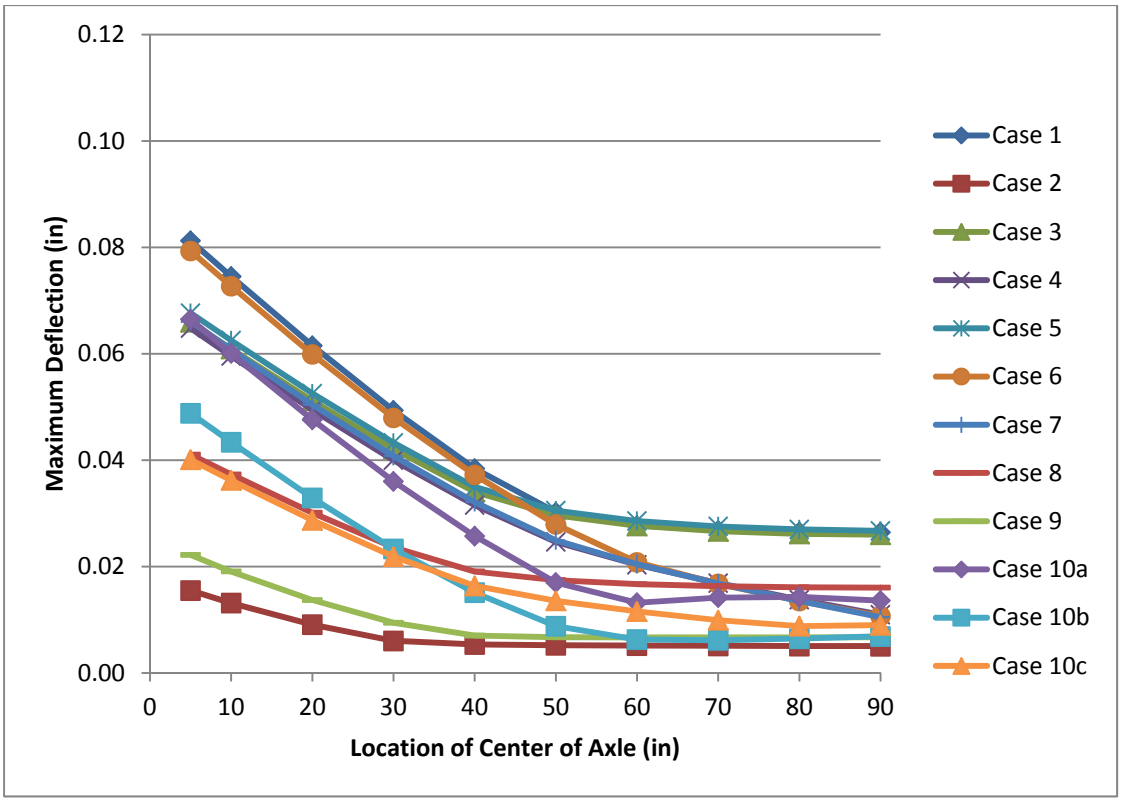

Figure 10. Maximum deflection values for each single axle longitudinal position and subgrade condition for no temperature differential and wheelpath loading.

For the tandem loading in the wheelpath (Figure 11), Case 8 had the highest overall tensile stress (421 psi), occurring at the transverse edge loading along with Cases 3, 4, 5, 7, and 10c having high stresses at that position as well. Cases 1 and 10a produced the highest stresses for the mid-slab longitudinal edge loading but were lower than the transverse edge loadings. Case 2 (uniform stiff) had the lowest overall tensile stress along with Case 9 (stiff edges). The deflections for the tandem cases were similar to the single axle cases. Cases 1 and 6 resulted in the highest deflections, occurring at the transverse edge, but dropped off and near the longitudinal edge. Cases 3 and 5 produced the largest deflections near the mid-slab edge, as seen in Figure 12.

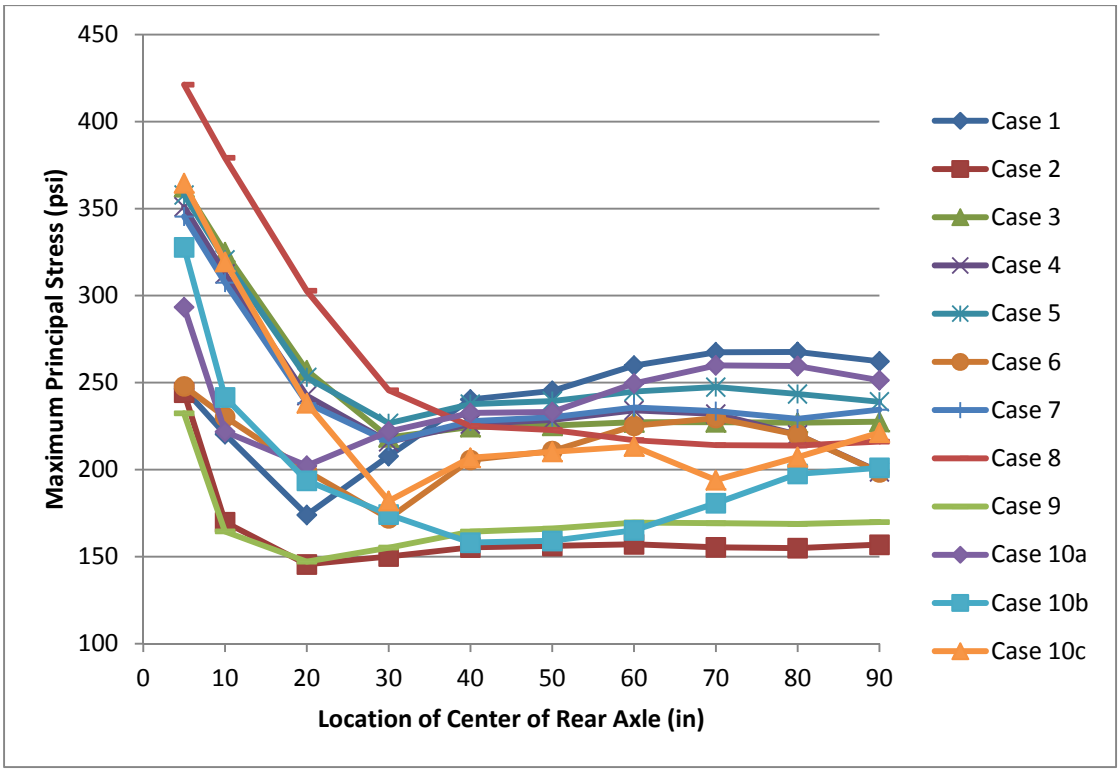

Figure 11. Maximum principal stress values for each tandem axle longitudinal position and subgrade condition for no temperature differential and wheelpath loading.

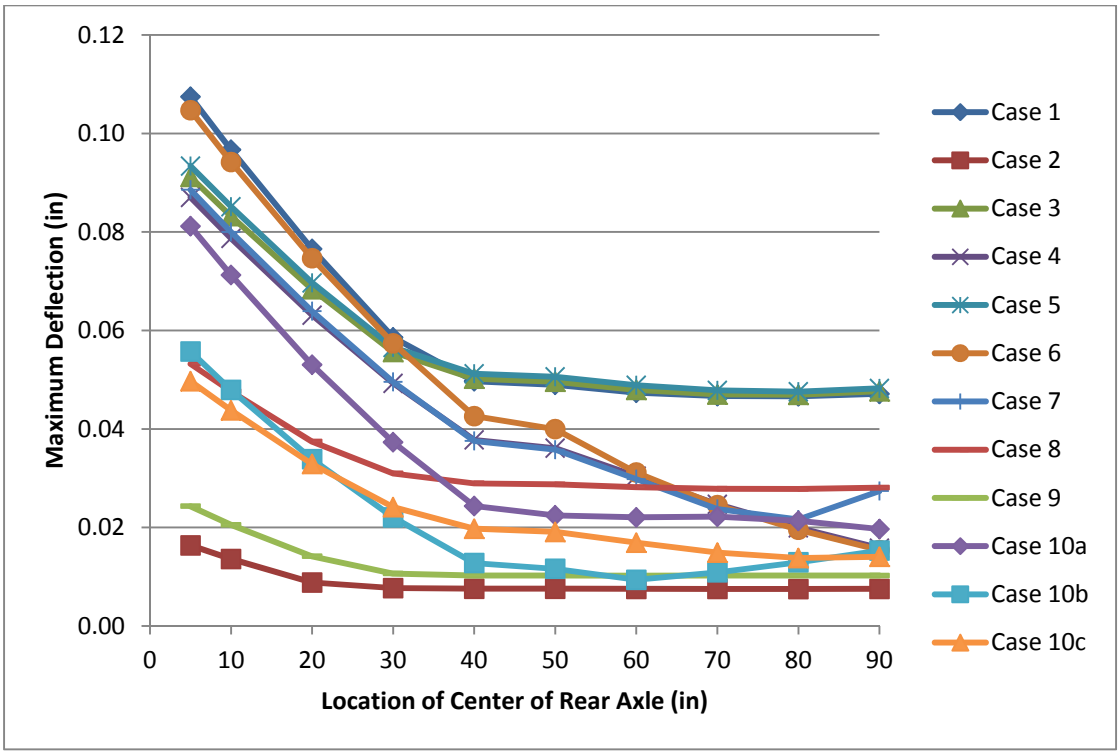

Figure 12. Maximum deflection values for each tandem axle longitudinal position and subgrade condition for no temperature differential and wheelpath loading.

The steer-drive results for the wheelpath loading were similar to the same cases for the edge loading. Case 8 in Figure 13 had the largest tensile stresses for the transverse edge (427 psi) and mid-slab load position (344 psi), and it was significantly higher than the other cases (see Figure 13). Cases 3, 4, 5, 7, 8, and 10c also had high tensile stresses at the transverse edge (approximately 350 psi) with the mid-slab longitudinal loading position also for these cases producing high tensile stresses but only around 300 psi. As seen in Figure 14, Cases 1 and 6 had the overall highest deflections occurring at the transverse edge, but Cases 1, 3, and 5 had the largest deflections at the mid-slab load position.

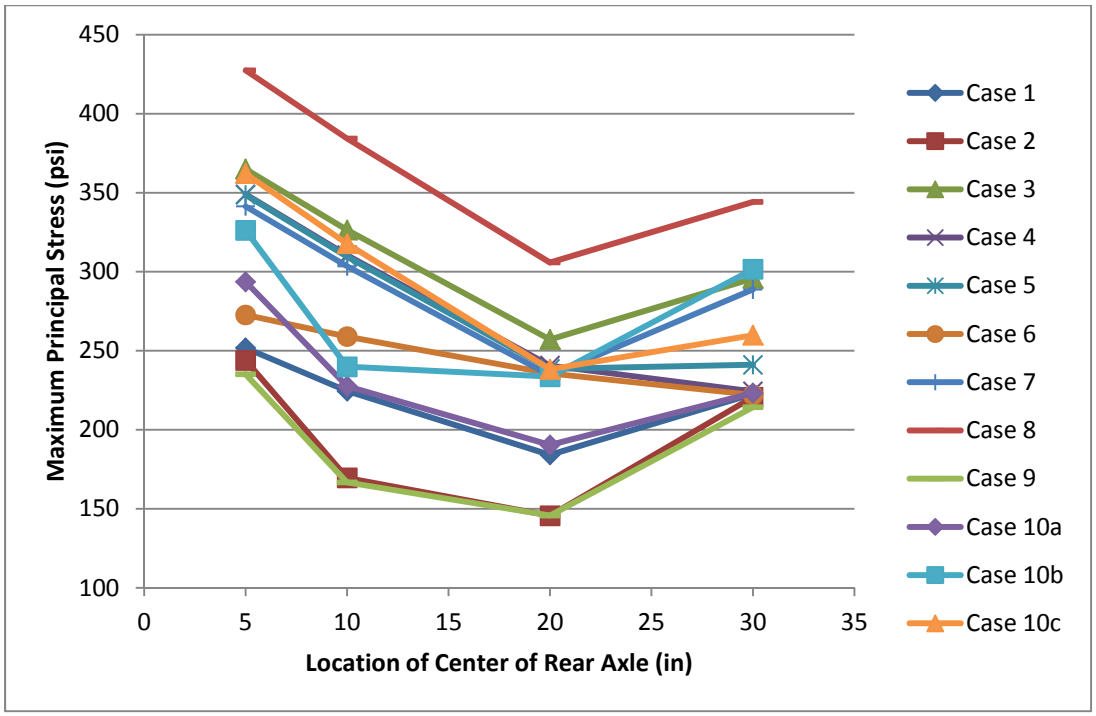

Figure 13. Maximum principal stress values for each steer-drive axle longitudinal position and subgrade condition for no temperature differential and wheelpath loading.

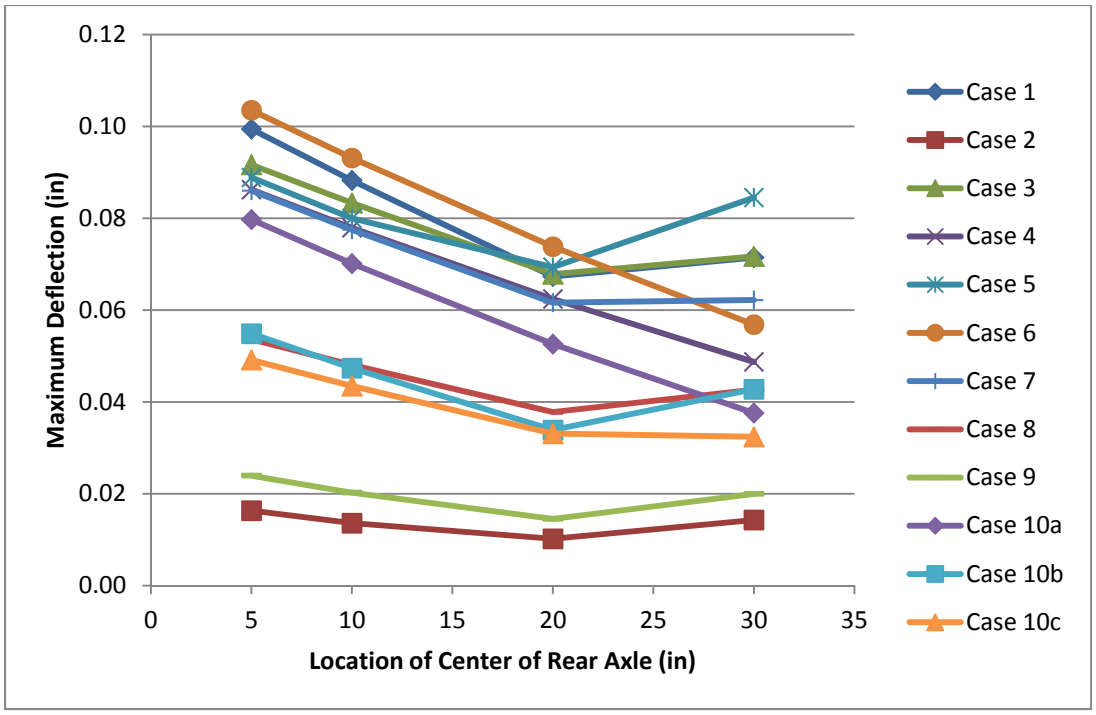

Figure 14. Maximum deflection values for each steer-drive axle longitudinal position and subgrade condition for no temperature differential and wheelpath loading.

2.3 Slab Response Results: Positive (+20°F) Temperature Differential

The addition of a positive linear temperature differential forces the concrete slab to curl downward, and it is expected to induce greater tensile stresses in the slab, especially under nonuniform support conditions and at the mid-slab longitudinal edge position. Deflection trends were not plotted in this section, since the deflection in ISLAB2000 is measured relative to a flat slab condition and not relative to an initial curled (unloaded) slab position.

2.3.1 Edge Loading

With the positive temperature differential, the nonuniform subgrade cases resulted in similar or higher tensile stresses than the uniform cases, as seen in Figure 15. Compared to the no temperature differential case, with the exception of Cases 1 and 2, the maximum stress was greater because of the added +20°F differential; the greatest stress differences occurred with the random subgrade cases, particularly Case 10c which had a 25% difference. Case 10a resulted in the highest tensile stresses (674 psi) for the single axle cases. The other random cases (Cases 10b and 10c) had much lower stresses between the transverse and mid-slab edges, although Case 10c drastically increased at the mid-slab edge, having almost the same stress as Case 8. Case 7 had the highest stress of the quadrant cases (Cases 4-7) as well as the second highest tensile stress (578 psi). Additionally, Case 8, which had high tensile stresses without a temperature differential, still had the same tensile stress as Case 7. Case 9, which had low tensile stresses without a temperature differential, had the highest transverse edge stress (480 psi) of all cases.

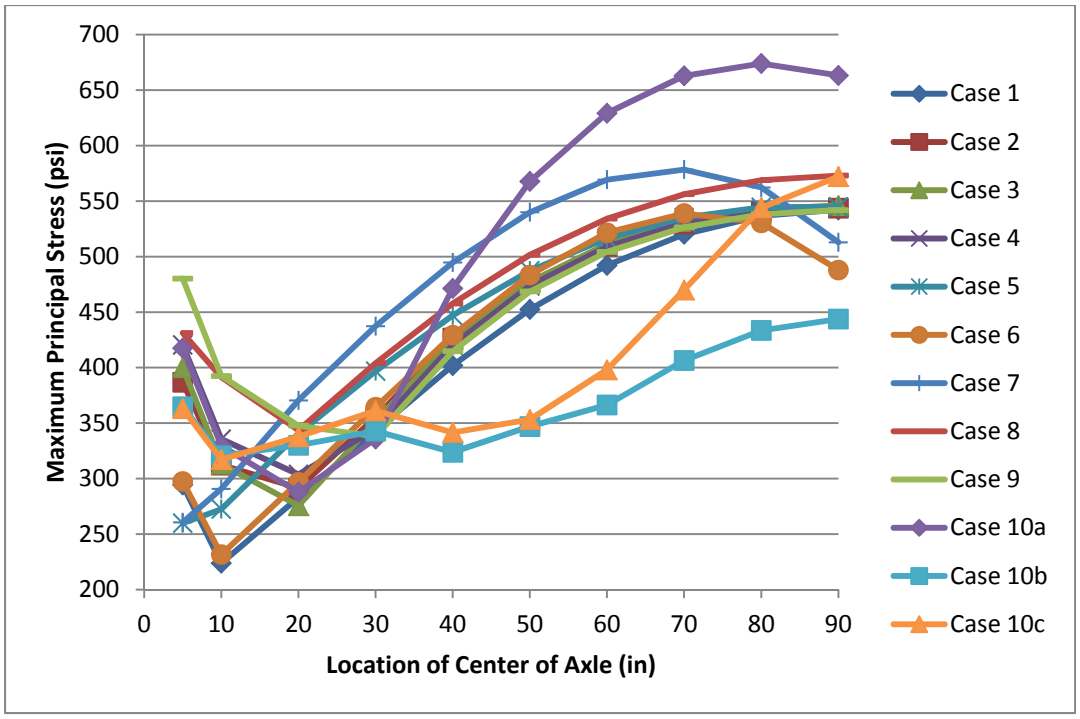

Figure 15. Maximum principal stress values for each single axle position and subgrade condition with a +20°F temperature differential and edge loading.

With the increased load from the tandem axle, numerous nonuniform cases experienced an increase in tensile stresses, as seen in Figure 16, over tandem axle results with no temperature differential. As with the single axle results, all cases (except Cases 1 and 2), experienced an increase in the maximum stress value because of the added positive temperature differential. However, it should be noted that the Case 2 stresses were nearly unaffected by the differential since the maximum stress value differed by only 0.3%. Because of the two axles in the tandem configuration with temperature loading, the maximum tensile stresses at each load position did not vary as much as the single axle cases in Figure 15. Case 10a produced the largest tensile stress in the bottom of the slab (676 psi) when the axle was positioned near the mid-slab edge, and this stress was 32% greater than the uniform soft (Case 1) maximum tensile stress. With the random nonuniform cases, while Case 10a had the highest tensile stresses, Case 10b resulted in the lowest tensile stresses at almost all axle positions. Case 8 had the highest transverse edge stresses and Case 7 produced the highest stresses of the four quadrant cases. The uniform subgrade cases (Cases 1 and 2) produced tensile stresses similar to other nonuniform cases.

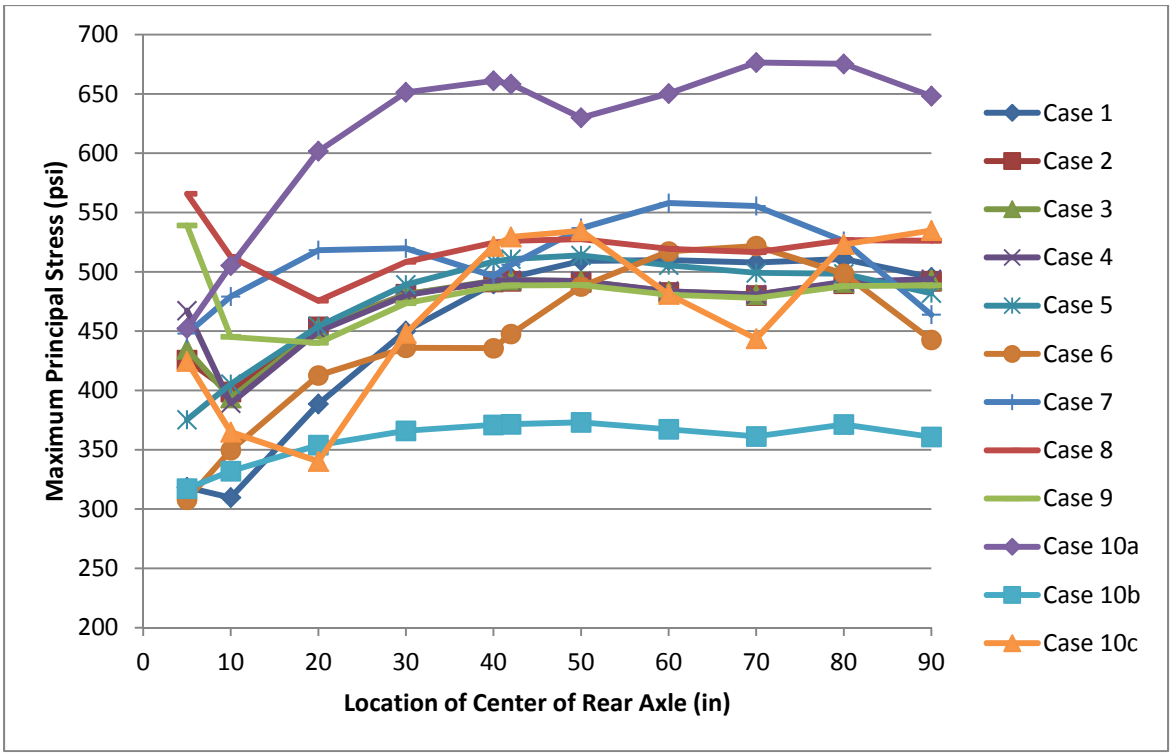

Figure 16. Maximum principal stress values for each tandem axle position and subgrade condition with a +20°F temperature differential and edge loading.

The steer-drive stress magnitudes were similar to the tandem results as seen in Figure 17. Case 10a had the highest overall tensile stress (616 psi), Cases 8 and 9 had the second and third highest tensile stresses and they occurred at the transverse edge load position. Again, Case 7 had the highest tensile stresses of the quadrant cases. The most interesting result from the steer-drive loading was Case 1 (uniform soft) which produced the lowest stresses in almost all load positions. The combination of multiple axles and lower curling stresses produced this outcome.

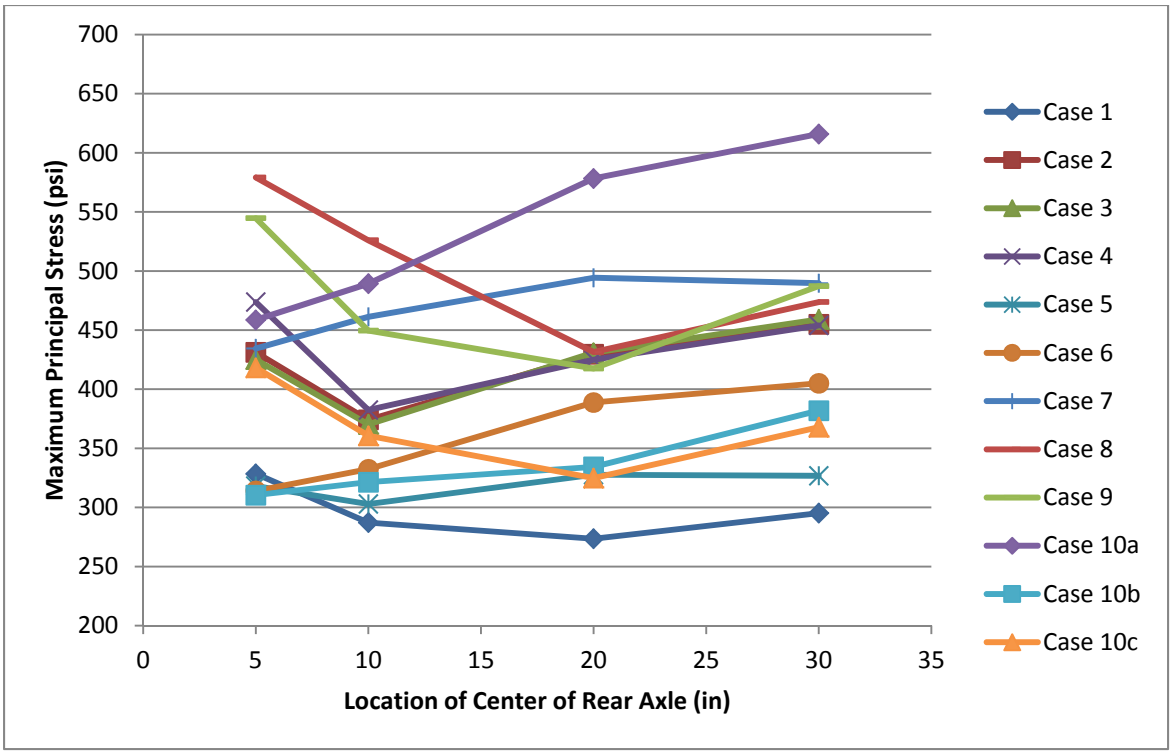

Figure 17. Maximum principal stress values for each steer-drive axle configuration position and subgrade condition with a +20°F temperature differential and edge loading.

2.3.2 Wheelpath Loading

Compared to the edge loading with single axle, the wheelpath loading resulted in lower tensile stresses for most cases (see Figure 18 versus Figure 15). Case 10a produced the maximum tensile stress (468 psi) near the mid-slab load position while Case 10b had the highest tensile stress (378 psi) at the transverse edge load position. Cases 2, 3, 4, and 7 had approximately the same stresses near the mid-slab load position (~420 psi). Like the steer-drive axle at the edge loading positions with positive temperature differential in the slab, Cases 1 had the lowest tensile stress at almost all axle positions.

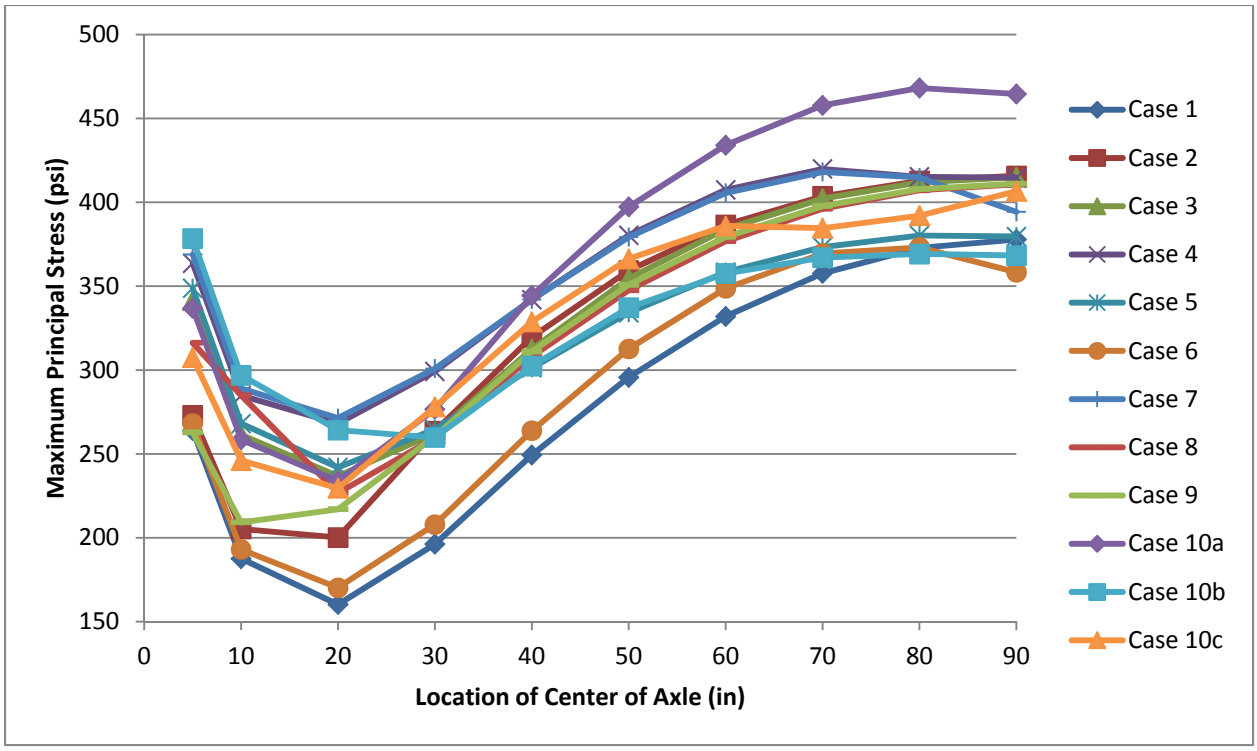

Figure 18. Maximum principal stress values for each single axle longitudinal position and subgrade condition for wheelpath loading with a +20°F temperature differential.

The tandem axle configuration with a positive differential increased the tensile stresses over the no temperature cases when comparing Figure 19 to Figure 11. Case 10a produced the maximum tensile stress (475 psi) near the mid-slab edge position with +20°F temperature differential compared to Case 8 (421 psi) in the no temperature case. Cases 4 and 7 also resulted in high tensile stresses (~420 psi) near the mid-slab edge position. At the transverse edge, the highest tensile stresses (~410 psi) occurred with Cases 8 and 10b. From the transverse edge to past a quarter into the slab, the lowest tensile stresses occurred with Cases 1 and 6 which had areas of weak uniform soil under the axle at these positions. At the mid-slab edge, Cases 5 and 10b produced the lowest tensile stresses.

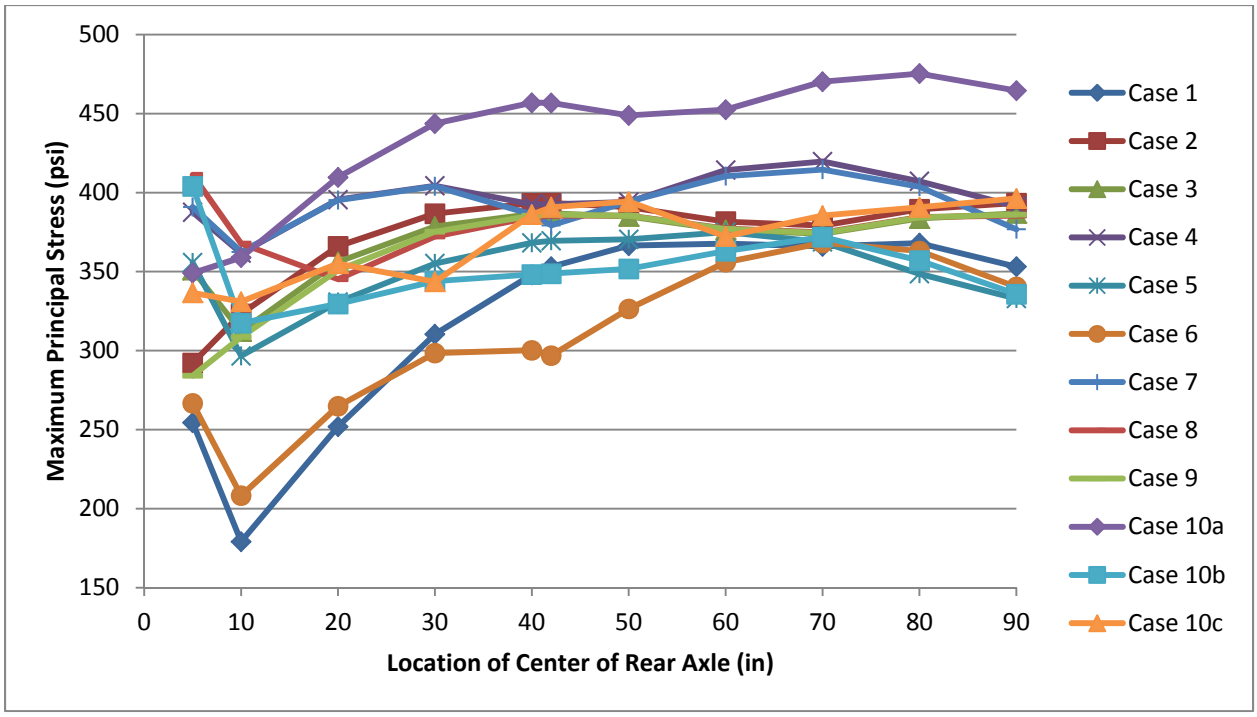

Figure 19. Maximum principal stress values for each tandem axle longitudinal position and subgrade condition for wheelpath loading with a +20°F temperature differential.

The results of the steer-drive axle configuration, shown in Figure 20, showed that Cases 10a (419 psi), 4, and 7 had the highest stresses away from the transverse edge while Cases 8 (414 psi) and 10b had the greatest tensile stress at the transverse edge load position. Case 1 produced the lowest tensile stress at each axle position similar to the steer-drive axle edge loading analyses in Figure 17.

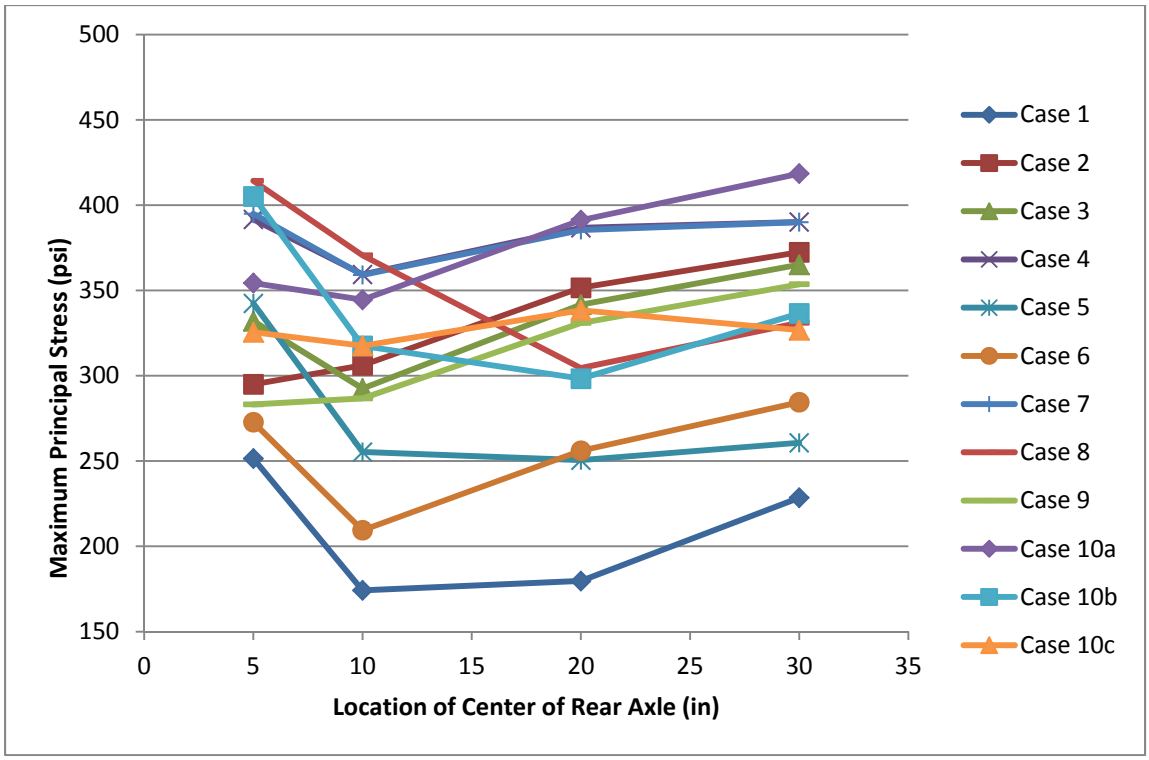

Figure 20. Maximum principal stress values for each steer-drive axle longitudinal position and subgrade condition for wheelpath loading with a +20°F temperature differential.

2.4 Slab Response Results: Negative (-20°F) Temperature Differential

The addition of a negative linear temperature differential should induce high stresses in the top of the slab since the slab will be forced to curl upwards. The critical tensile locations and magnitudes will be at different locations than the positive temperature differential cases because of the change in slab support under a negative temperature gradient. As with the positive differential, the deflection plots are not shown in this section because of the unrepresentative deflection calculation in ISLAB2000.

2.4.1 Edge Loading

The highest tensile stresses for the single axle occurred near the transverse edge load position as seen in Figure 21. Case 8, like the other input combinations, created the maximum tensile stress (476 psi) on top of the slab at the transverse edge whereas previous cases had critical stresses at the bottom of the slab. Cases 10b (445 psi) and 10c (420 psi) had high tensile stresses at the transverse edge on the top of the slab while Case 10a had the highest tensile stresses (340psi) near the mid-slab edge position. Like Case 10c, Cases 3 and 4 had similar tensile stresses, 426 and 424 psi, respectively, and stiff subgrade support areas near the critical tensile stress locations at the transverse edge. Case 9 (stiff edges) had high tensile stresses for the +20°F differential but produced the lowest tensile stresses because of the -20°F differential.

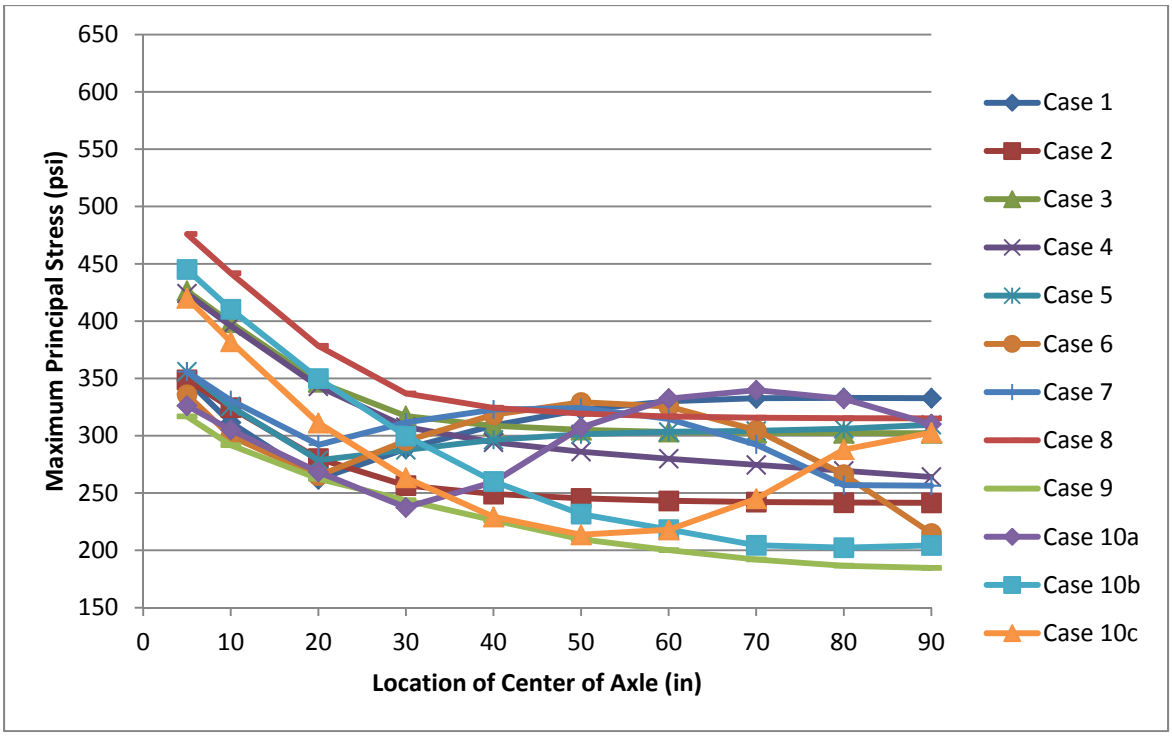

Figure 21. Maximum principal stress values for each single axle longitudinal position and subgrade condition with a -20°F temperature differential and edge loading.

The tandem axle loading produced greater tensile stresses than the single axle for the -20°F differential, as shown in Figure 22. Again, Case 8 produced the highest tensile stresses for all load positions with a maximum value (629 psi) occurring at the transverse edge position on the top of the slab. The -20°F temperature differential impacted cases that did not produce high tensile stresses in the slab such as Case 3, which had the second highest tensile stress (510 psi). Cases 4 and 10c also had high tensile stresses at the top of the slab at the transverse edge load position. The tensile stresses for Case 9 increased only slightly from the single axle loading and it still produced the lowest tensile stresses for all load positions.

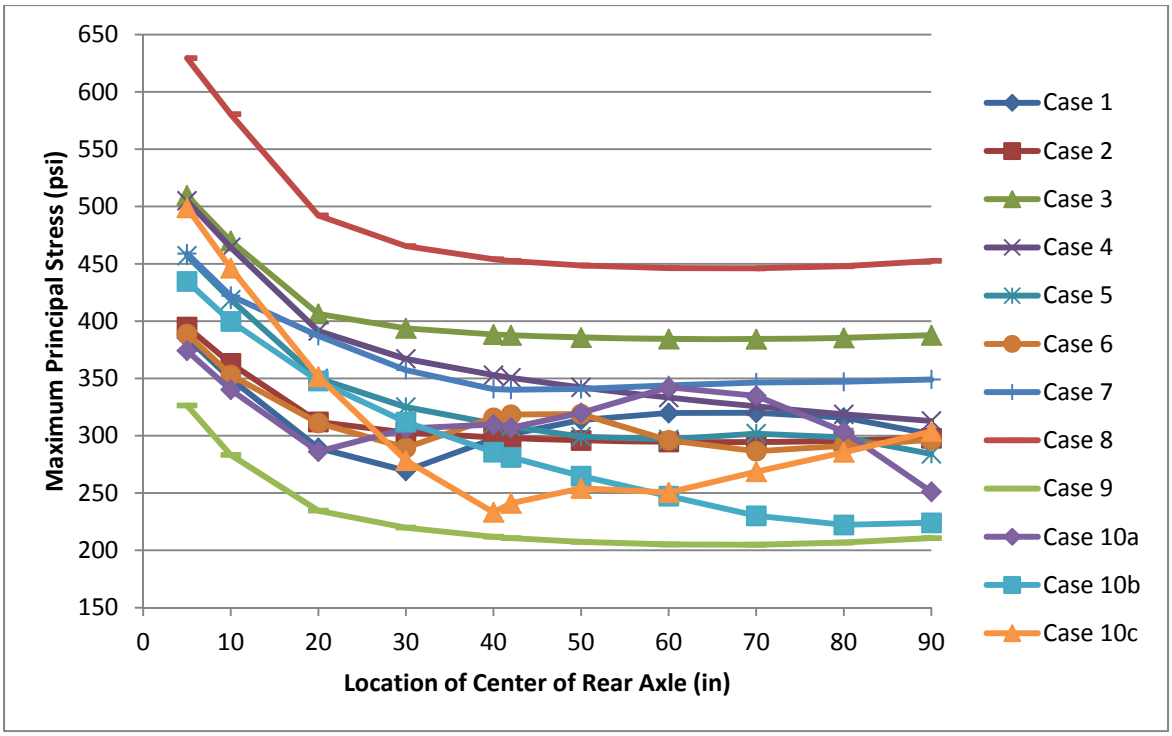

Figure 22. Maximum principal stress values for each tandem axle longitudinal position and subgrade condition with a -20°F temperature differential and edge loading.

The steer-drive results had similar trends to the tandem results but also had several cases that were critical as seen in Figure 23. Case 8 had the highest transverse edge stress at the top of the slab (637 psi), which is consistent with the previous single and tandem axle loadings. Case 6 had a high transverse edge stress of 629 psi and the greatest stress at the mid-slab edge loading position (578 psi) on the top of the slab. Case 7 also had high tensile stresses exceeding 550 psi for all load positions. Case 9 had the lowest tensile stresses, again like the single and tandem cases.

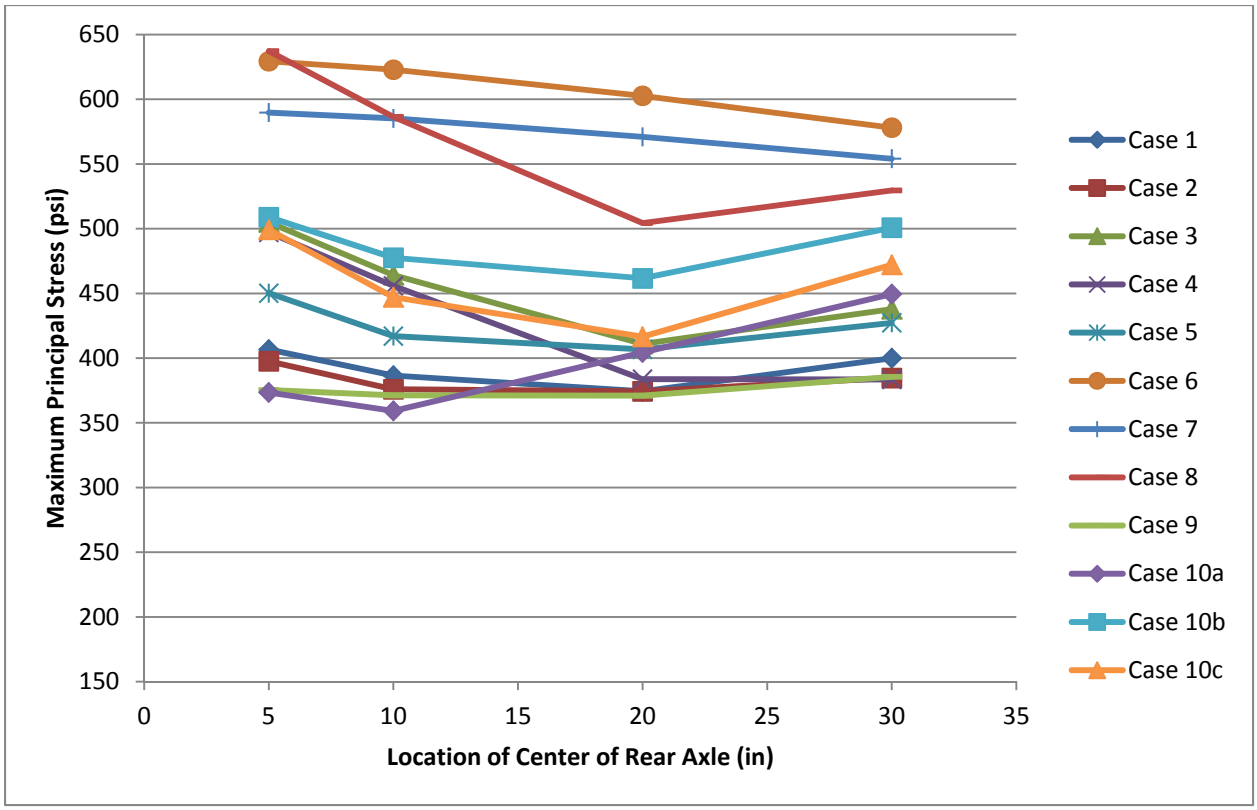

Figure 23. Maximum principal stress values for each steer-drive axle configuration position and subgrade condition with a -20°F temperature differential and edge loading.

2.4.2 Wheelpath Loading

With the single axle wheelpath loading for a -20°F temperature differential, shown in Figure 24, the critical tensile stress occurred at the transverse edge load position, mainly occurring at the top of the slab. Case 8 produced the largest tensile stress (421 psi) on the top of the slab between the axle (at x,y = 72,0 in) followed closely by Cases 3 (414 psi), 4 (412 psi), 5 (404 psi), and 7 (405 psi). Larger nonuniform areas with high soil stiffness produced these higher tensile stresses under negative temperature curling conditions. The random support cases (10a, 10b, 10c) also had reasonably high tensile stresses (366, 348, 395 psi, respectively) at the transverse edge loading. At the transverse edge, the lowest stresses occurred in Cases 1, 6, and 9, while Case 9 produced the overall smallest tensile stress at the mid-slab edge position.

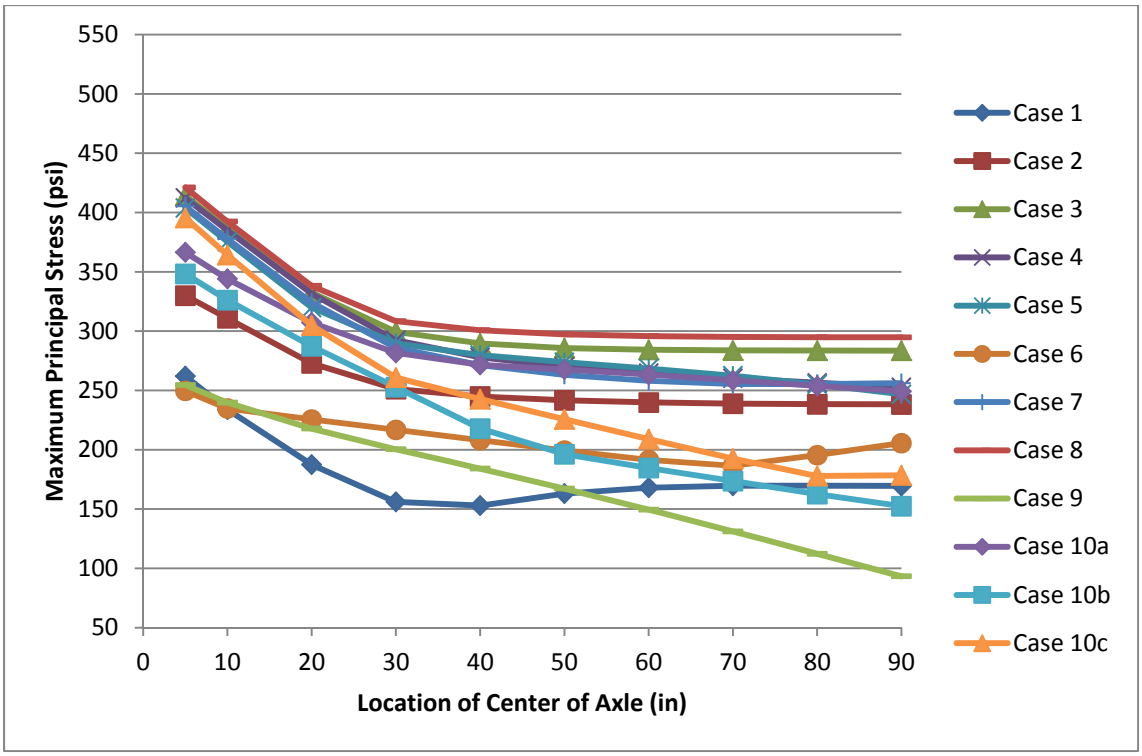

Figure 24. Maximum principal stress values for each single axle longitudinal position and subgrade condition for wheelpath loading with a -20°F temperature differential.

The tandem axle results were similar to the single axle behavior except for the tensile stress magnitudes, which were greater as seen in Figure 25 compared to Figure 24. Case 8 produced the largest tensile stress of 530 psi on the top of the slab between the axle (at x,y = 72,0 in) followed closely by Cases 3 (515 psi), 4 (505 psi), 5 (502 psi), and 7 (496 psi). Case 9 produced the lowest tensile stresses for all load positions. The analysis has clearly shown that the nonuniformity in the soil support layer produces greater tensile stresses in the slab than the uniform higher stiffness soil under curling conditions (i.e., comparing the peak tensile stress cases with Cases 1 and 2).

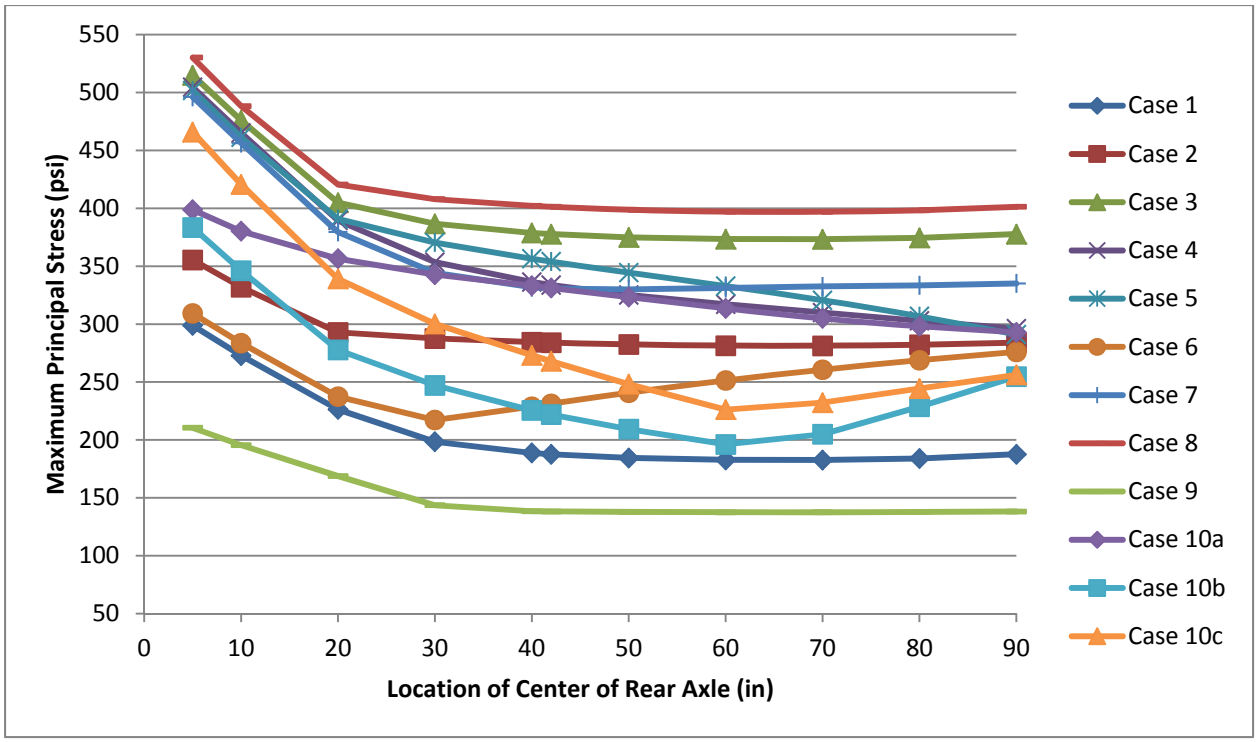

Figure 25. Maximum principal stress values for tandem axle longitudinal position and subgrade condition for wheelpath loading with a -20°F temperature differential.

Overall, the tensile stresses are higher because of the combined effect of curling and steer-drive loading, but the maximum tensile stress values are not much greater than the tandem axle, as seen in Figure 26. Case 8 again produced the largest tensile stress (530 psi) at the transverse edge load position on the top of the slab between the axles. Case 3 also had a high tensile stress (512 psi) at the transverse edge. Cases 6 and 8 had the highest tensile stresses, 450 and 447 psi, respectively, at the mid-slab loading position. Cases 1 and 9 had the lowest tensile stresses for all load positions followed by Case 2. For the steer-drive combination and negative temperature curling, the greatest tensile stresses in the slab were generated with nonuniform support conditions on the top of the slab.

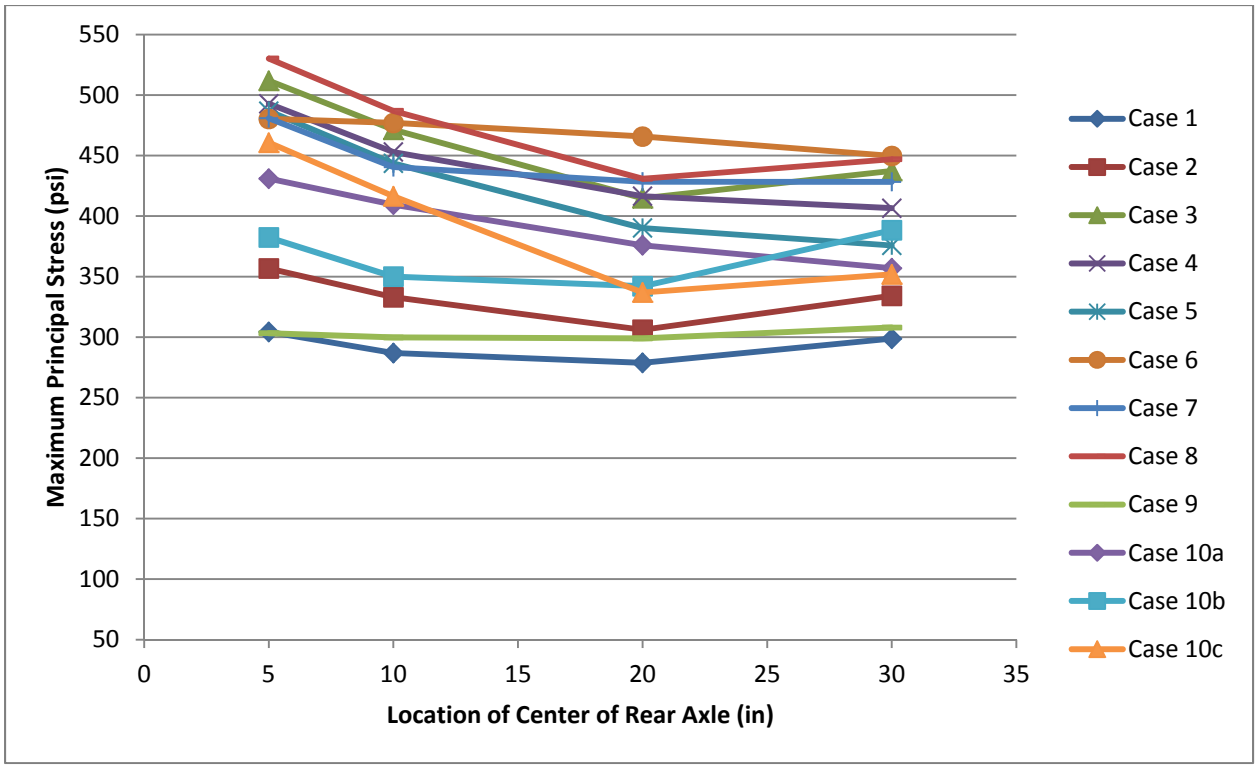

Figure 26. Maximum principal stress values for each steer-drive axle configuration position and subgrade condition for wheelpath loading with a -20°F temperature differential.

2.5 Effects Analysis on Peak Tensile Stresses with Linear Regression

A multiple linear regression analysis was performed in order to determine the overall effects of the input variables on the factorial analysis. A similar methodology was performed as previously conducted by Evangelista and Roesler (2009). For each of the individual 12 subgrade conditions, a multiple linear regression equation was used to evaluate the effects of the first-order, second-order, and third-order interactions of the linear temperature differential (0, -20, +20°F), lateral offset position (edge and wheelpath loading), and axle type (single and tandem). To simply the analysis, only two temperature differentials were compared simultaneously. Similarly, only two axle types were compared (single and tandem) since the steer-drive axle often produced similar or lower stresses than the tandem axle. Subsequently, this left two values for each variable to consider.

The overall peak tensile stress was selected from each set of runs with the axle traveling along the slab. Each of the variables in the regression was coded based on “high” (+1) and “low” (-1) conditions. The multiple linear regression model used the following form, where *Y* is the peak tensile stress (maximum principal stress), μ is the average peak tensile stress for the given subgrade condition, $x_{i,j,k}$ are the coded variables, and α are the regression coefficients (*i* is a first-order, *j* is a second-order, and *k* is a third-order interaction):

$$Y = \mu + \sum_{i=1}^{3} \alpha_i x_i + \sum_{i<j}^{3} \sum \alpha_{ij} x_i x_j + \sum_{i<j<k}^{3} \sum \sum \alpha_{ijk} x_i x_j x_k$$

For comparability, each regression coefficient was divided by the mean value in order to normalize the effect. The magnitude of each regression coefficient provides information on the

"effect" of each variable on the mean. For example, a positive regression coefficient with a very high magnitude would indicate that as that variable is increased from the low (-1) condition to the high (+1) condition, the mean would increase.

2.5.1 Input Variable Effects for 0 and +20°F Differentials

In this regression analysis, the variables were coded as shown in Table 3. As previously discussed, this regression analysis only considered two changes in each variable: temperature differential (0 and +20°F), axle type (single and tandem), and lateral offset (wheelpath and edge loading). The first-order normalized regression coefficients (percentage) are shown in Figure 27, and the second- and third-order interactions are plotted in Figure 28.

Table 3. Coded Variables Comparing for the Regression Analysis with 0°F and +20°F Differentials

Variable	**Coded Variable**	
	"Low" (-1)	**"High" (+1)**
Temperature Differential	0°F	+20°F
Lateral Offset	Wheelpath Loading	Edge Loading
Axle Type	Single	Tandem

The most prominent "effects" are the first-order interactions (Figure 27), particularly the temperature differential and lateral offset variables. The regression coefficients suggest that as the differential is "increased" from 0°F to +20°F, the peak tensile stresses will increase as one would expect. Cases 2 (uniform stiff), 9 (stiff edges), and 10a (random) are most affected by the change in temperature differential. The regression coefficients suggest that the slab tensile stresses caused by a nonuniform support may be more or less affected by a positive temperature differential relative to a uniformly supported slab depending on the position of the load and the local support condition. The regression coefficients also showed that as the lateral offset is changed (increased) from wheelpath to edge loading, the peak tensile stress is expected to increase. This result was expected because edge loading is almost always greater than loading in the wheelpath. The final first-order interaction, axle type, revealed that most cases were not very significantly influenced as the axle type "increases" from a single to a tandem axle, with the exception of Case 8 (soft edges). For the uniform support conditions (Cases 1 and 2), the stress is expected to decrease as the axle type "increases" from single to tandem. Of the higher-order interactions (Figure 28), it is evident that there was not much interaction between the variables to significantly affect the mean maximum peak tensile stress.

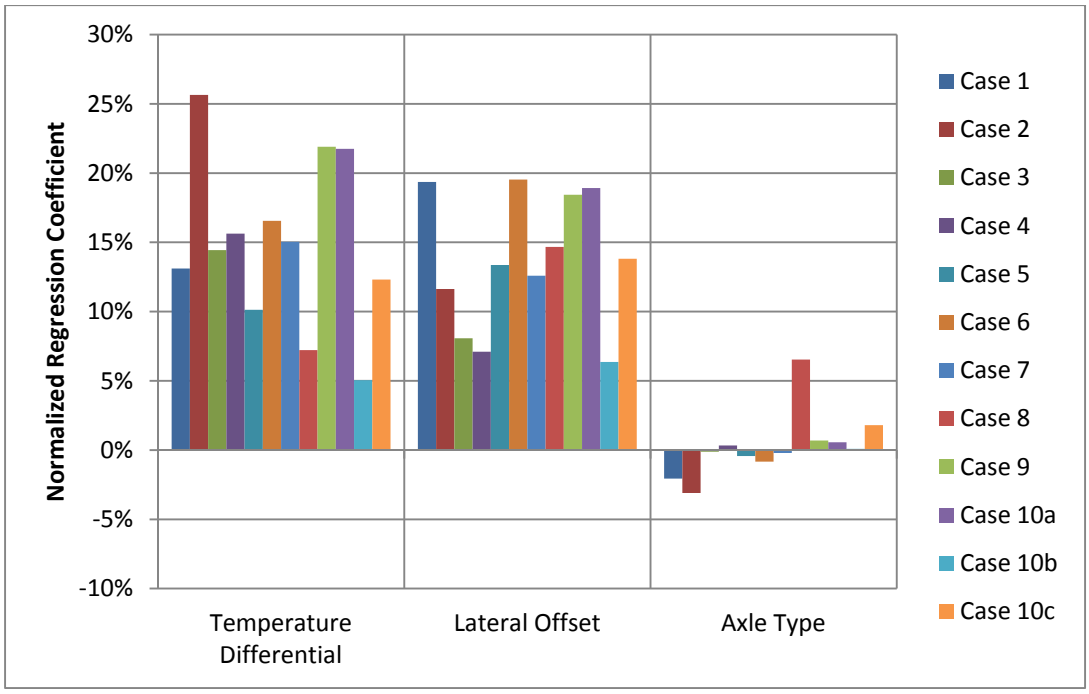

Figure 27. The first-order regression coefficients for temperature differential, lateral offset, and axle type for the 0 and +20°F comparison.

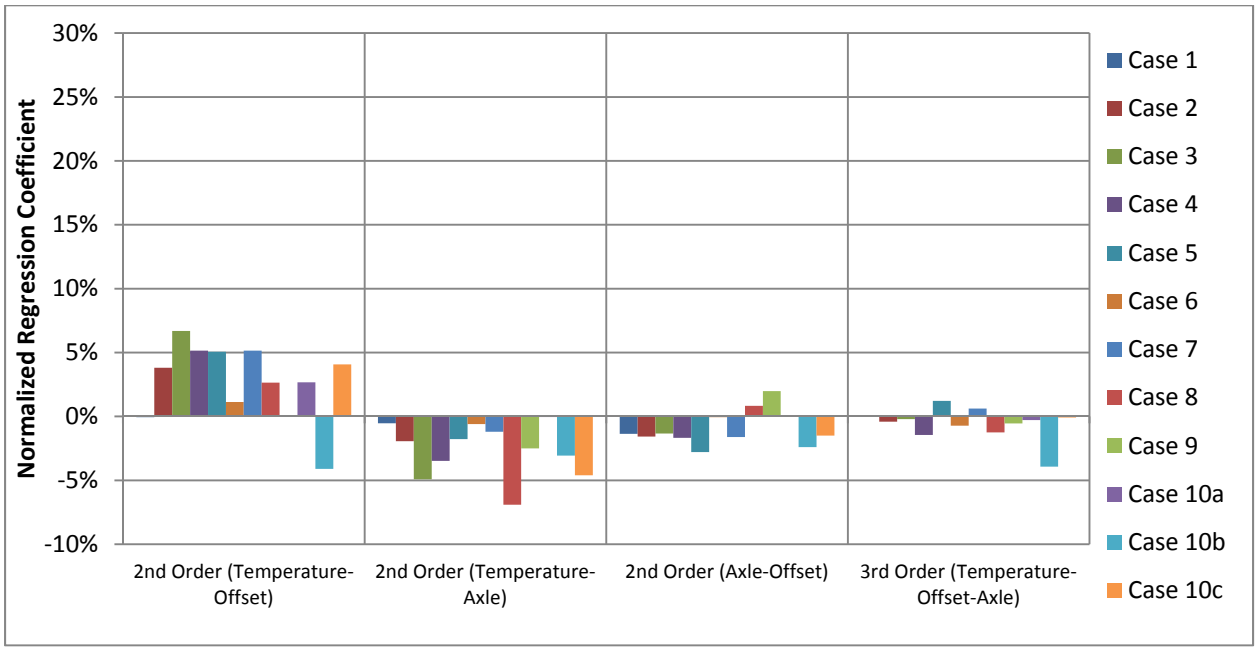

Figure 28. The second- and third-order regression coefficients for temperature differential (0 and +20°F), lateral offset, and axle type.

2.5.2 Input Variable Effects for 0 and -20°F Differentials

A similar linear regression analysis was conducted to compare two values per variable, as shown in Table 4, for the 0°F and -20°F differentials. As can be seen in Figure 29, the effect of a negative temperature differential may not necessarily result in an increase in the peak slab

tensile stress for a certain subgrade support condition. Overall, the slab tensile stresses were more affected by a positive than a negative differential. As expected, the regression coefficients suggest that the slab tensile stresses would decrease when moving from an edge-loaded to a wheelpath-loaded condition. The axle type appeared to have a greater impact for this linear regression since the coefficients demonstrate that the tensile stresses would increase when loading the slab with a tandem versus a single axle. Although this finding is contradictory to the zero temperature differential case in Figure 27, the influence of the negative temperature on the mean value produces this higher sensitivity when moving from single to tandem. The higher-order regression coefficients (Figure 30) suggest that there are slightly more variable interactions than in the previous analysis (see Figure 28).

Table 4. Coded Variables Comparing for the Regression Analysis with 0°F and -20°F Differentials

Variable	**Coded Variable**	
	"Low" (-1)	**"High" (+1)**
Temperature Differential	0°F	-20°F
Axle Type	Single	Tandem
Lateral Offset	Wheelpath Loading	Edge Loading

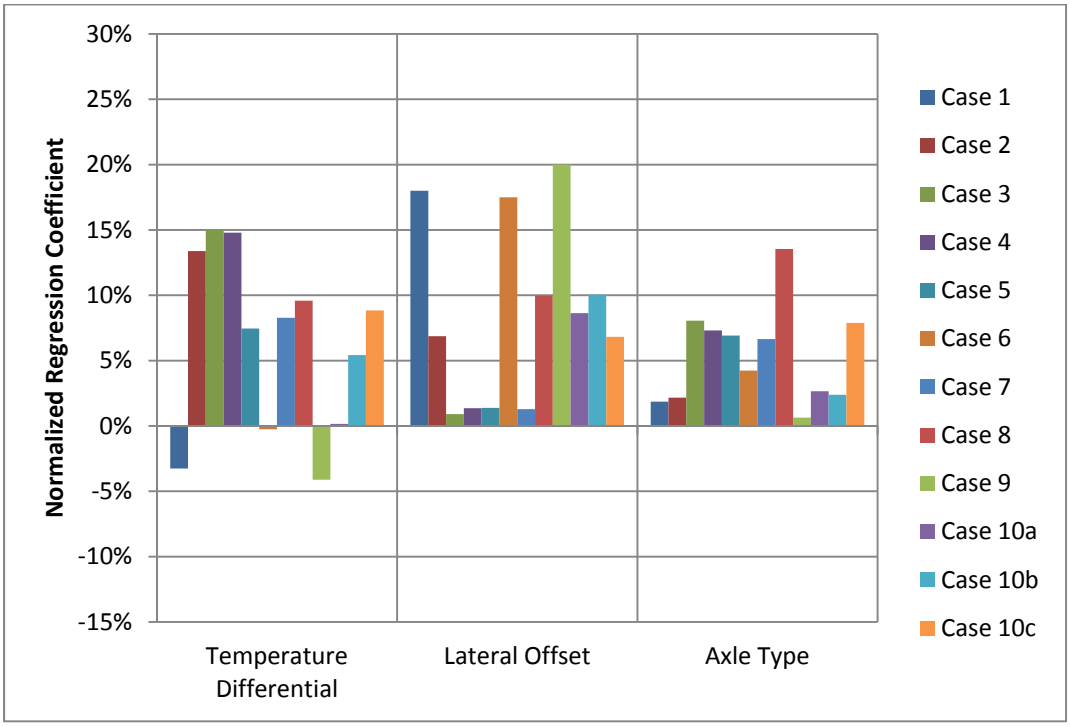

Figure 29. The first-order regression coefficients for temperature differential (0°F and -20°F), lateral offset, and axle type.

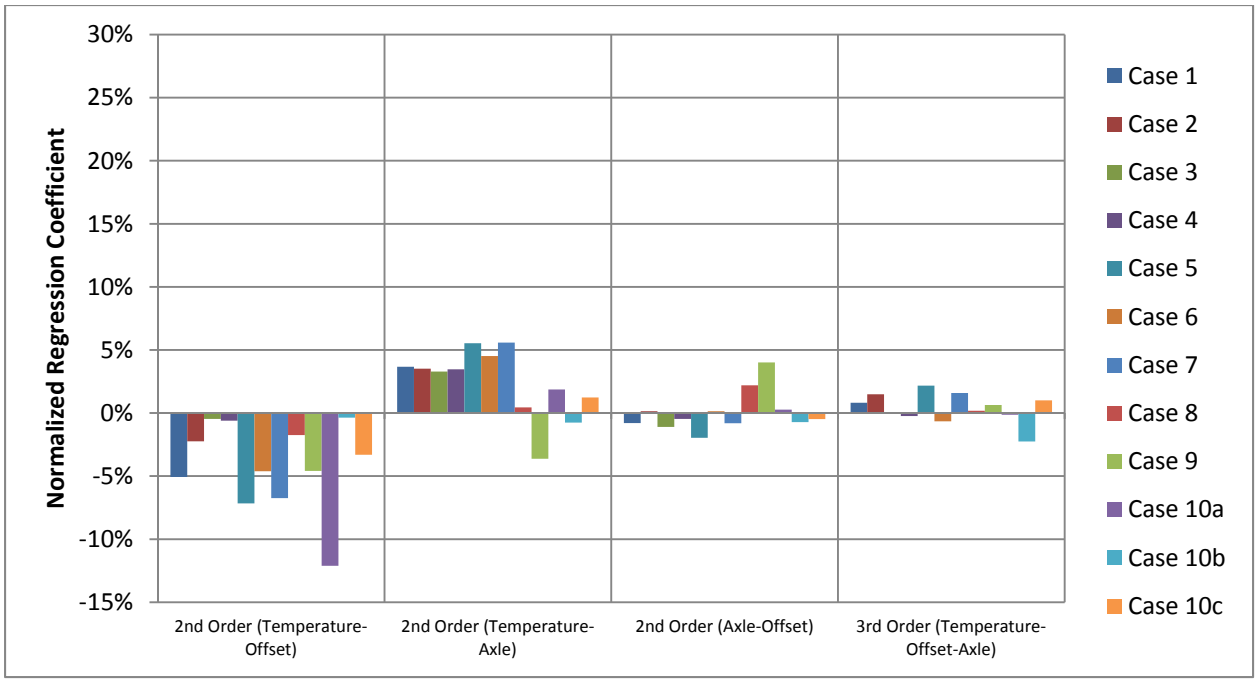

Figure 30. The second- and third-order regression coefficients for temperature differential (0°F and -20°F), lateral offset, and axle type.

2.5.3 Statistics of the Peak Tensile Stresses

While the linear regression "effects" analyses demonstrated that certain input variables and interactions have a more profound impact on the resultant peak tensile stresses, it does not provide any indication of the magnitude of the resultant stress. Figure 31 shows the average of the peak tensile stresses for each subgrade condition. Case 8 produced the highest average stresses followed by Cases 7 and 10a. So while the regression results (Figure 27 and Figure 29) show that Cases 1, 2, 6, and 9 are among the cases most affected by the variables and interactions, it is evident that these cases did not result in the highest tensile stresses (Figure 31) but were rather among the cases with the lowest stresses. The statistics of the peak tensile stresses are shown in Table 5, and the variation in stresses correlated with the effects results. The cases that had the highest coefficients of variation (COV) were the cases that showed the highest effects results, such as Cases 1, 2, 6, 9, and 10a.

The top ten highest tensile stresses developed from all simulations are shown in Table 6. All of these tensile stresses were for nonuniform support conditions with temperature curling. Case 10a resulted in the highest two tensile stresses, and Case 8 produced four out of ten highest stresses (and also seven of the top twenty highest stresses). The highest tensile stresses from the uniform support conditions were 543.7 psi for Case 2 (ranked #20 for highest overall stresses) and 542.1 psi for Case 1 (ranked #21), both of which occurred because of edge loading by a single axle with a +20°F temperature differential. Assuming that a typical concrete pavement has a design flexural strength of 650 psi, tensile stresses caused by a nonuniform support condition could lead to premature slab cracking.

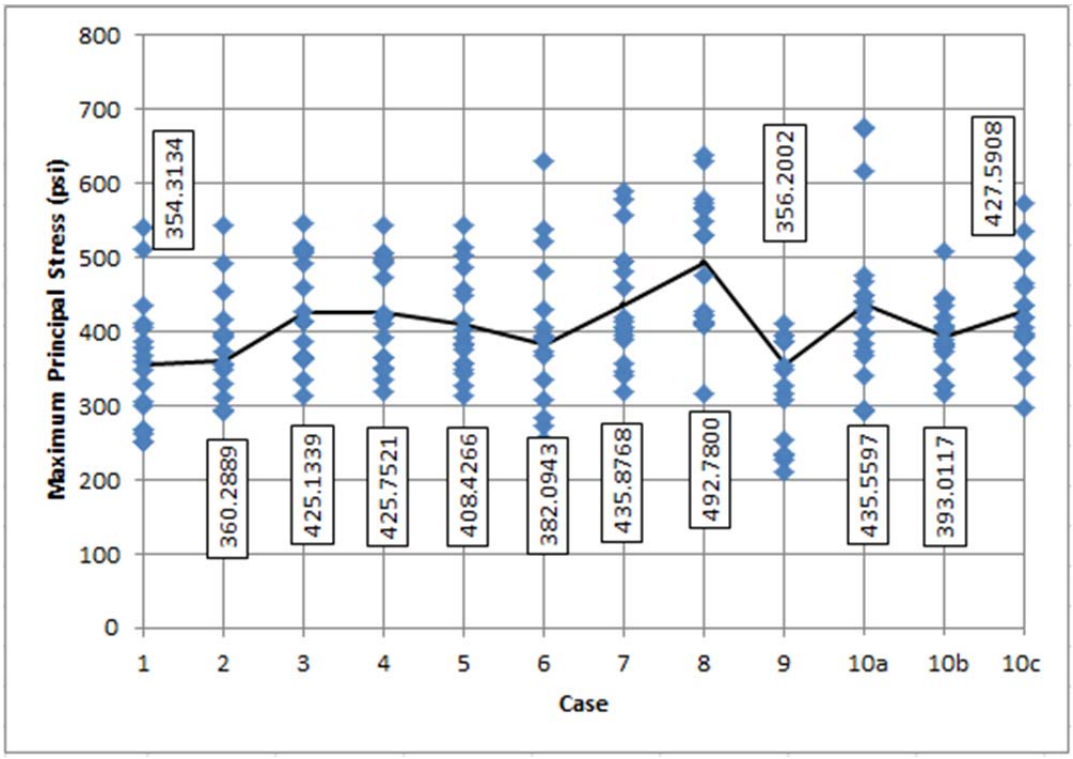

Figure 31. Peak tensile stresses for each input variable combination and subgrade support (i.e., axle type, lateral offset, temperature differential) and overall average tensile stress for each subgrade condition.

Table 5. Statistical Values for Peak Tensile Stress Results

Case	Average Peak Tensile Stress (psi)	Standard Deviation (psi)	Coefficient of Variation
1	354.3	85.6	24.2%
2	360.3	84.0	23.3%
3	425.1	72.8	17.1%
4	425.8	69.9	16.4%
5	408.4	68.7	16.8%
6	382.1	108.2	28.3%
7	435.9	81.7	18.7%
8	492.8	91.6	18.6%
9	356.2	106.9	30.0%
10a	435.6	117.3	26.9%
10b	393.0	48.1	12.2%
10c	427.6	69.5	16.2%

Table 6. Top Ten Peak Tensile Stresses for All Input Variable Combinations

Rank	Case	Temperature Differential	Lateral Position	Axle Type	Maximum Principal Stress (psi)	Maximum Principal Stress Location (x,y,z)
1	10a	+20°F	Edge	Tandem	676.4	(0,70,b)
2	10a	+20°F	Edge	Single	674.0	(0,80,b)
3	8	-20°F	Edge	Steer-drive	637.2	(50,0,t)
4	8	-20°F	Edge	Tandem	629.5	(52,0,t)
5	6	-20°F	Edge	Steer-drive	629.4	(0,100,t)
6	10a	+20°F	Edge	Steer-drive	615.9	(0,78,b)
7	7	-20°F	Edge	Steer-drive	589.7	(0,100,t)
8	8	+20°F	Edge	Steer-drive	579.1	(46,0,t)
9	7	+20°F	Edge	Single	578.4	(0,70,b)
10	8	+20°F	Edge	Single	573.0	(0,90,b)

t: top of slab, b: bottom of slab

2.6 Chapter 2 Summary and Conclusions

An investigation was undertaken to evaluate the effects of various predetermined nonuniform support conditions. In all cases, the subgrade support was deterministically assigned soft (50 psi/in) and stiff (500 psi/in) values. A total of 12 cases were studied, two of which were uniform support conditions. The nonuniform conditions consisted of the following: four nonuniform quadrants, two nonuniform edges, and three “random” cases where the stiffness varied between soft and stiff in 20 predefined areas. A two-dimensional finite element analysis program was used to evaluate the maximum tensile stresses and maximum deflections in the slab as an axle traversed the slab from the transverse edge to the mid-slab edge. The additional variables considered were: axle type (single, tandem, and steer-drive), lateral offset (edge loading and wheelpath loading), and linear temperature differential (-20, 0, and +20°F).

The development of maximum principal (tensile) stresses were determined for each subgrade support condition as the axle was moved along the slab. The main results demonstrated that a nonuniform support condition can result in a significant increase in slab tensile stresses. The influence of axle type generally demonstrated that the tandem and steer-drive axles increased the stresses versus a single axle, although the stresses caused by tandem and steer-drive axles were relatively similar. The edge loading positions were clearly higher than the wheelpath loading. The addition of a temperature differential increased the tensile stresses with the location of peak stresses depending on how the slab was curled (i.e., the -20°F differential increased the stresses at the transverse edge as the slab was curled upward).

Overall, the deflection responses suggest that there was not a quantifiable difference between uniform and nonuniform support conditions. Therefore, testing after concrete slab construction, such as with a falling weight deflectometer, would likely not indicate the presence of a nonuniform support.

A multiple linear regression analysis provided the insight into the overall “effect” of each variable on the change in peak tensile stresses (i.e., axle type, lateral offset, linear temperature differential). In general, the peak tensile stresses were affected most by temperature curling,

both positive and negative, although the regression coefficients were greater for the positive differential. As expected, the slab stresses were found to decrease as loading moved from the edge to the wheelpath. The axle type was not overall as critical as originally thought, although the general trend was that the tensile stresses increased because of a tandem versus a single axle. The variable interactions were relatively minimal, having little affect compared to the first-order interactions.

The worst cases were one of the “random” cases and the soft edges case. The overall highest peak tensile stress was 676 psi from one of the random nonuniform support cases, while the highest tensile stress from the soft edges case was 637 psi. Assuming that a concrete pavement will have a minimum flexural strength of 650 psi and these extreme support conditions, the considered nonuniform support cases will produce significant damage in the concrete pavement and result in premature cracking and/or failure.

In conclusion, the cases presented in this section were essentially extreme situations with high differences in subgrade support stiffness (50 to 500 psi/in) and high linear temperature differentials (-20 and +20°F) and not actual field conditions. The probability of such extreme conditions occurring in the field is low but shows that support nonuniformity may lead to high tensile stresses over the existing uniform support design assumptions. In addition, only a single unrestrained slab was considered and with the inclusion of adjacent slab and load transfer, the stresses (particularly at the free transverse edge) would be expected to decrease. Ultimately, this study demonstrated that nonuniform support conditions need to be considered in the design and construction of concrete pavements since they can lead to premature failures.

CHAPTER 3 THREE-DIMENSIONAL FINITE ELEMENT ANALYSIS OF THE CRACK GROWTH POTENTIAL IN A SLAB WITH PREDETERMINED NONUNIFORM SUBGRADE SUPPORT

It was shown in Chapter 2 that subgrade nonuniformity can increase the peak tensile stresses in the slab under certain differences in support stiffness, area, and its distribution in the zone of expected peak stresses. If this nonuniformity in support is coupled with preexisting, noncritical cracks that developed during the early life of the concrete slab (such as from shrinkage), high-stress conditions along the crack front may be produced and lead to premature failure. The main objective of this chapter is to investigate the three-dimensional (3D) crack growth potential of concrete slabs supported by a nonuniform foundation layer in the presence of existing cracks of various sizes, geometries, and positions. The quantification of the crack growth potential of mechanically loaded concrete pavements is performed through the evaluation of crack front parameters using linear elastic fracture mechanics (LEFM) quantities, such as the stress intensity factor (SIF) for the crack opening (K_I) mode. In this study, partial-depth cracks were inserted at the critical top and bottom tensile stress locations determined from the previous 2D (uncracked) slab analyses in Chapter 2. The analysis was expanded to include several nonuniform support conditions and different crack sizes and geometries, all located at the most critical tensile stress positions. The framework for the analysis is a 3D generalized finite element method (GFEM) program developed at the University of Illinois (Duarte et al. 2007, Duarte and Kim 2008, Pereira et al. 2010) with the geometric and numerical engine to model and handle arbitrary crack surfaces in 3D domains.

3.1 Three-Dimensional Application of Partial-Depth Cracks and Nonuniform Support

Based on the results of two-dimensional (2D) finite element analysis of slabs without cracks (Chapter 2), the critical loading positions that induce the maximum tensile stress on the top of a 15- x 12-ft slab were selected to investigate the crack growth potential, as shown in Figure 32. Figure 32(a) shows the finite element mesh and load locations on the slab with a rectangular through-length (15 ft) crack placed at the top of the slab, with a depth of one-third of the slab thickness (2.67 in). Figure 32(b) shows the same slab geometry and loading condition but for a quarter-elliptical crack of length of 12 in and depth of 2.67 in (one-third of the slab thickness). Figure 32(c,d) shows the details of the crack surfaces placed at the top edge of the slab. For this analysis, there are no adjacent slabs offering load transfer to the free edge loading. The load configuration used is a tandem axle with the same load (36-kips), contact pressure (90 psi), and axle/wheel spacing (4 ft and 8 ft, respectively) as the Chapter 2 analysis.

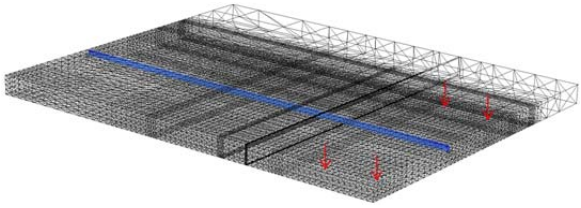

(a) Rectangular through-the-length crack

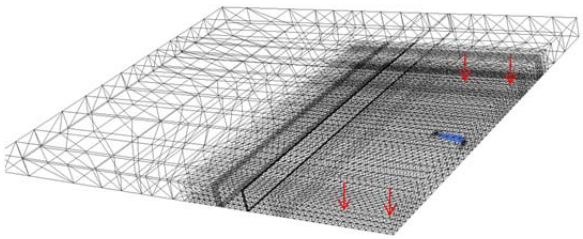

(b) Quarter-elliptical partial crack

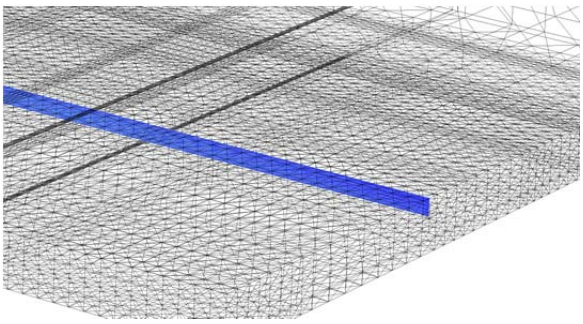

(c) Detail of the edge with the rectangular crack

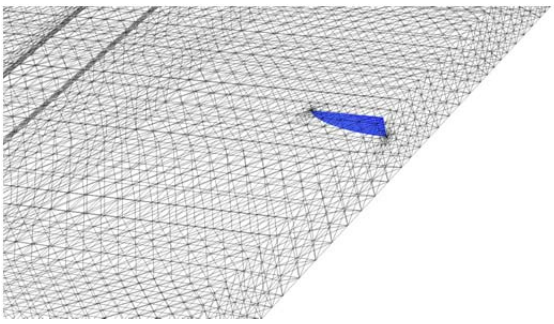

(d) Detail of the quarter-elliptical crack

Figure 32. Highway concrete slab geometry (15 x 12 ft), finite element mesh, loading positions for slabs with surface-initiated cracks with crack geometry of rectangular (a,c) and quarter-elliptical (b,d).

Similarly to the surface cracks, the critical loading position that induces the maximum tensile stresses at the bottom of the 15- x 12-ft slab were selected to investigate the slab cracking potential, as shown in
Figure 33.

Figure 33(a) shows the finite element mesh and loading for the slab with the presence of a through-the-length (12 ft) rectangular crack placed at the bottom of the slab, with a depth of one-third of the slab thickness (2.67 in).

Figure 33(b) shows the same slab geometry and loading condition but for a quarter-elliptical crack of length of 12 in and depth of 2.67 in.

Figure 33(c,d) shows the details of the crack surfaces placed at the bottom edge of the slab. Again, no load transfer was assumed in the analysis between adjacent slabs.

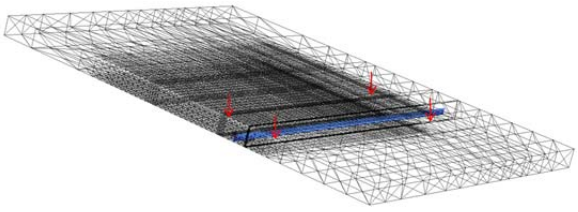

(a) Rectangular through-the-length crack

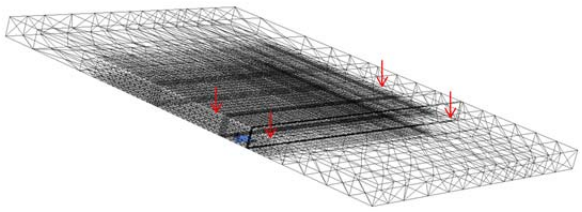

(b) Quarter-elliptical partial crack

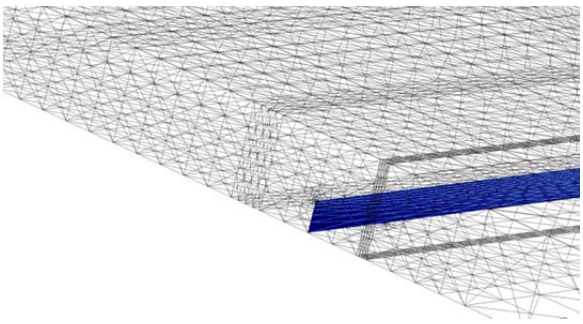

(c) Detail of the edge with the rectangular crack

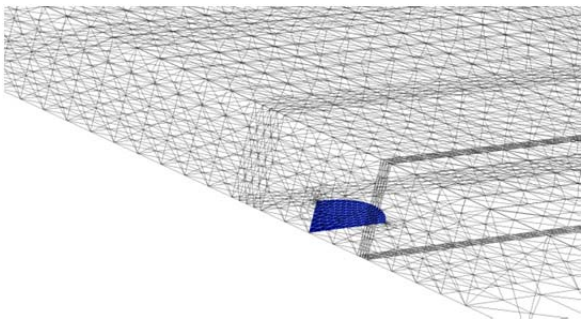

(d) Detail of the quarter-elliptical crack

Figure 33. Highway concrete slab geometry (15 x 12 ft), finite element mesh, loading positions for slabs with bottom-initiated cracks with crack geometry of rectangular (a,c) and quarter-elliptical (b,d).

Figure 34 presents the geometry of the crack surfaces previously shown in Figure 32 and

Figure 33. The cracks have rectangular and quarter-elliptical surfaces with depth (a) and length (L) with the normalized variable (s) varying from 0 to 1, which defines the local position along the crack front ($\overline{AB}$). The topology of the 2D triangular elements is only used to represent the crack surface geometry to be inserted in the 3D model of the slab. The nodes do not have degrees of freedom like standard finite elements and the crack surface mesh is independent of the 3D finite element mesh. For the bottom cracks, shown in

Figure 34(a,c), the crack front ($\overline{AB}$) is at the top of the crack surfaces, which induces bottom-up cracking when those cracks are placed in the slab. Similarly, for the top cracks, shown in

Figure 34(b,d), the crack front ($\overline{AB}$) is at the bottom of the crack surfaces, which induces top-down cracking when those cracks are placed in the slab.

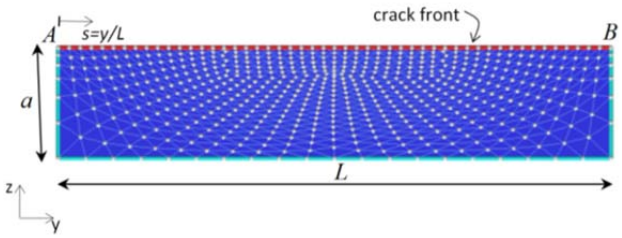

(a) Rectangular crack on bottom of the slab

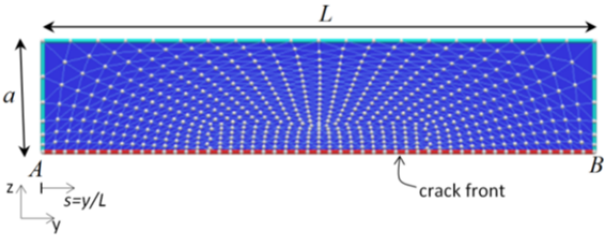

(b) Rectangular crack on top of the slab

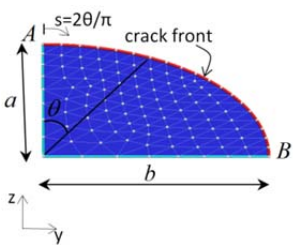

(c) Elliptical crack for bottom of the slab

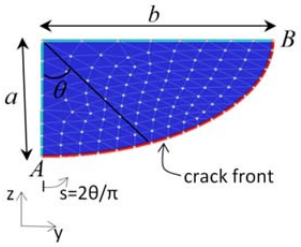

(d) Elliptical crack for top of the slab

Figure 34. Geometry for rectangular and quarter-elliptical surfaces for bottom-initiated (a,c) and surface-initiated (b,d) cracks.

Different subgrade conditions were simulated for both the top and bottom positions in order to assess the effect of nonuniform support on the slab crack growth potential. Figure 35 details the positions of the tandem axle and crack for each support condition, while Table 7 summarizes the four support conditions considered in the analysis. All support conditions (uniform and nonuniform) were analyzed for both load locations (transverse and longitudinal edge) and crack types (rectangular and quarter-elliptical) for a total of 16 cases. Based on the critical results from Chapter 2, the nonuniform conditions considered were soft edges (Case 8 from Chapter 2), stiff edges (Case 9), and the uniform conditions (Case 1, uniform soft; Case 2, uniform stiff).

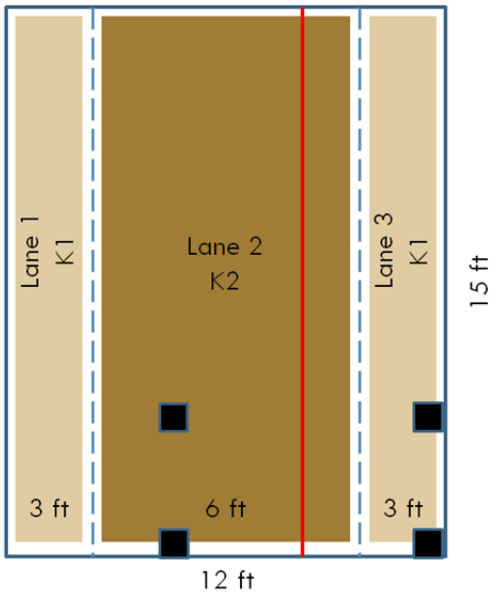

(a) Transverse edge load and rectangular crack

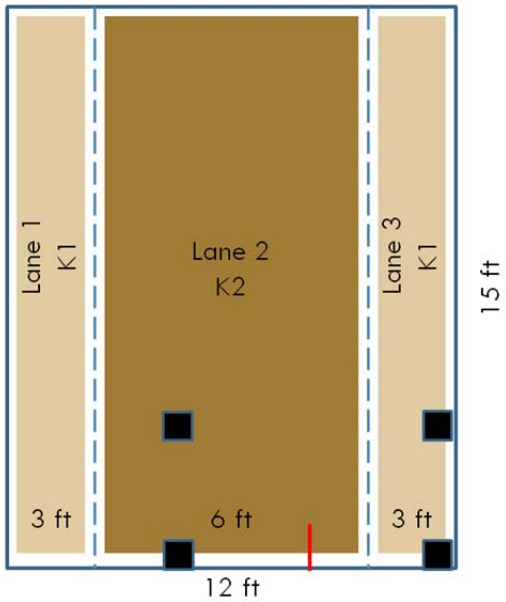

(b) Transverse edge load and quarter-elliptical crack

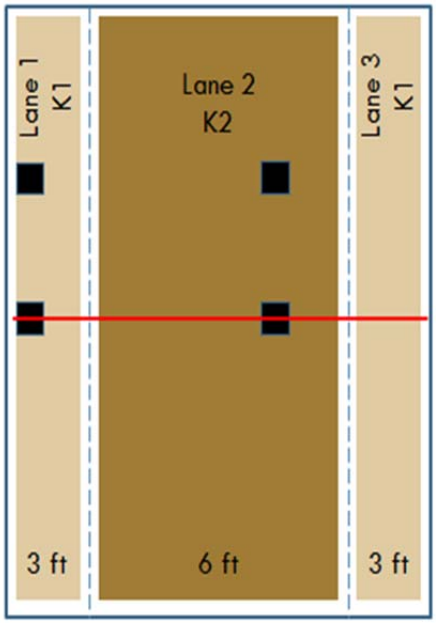

(c) Longitudinal edge load and rectangular crack

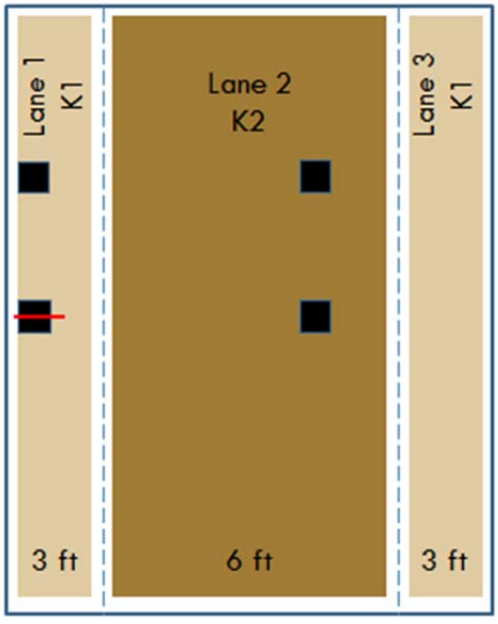

(d) Longitudinal edge load and quarter-elliptical crack

Figure 35. Slab geometry, load configuration, and crack positions for one case of nonuniform support.

Table 7. Subgrade Conditions Analyzed for Various Load and Crack Positions

Label	Subgrade Stiffness (psi/in)		Condition
	Central region (lane 2)	Edges (lanes 1 and 3)	
K1=50; K2=50	50	50	Uniform with soft support
K1=50; K2=500	50	500	Nonuniform with stiff edges
K1=500; K2=500	500	500	Uniform with stiff support
K1=500; K2=50	500	50	Nonuniform with soft edges

3.2 Analysis of Crack Front Parameters for the Different Slab Support Cases

Crack front parameters, such as SIFs for the opening mode (K_I) are extracted using the cut-off function method (CFM) presented by Szabó and Babuška (1991). In the CFM, a smooth extraction function is used along with the displacements of the finite element solution to calculate the stress intensity factors through evaluations of contour integrals ahead of the crack front. The SIFs are extracted at each crack front vertex as illustrated by the white dot vertices along the crack front (red line) in Figure 34.

3.2.1 Surface-Initiated Cracks with Transverse Edge Loading

The deformed shape of the slabs with a through-the-length and quarter-elliptical cracks can be seen in Figure 36. Figure 37(a) compares the four different subgrade support conditions listed in Table 7 for the slab with a rectangular crack placed at the top of the slab. For all subgrade conditions, the maximum mode I (K_I) value of *2.0 MPa-m$^{1/2}$* is induced by the rectangular through-the-length crack for a slab with soft edges (K1=50 and K2=500 psi/in). When slab had stiff edges (K1=500 and K2=50 psi/in), the K_I values decreased significantly (around 0.95 *MPa-m$^{1/2}$*) regardless of the stiffness of the central part of the slab. The uniform soft subgrade (K1=50 psi/in) produced an intermediate response (*1.34 MPa-m$^{1/2}$*) with the presence of the rectangular crack. For all cases, the K_I values decreased as *s* increased (i.e., as the crack front was further from the loaded edge the mode I SIF decreased). This behavior was expected since *s* is the normalized distance from the edge where the maximum tensile stress was induced and it decays further away from the edge. For the uniform soft subgrade condition, the K_I increased by almost 50% when the slab was not uniformly supported with soft edges. For the same nonuniform analysis with stiff edges, the K_I increased 120% relative to the soft edge case.

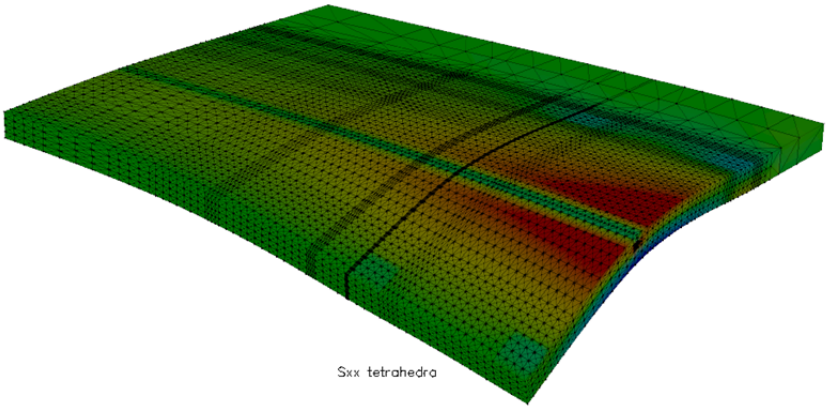

(a) Rectangular through-the-length crack

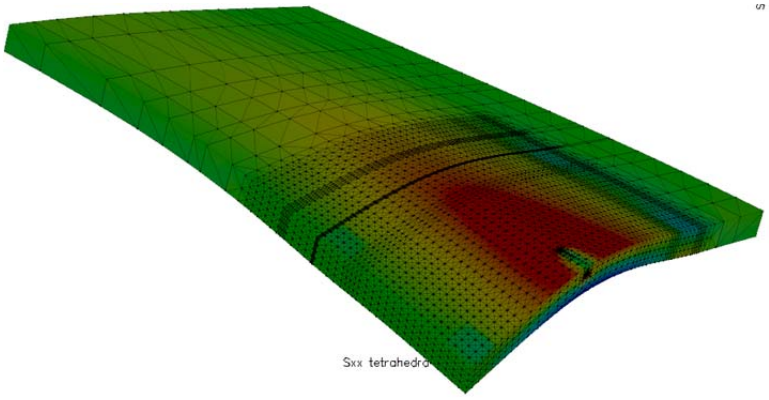

(b) Quarter-elliptical crack

Figure 36. Deformed shape and stress contours for slabs with surface-initiated cracks and transverse edge loading.

The same trends were observed for the quarter-elliptical crack as shown by Figure 37(b). However, the magnitudes of the quarter-elliptical SIFs are smaller than for the rectangular crack which extended through-the-length of the slab. The critical mode I SIF for the soft edges support condition decreased by 38% going from through-the-length rectangular crack to partial-length elliptical crack. For the uniform soft subgrade condition, the K_I increased by almost 51% when the slab was nonuniformly supported with soft edges. For the same nonuniform analysis with stiff edges, the K_I increased 122% relative to the soft edge case.

In general, the mode I critical SIF (K_{IC}) for concrete typically ranges between *0.50 to 1.5 MPa-m$^{1/2}$* (Shah et al. 1995; Bažant and Planas 1998; Mindess et al. 2003), depending on the type, age, aggregate, and maturity of the concrete. The shaded area in Figure 37 graphically illustrates the typical range of K_{IC} values for concrete indicated in the literature. Assuming LEFM conditions are valid, only the rectangular crack will propagate for most types of concrete. All the other crack geometries have the probability of propagating depending on the specific K_{IC} of the concrete (age of loading) and initial flaw size in the slab.

Although the tensile stresses and mode I SIF increase at approximately the same magnitude when going from uniform soft support to nonuniform soft edges support, the significant finding is that the mode I SIF exceeded the K_{IC} for nonuniform soft edges whereas the peak tensile stress without cracks (550 psi) did not exceed the concrete flexural strength

(assumed to be 650 psi). Thus, partial-depth and full-length cracks in slabs coupled with subgrade nonuniformities will be more likely to propagate cracks in slab relative to slabs without preexisting flaws and nonuniform support.

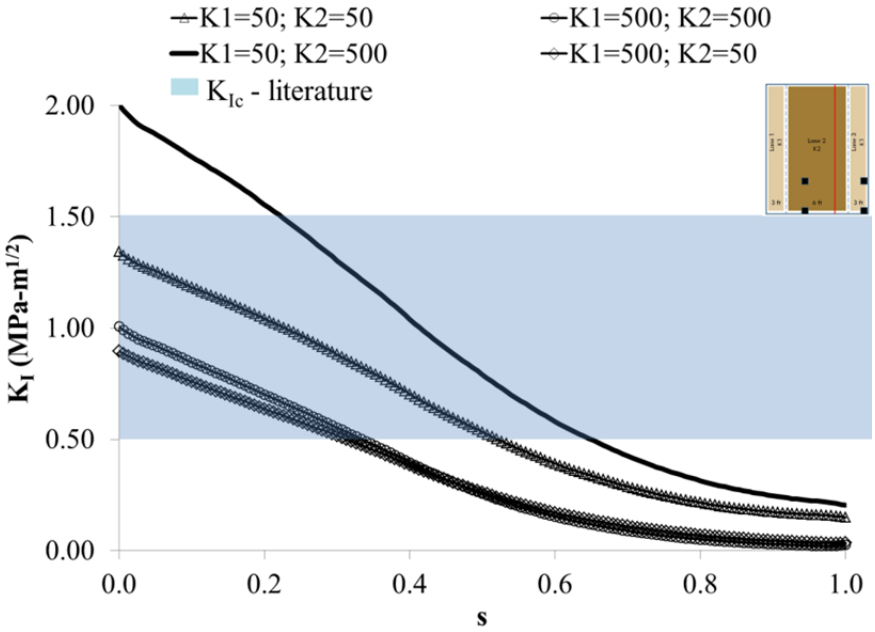

(a) Rectangular through-the-length crack

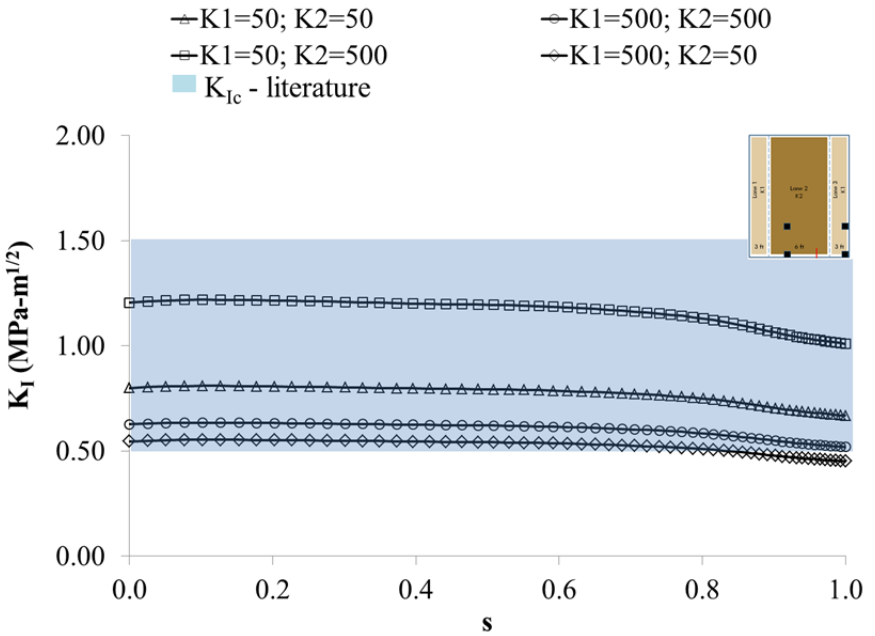

(b) Quarter-elliptical crack

Figure 37. SIFs versus position along the crack front (s) for surface-initiated cracks with transverse edge loading.

3.2.2 Bottom-Initiated Cracks with Longitudinal Edge Loading

Figure 38(a) compares the four different subgrade support conditions for the slab with the through-the-length rectangular crack placed at the bottom of the slab perpendicular to the longitudinal edge. For all subgrade conditions, the maximum mode I value of 1.22 MPa-$m^{1/2}$ was produced by the rectangular crack and uniform soft subgrade (K1=K2=50 psi/in). For the uniform stiff subgrade (K1=K2=500 psi/in), the K_I values decreased significantly to 0.74 MPa-$m^{1/2}$. For the nonuniform soft edges, the K_I values decreased by 22% from the uniform soft condition. There was little difference in mode I SIF between the uniform stiff and stiff edges supports. In Figure 38(a), the secondary peak observed for the K_I values was a result of the second axle wheel straddling the crack at approximately s=0.7. Similar trends are observed for the quarter-elliptical crack placed at the longitudinal edge as shown by Figure 38(b). The maximum mode I SIFs was 30% smaller for the quarter-elliptical cracks relative to the rectangular crack.

The range of K_{IC} values for concrete, indicated in the literature, is also shown as the shaded areas in Figure 38(a,b). Unlike the surface crack analyses, both crack geometries and nonuniform conditions for the longitudinal edge loading have less chance of propagation and require smaller concrete K_{IC} values. The other significant finding with this load location for bottom-initiated cracks is that the nonuniform support did not produce the most critical mode I SIF as in the transverse edge loading for surface cracks. The propagation of preexisting cracks is more sensitive to nonuniform support with loads that produce top tensile stresses.

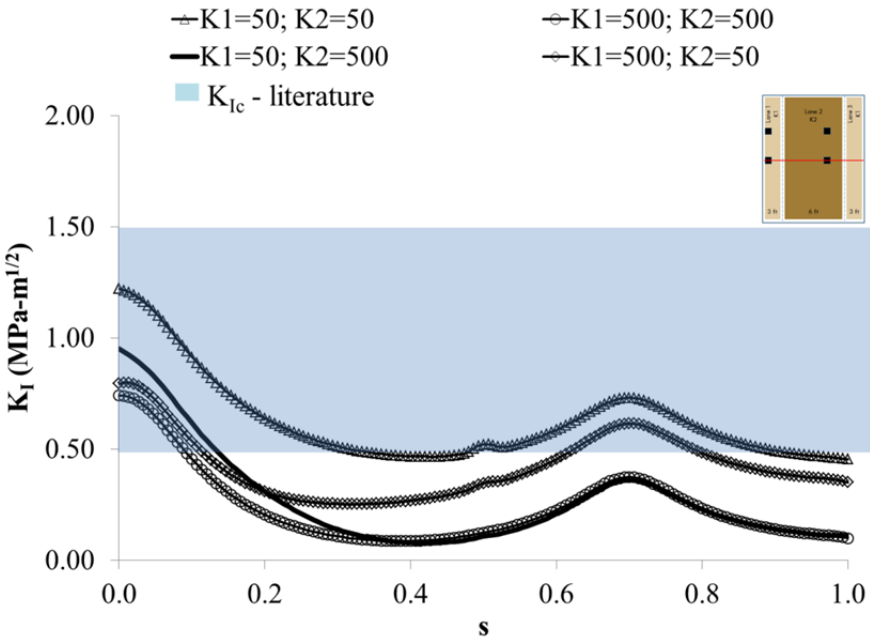

(a) Rectangular through-the-length crack

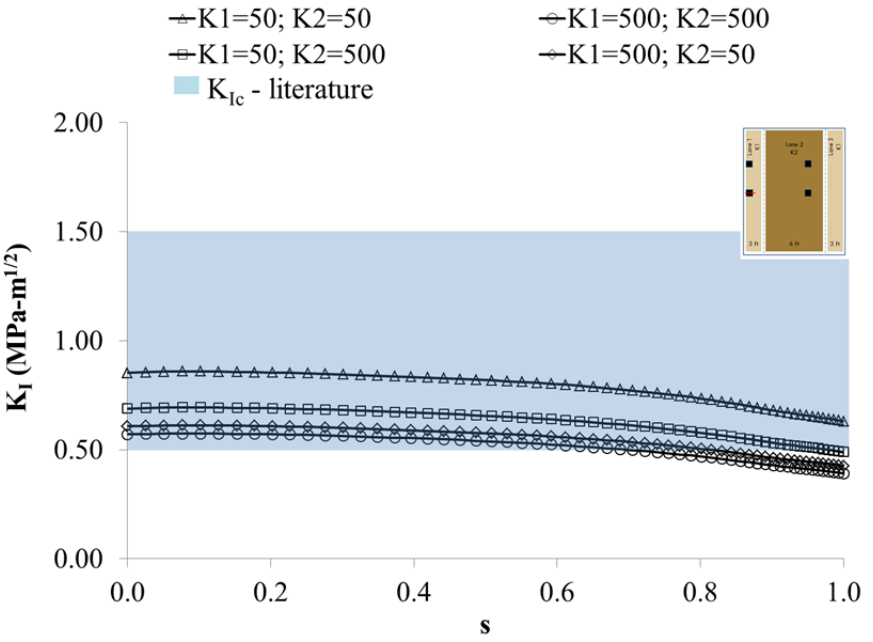

(b) Quarter-elliptical crack

Figure 38. SIFs versus position along the crack front (s) for bottom-initiated cracks with longitudinal loads.

3.3 Chapter 3 Summary and Conclusions

This 3D analysis demonstrated the potential for crack growth in concrete slabs through the insertion of two crack geometries (rectangular and quarter-elliptical) placed at different positions for several nonuniform subgrade conditions. Partial-depth and full-length cracks were inserted at locations where peak tensile stresses were produced along the longitudinal and

transverse edge. The through-the-length rectangular and quarter-elliptical cracks were inserted on both the top and bottom of the slab at the transverse and longitudinal edge, respectively. Four subgrade conditions were chosen to support the concrete slab: uniform stiff, uniform soft, nonuniform soft edges, and nonuniform stiff edges. The three-dimensional generalized finite element method results showed significantly higher mode I stress intensity factor (K_I) values for surface-initiated cracks (maximum of 2.0 MPa-$m^{1/2}$) rather than bottom-initiated cracks (maximum of 1.22 MPa-$m^{1/2}$), given the same slab and crack geometry, support conditions, and load configuration. The nonuniform soft subgrade support with surface cracks resulted in a 50% increase in the K_I values compared with the uniform soft support condition and a 120% increase relative to the uniform stiff support. For the bottom-initiated cracks, the uniform soft support produced the highest K_I values for the longitudinal edge loading cases but these values were 38% less than the maximum K_I value for surface-initiated cracks. The maximum K_I values were high enough to cause unstable crack propagation based on concrete critical stress intensity factors (K_{IC}) published in the literature. Likewise, other support conditions and crack geometries were in the critical range of the concrete K_{IC}. Preexisting cracks coupled with nonuniform support were shown to produce conditions that could cause unstable crack propagation whereas uncracked slabs with nonuniform support will produce higher tensile stresses but will not immediately produce failure of the concrete slab.

CHAPTER 4 TWO-DIMENSIONAL FINITE ELEMENT ANALYSIS OF A SLAB WITH NONUNIFORM SUBGRADE SUPPORT DETERMINISTICALLY ASSIGNED FROM FIELD CONDITIONS

Based on the findings presented in the previous chapters, it was evident that a similar 2D analysis should be conducted using actual field data. This would validate if the extreme conditions assumed in the subgrade conditions in Chapters 2 and 3 (see Figure 1, shown previously) were representative of the "real world" conditions. In this chapter, field data taken from two sites – a section of I-94 in Michigan and a section of I-96 in Michigan – was used in the analysis. The field data from these sites were deterministically assigned to a grid beneath a set of multiple concrete slabs, and a two-dimensional finite element analysis (ISLAB2000, Version 1.1, provided by Applied Research Associates) was carried out similar to the one presented in Chapter 2.

4.1 MI I-94: Field Data and Deterministic Assignment of k-Values

4.1.1 Test Site Overview

Field measurements and data analysis conducted by the research team from Iowa State University formed the basis for the evaluation of the practical effects of subgrade nonuniformity. The nonuniformity of the subgrade was primarily quantified in terms of the spatial variation of modulus of subgrade reaction (k-value). The Michigan Department of Transportation (MDOT) was reconstructing a section of I-94 in St. Clair and Macomb Counties, Michigan, between mile posts 23.0 and 6.1, due to poor ride quality. Based on AASHTO pavement design guide (AASHTO 1993), the new pavement structure would consist of an 11-in thick jointed Portland cement concrete (PCC) slab, 16-in open-graded drainage course (OGDC) placed over the subgrade with a geotextile separation layer to be placed at the interface of the subgrade and OGDC.

Although intelligent compaction (IC) equipment was utilized for this MI I-94 construction project, it was not used as part of the spatial test bed field data collection to characterize the effect of nonuniform subgrade support on the stresses in the concrete pavement. In order to rapidly assess spatial variability, in situ test data obtained from static plate load tests (PLT) and dynamic cone penetrometer (DCP) tests were correlated. The modulus of subgrade reaction (k-value) was obtained from PLTs carried out along the length of test bed 3a (TB3a) with measurements located at every 50 ft between stations 839+50 and 866+00. The PLTs were conducted on top of the newly constructed OGDC base layer to determine the static (composite) k-values. DCP tests at the same station locations were run in accordance with ASTM D6951 (2003) to determine the dynamic penetration index (DPI). From the DPI profiles, the California Bearing Ratio (CBR) was calculated from the following equation from ASTM D6951:

$$CBR = \frac{292}{DPI^{1.12}} \tag{4.1}$$

Intensive in situ tests over a 7 x 7 m^2 spatial grid area were also carried out on test bed 1b (TB1b), as shown in Figure 39, in order to analyze spatial stiffness of the foundation layer over a small area.

Figure 40a shows the TB3a upon which the PLT was carried out whereas Figure 40b shows the coordinates of the TB3a having 121 individual field testing locations. These 121 test

locations and spacing of each test for TB1b on the MI I-94 section are shown in Figure 41. The DCP tests were conducted through the OGDC base layer and into the subgrade layer.

Figure 39. DCP test being carried out on an OGDC layer on TB1b.
Source: White et al. (2011)

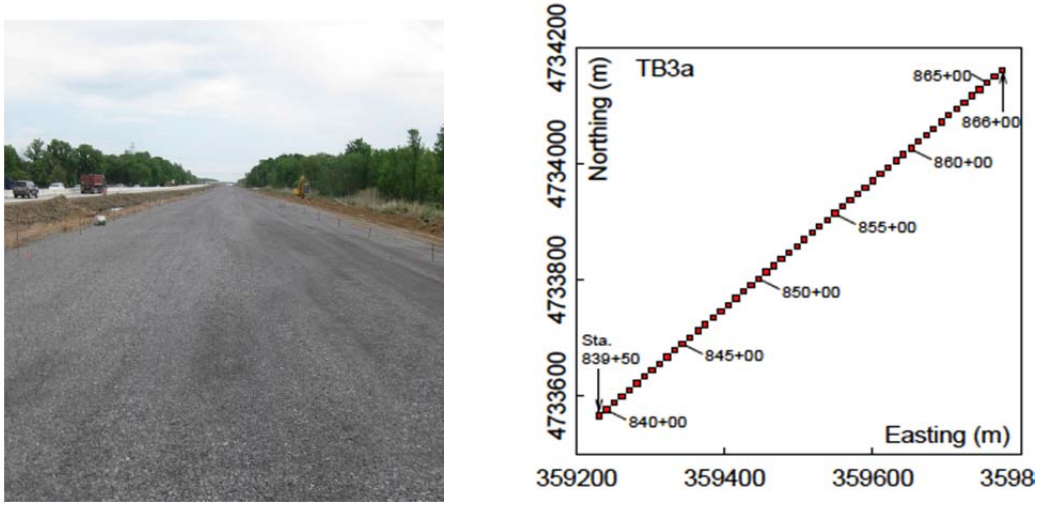

(a) (b)

Figure 40. (a) Test bed 3a (TB3a) site location with OGDC base layer and (b) coordinates of each PLT and DCP test location. Source: White et al. (2011)

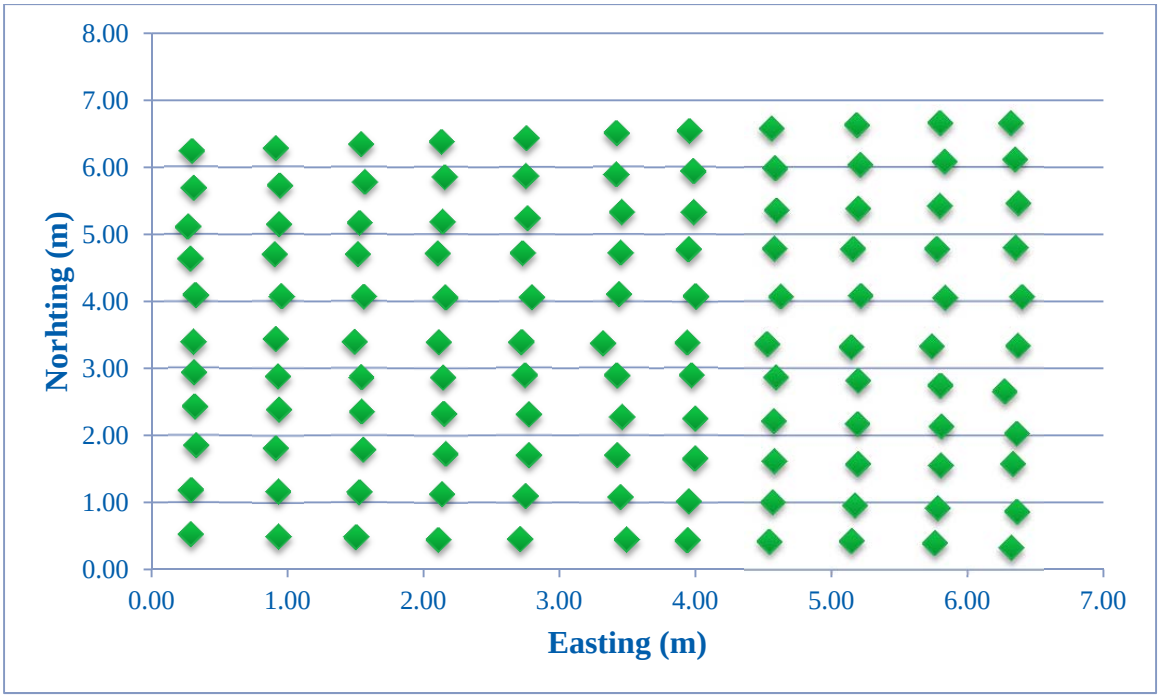

Figure 41. MI I-94 DCP test locations on TB1b.

All PLTs in the field were performed with a 12-in-diameter plate. A 30-in diameter plate is prescribed by AASHTO (1993) to carry out PLT and determine the foundation k-value. The measured k_{comp}, which is the modulus of subgrade reaction for both the soil and OGDC base layer, was corrected for the discrepancy in the plate size using a theoretical relationship proposed by Terzaghi and Peck (1967) for granular materials as follows, where *k* is the modulus of subgrade reaction using 30-in-diameter plate, k_1 is the modulus of subgrade reaction using a 12-in-diameter plate, B_1 is 300 mm, and *B* is 720 mm.

$$k = k_1 \left[\frac{B + B_1}{2B}\right]^2 \tag{4.2}$$

4.1.2 Development of Support Stiffness Correlation Equation

The next step of the analysis involved correlating the simple field test (DCP) to the required input value for finite element analysis (k-value). Only the DCP penetration results in the subgrade layer were utilized in the DPI to CBR correlation from Equation 4.1. Correlation equations from literature were first investigated between k-value and CBR. The following equation was developed by the Federal Aviation Administration (FAA) based on the Advisory Circular (AC) 150/5320-6E (2009):

$$k = \left[\frac{1500\ CBR}{26}\right]^{0.7788} \tag{4.3}$$

The FAA AC states that the values obtained from Equation 4.3 are approximate in nature (i.e., the values are not exact or unique).

Another correlation is based on charts developed by Darter et al. (1994) for NCHRP 1-30. These relationships are also empirical in nature with a range of k-value that varies with the

soil type. The upper, middle, and lower curves in Figure 42 show the range of k-values for a particular CBR value.

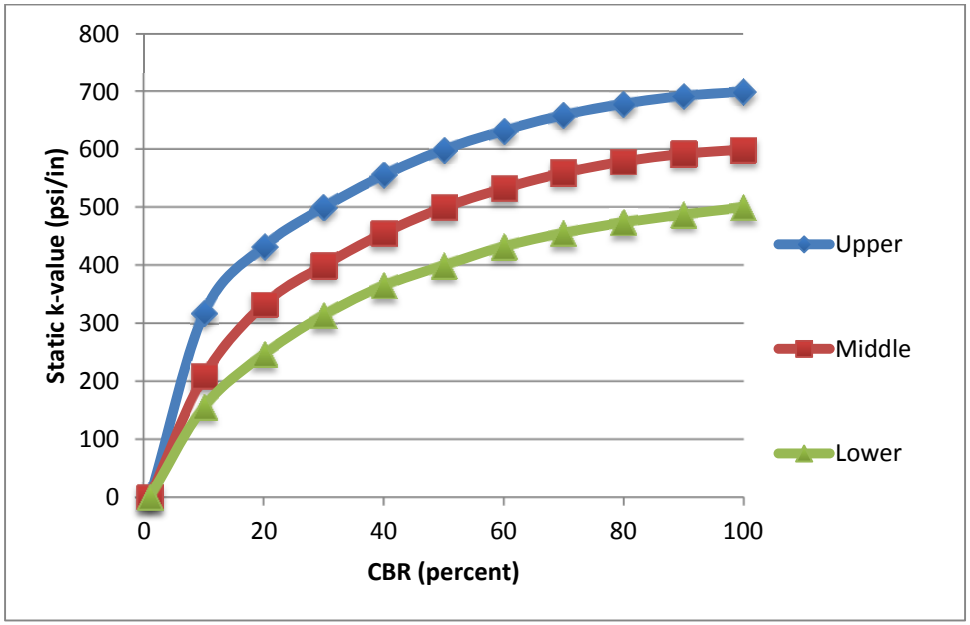

Figure 42. Approximate relationship of k-value. After: Darter et al. (1994)

Another correlation equation is from the AASHTO design guide (1993), as shown in Equations 4.4a and 4.4b where M_r is modulus of soil.

$$M_r = CBR \times 1500 \quad (4.4a)$$

$$k = \frac{M_r}{19.4} \quad (4.4b)$$

Two other theoretical linear relationships, based on empirical data from Lysmer and Duncan (1969) and Department of the Army and the Air Force (1966), are:

$$k = 6.5 \times CBR \quad (4.5)$$

$$k = 20 \times CBR \quad (4.6)$$

Since the MI I-94 TB3a had DCP and k-value measurements, a correlation equation could be developed, which could then be used to calculate the k-values from the 7 x 7 m^2 TB1b. The existing field data from the MI I-94 site was used to develop a DCP-CBR to k-value correlation equation, which would give more realistic values of subgrade stiffness of the site under investigation. CBR values obtained from DCP tests and k-value obtained from PLT at TB3a are listed in Table 8.

Table 8. CBR and k-Value Field Data for TB3a

k-value (psi/in)	CBR Subgrade (%)
166	5.3
150	7.0
175	6.9
81	6.2
100	5.7
145	6.2
91	4.0
59	7.9
173	7.3
104	8.4

The FAA correlation (Equation 4.3) was re-calibrated based on the field data from Table 8 to generate the following equation:

$$k = 23.532 \times CBR^{0.7787} \quad (4.7)$$

The 121 field-correlated CBR to k-value data from Equation 4.7 are listed in Appendix A. The use of this correlation equation is an approximation of the subgrade k-values given the results of the DCP-CBR. As conducting 121 PLTs on an intensive plot such as TB1b was not practical, the use of a correlation equation was the best alternative based on the available field data.

4.1.3 Discretization of Spatial Plot

In order to determine if the actual field-measured foundation variability produces changes in the critical slab tensile stresses, TB1b data was used to theoretically analyze a certain slab geometry, load configuration and load path, and temperature condition. Based on the above soil CBR to composite k-value correlation analysis, discretized spatial plots for the foundation layer for TB1b were created for a two-dimensional finite element analysis. As shown in Figure 43, the test grid of 121 data points (called Case 121) was over a 7 x 7 m^2 square plot and is based on assigning the field data locations in Figure 41 for the subsequent finite element analysis. The spacing of each uniform foundation area was approximately 0.7 x 0.7 m^2 with the corner areas being approximately 0.35 x 0.35 m^2.

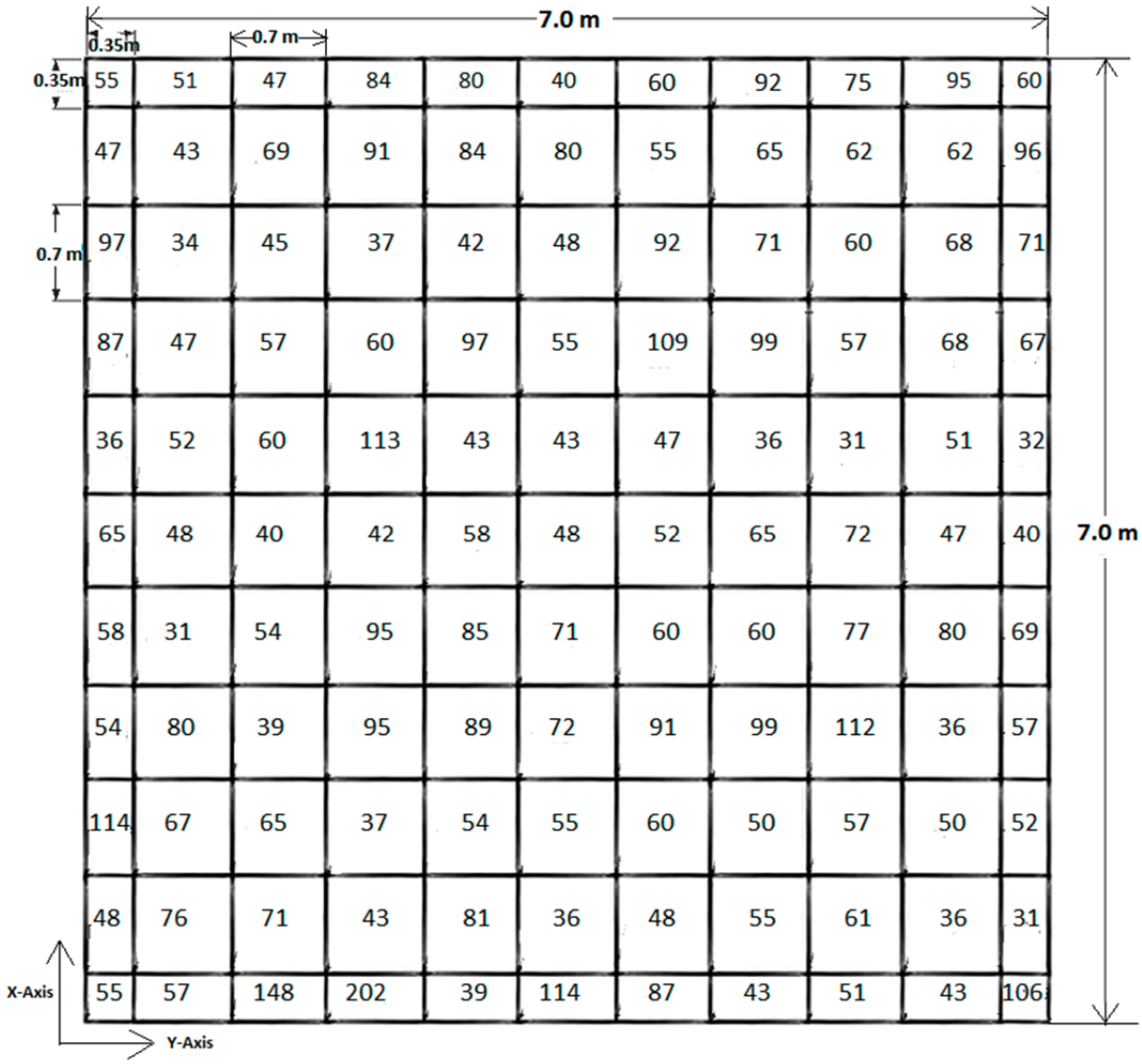

Figure 43. The 121 correlated k-value (psi/in) areas (Case 121)

The range of the k-values for Case 121 was 32 to 202 psi/in with a mean of 63 psi/in and a standard deviation of 25.6 psi/in. This case represents the practical field conditions and is quite different than the arbitrary deterministic distributions assumed previously in Chapter 2 of 50 and 500 psi/in. However, the range between the minimum and maximum value of k-value for this 7 x 7 m^2 was still a factor of 6 versus 10 for the analysis in Chapter 2. In the study by Barenberg et al. (1976), the range of the k-values assumed was from 11 to 197 psi/in having a factor of approximately 20 with a mean of 90 psi/in and standard deviation of 30.1 psi/in.

Another support condition considered from the field data was to assume that the support was uniform. Figure 44 represents the uniform case with a single k-value (called Case 1) which was derived by averaging all 121 k-values from Case 121. As previously mentioned, the mean value was 63 psi/in.

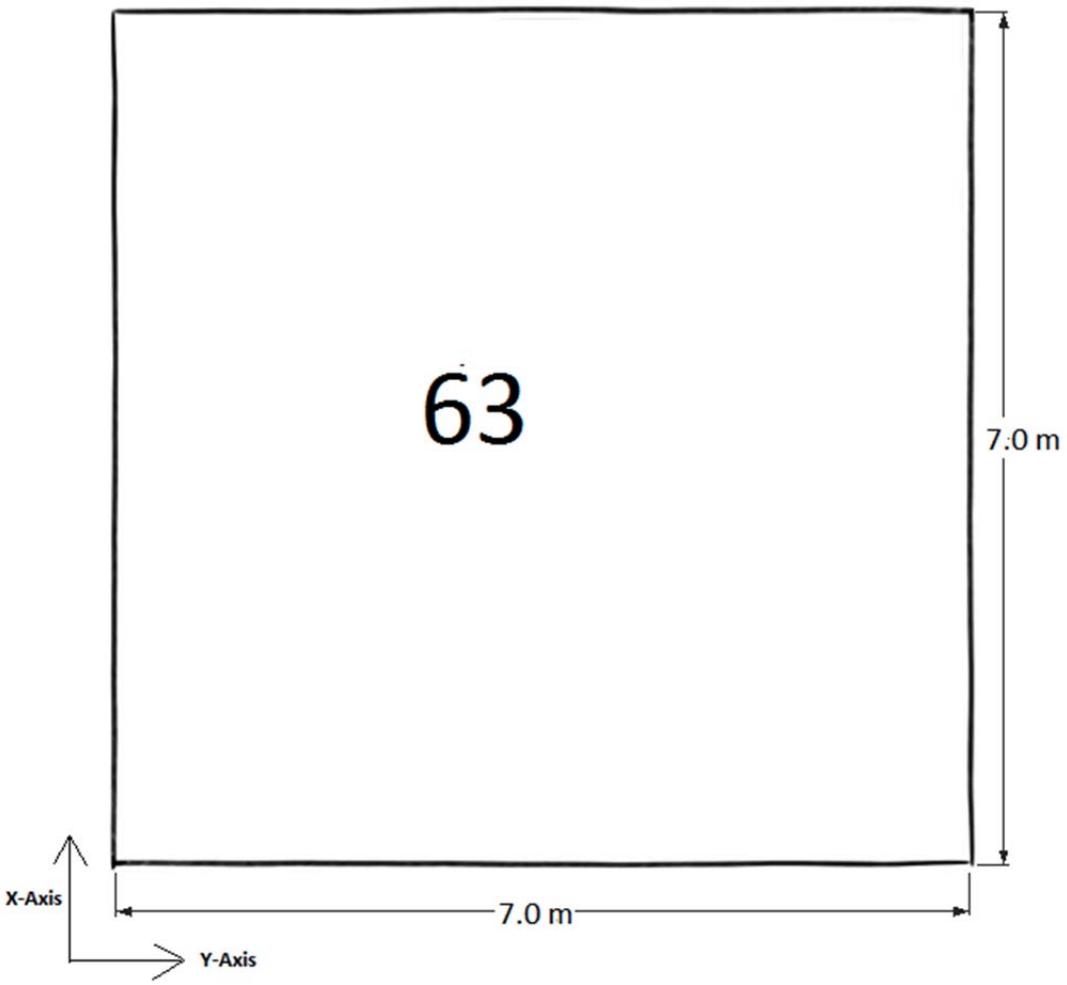

Figure 44. Case 1 with the mean k-value (psi/in) for the 121 data points collected.

A third nonuniform support condition was analyzed for MI I-94 to investigate the size of the nonuniform areas and its effect on the tensile stress change relative to the uniform single k-value and 121 k-value cases. As shown in Figure 45, this case used a weighted average to produce k-value areas of 1.16 x 1.16 m^2 for a total of 36 k-values for the 7 x 7 m^2 area. This is known as Case 36. Due to the weighted average approach to create the 36 k-value areas, the range of k-values was only 39 to 116 psi/in or a factor of 3 difference. Although the mean remained at 63 psi/in, the standard deviation reduced to 14.1 psi/in compared to 25.6 psi/in for Case 121, and inherently this averaging technique reduced the variation of stiffness support.

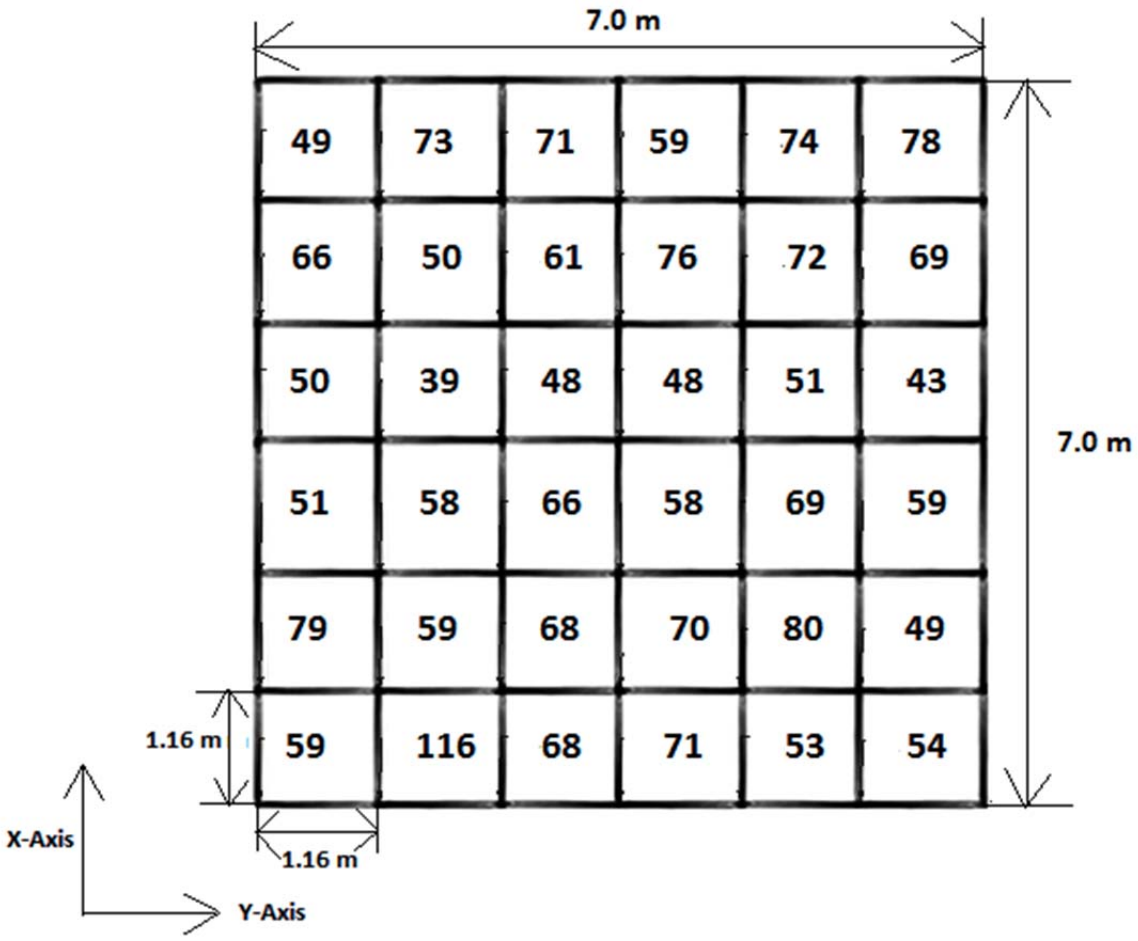

Figure 45. The 36 discretized k-value areas (Case 36) of 1.16 x 1.16 m^2 area each

4.1.4 Analyses Inputs and Factor Levels

Two-dimensional finite element analysis with ISLAB2000 was employed for calculating the critical tensile stresses in the concrete slab for the variety of inputs and nonuniform support conditions. The x-y location and magnitude of tensile stresses developed at the top or bottom of the concrete slab was recorded for each case and axle position. Table 9 lists the pavement input parameters used in the analysis.

Table 9. Input Parameters for ISLAB2000 Analysis

Slab Size	23 x 23 ft (7 x 7 m)
Slab Thickness	8 in
Elastic Modulus	4.0 x 10^6 psi
Poisson Ratio	0.15
Coefficient of Thermal Expansion	5.5 x 10^{-6}/°F
Unit Weight	0.087 psi/in
Tire Pressure	90 psi
Aspect Ratio (b/a)	1
Element Size	2 x 2 in^2
Wheel Spacing	96 in
Axle Spacing (Tandem Axle)	48 in
Axle Spacing (Steer-Drive Axle)	96 in
Single Axle	18 kip
Tandem Axle	36 kip
Steer Drive	54 kip
Joint Load Transfer Efficiency (LTE)	70%

In contrast to the theoretical analyses conducted in Chapter 2 with a single slab, the field-measured foundation support was done over a larger area, approximately 7 x 7 m^2, and required a total of four slabs, each measuring 3.5 x 3.5 m^2, as shown in Figure 46. The analysis matrix consisted of five different loading paths (lateral offsets) that traverse the slab longitudinally: right lane edge (RE), middle of the lane (M), left lane edge (LE), right lane wheelpath (RW) and left lane wheelpath (LW), as shown in Figure 46. Based on the results from Chapter 2 for extreme changes in k-value (i.e., 50 to 500 psi/in), the axle loading along the longitudinal edge produced the most critical tensile stresses. Case RE was the movement of the axles along the right free edge whereas Case LE was along left free edge. Case M represents movement of the axles at the exact center of the two lanes which would not be expected to produce the overall greatest tensile stress of all loading paths. Finally, Cases RW and LW represent wheelpath loading (a lateral offset of approximately 15.75 in) in either the right or left lane, respectively.

The objective of assessing five different lateral offsets or loading paths, shown in Figure 46, was to identify the most critical loading location and critical tensile stress position in the slab for the measured foundation variability. The critical slab stresses are an interaction between the axle type, loading path and location on the slab, the relative location of the nonuniform soil support areas, size of the nonuniform area, and curling condition.

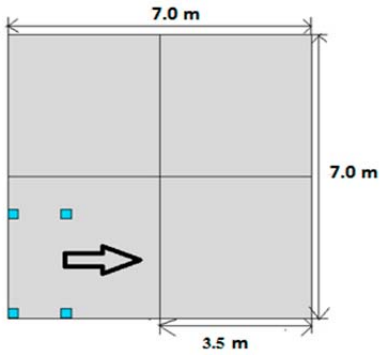

a) Case RE: Right Lane Edge

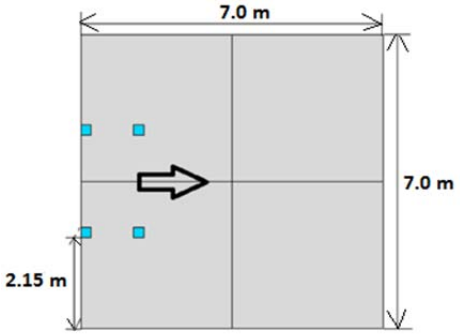

b) Case M: Middle of Lane

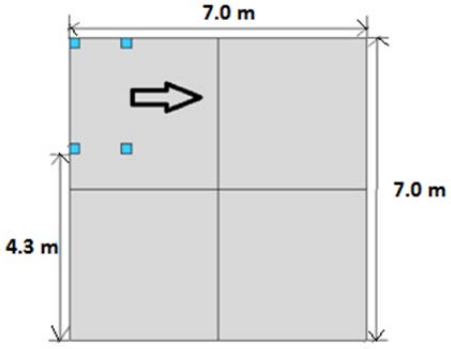

c) Case LE: Left Lane Edge

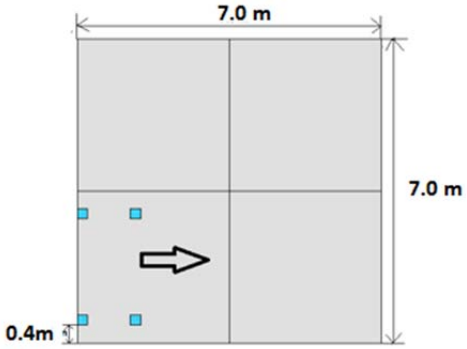

d) Case RW: Right Lane Wheelpath

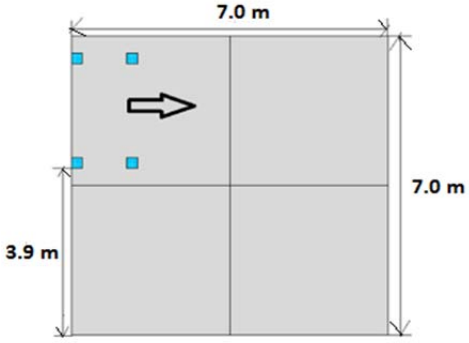

e) Case LW: Left Lane Wheelpath

Figure 46. Five load paths (lateral offsets) analyzed for all three axle configurations and subgrade uniformity on four-slab assembly.

Three axle configurations (single, tandem, and steer-drive axles) were traversed in the longitudinal direction to determine the critical load location and tensile stress magnitude, as shown in Figure 47. The loaded area was 10 x 10 in. After the first analysis point at the free edge of the transverse joint, the longitudinal position of the axles were traversed at 20-in intervals for the single axle and until the front axles of the tandem and the steer-drive cross the opposite transverse free edge. The single axle required a total of fourteen load positions, the tandem axle required twelve, and the steer-drive axle required seven load positions to traverse

the 275-in (7-m) slab sections. The last single axle position analyzed was 260 in while for the tandem axle it was 210 in (210 + 48 in = 258 in).

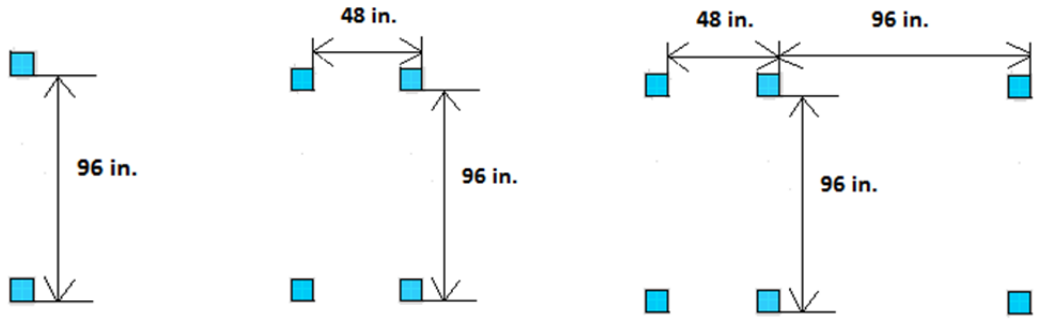

a) Single Axle b) Tandem Axle c) Steer-Drive Axle

Figure 47. Single, tandem, and steer-drive axle configurations used for stress analysis

Three linear temperature differentials (curling conditions) were considered: no differential, positive (+20°F), and negative (-20°F). The joint load transfer efficiency was selected to be 70% at the joints in both the x- and y-coordinate directions. The other input variables listed in Table 9 such as slab thickness, concrete elastic modulus, slab size, and coefficient of thermal expansions were not changed even though they may have had an effect on the magnitude of the stress sensitivity due to the changes in spatial foundation properties. Note that the standard axes used in ISLAB2000 and in this analysis are inverted from the normal Cartesian coordinate system.

A mesh size of 2 x 2 in^2, shown in Figure 48, was chosen to ensure convergence of the outputted stresses and deflections. The pavement response recorded for this study was the maximum tensile stress at either the bottom or top of the slab at each load location. For certain cases, this critical tensile stress was a result of load plus temperature curling. With ISLAB2000, it is possible with daytime curling (+20°F) or nighttime curling (-20°F) that gaps beneath certain nodes exist prior to mechanical loading with the axle.

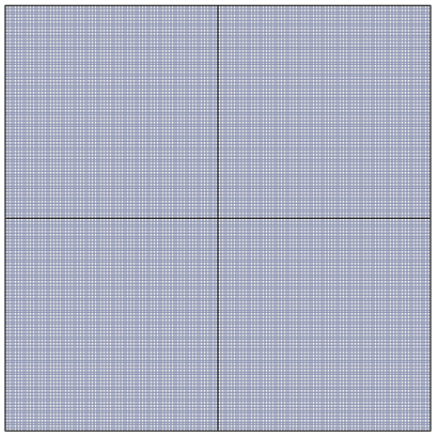

Figure 48. The 2 x 2 in^2 mesh resolution for ISLAB2000 analysis.

4.1.5 Tensile Stress Analysis Nomenclature

Table 10 gives the nomenclature of the cases analyzed for the 121 discrete k-value locations, 36 k-values based on weighted average of 121 k-values, and one mean k-value based on the 121 measurement points. In all subsequent plots, the legend describes what cases are being plotted in terms of the loading path and number of discrete k-value areas under the four-slab assembly.

Table 10. Case Nomenclature for Finite Element Analysis Runs

Case RE121	RE: Right Lane edge; 121: 121 k-values
Case RE1	RE: Right Lane edge; 1: 1 k-value
Case RE36	RE: Right Lane edge; 36: 36 k-values
Case M121	M: Middle of Slab; 121: 121 k-values
Case M1	M: Middle of Slab; 1: 1 k-value
Case M36	M: Middle of Slab; 36: 36 k-values
Case LE121	LE: Left Lane edge; 121: 121 k-values
Case LE1	LE: Left Lane edge; 1: 1 k-value
Case LE36	LE: Left Lane edge; 36: 36 k-values
Case RW121	RW: Right Lane wheelpath; 121: 121 k-values
Case RW1	RW: Right Lane wheelpath; 1: 1 k-value
Case RW36	RW: Right Lane wheelpath; 36: 36 k-values
Case LW121	LW: Left Lane wheelpath; 121: 121 k-values
Case LW1	LW: Left Lane wheelpath; 1: 1 k-value
Case LW36	LW: Left Lane wheelpath; 36: 36 k-values

The 121 k-value (Case 121) was considered first and subjected to the five loading paths and three axle configurations (single, tandem and steer-drive axle) at three linear temperature differentials (+20°F, 0°F, -20°F). In all plots, “S” represents single axle, “T” represents tandem axle, and “D” represents steer-drive axle while “0F,” “20F,” and “-20F” are the respective linear temperature differential used in that particular case.

4.2 MI I-94: Slab Response Results

This section presents the results from all of the cases previously presented in Table 10. The subsections are divided by the various loading locations (i.e., RE, M, LE, RW, LW). Each subsection compares the three different support conditions (i.e., 121, 36, and 1 discrete k-value areas).

4.2.1 Stress Analysis for Right Edge (RE) Loading Case

Figure 49 shows the results of the maximum tensile stresses recorded at the each longitudinal position for Case RE121 (right edge with 121 areas with discrete k-values) for single, tandem, and steer-drive axle combinations and three temperature differentials. For Case RE121, critical tensile stress regions were observed at similar, but not identical, locations in the two slabs since the distribution of measured spatial k-values were not symmetrical (see Figure 43, shown previously). The difference in maximum tensile stresses is less than 10% despite the significant difference in local k-values at both mid-slab locations (from 43 to 202 psi/in in one location along the edge in Figure 50). The peak tensile stress recorded for all RE121 simulations was for a single axle configuration during daytime curling conditions. The reason for

this behavior was that the discretized k-value areas were relatively small (i.e., 0.7 x 0.7 m^2) with low k-values near mid-slab, coupled with the single axle producing a highly concentrated tensile stress, especially under positive curling. The drop in tensile stresses in Figure 49 around 137.5 in from the initial load position was the location of the transverse joint and thus there was a reduction in tensile stresses due to a high joint LTE of 70%. The red areas in Figure 50 show the locations with nonuniform adjacent stiffness area and the orange area represents the location of the peak tensile stress for Case RE121.

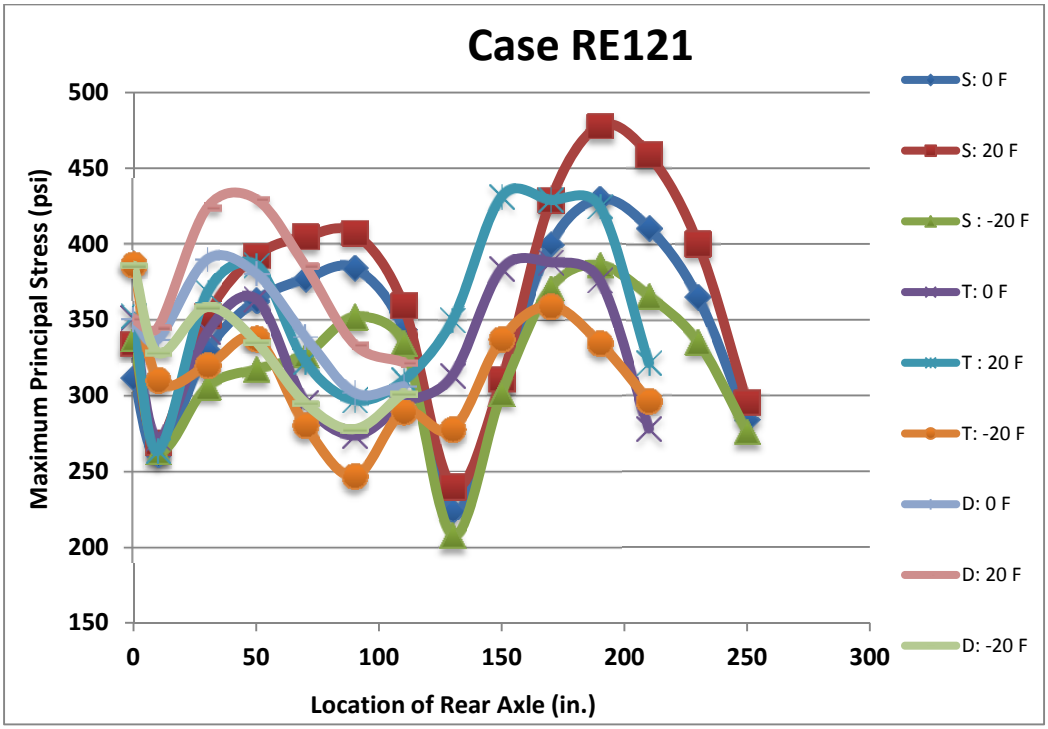

Figure 49. Maximum principal (tensile) stress at each axle position for Case RE121.

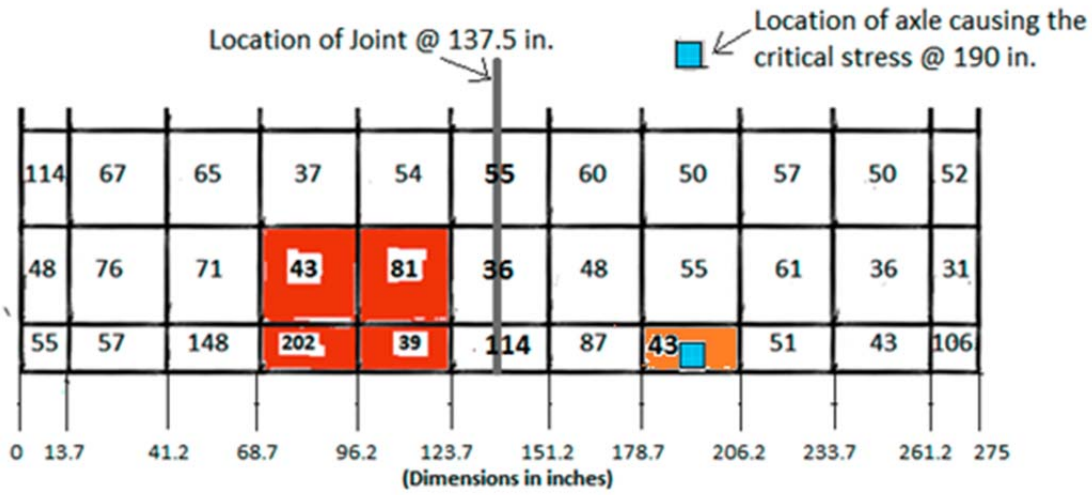

Figure 50. Local variation in k-values along right hand edge of the slab for Case RE121.

Similarly, the maximum tensile stresses at each longitudinal position for Cases RE1 and RE36 are shown in Figure 51 and Figure 52, respectively. Although, the peak tensile stresses for the three discretized support cases at the right edge is similar (within 5% of each other), the standard deviation of the range of k-values for Case 121 and Case 36 reduces from 25.6 to 14.1 psi/in on account of weighted averaged k-values for the latter case. This reduces the variation in the stiffness of the subgrade support and, therefore, Case 36 would not be an important parameter for critical stress development for the other loading location cases. The magnitude of the peak tensile stresses for Case 121 is 478 psi, 470 psi for Case 36, and 463 psi for Case 1. For these cases, a decrease in the peak tensile stress corresponded to an increased size of the predefined uniform k-value condition. The peak tensile stress occurred at the mid-slab edge (i.e., 190 in from the initial loading location) for all three discretized support conditions.

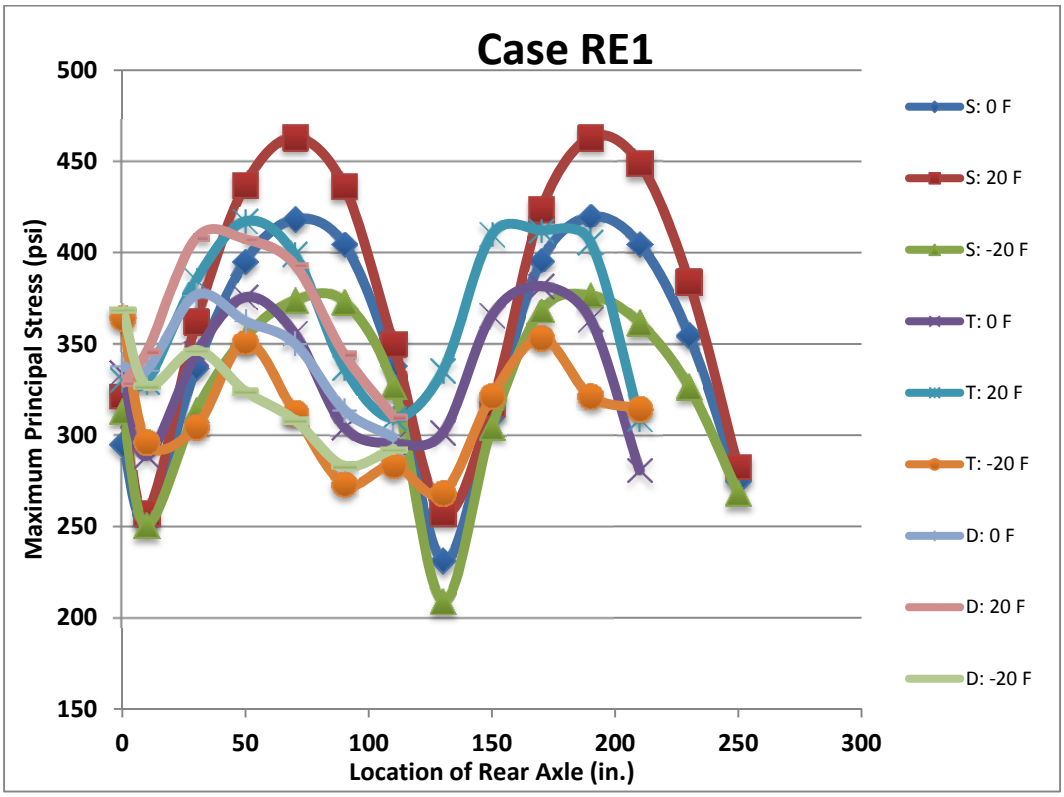

Figure 51. Maximum principal (tensile) stress at each axle position for Case RE1.

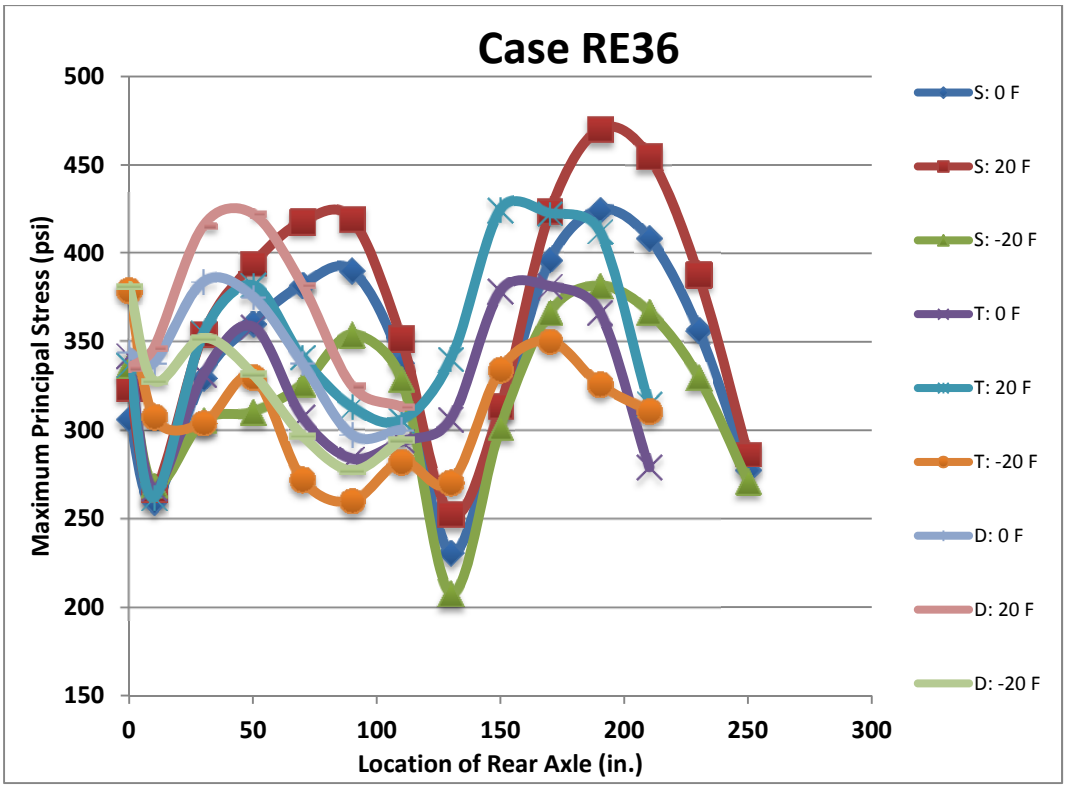

Figure 52. Maximum principal (tensile) stress at each axle position for Case RE36.

The peak tensile stresses in Figure 49 and Figure 52 correspond to soft areas under the slab for Cases 121 and 36, respectively. The k-values at the location of the peak tensile stress were 43 psi/in and 53 psi/in, respectively, which are lower than the 63 psi/in for the uniform support case. Hence, the peak tensile stresses for each support type corresponded to the magnitude of the local k-values at the expected peak stress location.

Figure 53 compares the peak tensile stresses produced by the combination of axle configuration and temperature loading for Cases RE1, RE36, and RE121. For each individual axle type, the overall peak tensile stress occurred during positive temperature differential condition. The tandem axle and steer-drive axle at nighttime curling condition produced the peak tensile stresses at the top of the slab for the three support conditions. A summary of the maximum tensile stresses and their respective location (x,y,z) are given in Table 11.

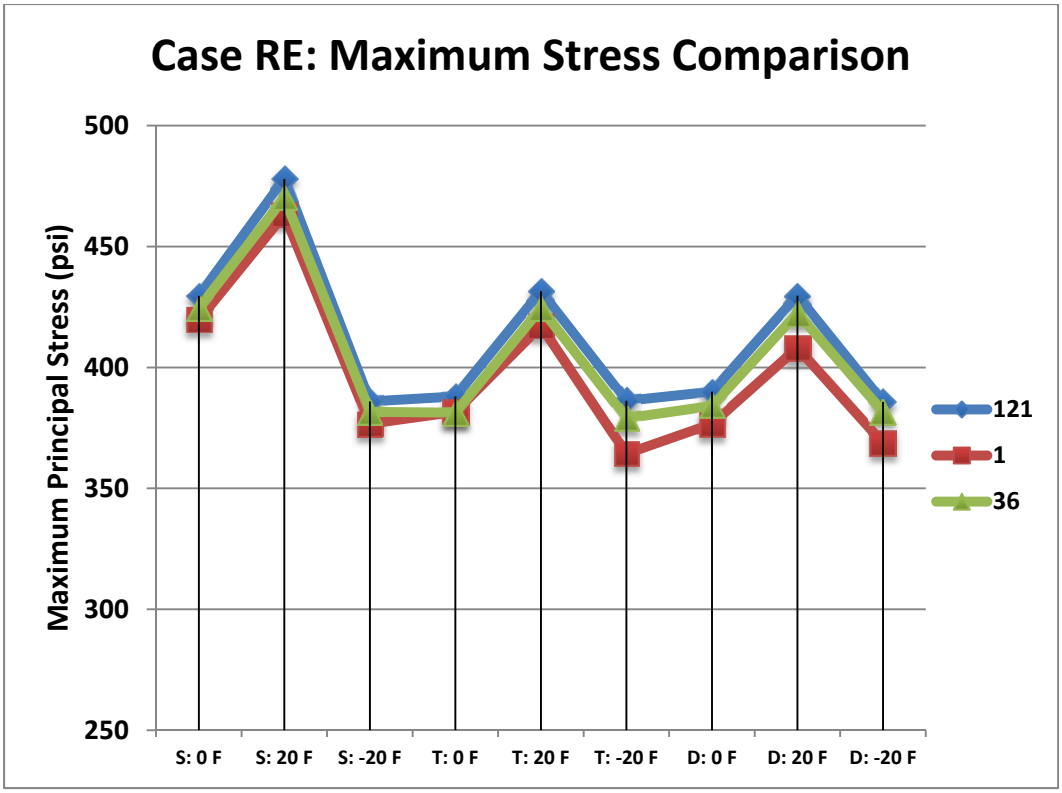

Figure 53. Comparison of the critical tensile stresses for Case RE for each input factor level and the three nonuniform support conditions.

Table 11. Summary of Peak Tensile Stress for Each Subcase for RE Loading Location (Note: "t" and "b" is the location of the critical stress at the top or bottom of the slab)

Axle and Temperature Differential	Case RE121 Peak Stress (psi)	Location (x,y,z)	Case RE1 Peak Stress (psi)	Location (x,y,z)	Case RE36 Peak Stress (psi)	Location (x,y,z)
S: 0 F	430	(0,195,t)	420	(0,195,b)	424	(0,195,b)
S: 20 F	478	(0,195,t)	463	(0,195,b)	470	(0,195,b)
S: -20 F	386	(0,195,t)	377	(0,195,b)	382	(0,195,b)
T: 0 F	388	(0,175,t)	382	(0,175,b)	381	(0,223,b)
T: 20 F	431	(0,203,t)	417	(0,55,b)	424	(0,203,b)
T: -20 F	386	(45,0,t)	364	(42,0,t)	379	(45,0,t)
D: 0 F	390	(0,179,b)	377	(0,179,b)	384	(0,179,b)
D: 20 F	430	(0,199,b)	408	(0,179,b)	422	(0,199,b)
D: -20 F	386	(45,0,t)	369	(44,0,t)	382	(45,0,t)

The most notable finding in Figure 53 and Table 11 is that the peak tensile stress for all cases changes very little as the subgrade support goes from uniform (single k-value of 63 psi/in) to nonuniform (121 k-values). The difference between the average peak tensile stress for Case 121 (nonuniform) and Case 1 (uniform) was 3.6%. This difference is attributed to the fact that

the size of each uniformly defined area was only 0.7 m by 0.7 m and the range of k-value was only 6 as compared to the “random” cases in Chapter 2, which used a predefined area of 0.9 m (3 ft) and only two discrete k-values (50 and 500 psi/in). Furthermore, to assign k-value for Case RE36, a weighted average of Case RE121 values were used which additionally reduced the range in expected k-values to a factor of 3.

Several other observations from Figure 53 are that the single axle loading for this support assumption produced the highest tensile stresses for no curling and daytime curling, and the nighttime curling condition produced the lowest tensile stresses for all axle types. These findings were slightly different than those from Chapter 2, which found that the tandem axles were the dominant axle in the majority of cases analyzed. This reinforces that determination of the critical axle type depends on the distribution and size of the nonuniform area, slab geometry, and load location.

4.2.2 Stress Analysis for Left Edge (LE) Loading Case

Case LE121 represented the movement of the axles along the left edge of the slab, similar to RE121 with 121 k-values, as shown in Figure 54. The distribution of stresses for Case LE121 is similar to Case RE121 (previously shown in Figure 49), with the critical tensile stresses occurring near the center of each slab. The single axle configuration with daytime curling produced the peak tensile stress like Case RE121. The critical tensile stress was found at the bottom of the slab. Similarly, the maximum tensile stresses at each longitudinal position for Cases LE1 and LE36 are included in Appendix B in Figures B1 and B2. The maximum tensile stresses for LE1 were the same as RE1 while case LE36 had similar trends and findings as RE36. A summary of the peak tensile stresses for the left edge loading path can be seen in Table 12.

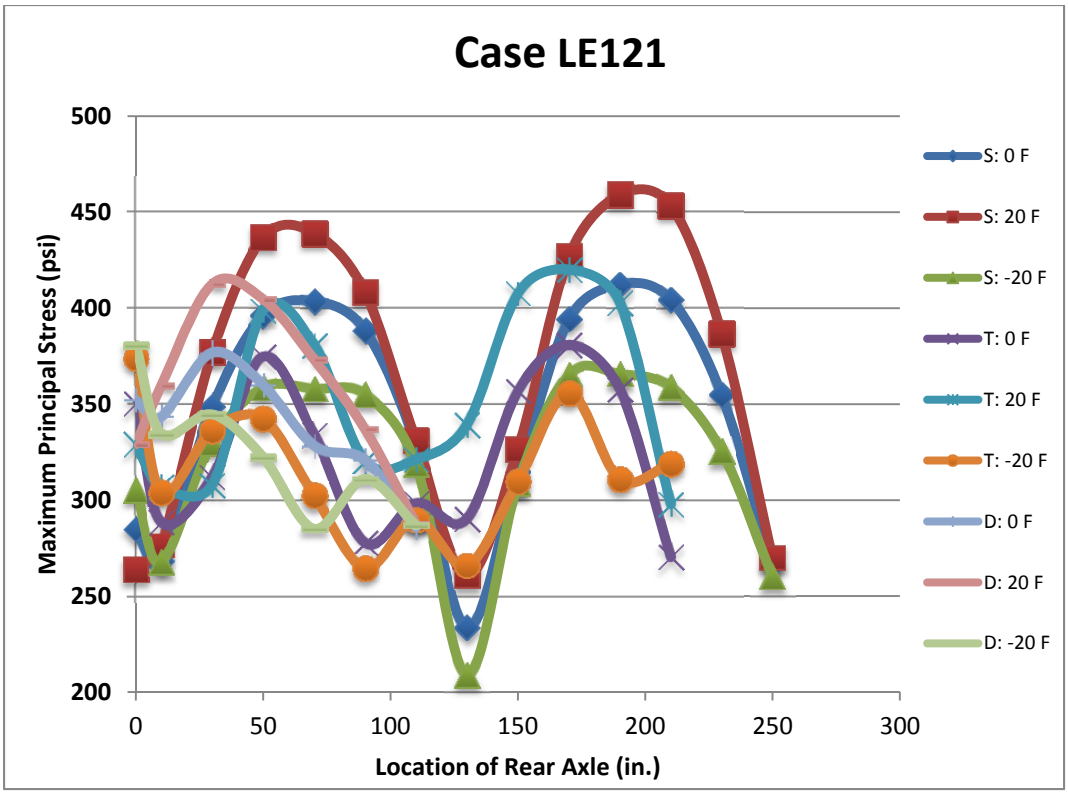

Figure 54. Maximum principal (tensile) stress at each axle position for Case LE121.

Figure 55 shows the location of the axle causing the peak tensile stress for LE121. The overall peak tensile stress (463 psi) occurred under the uniform support condition case (LE1) as seen in Table 12. However, the overall peak tensile stress for each of the support condition is within 1%. Figure 56 shows that Case LE121 (with discretized area of 0.7 x 0.7 m^2) and Case LE36 (with discretized area of 1.16 x 1.16 m^2) had a similar magnitude of tensile stress relative to the uniform support assumption (Case LE1). Therefore, the size of the nonuniform area or number of discretized areas did not play a role in the tensile stress changes (0.8% decrease in average peak tensile stress was observed when moving from a nonuniform subgrade support to a uniform subgrade support). This can be attributed to the distribution of k-values being closer to mean (63 psi/in) along the left lane edge case, as seen in Figure 55.

Figure 55. Local variation in k-values along left edge of the slab for Case LE121.

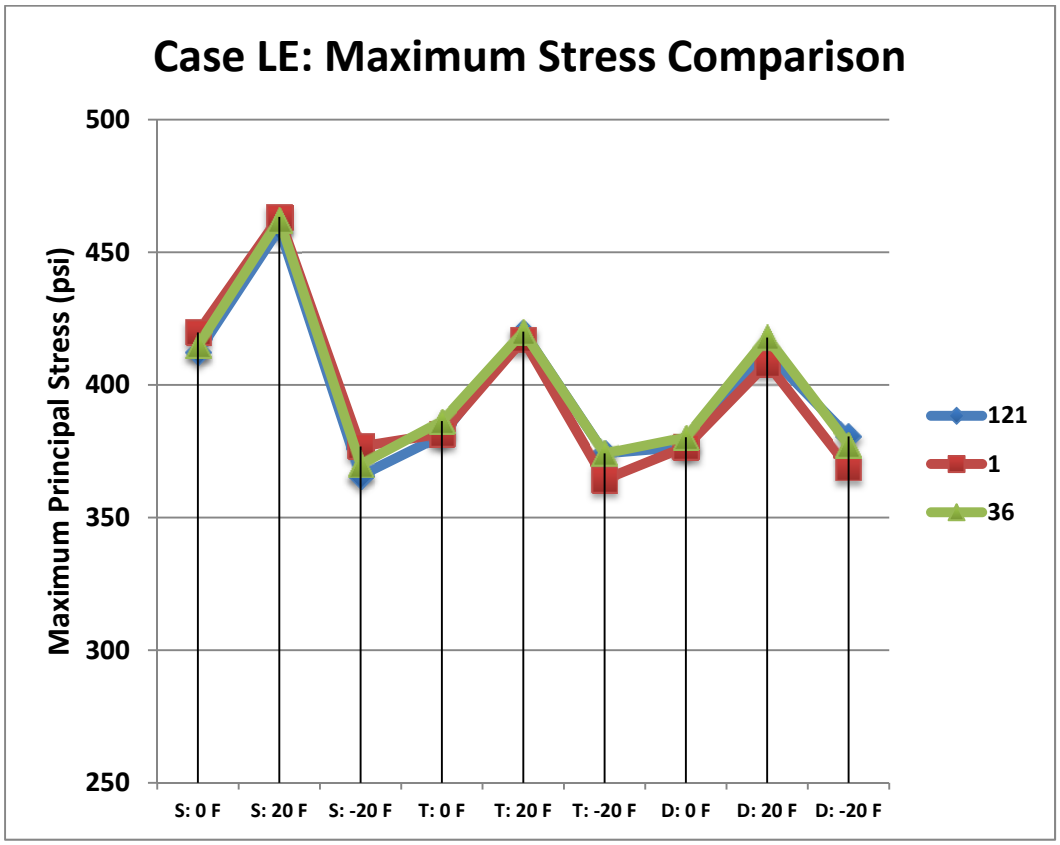

Figure 56. Comparison of the critical tensile stresses for Case LE for each input factor level and three nonuniform support conditions.

To calculate the mean k-value along the edge for Cases RE and LE, only the k-values along the respective edges (i.e., two corner stiffness areas with size 0.35 x 0.35 m^2) and the remaining stiffness areas of 0.35 x 0.70 m^2 at each edge location were selected. The mean of the k-values at the left hand edge was 67 psi/in with a standard deviation of 17.8 psi/in while the right hand edge had a higher mean of 86 psi/in, but the standard of deviation was almost 50

psi/in. From Figure 57 and Figure 58 it can be seen that k-values have wider distribution for RE compared to LE, hence, the higher critical stress at RE compared to LE is due to higher variation in the adjacent k-values. In Table 12, the k-value at the overall peak tensile stress location for Case 121 was 84 psi/in, which is higher than the uniform support k-value of 63 psi/in. Even though the peak tensile stress for Case LE121 occurs at higher k-value (almost 30 psi/in difference), this tensile stress was comparable to Case LE1 on account of the variation in the adjacent area stiffness.

Table 12. Summary of Peak Tensile Stress for Each Subcase for LE Loading Location

Axle and Temperature Differential	Case LE121 Peak Stress (psi)	Location (x,y,z)	Case LE1 Peak Stress (psi)	Location (x,y,z)	Case LE36 Peak Stress (psi)	Location (x,y,z)
S: 0 F	412	(275,195,b)	420	(275,195,b)	415	(275,195,b)
S: 20 F	459	(275,195,b)	463	(275,75,b)	462	(275,195,b)
S: -20 F	366	(279,195,b)	377	(279,195,b)	370	(279,175,b)
T: 0 F	381	(275,175,b)	382	(275,175,b)	386	(275,175,b)
T: 20 F	420	(275,175,b)	417	(275,55,b)	420	(275,175,b)
T: -20 F	374	(229,0,t)	364	(233,0,t)	374	(229,0,t)
D: 0 F	377	(275,179,b)	377	(275,179,b)	380	(275,179,b)
D: 20 F	412	(275,179,b)	408	(275,179,b)	418	(275,179,b)
D: -20 F	381	(229,0,t)	369	(231,0,t)	377	(229,0,t)

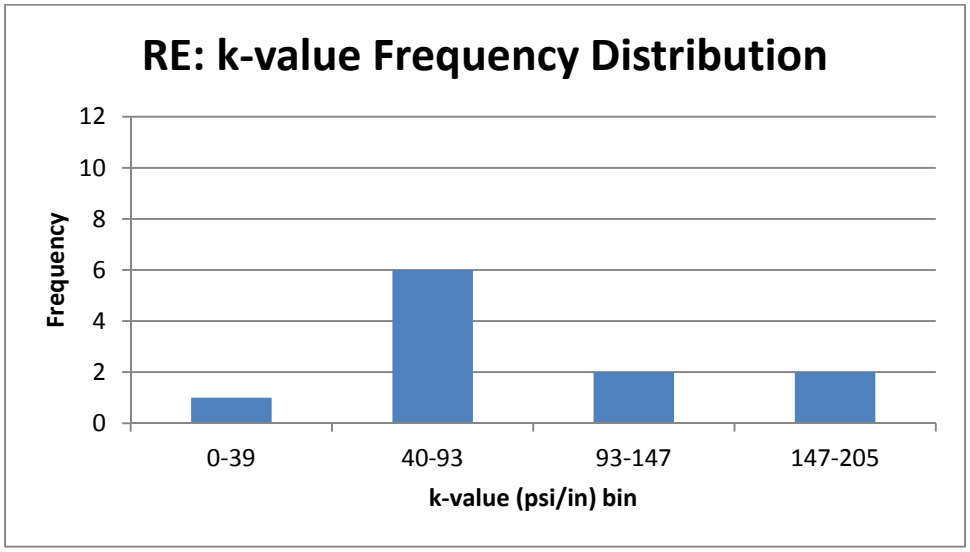

Figure 57. The k-values along the right hand edge for Case RE121 of MI I-94 roadway.

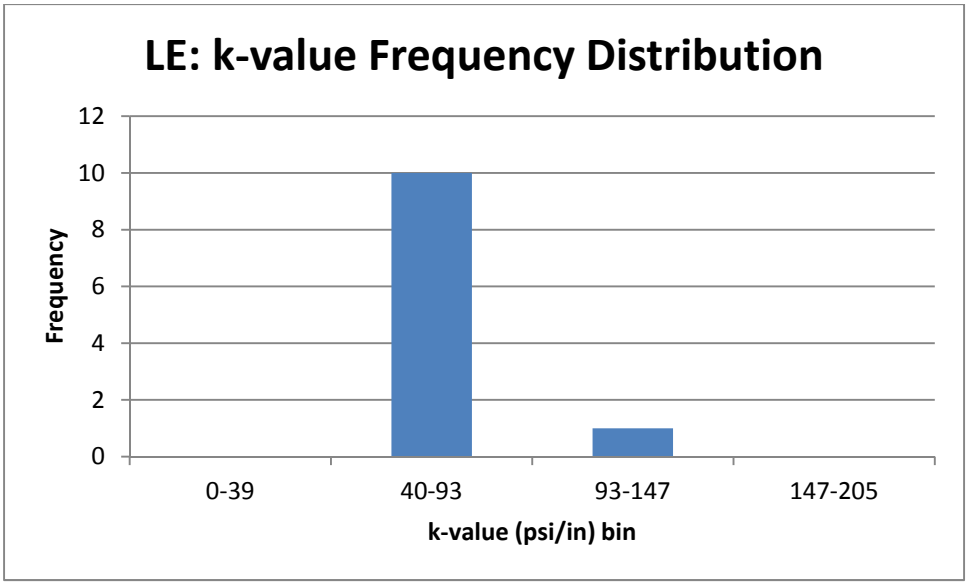

Figure 58. The k-values for Case LE121 of MI I-94 roadway.

4.2.3 Stress Analysis for Middle of Lane (M) Loading Case

For the middle of the lane cases with the axle straddling the longitudinal joint (Case M), the same analysis matrix was applied. The results for Case M121 in Figure 59 show that the maximum tensile stress patterns at different longitudinal positions are significantly different than Case RE (shown previously in Figure 49). The maximum tensile stresses are much higher at the initial transverse joint relative to the RE case. Positive temperature differentials produced the highest tensile stresses for all three axle types. When the rear axle of the tandem and steer-drive axles reached around 90 in, a large tensile stress increase was observed, which was related to local variation in k-value (36 to 113 psi/in over 90 in), as shown in Figure 60. This behavior again confirms the importance of local nonuniformity on the tensile stresses in the slab. Although the highest tensile stresses are observed at the initial transverse edge, this location would not have been controlling if there was an adjacent slab to offer load transfer to the transverse free edge. The interior loading locations had lower tensile stresses as compared to free edge loading Case RE. For Case M, the mean of the k-value covers all of the k-value areas that the width of the axle will cover through its longitudinal traverse from the initial loading location to the transverse end of the slab. Since the interior loading location is not as critical as the edges, the slab should not have the same response sensitivity to changes in the local k-values. The mean k-value of the loading locations was 63 psi/in with a standard deviation of 20.3 psi/in. From Figure 62 it can be seen that Case M had a higher frequency distribution of k-values within one standard deviation of the mean and hence does not behave in the same nonuniform way as the free edge RE case. The interior loading path coupled with the presence of a contraction joint are contributing factors to lower tensile stresses along the middle of the slab loading path compared to the edge loading path.

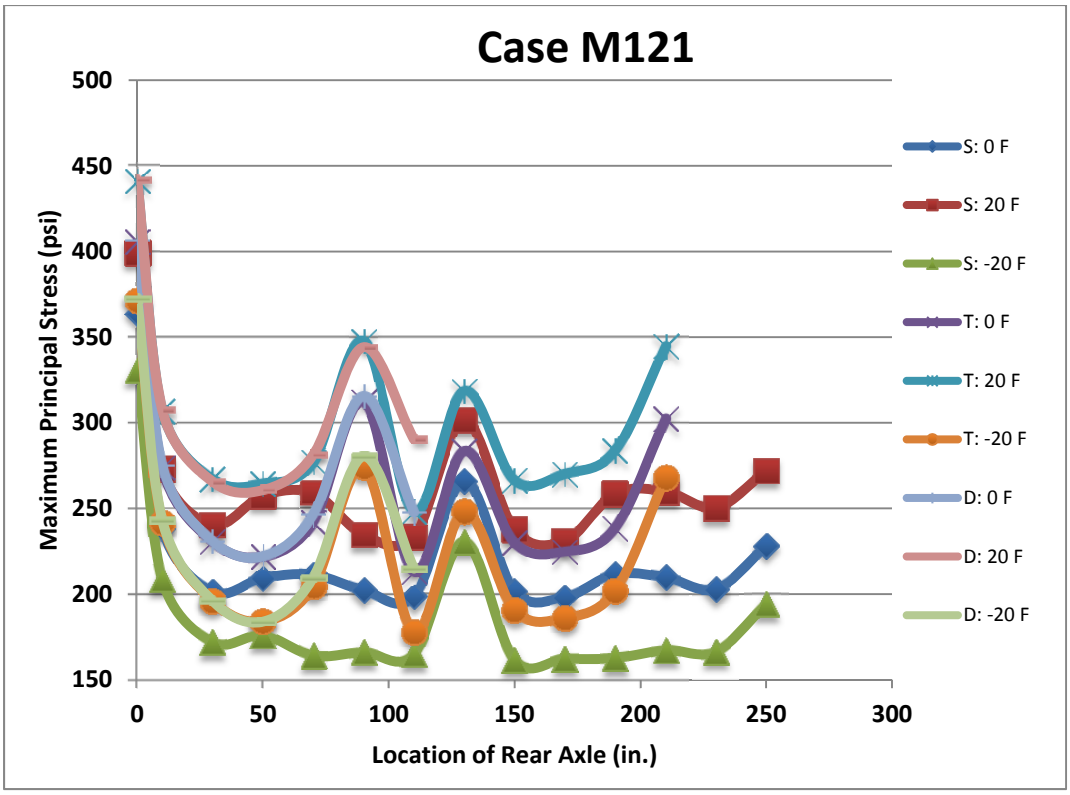

Figure 59. Maximum principal (tensile) stress for Case M121 versus axle position.

As expected, the middle loading path with a single k-value (Case M1) or 36 discrete k-values (Case M36) produced similar peak tensile stresses to Case M121, as shown in Figure 61, with a slight decrease in average peak tensile stress from nonuniform to a uniform subgrade support of 0.8%. All the critical stresses in Figure 61 are at the bottom of the slab with negative temperature curling causing the lowest tensile stresses for each axle configuration. The maximum tensile stresses at each longitudinal position for cases M1 and M36 can be seen in Figures B3 and B4 in Appendix B.

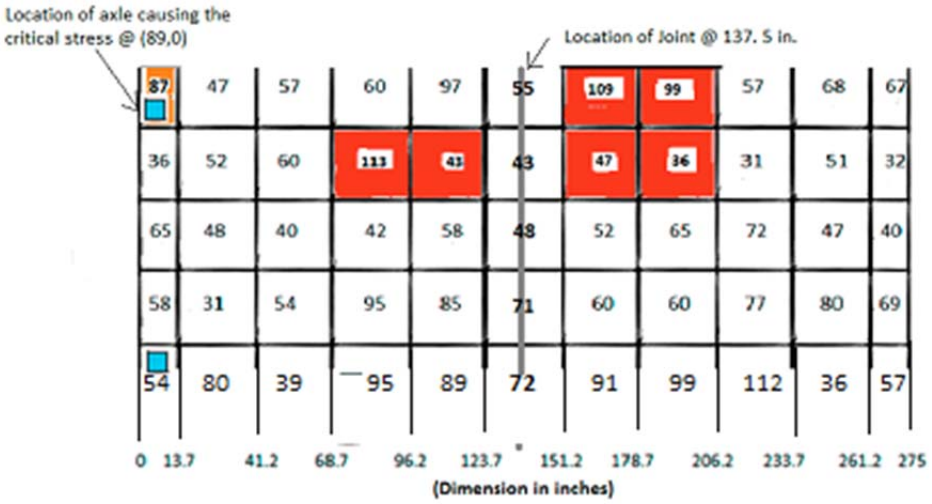

Figure 60. Local variation in k-values along interior of the slab for Case M121.

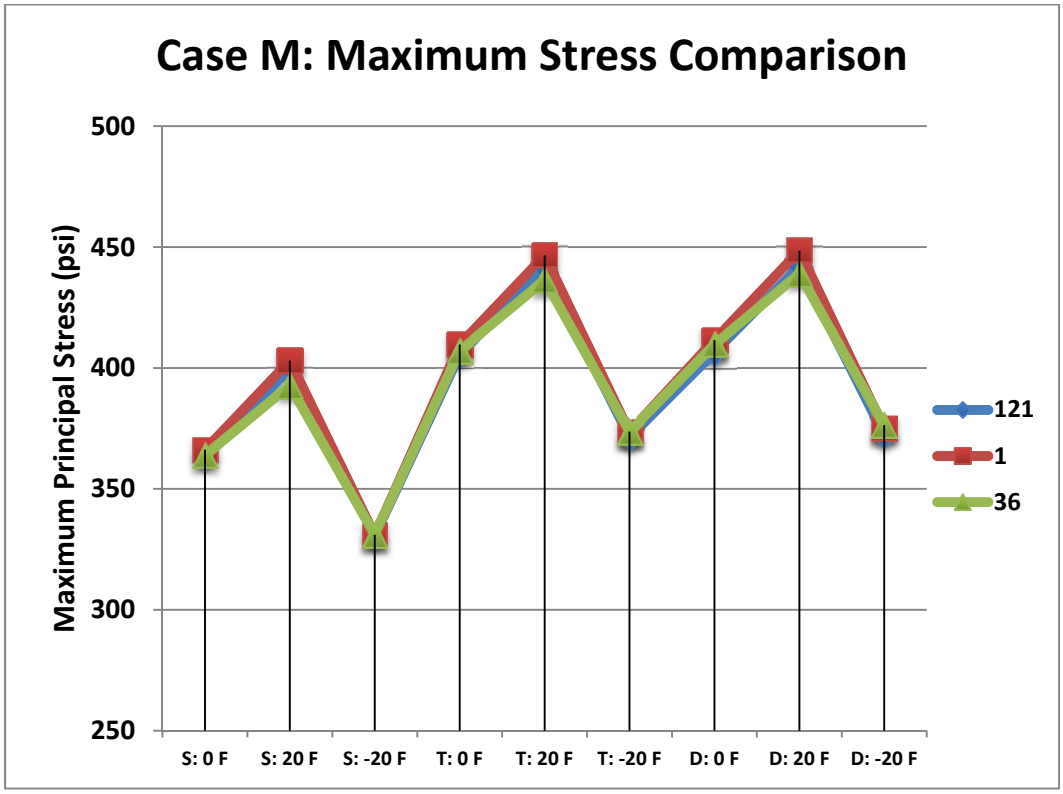

Figure 61. Comparison of the peak tensile stresses for Case M for each input factor level and three nonuniform support conditions.

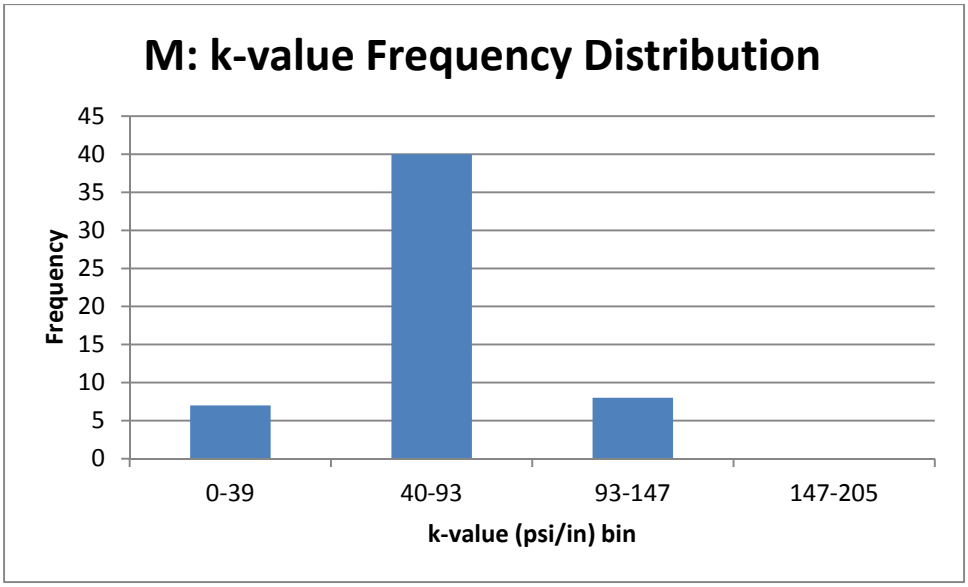

Figure 62. The k-values for Case M121 of MI I-94 roadway.

Figure 63 compares the peak stresses of the three loading locations (RE, LE, M) with the three axle types and temperature differentials. The distribution stresses for the two edges, RE and LE, follow a similar pattern for each case with the RE cases having a higher variation of subgrade stiffness relative to LE. As seen in Figure 63, RE produced the most critical tensile stresses for each variable combination with the maximum tensile stress occurring because of a single axle during daytime curling. However, the difference between the maximum tensile stresses between RE and LE was only 3%. Although for Case M loading the tandem and steer-drive axles developed the most critical tensile stresses, these stresses were located at the free transverse edge, which were greatly reduced in the presence of joint load transfer. The longitudinal edge loading had a 19% increase in peak tensile stress between Case RE and Case M. The most important finding so far was the effect of discretization of the nonuniform subgrade stiffness areas. There was not a significant difference between the overall peak tensile stress of uniform and nonuniform support condition with a maximum of 3.2% for the most critical location (RE121 for S: 20F) and the difference of 3.6% in average peak tensile stress. One reason for this is that the change in adjacent k-values at the critical loading location (Case RE121) was 2 (i.e., k-value of 87 and 43 psi/in from Figure 50) while the “random” cases from Chapter 2 had a factor of 10 (50-500 psi/in) for a change in k-values, which produced a tensile stress change of 32%.

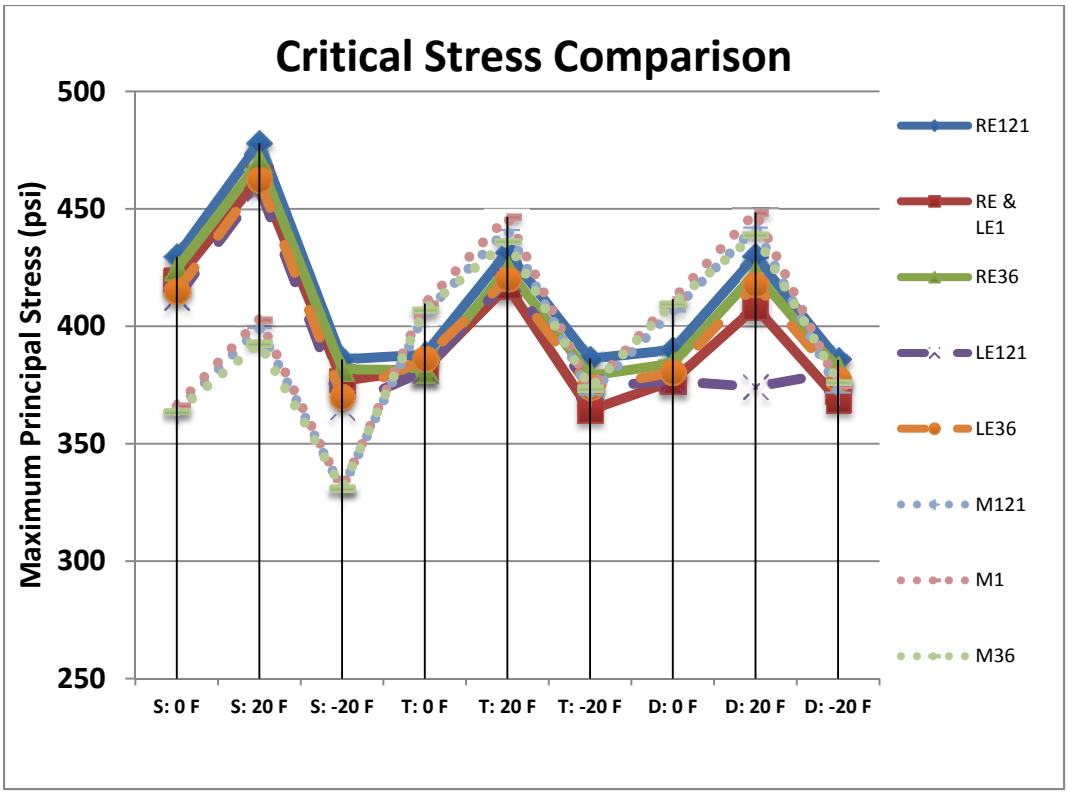

Figure 63. Comparison of peak tensile stresses for Cases RE, LE and M for each combination of support condition, axle type and temperature differentials.

4.2.4 Stress Analysis for Right Wheelpath (RW) and Left Wheelpath (LW) Cases

Two additional analyses were carried out, Cases RW121 and LW121, representing longitudinal movement of the axles in the right and left wheelpaths, respectively. Figure 64 and Figure 65 show intuitively that lower tensile stresses resulted when axles were not traversing along the free edge of the pavement (i.e., there is a significant drop in peak tensile stresses relative to Cases LE and RE in Figure 63). Cases RW121 and LW121 also show some similar trends in the maximum tensile stresses for the different axle configurations, temperature differentials, and longitudinal position, as seen in Figure 64 and Figure 65, but there are some minor differences, depending on the changes in local support stiffness. This tensile stress behavior is due to the interior slab loading location along with the distribution of k-values under the outer wheel at the various axle loading locations in the wheelpath being closer to the overall mean k-value of 63 psi/in. The mean was calculated by including all the k-value areas loaded by the right or left wheel as the axle traversed longitudinally along the RW and LW. The RW case had a mean k-value of 60 psi/in and standard deviation of 18.1 psi/in, while LW had a mean of 67 psi/in and standard deviation of 19.8 psi/in, compared with Case RE with a mean of 86 psi/in and a standard deviation of 50 psi/in. The distribution of k-values under for RW121 and LW121, shown in Figure 68 and Figure 69, respectively, suggests that the frequency distribution of the majority of the k-values are close to the uniform support k-value of 63 psi/in and within one standard deviation from the mean resulting is similar tensile stress development.

The single axle and positive temperature differential combination produced the overall peak tensile stress for both RW121 and LW121 cases. The location of the overall peak tensile

stress developed when the axle was at 190 in from the first loading location, which is approximately mid-slab of the second concrete slab. The overall peak tensile stresses for RW121 and LW121 were approximately 35% lower than the RE121 overall peak tensile stress with only 2% difference between the overall peak tensile stress of RW121 and LW121.

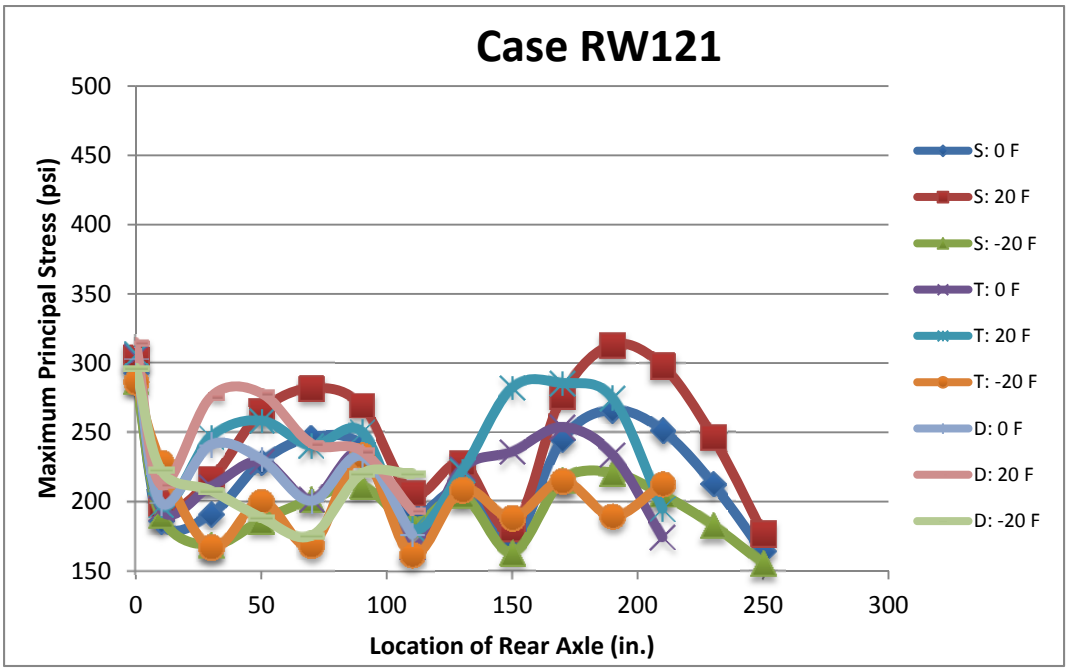

Figure 64. Maximum principal (tensile) stress for Case RW121 versus axle position.

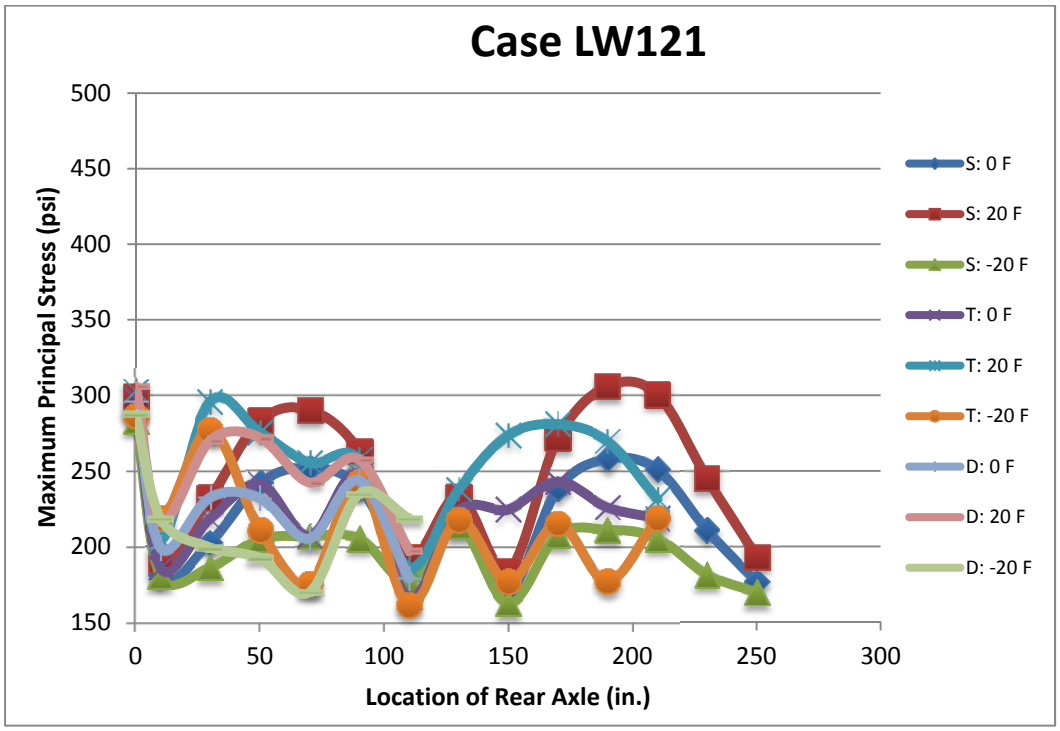

Figure 65. Maximum principal (tensile) stress for Case LW121 versus axle position.

The maximum tensile stresses at each longitudinal position for Cases RW1, RW36, LW1, and LW36 can be found in Appendix B. A summary of the tensile stress analysis for all three distribution of k-values (1, 36, and 121 support areas), shown in Figure 66 and Figure 67, demonstrated that 0.7 x 0.7 m^2 uniform areas (121 k-values) produced the highest slab tensile stresses for all but one loading configuration and temperature curling condition. The average peak tensile stresses increased by 5.3% and 3.5%, respectively, for the right wheelpath and left wheelpath when going from fully uniform support to 121 support values. The overall peak tensile stress difference between uniform support and nonuniform 121 support for RW and LW was 2% and 1%, respectively. The effect of the nonuniformity of support on slab stresses in these cases were not significant enough to cause premature cracking failures if it is ignored as the critical tensile stress of 313 psi for RW121 and 307 psi for LW121, which are almost half of the typical concrete flexural strength of 650 psi. For the wheelpath loading positions, all peak tensile stresses in Figure 66 and Figure 67 were located at the bottom of the slab.

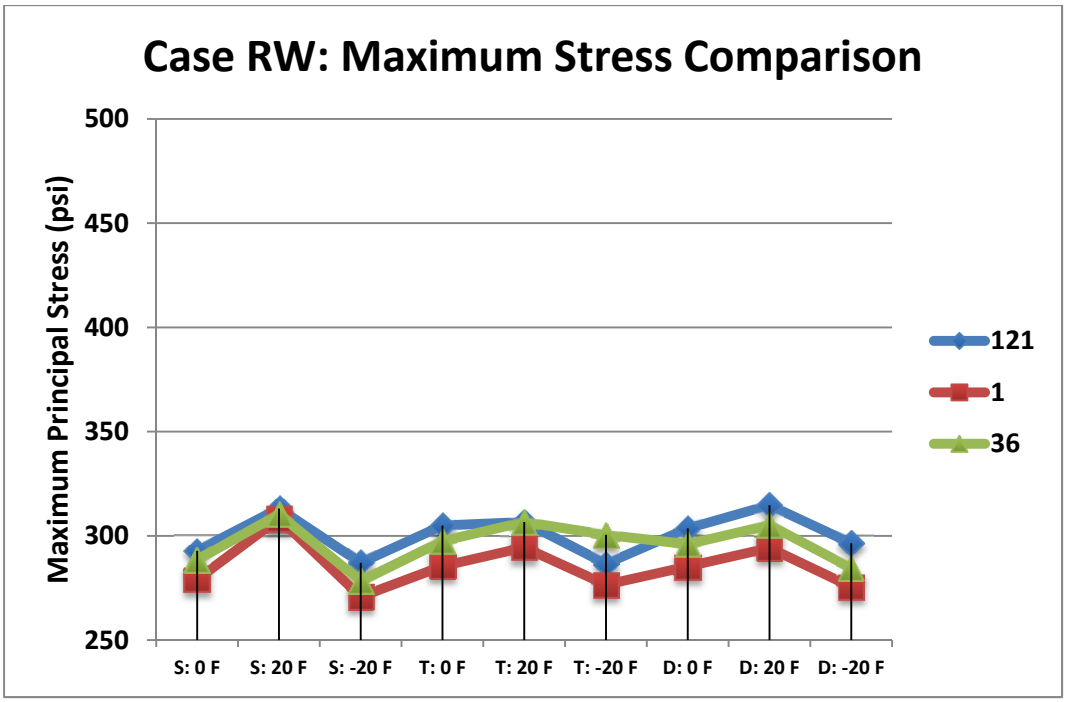

Figure 66. Comparison of the peak tensile stresses for Case RW for each input factor level and the three levels of nonuniform support.

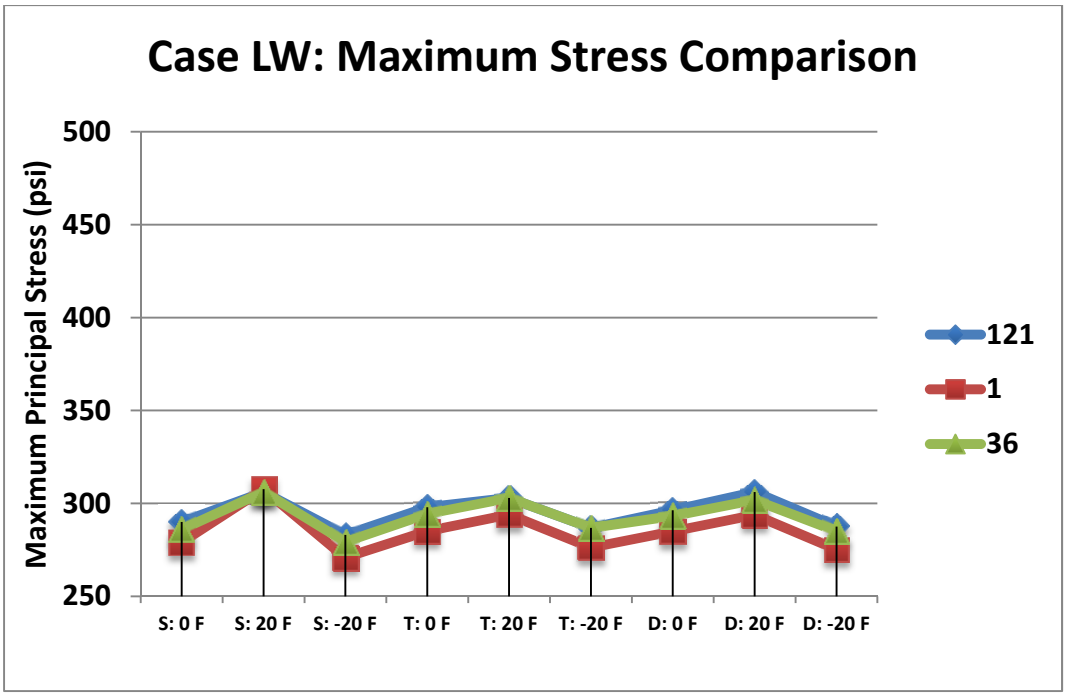

Figure 67. Comparison of the peak tensile stresses for Case LW for each input factor level and the three levels of nonuniform support.

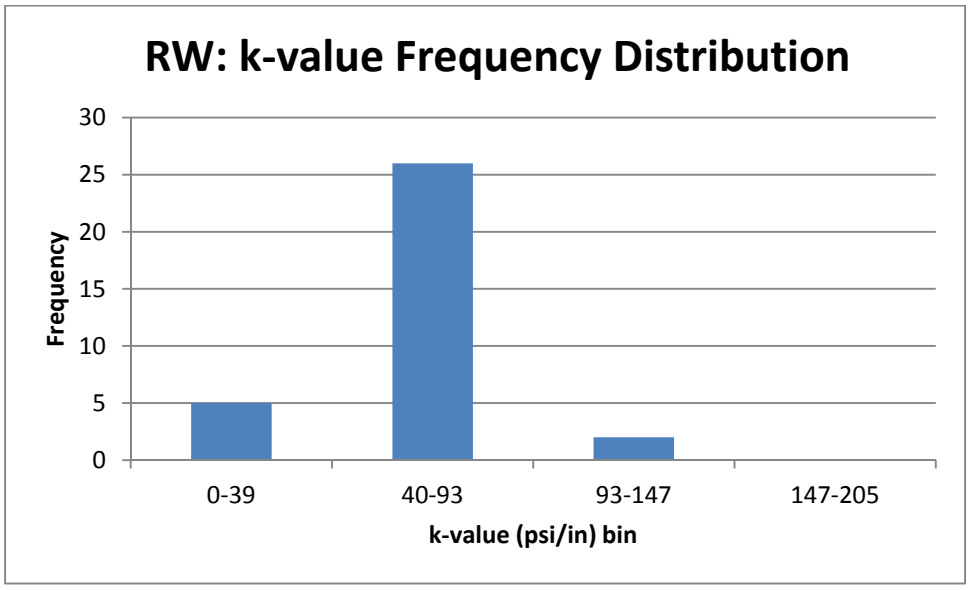

Figure 68. The k-values for Case RW121 of MI I-94 roadway.

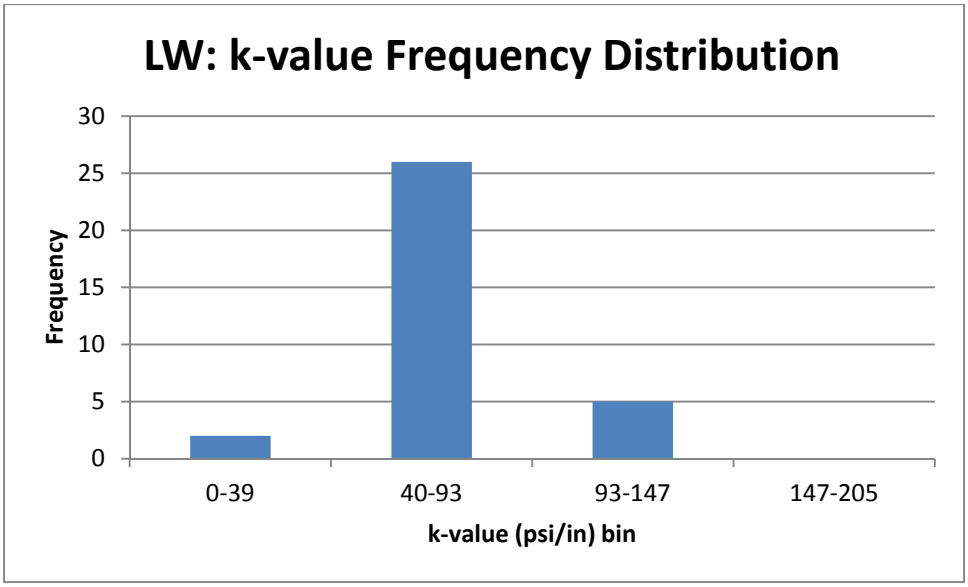

Figure 69. The k-values for Case LW121 of MI I-94 roadway.

4.3 Summary of MI I-94

Based on the analysis of the MI I-94 deterministically assigned spatial field data, several conclusions can be made regarding the effect of subgrade nonuniformity. From Figure 70, the loading paths, Case RE followed by Case LE, produced the largest tensile stresses. The change in tensile stresses from the uniform subgrade case was the highest with the 121 discrete k-value areas, in particular for Cases RE and RW. However, Table 13 shows that the tensile stress increased from the uniform support condition for all loading paths but was not at the significance level found in Chapter 2. In fact, in several loading paths (Cases M and LE) the uniform case had higher peak tensile stresses because of the spatial distribution of the k-value under the slab relative to the expected critical load location. Overall, the range in k-values was less than a factor of 7 (31 to 202 psi/in), which was less than the factor of 10 used in the "random" cases in Chapter 2. Furthermore, the "random" cases in Chapter 2 had much greater local variation in the k-value since only two discrete k-values were used (i.e., 50 and 500 psi/in).

The field measurements and analysis did confirm findings from Chapter 2 that the support condition along the longitudinal edge was the most critical tensile stress location and should be the zone most controlled if intelligent compaction is going to be efficiently used. Finally, the local variation in k-value relative to the critical load location (i.e., Cases RE versus LE) affects which loading path has the overall peak tensile stress.

Table 13. Change in Average Peak Tensile Stress between Nonuniform (121 k-values) to Uniform (single k-value) for Each Loading Path

Loading Path	Change in Average Peak Tensile Stress
Case RE (Right Lane Edge)	3.6% (Increase in stress)
Case M (Middle of Lane)	0.8% (Decrease in stress)
Case LE (Left Lane Edge)	0.8% (Decrease in stress)
Case RW (Right Lane Wheelpath)	5.3% (Increase in stress)
Case LW (Left Lane Wheelpath)	3.5 % (Increase in stress)

One reason for the lack of significant change in tensile stress moving from uniform support (1 k-value) to nonuniform support (121 k-value), besides a relatively lower standard deviation in k-value in the field measurement, is the definition of the size of the nonuniform area. For the same k-value distribution, as the nonuniform area decreases, its effect on slab tensile stresses decreases as well; likewise as the nonuniform area approaches the size of the slab, the slab stresses tend to the uniform support tensile stresses. The discretization of larger nonuniform area of 1.16 x 1.16 m^2 (which was 36 k-values) was thought to be a more critical size, as noted in Chapter 2, but failed to develop the most critical tensile stresses. Further review revealed that the 36 k-value cases were developed by weighted average of adjacent k-values from Case 121 and thus the extreme k-value values were eliminated when converting the measured 121 k-values to 36 k-values. Therefore, the technique to create the other nonuniform support cases inherently reduced the tensile stress sensitivity. Figure 70 shows that the critical tensile stresses produced by Cases RW and LW were considerably lower (approximately 33% less than RE) then edge-loaded or middle of lane cases and hence can be deemed as noncritical in nature primarily on account of their interior loading location. As mentioned earlier, the high critical stress of Case M is due to the presence of a free transverse edge loading condition.

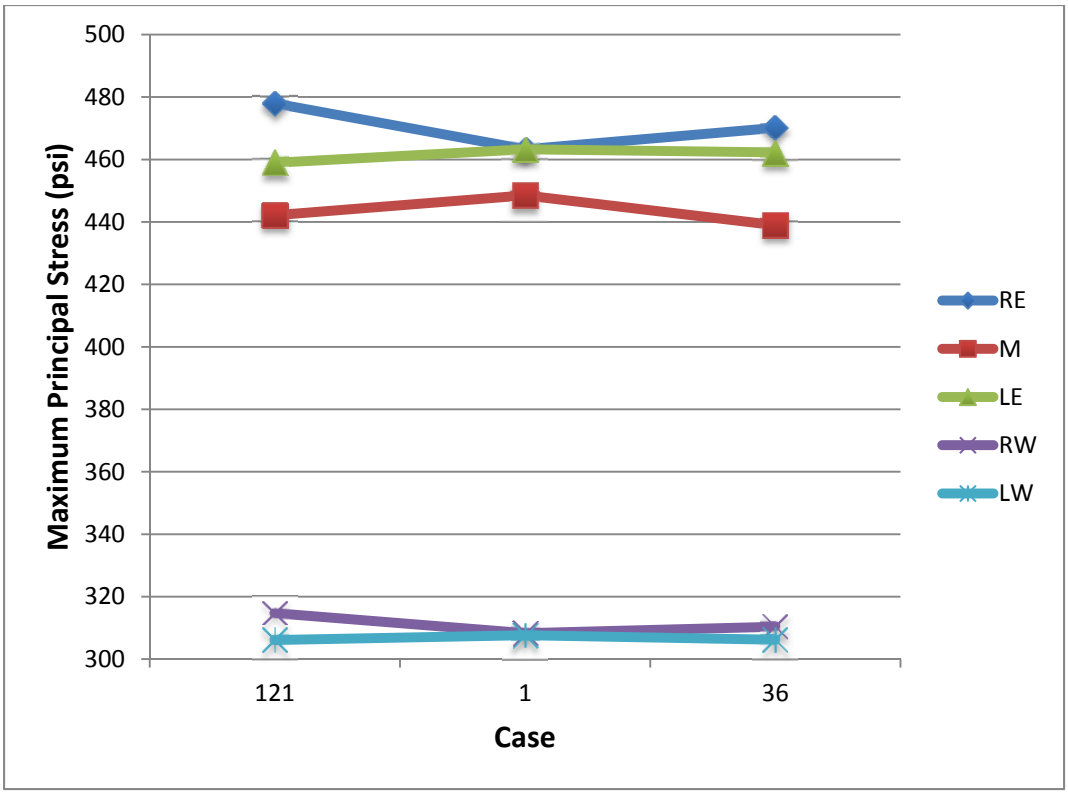

Figure 70. Comparison of peak tensile stress for each loading path with three subgrade support conditions.

As noted above, the spatial distribution and range of k-values was a factor in the peak tensile stress for each case. The percentage frequency distribution of k-values for Cases 36 and 121, shown in Figure 71, demonstrated a 27% greater occurrence for Case 36 in the bin 56-80 which represents the k-values closer to the mean. Case 121 distribution was created for a mean of 63 psi/in, standard deviation of 25.6 psi/in, and range of 31 to 202 psi/in, whereas Case 36 had a mean of 63 psi/in, standard deviation of 14 psi/in and range of 39 to 116 psi/in. It is obvious that Case 36 had the same mean and lower standard deviation since it was defined based on creating uniform discrete areas of 1.16 m x 1.16 m^2 by weighted average of the 121 k-values measurements.

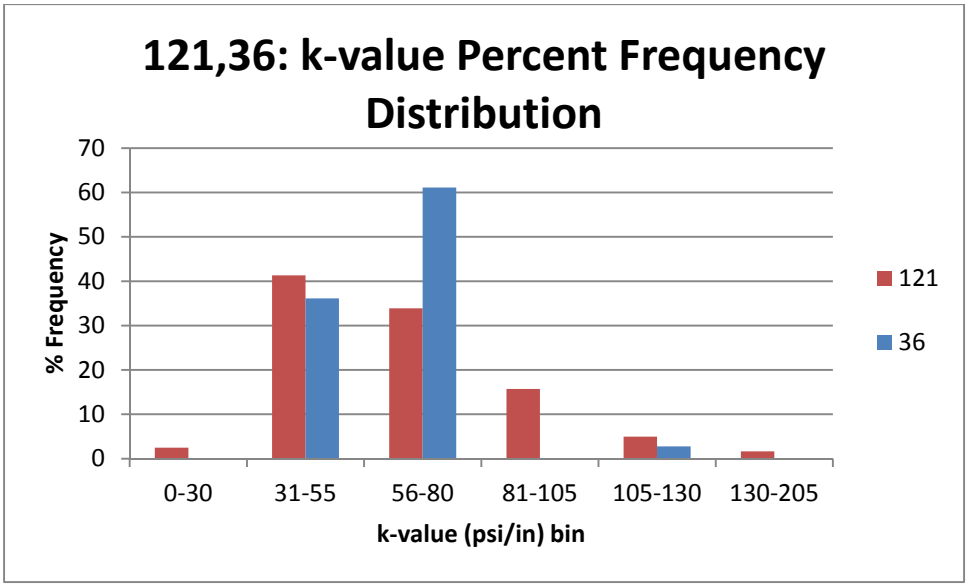

Figure 71. Percent frequency distribution of k-values for cases 36 and 121.

Table 14 shows the location of the peak tensile stress for each factor level and loading path. The positive temperature differential was the most critical temperature loading case for all axle types. As expected, edges were the most critical loading locations with right hand edge location having slightly higher magnitude in the peak tensile stress than left hand edge because of a greater variation in k-values along the loading path. For the right and left edge, the peak tensile stresses were located at the mid-slab edges. The single axle was the critical axle configuration both the edge cases (RE and LE) and middle of lane (Case M), whereas steer-drive and tandem axles were critical for the wheel path (Cases RW and LW). Single axle generated tensile stresses along the edge were more sensitive to local variations in k-values. Relative to the uniform support case with the mean k-value of the field measurements, the nonuniformity in subgrade support did not produce significant tensile stress changes (maximum of 3.2% along the critical loading path) as seen in Chapter 2, which showed a 32% change in peak tensile stresses for an arbitrary, predefined nonuniform support compared to a uniform support condition.

Table 14. Location and Magnitude of Critical Tensile Stress for Each Factor Level Analyzed

Case	Single Axle			Tandem Axle			Steer-Drive Axle		
	0 F	20 F	- 20 F	0 F	20 F	- 20 F	0 F	20 F	-20 F
RE121	429 (0,195,b)	478 (0,195,b)	385 (0,195,b)	387 (0,175,b)	331 (0,203,b)	386 (45,0,t)	389 (0,179,b)	429 (0,199,b)	385 (45,0,t)
RE1	419 (0,195,b)	463 (0,175,b)	376.7 (0,195,b)	381 (0,175,b)	417 (0,55,b)	364.3 (42,0,t)	376.7 (0,179,b)	408.0 (0,179,b)	368.7 (44,0,t)
RE36	424 (0,195,b)	470 (0,195,b)	381 (0,195,b)	381 (0,223,b)	424 (0,203,b)	378 (45,0,t)	384 (0,179,b)	422 (0,199,b)	381 (45,0,t)
LE121	412 (275,195, b)	458.9 (275,195, b)	365 (275,195, b)	380 (275,175, b)	420.0 (275,175, b)	374 (229,0,t)	376 (275,179, b)	412 (275,179, b)	380 (229,0,b)
LE1	419 (275,195, b)	463 (275,95,b)	376 (275,195, b)	381 (275,175, b)	417 (275,55,b)	364 (233,0,t)	376 (275,179, b)	408 (275,179, b)	368 (231,0,b)
LE36	414 (275,195, b)	462 (275,195, b)	369 (275,175, b)	386 (275,175, b)	420 (275,175, b)	374 (229,0,t)	380 (275,179, b)	417 (275,179, b)	377 (229,0,b)
M121	363 (89,0,b)	399 (89,0,b)	330 (89,0,b)	405 (89,0,b)	441 (89,0,b)	371 (89,0,b)	406 (89,0,b)	442 (89,0,b)	372 (89,0,b)
M1	366 (89,0,b)	403 (89,0,b)	330 (89,0,b)	409 (89,0,b)	446 (89,0,b)	373 (89,0,b)	411 (89,0,b)	448 (89,0,b)	374 (89,0,b)
M36	363 (89,0,b)	392 (89,0,b)	331 (89,0,b)	407 (89,0,b)	436 (89,0,b)	373 (89,0,b)	409 (89,0,b)	438 (89,0,b)	376 (89,0,b)
RW121	292 (117,0,b)	313 (20,195,b)	287 (117,0,b)	304 (117,0,b)	306 (117,0,b)	286 (117,0,b)	303 (117,0,b)	314 (117,0,b)	296 (117,0,b)
RW1	279 (117,0,b)	308 (20,75,b)	270 (117,0,b)	285 (117,0,b)	294 (117,0,b)	276 (117,0,b)	285 (117,0,b)	294 (117,0,b)	275 (117,0,b)
RW36	288 (117,0,b)	310 (20,195,b)	278 (117,0,b)	297 (117,0,b)	306 (117,0,b)	300 (117,0,b)	296 (117,0,b)	305 (117,0,b)	284 (117,0,b)
LW121	290 (157,0,b)	306 (255,195, b)	283.0 (157,0,b)	297 (157,0,b)	302 (157,0,b)	286 (157,0,b)	296 (157,0,b)	306 (157,0,b)	287 (157,0,b)
LW1	279 (157,0,,b)	307 (255,175, b)	270 (157,0,b)	285 (157,0,b)	294 (157,0,b)	276 (157,0,b)	284 (157,0,b)	293 (157,0,b)	275 (157,0,b)
LW36	286 (157,0,b)	306 (255,195, b)	279 (157,0,b)	294 (157,0,b)	302 (157,0,b)	286 (157,0,b)	293 (157,0,b)	301 (157,0,b)	285 (157,0,b)

t: Top of slab; b: Bottom of slab

4.4 MI I-96: Field Data and Deterministic Assignment of k-Values

4.4.1 MI I-96 Project Background

The field analysis was extended to another site in Michigan, along I-96. In situ testing was carried out in a similar manner to the test sections of MI I-94. The subgrade was classified according to the AASHTO soil classification as an A-4 ML, which is a medium plasticity silt. The pavement structure to be constructed was an 11.5-in PCC over a 5-in cement-stabilized open-graded drainage course and an 11-in sand subbase on top of the subgrade. The subbase was a poorly graded sand, which resulted in it having lower CBR values than the subgrade. The in situ testing consisted of intensive testing on a spatial test bed comprising of an 8 x 8 m^2 plot, as shown in Figure 72. The test locations are represented in the form of nodes spaced at approximately one meter from each other in both the longitudinal and transverse direction. DCP tests were carried out on top of the sand subbase layer underlain by subgrade. CBR values were obtained at each nodal location based on the dynamic penetration index as seen in

Equation 4.1. DCP tests were carried out at all nodal locations except for the ones marked with black dots in Figure 72. The moisture content of each test location was known based on nuclear moisture density gauge. A linear relationship was developed between moisture content and CBR at all the nodal locations except for the eight unknown CBR nodes. Based on this linear relationship, the CBR at the locations without DCP tests were estimated. The limitation of such a procedure is noted, but because of the lack of specific field data for k-value, such assumptions were made. Based on these nodal CBR values, k-values were correlated based on the empirical relationship in Equation 4.7. As no PLTs were carried on this roadway section, an empirical correlation for CBR to k-values specific to this test section could not be made. Hence, based on geographical proximity and to provide a base of comparison between the two roadway sections (i.e., MI I-94 versus MI I-96), Equation 4.7 was used for deriving the support conditions. There were 81 CBR values which were correlated to k-values (see Appendix A for the values). As the conclusions from the MI I-94 analysis suggested that an area of approximately one meter was critical for stress development and based on the spacing of the in situ testing locations being one meter apart on a slab geometry measuring 8 x 8 m^2, the discretized support case was developed. The 81 k-values with its assigned areas of 1 x 1 m^2 were called Case 81, as shown in Figure 73.

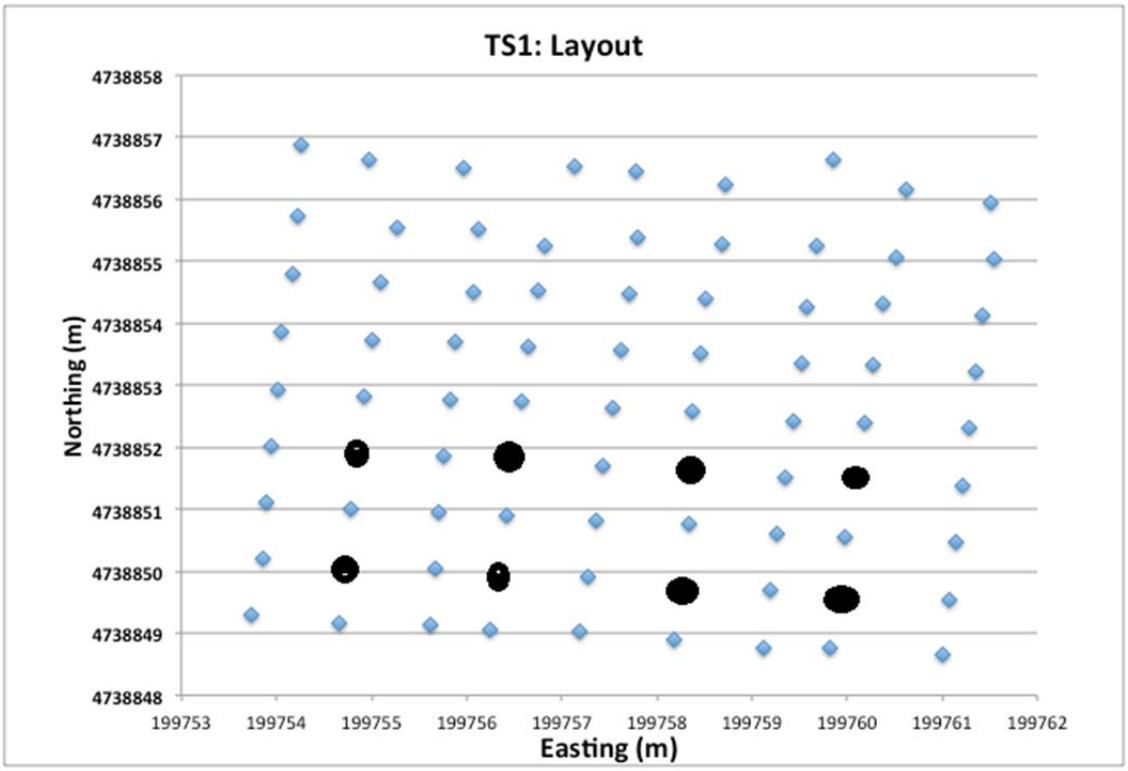

Figure 72. Coordinates of DCP tests for test section 1 on MI I-96.

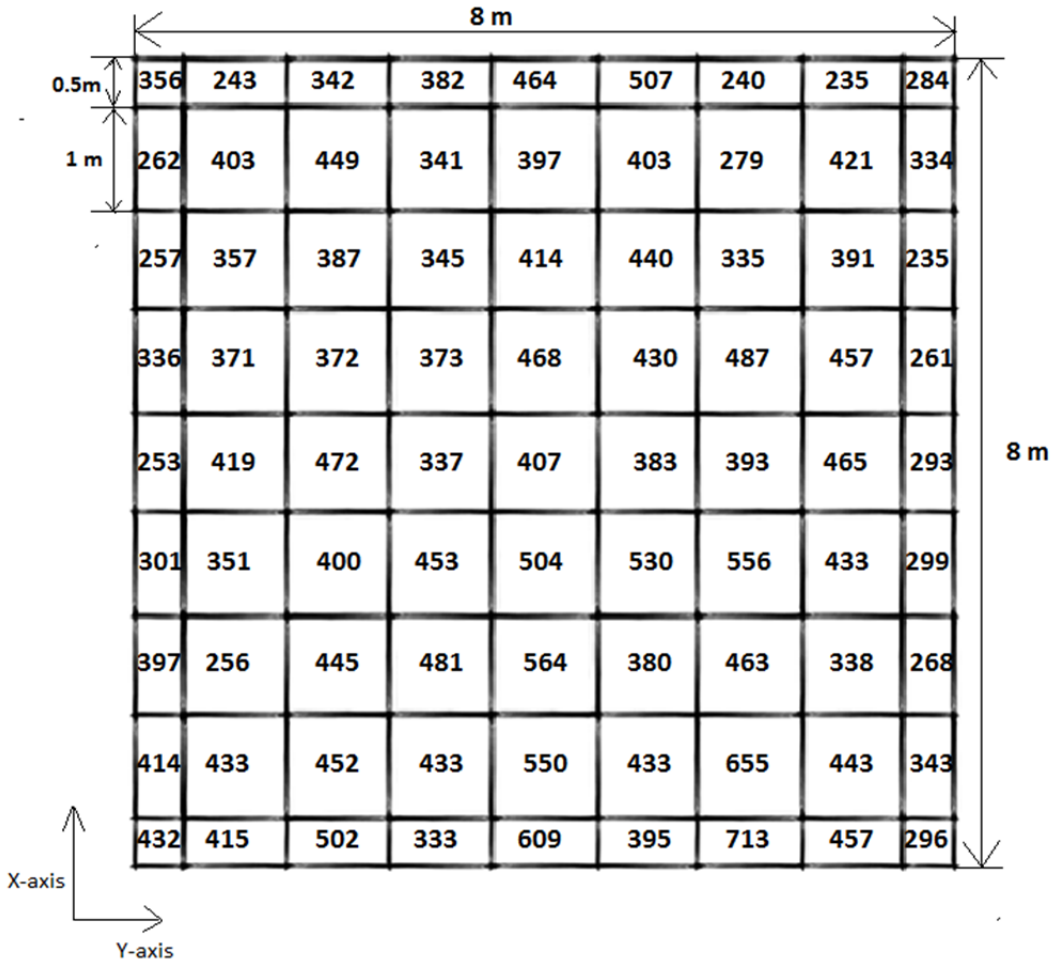

Figure 73. Case 81 with 81 discretized k-value areas assigned to test section 1 of MI I-96 roadway.

The frequency distribution of the field-correlated k-values, as seen in Figure 74, shows that MI I-96 is a distinctly stiffer subgrade as compared to MI I-94. Figure 74 shows the subgrade stiffness distribution for Case 81 was skewed left of the mean but still had rather good k-values for pavement construction. The range of the k-values for MI I-96 was 235 to 713 psi/in, with a mean of 397 psi/in and a standard of variation of 95.1 psi/in. The coefficient of variation of k-values in the dataset was 24%. Hence, this roadway section is a good case to compare with MI I-94, which was a significantly softer subgrade support. The directions of x- and the y-axes have been reversed form the conventional Cartesian coordinate system to conform to the coordinate system in ISLAB2000. The second support condition analyzed was the uniform Case A1, which was based on averaging the 81 k-values (397psi/in), as seen in Figure 75. The prefix “A” is used to avoid ambiguity with the uniform support condition of MI I-94.

The input parameters for the stress analysis are the same as used for MI I-94 (shown previously in Table 9). Three axle configurations (single, tandem and steer drive) were used for loading of the slab subject to three linear temperature differentials: 0°F, 20°F and -20°F. However, based on the conclusions of MI I-94 analysis wheelpath loading cases were not considered because they never produced the peak tensile stress for a set of inputs.

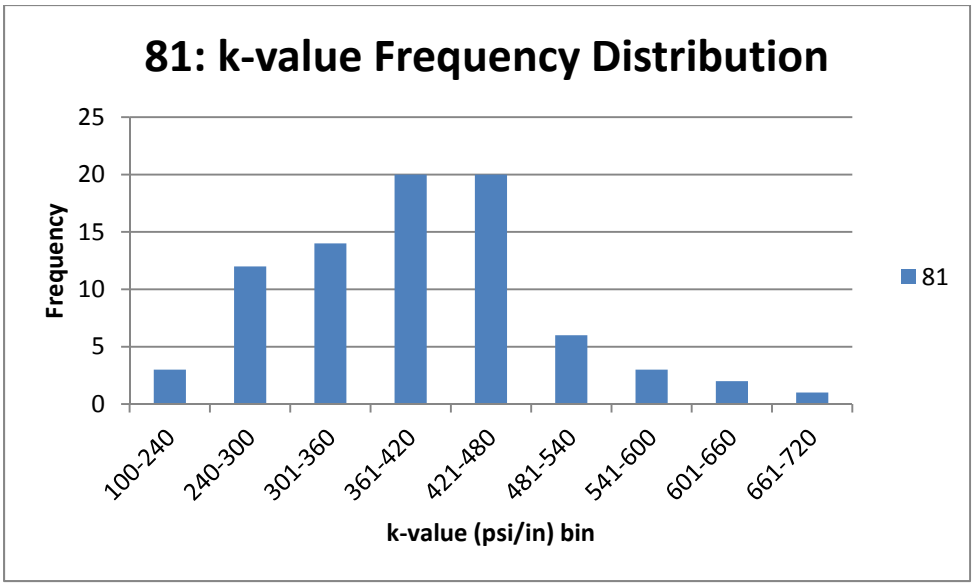

Figure 74. Frequency distribution of k-values for Case 81.

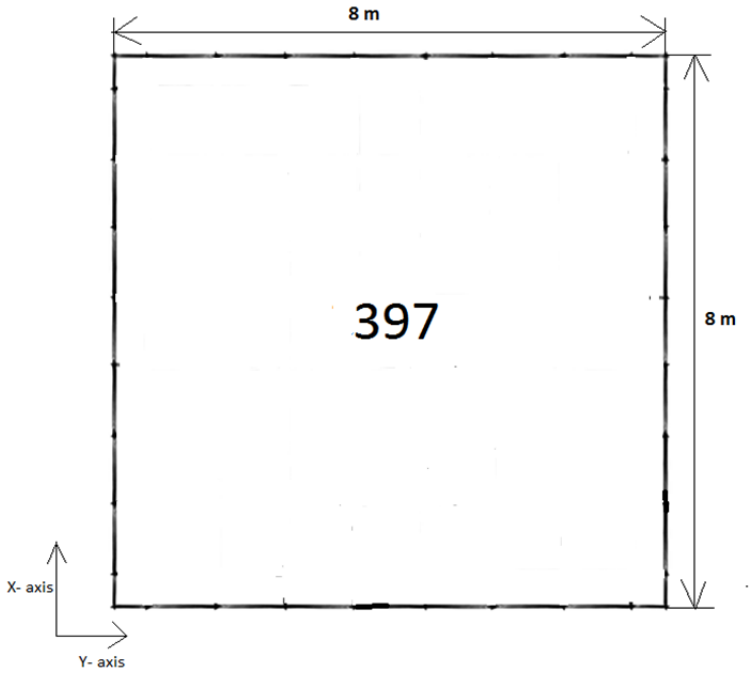

Figure 75. Case A1 with single, uniform k-value area assigned to TS1 on MI I-96 roadway.

Figure 76 shows the three loading paths for the three axles used to longitudinally traverse the slab. The slab geometry was slightly modified from MI I-94. The support measurements were over an area of 8 x 8 m^2 (~26 x 26 ft^2) area and the four-slab assembly, each 4 x 4 m^2 (~13 x 13 ft^2), was used to assess the effects of the nonuniform support. This slab geometry was adopted for analysis primarily to encompass the entire field data measurements. The distinction between left lane and right lane was made with respect to the longitudinal direction. The three axle configurations were the same as those shown previously in Figure 47. The axles started at the transverse free edge with the first movement at 10 in (0.25 m) followed

by subsequent loading locations at 20-in intervals with respect to the rear axle. Based on the dimensions of the slab and axles, the single axle needed 17 movements, the tandem required 14, and steer-drive nine loading locations in order to simulate movement of the axle across the 8 m section as seen in Figure 76. The nomenclature designating the axle types and temperature differential (see previous Table 10) remains the same as the MI I-94 field analysis.

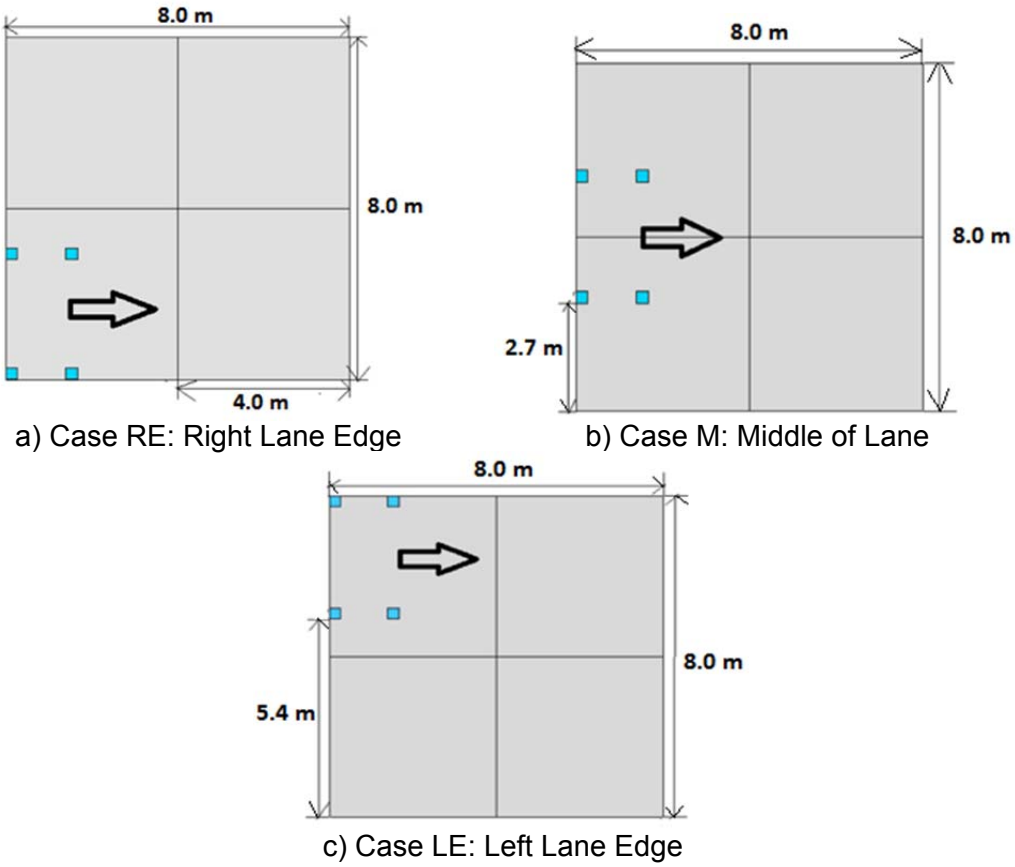

a) Case RE: Right Lane Edge

b) Case M: Middle of Lane

c) Case LE: Left Lane Edge

Figure 76. Axle loading location and paths for analysis of MI I-96 field data.

4.5 MI I-96: Slab Response Results

This section presents the results of the deterministically assigned k-values from the I-96 field measurements. The subsections are divided into the various axle locations (i.e., RE, LE, M), with each subsection presenting the results for the assumed uniform (Case A1) and the nonuniform (Case 81) simulations.

4.5.1 Stress Analysis of Right Edge (RE) Case for MI I-96 Roadway

Case RE81 represents the longitudinal movement of the vehicle along the right lane edge of the slab. Figure 78 shows the results of the peak tensile stresses recorded at each axle position. The overall peak tensile stress was near the mid-slab location for both slabs with slightly varying magnitudes (approximately 5%) on account of different local stiffness. Two important distinctions for MI I-96 are that it is a stiffer subgrade support and the individual slabs are 0.5 longer and wider relative to the MI I-94 analysis.

The percent change in k-value is not as great for the MI I-96. The MI I-96 has a k- value range of approximately 500 psi/in, which is 2.5 times the maximum k-value for MI I-94 section. The peak tensile stress at the mid-slab location on the first slab was primarily due to the presence of a lower stiffness area next to an adjacent higher stiffness area (502 psi/in and 333 psi/in), as seen in Figure 77, which controlled for all three axle types with daytime curling conditions. Although the single axle produced the peak critical stress, the peak tensile stress for the tandem and steer drive during daytime curling was within 5% of each other. Even with a large range in k-value, the peak tensile stresses are very similar in magnitude to the uniform subgrade support (Case A1), as seen in Figure 79. The overall peak stress change from uniform to Case 81 decreased 1% while the average peak stress increased by 1%. The maximum tensile stresses at each longitudinal position for case REA1 is in Appendix B.

Overall, the peak tensile stresses were highest for daytime curling conditions for all axle types and both support conditions. The average peak tensile stress increase between the no temperature differential and positive temperature differential case was 43% and there was a 32% increase in average peak tensile stress between the negative temperature differential and positive temperature differential cases, as seen in Figure 79. For input combinations, the peak tensile stress always occurred at the bottom of the slab.

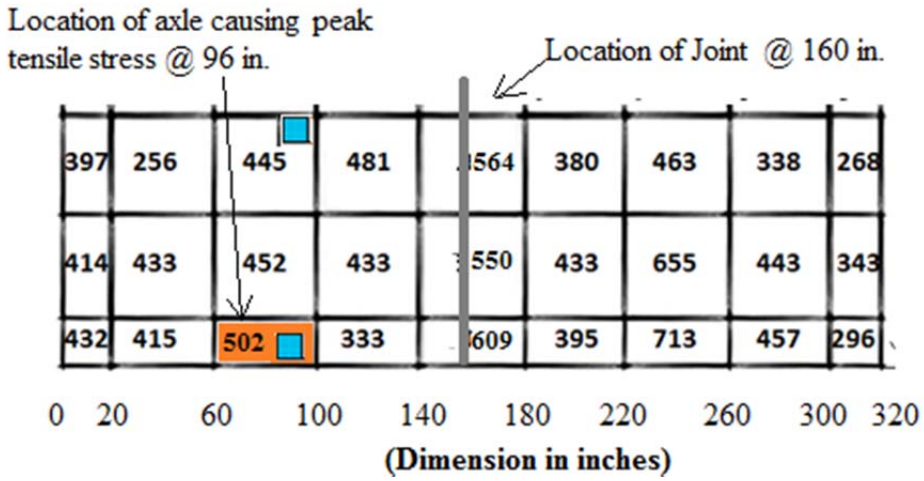

Figure 77. Local variation in k-values along right hand edge of the slab for Case RE81.

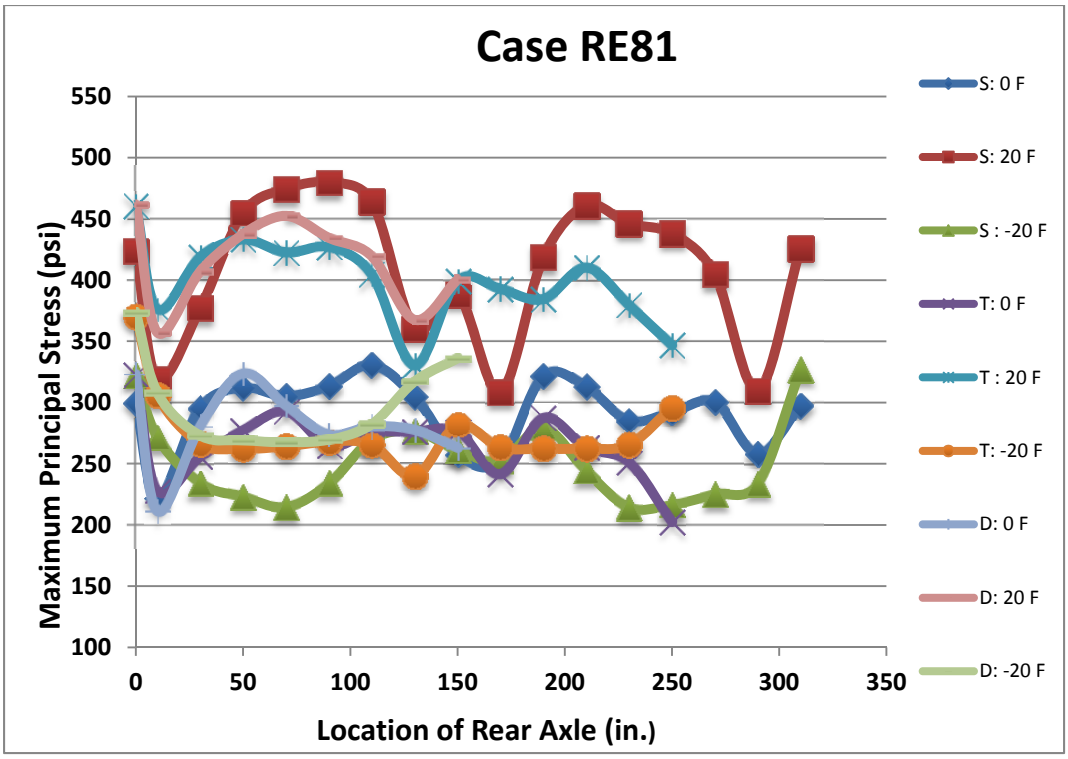

Figure 78. Maximum principal (tensile) stress for Case RE81 versus axle position.

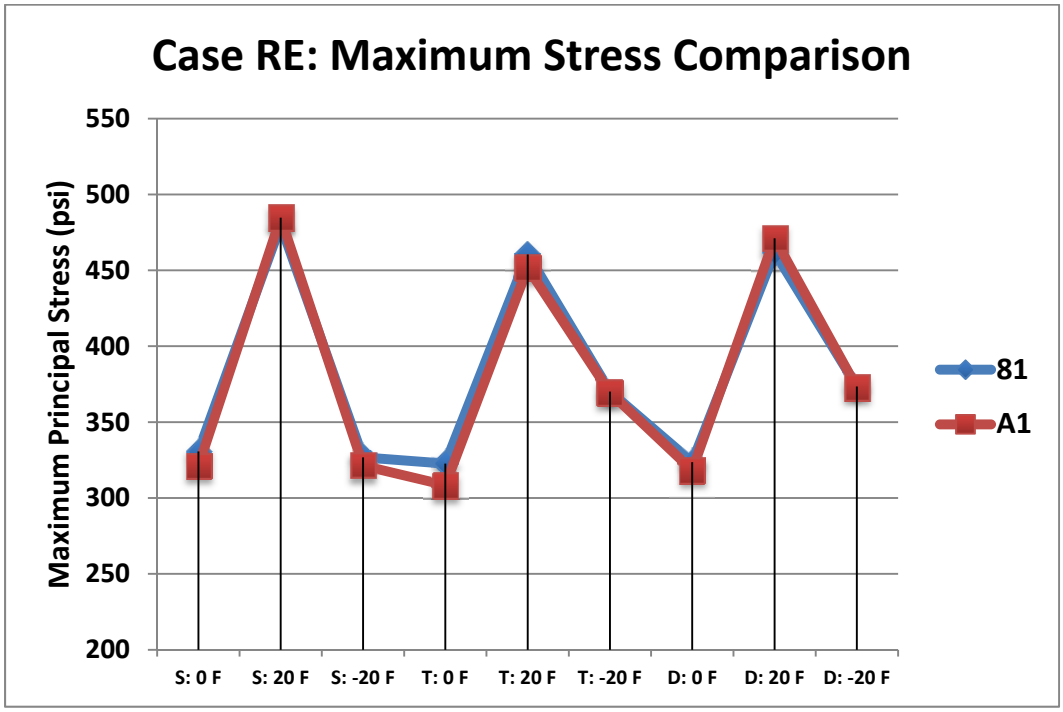

Figure 79. Comparison of the peak tensile stresses for Case RE of MI I-96 roadway for each input factor level and the two levels of nonuniform support.

4.5.2 Stress Analysis of Left Edge (LE) Case for MI I-96 Roadway Section

Case LE81 represents the movement of the vehicle along the longitudinal left lane edge of the slab, and the peak tensile stresses are shown in Figure 81. The peak tensile stresses occurred near the mid-slab position but not at the same position of RE81, as seen in Figure 80, because of the different localized support stiffness. The overall peak tensile stress of LE81 was approximately 6% higher than RE81 mostly because the frequency of k-values on LE was higher for the lowest stiffness bin of 250-350 psi/in, as shown in Figure 83. The mean of the k-value along the left edge is 339 psi/in with a standard deviation of 93.6 psi/in compared to the higher mean of 461 psi/in with standard deviation of 123.8 psi/in at the right edge. The overall peak stress change from uniform to nonuniform (LE81) increased 6% with an average increase in peak tensile stress of 4%. A 52% increase in average peak tensile stress between the no temperature differential and positive temperature differential case and a 36% increase in average peak tensile stress between negative temperature differential and positive temperature differential cases is observed as seen in Figure 82.

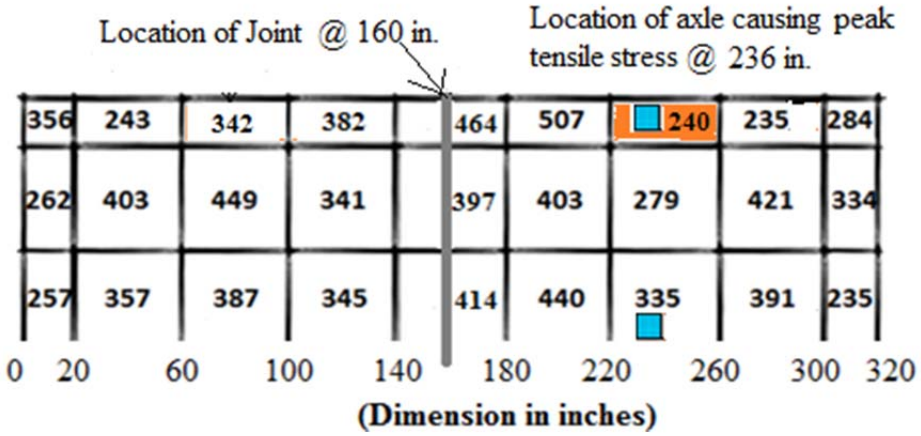

Figure 80. Local variation in k-values along left hand edge of the slab for Case RE81.

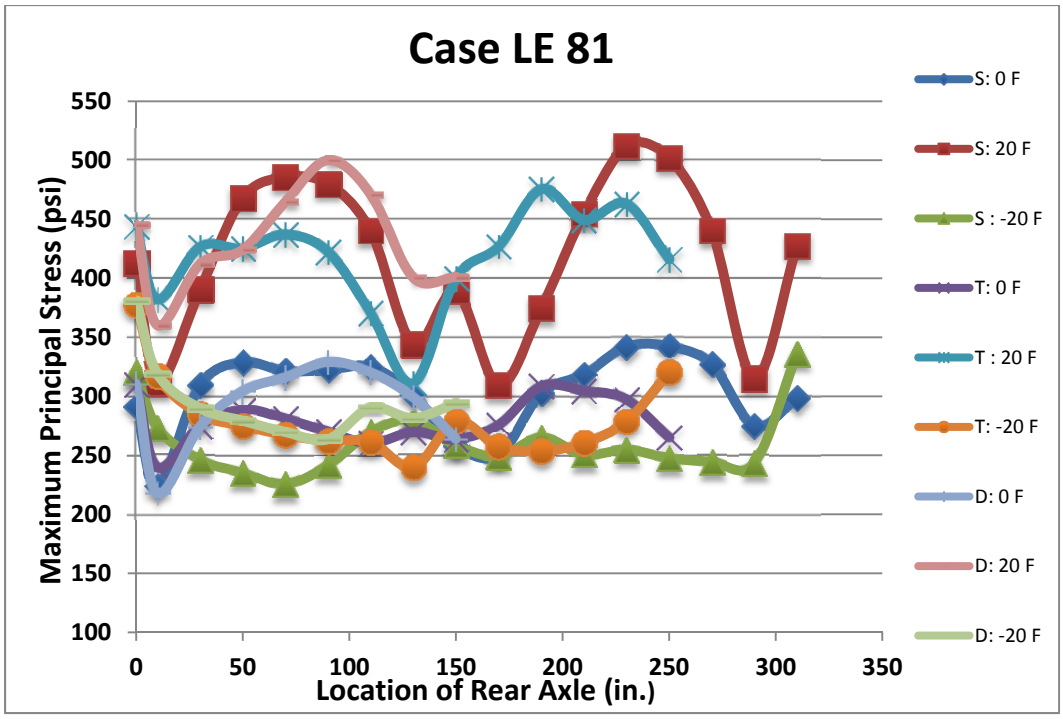

Figure 81. Maximum principal (tensile) stress for Case LE81 versus axle position.

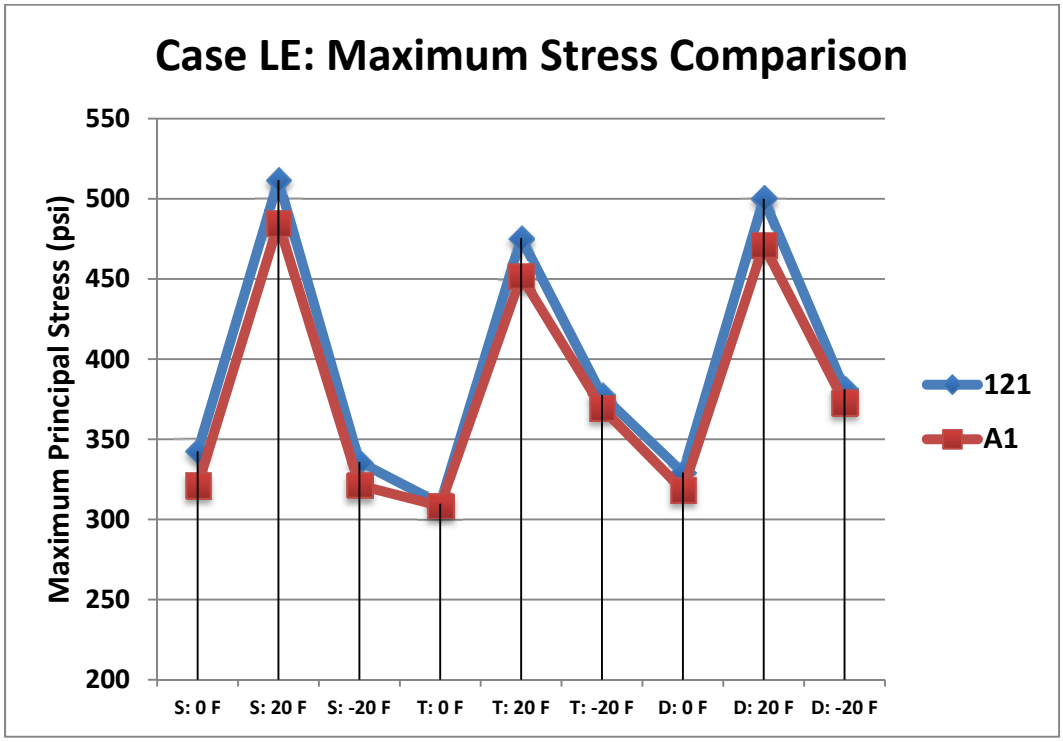

Figure 82. Comparison of the peak tensile stresses for Case LE of MI-I-96 roadway for each input factor level and the two levels of nonuniform support.

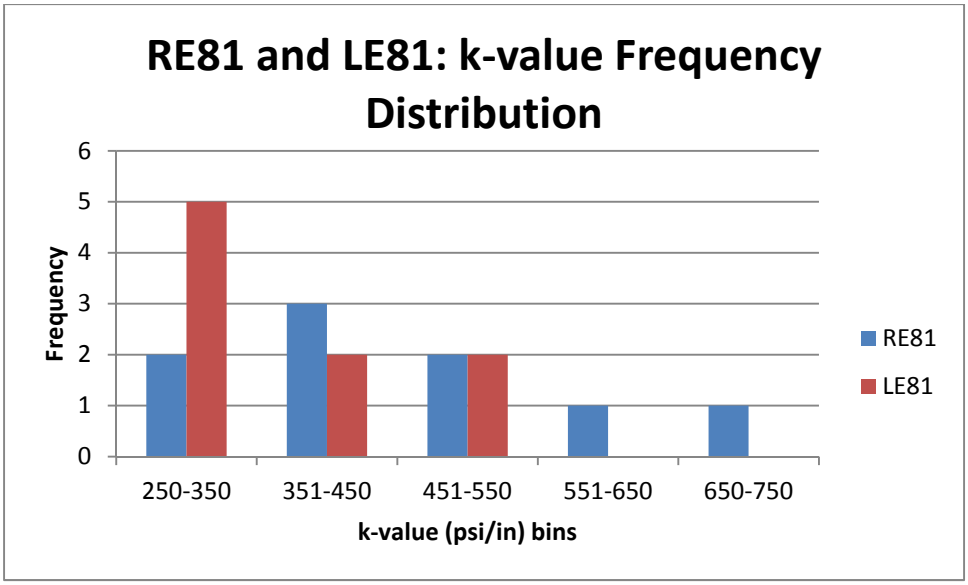

Figure 83. The k-values for Cases RE81 and LE81 on MI I-96 roadway.

4.5.3 Stress Analysis of Middle of Lane (M) Case for MI I-96 Roadway Section

As expected, the M81 results for the maximum tensile stresses were lower in magnitude than LE81, as seen in Figure 84. The maximum tensile stresses occurred at the free transverse edge, which would be reduced with the addition of adjacent slabs and load transfer. With higher k-values a difference of 100-150 psi/in does not constitute the same definition of nonuniformity as seen in support condition of MI I-94. The frequency distribution of k-values in Figure 87 suggests the presence of relatively uniform subgrade support in the middle of the slab with a mean of 382 psi/in and standard deviation of 116.4 psi/in. The plot of maximum tensile stresses at each longitudinal position for Case MA1 is presented in Appendix B. No significant difference between the overall peak tensile stresses of uniform and nonuniform cases was observed, as seen in Figure 85, because of the interior loading position of the axle and relatively lower nonuniformity. The overall peak tensile stress had a 2% increase from uniform to nonuniform (M81), while there was an increase in the average peak tensile stress of 4%. With the higher k-values, there was a 34% increase in the average peak tensile stress between no temperature differential and positive temperature differential case and 78% increase in average peak tensile stress between no temperature differential and positive temperature differential case as observed in Figure 86. The three axle types behaved in a similar pattern in terms of magnitude of tensile stresses and location of critical stresses.

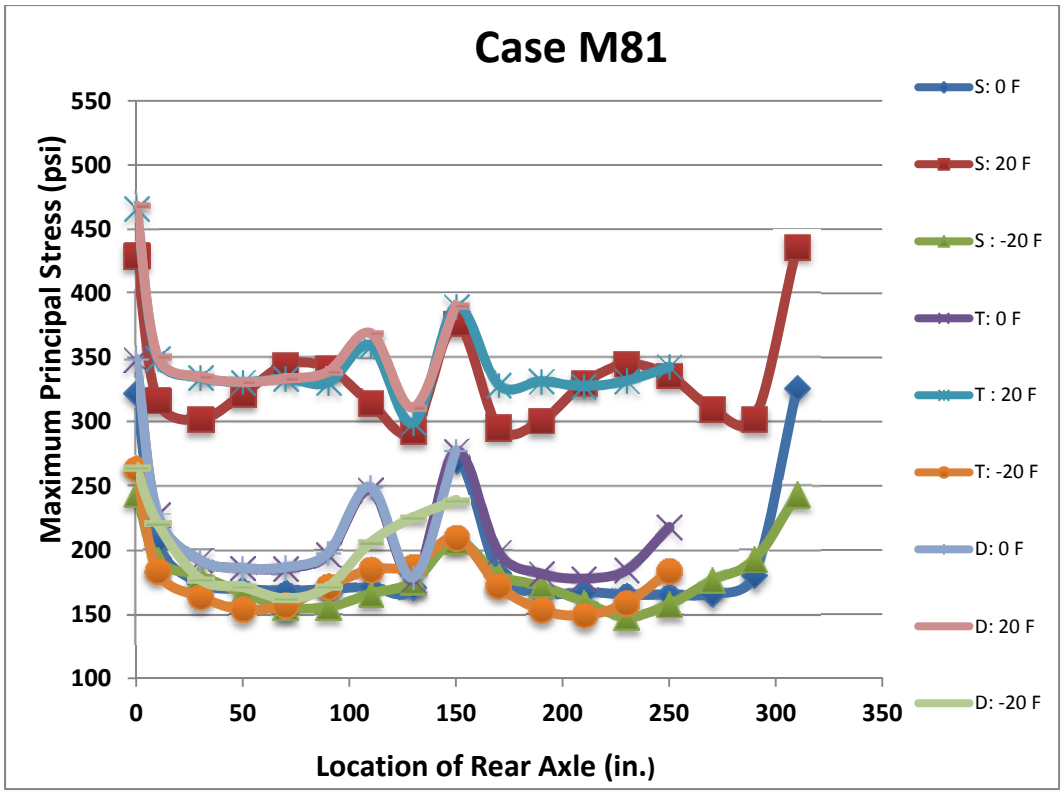

Figure 84. Maximum principal (tensile) stress for Case M81 versus axle position.

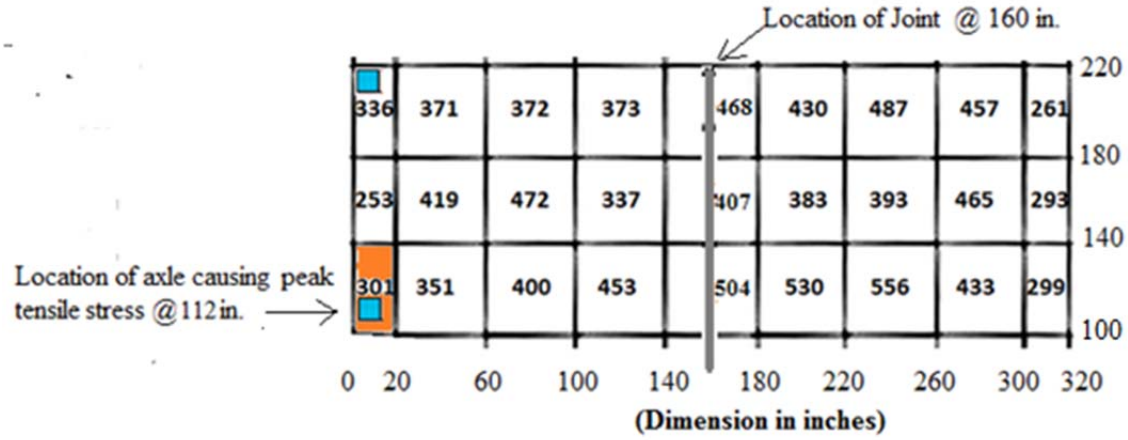

Figure 85. Local variation in k-values along middle of the slab for Case M81.

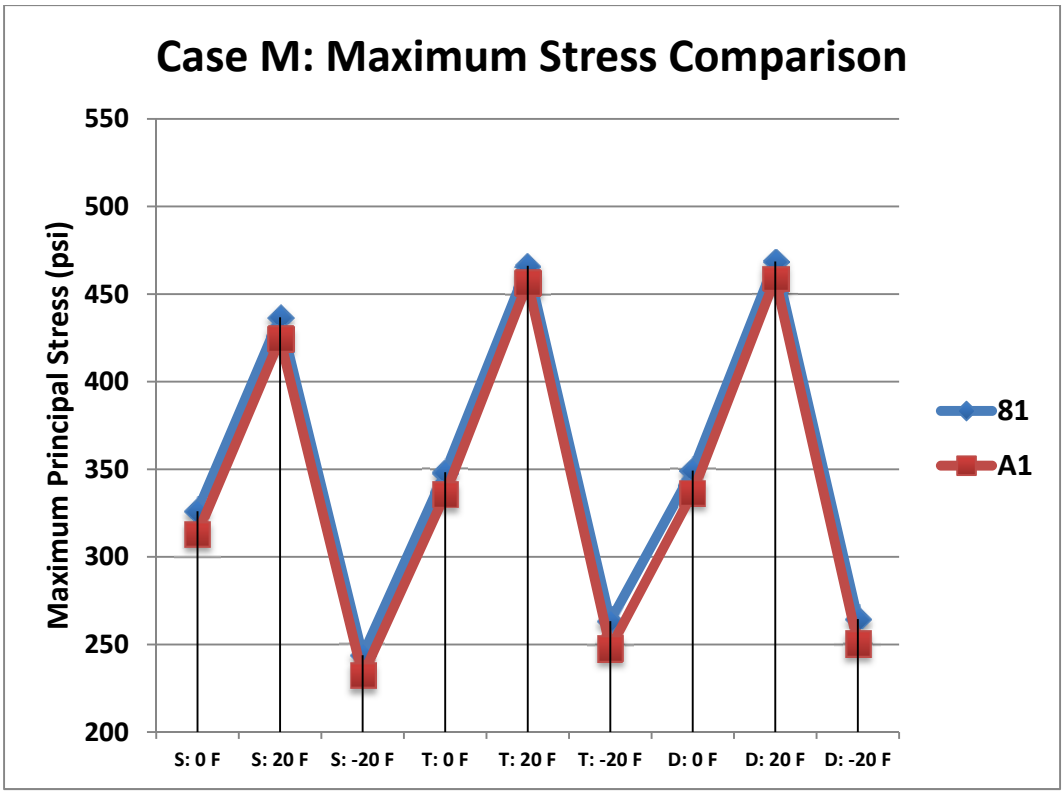

Figure 86. Comparison of the peak tensile stresses for Case M of MI I-96 roadway for each input factor level and the two levels of nonuniform support.

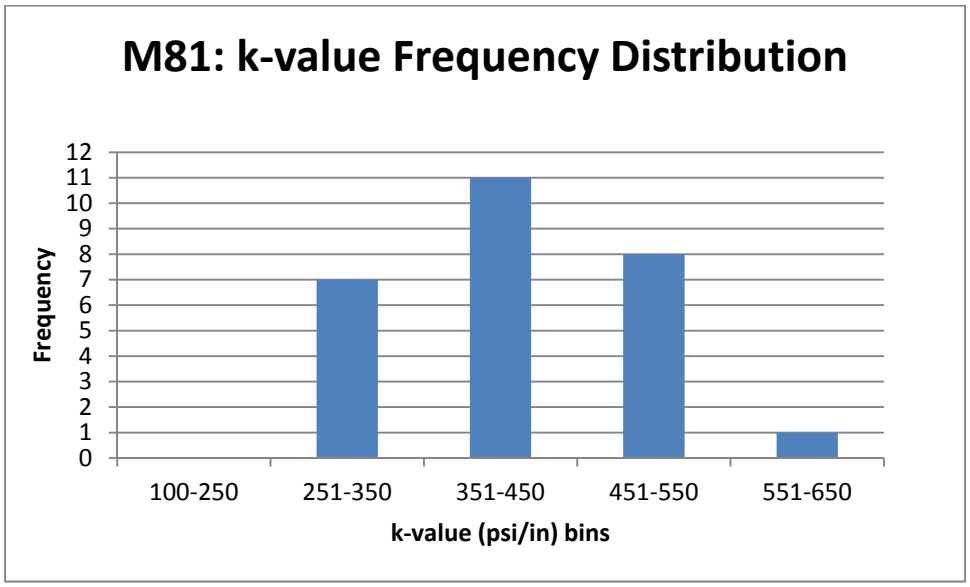

Figure 87. The k-values for case M81 on MI I-96 roadway.

4.6 Summary of MI I-96

As seen in Table 15, most of the critical tensile stresses cases occurred at the free transverse edge. In general, it appears that the peak maximum tensile stresses are not as significantly different when comparing the uniform (A1) to nonuniform (81) conditions. The

highest peak tensile stress reached was 511 psi, which occurred when a single axle was loaded on the left edge over a nonuniform support with a positive curling. The next highest tensile stress reached because of a single axle was 484 psi, which was with a uniformly supported slab and positive curling.

Table 15. Location and Magnitude of Peak Tensile Stresses for Nonuniform Support Condition on MI I-96 Roadway

Case	Single Axle			Tandem Axle			Steer-Drive Axle		
	0 F	20 F	- 20 F	0 F	20 F	- 20 F	0 F	20 F	- 20 F
RE81	330 (0,116.b)	479 (0,96,b)	326 (44,320,t)	322 (102,0,b)	460 (102,0,b)	370 (44,0,t)	323 (102,0,b)	461 (102,0,b)	373 (44,0,t)
REA1	321 (102,0,b)	484 (102,0,b)	321 (46,0,t)	308 (102,0,b)	451 (102,0,b)	369 (46,0,t)	318 (0,200,b)	471 (0,240,b)	372 (44,0,t)
LE81	342 (320,236,b)	511 (320,236,b)	335 (276,320,t)	309 (218,0,b)	475 (320,244,b)	377 (274,0,t)	329 (320,240,b)	499 (320,240,b)	381 (274,0,t)
LEA1	321 (320,114,b)	484 (320,76,b)	321 (274,0,t)	308 (218,0,b)	451 (218,0,b)	369 (274,0,t)	318 (320,200,b)	471 (320,220,b)	372 (276,0,t)
M81	326 (208,320,b)	436 (208,320,b)	243 (112,0,b)	348 (112,0,b)	466 (112,0,b)	263 (112,0,b)	349 (112,0,b)	468 (112,0,b)	264 (112,0,b)
MA1	313 (208,0,b)	424 (208,0,b)	232 (112,0,b)	335 (208,0,b)	456 (112,0,b)	247 (112,0,b)	336 (208,0,b)	458 (112,0,b)	250 (112,0,b)
b= Bottom of slab; t: Top of slab									

4.7 Chapter 4 Summary and Conclusions

Field data on the nonuniformity of a pavement foundation layer was utilized in this two-dimensional finite element analysis of a four-slab configuration. The field data was collected from two project sites in Michigan: I-94 and I-96. For both projects, field data was obtained in a grid pattern, which was correlated to a static k-value. The I-94 and I-96 grid k-value data was then discretized into fixed area sizes to model the nonuniform support condition. The two-dimensional finite element analysis was conducted using the ISLAB2000 program. Placing a four-slab assembly on top of the nonuniform support, the maximum tensile stresses were determined as various axle types (single, tandem, steer-drive) traversed the slab at various locations (right edge, left edge, middle, wheelpath) and under different curling conditions (0, 20, -20°F linear temperature differential).

The data from MI I-94 consisted of 121 k-values discretized to 0.7 x 0.7 m^2 areas over a total project area of 7 x 7 m^2. From this data, three support conditions were considered: one with the 121 discretized areas, one of 36 weighted discretized areas, and one of a single uniform k-value. All support conditions were developed from the original 121 data points. Five loading offsets were also considered: right edge, left edge, middle (straddling two slabs), right slab wheelpath, and left slab wheelpath. The results demonstrated that the nonuniform support may not result in as high of stresses as a uniform support. Rather, the peak maximum tensile stresses were dependent on the location of the nonuniformity, severity of differences in adjacent nonuniform support, and loading conditions. When loaded along the right edge of the pavement, the nonuniform support condition with 121 discretized areas resulted in greater stresses than the uniform condition, but along the left edge of the pavement, the uniform support condition resulted in greater stresses than the nonuniform condition with 121 areas. Overall, the highest

peak tensile stress reached was due to the nonuniform support condition with 121 areas, which was 478 psi, while the highest peak tensile stress caused by the uniform support was 463 psi.

The data from MI I-96 consisted of 81 k-values discretized to 1 x 1 m^2 areas over a total project area of 8 x 8 m^2. Two support conditions were considered: one with the 81 discrete areas and one with a single uniform support based on the average of the 81 k-values. The results indicated that while the nonuniform support condition resulted in the highest overall tensile stress (511 psi), it was not significantly different from the uniform support condition (484 psi).

Overall the result of a nonuniform support condition based on the actual field conditions demonstrated that the resultant tensile stresses are dependent on the location and severity of adjacent support conditions. However, the results also demonstrated that there are instances where the nonuniform support results in lower tensile stresses than the uniform condition, mainly when there is an area of stiffer support. As particularly shown by the I-94 field data, significant stress concentrations can develop as a result of nonuniform support when there is a soft area adjacent to a very stiff area. Based on this deterministic assignment of k-values and analysis, nonuniform support conditions do not appreciably increase the tensile stresses in the slab (i.e., less than 6%).

CHAPTER 5 TWO-DIMENSIONAL FINITE ELEMENT ANALYSIS OF A SLAB WITH NONUNIFORM SUBGRADE SUPPORT RANDOMLY ASSIGNED FROM FIELD CONDITIONS

From the results presented in Chapter 4, it is evident that nonuniform field conditions measured from MI I-94 and MI I-96 may not greatly increase the tensile stress development in the concrete slab. Therefore, to further investigate the effect of the difference in k-value of adjacent areas, as was discussed in Levey and Barenberg (1970) and Barenberg et al. (1976), the MI I-94 and MI I-96 field data was randomly assigned to predefined areas. The MI I-94 data was randomly assigned by normal and beta distributions and the MI I-96 data was assigned by just a normal distribution.

The initial approach of assigning k-values correlated from field DCP measurements did not suggest overwhelmingly that nonuniformities could produce premature slab cracking. In order to further refine the stress analysis, a statistical process to randomly assign k-values to the same spatial grid patterns used for the Chapter 4 deterministic analyses was implemented. The main assumption for this analysis was that each user-defined area, when spatially connected forms a nonuniform support, and has a probability distribution similar to the measured field data. Thus each user-defined area is independently assigned a k-value and does not depend on adjacent areas.

5.1 MI I-94: Random Assignment of Support Condition by a Normal Distribution to Arbitrary Predefined Discrete Areas

A random function generator for a normal distribution was used to assign the MI I-94 k-values to the predefined spatial grid previously described in Chapter 4. The mean and the standard deviation of the correlated k-values from the MI I-94 data (Case 121) were used as inputs to produce the normal distribution shown in Figure 88, which shows the possibility of assignment of k-values below 0 psi/in. Therefore, a set of nonuniform support cases related to the actual measured stiffness distribution on MI I-94 would be produced to determine their effect on the slab's peak tensile stresses. Figure 89 and Figure 90 show the 7 x 7 m^2 nonuniform support areas with 121 and 36 randomly assigned k-values without bias, respectively. For the initial analysis, any randomly generated value less than zero is assigned a k-value of 1 psi/in. This low to no support condition could be interpreted as a void, area of localized erosion, or soft spot.

For this analysis, the slab geometry and ISLAB2000 input parameters previously defined in Table 9 are the same as in Chapter 4 including the axle types, loading locations and linear temperature differentials. The nomenclature for the analyses is update to add the prefix "R-" for random k-value assignment (i.e., Case R-121). For the randomly assigned nonuniform support case with 36 k-values (1.16 x 1.16 m^2 uniform area size), five independently generated subcases, shown in Figure 90, were developed because the "random" assignment of two k-values in Chapter 2 clearly demonstrated that high and low tensile stresses could be generated for a particular case depending on the location and variation of the support relative to the potential maximum stress location. The areas marked in red are areas of large changes in support stiffness. As seen in Table 16, all options had similar mean k-values and standard

deviations with the maximum mean k-value only 10% different and standard deviation difference of only 20%. Based on preliminary ISLAB2000 runs for each subcase along the edge loading path, option IV was selected for the full stress analysis because the changes in support were the greatest in the region of maximum tensile stress. Figure 91 represents the loading case R-36 with areas of potential critical stresses highlighted as an indicator.

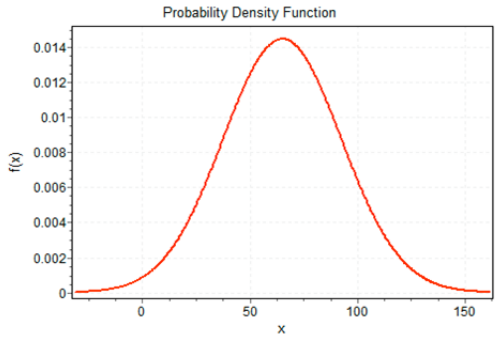

Figure 88. Theoretical distribution curve for randomly assigned k-values for cases R-121 and R-36.

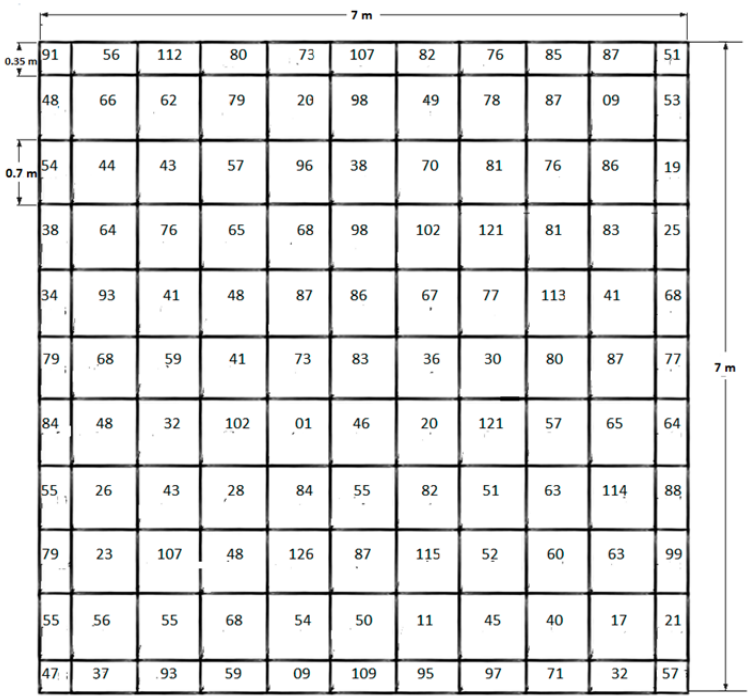

Figure 89. Spatial distribution of k-values for Case R-121.

Table 16. Spatial k-Value Data for Five Subcases of Case R-36

Case R-36	Range	Mean	Standard Deviation
Option I	01 to 126	64	27.5
Option II	23 to 115	67	24.6
Option III	01 to 143	67	30.5
Option IV	03 to 114	61	29.3
Option V	07 to 126	63	26.3

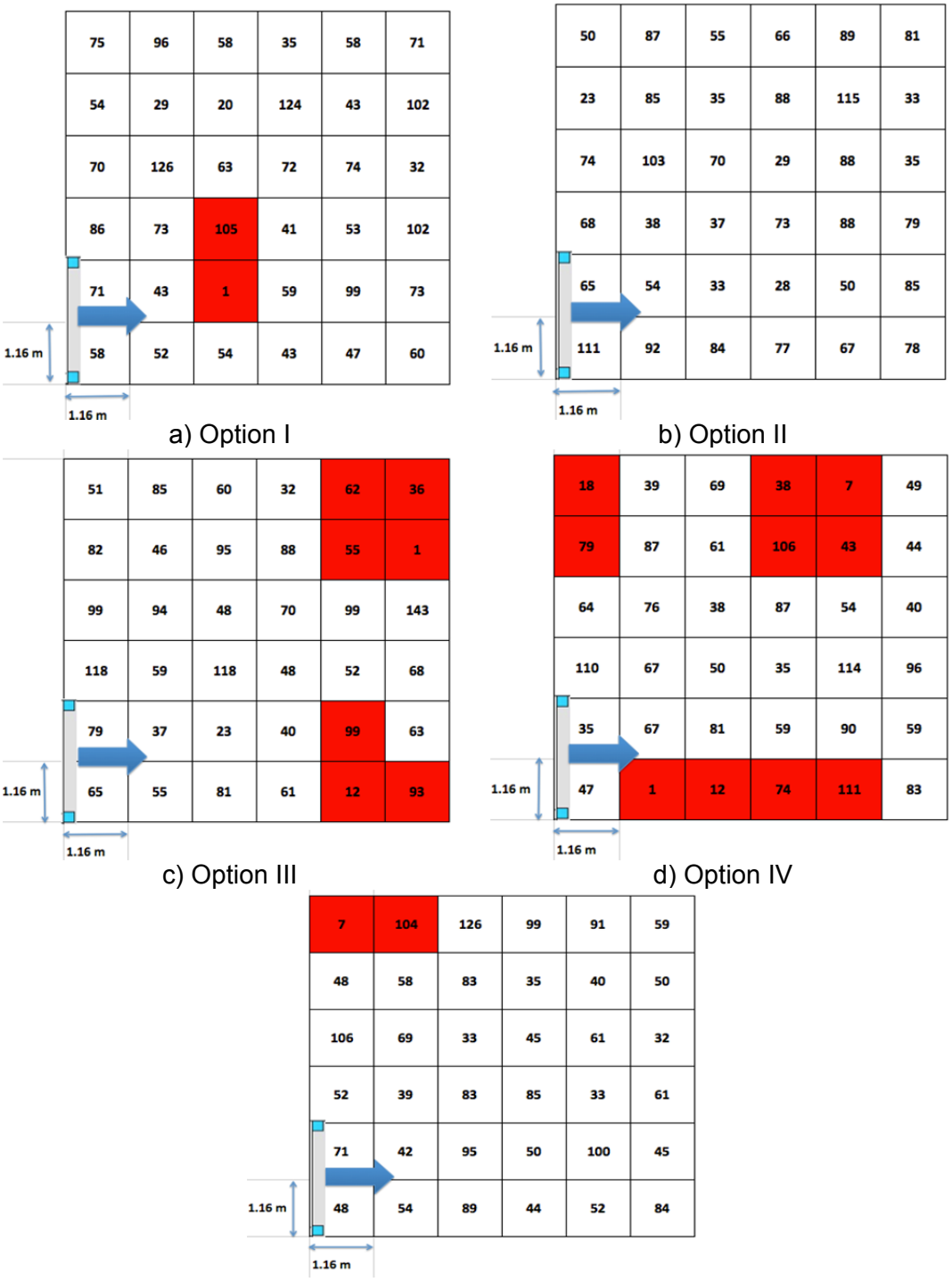

Figure 90. Spatial distribution of k-values for five subcases of R-36.

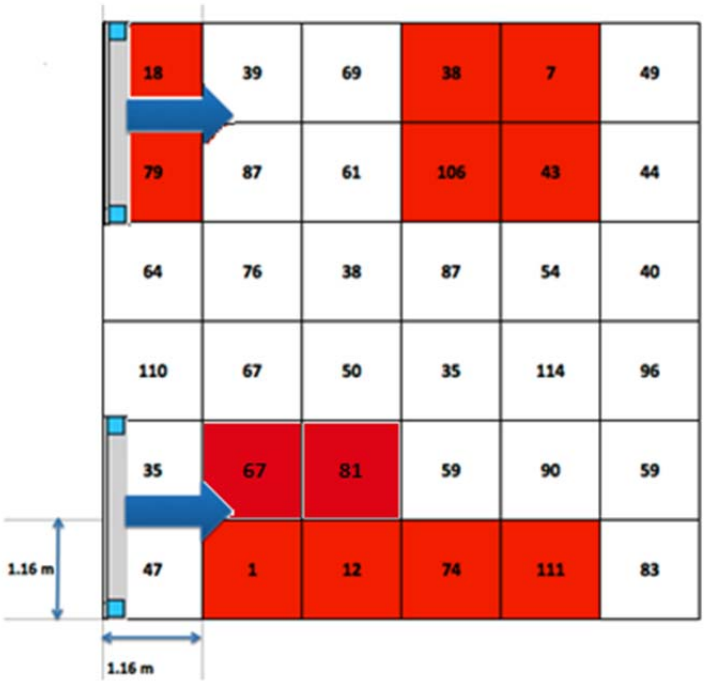

Figure 91. Spatial distribution of k-values with axle loading on RE and LE for option selected for Case R-36 Option IV.

5.1.1 Stress Analysis of Randomly Assigned Support Condition for Right Edge (R-RE) and Left Edge (LE) Cases

The critical tensile stress at each longitudinal position for Cases R-RE121 and R-LE121 that are shown in Figure 92 and Figure 93 have similar magnitudes in stresses compared to Cases RE121 and LE121. In the case of R-RE121, the maximum tensile stress of 479 psi/in is similar to RE121 with 478 psi/in. The mean of k-values for R-RE and R-LE are calculated in the same way as that for RE and LE based only on the edge k-values. Although the mean and standard deviation of the k-values at the edges for both cases are not the same (a mean of 85 psi/in and standard deviation of 50 psi/in for RE121 and mean of 64 psi/in and standard deviation of 30 psi/in for case R-RE121), the mid-slab longitudinal edge was still the critical location and their peak tensile stress magnitudes were similar as seen in Figure 96.

The randomly assigned k-values at 121 discrete locations for the left edge loading path had a smaller range of values with the mean k-value for R-LE121 of 81 psi/in, which was higher than that of LE121 having 67 psi/in as its mean with both cases having a standard deviation of 17 psi/in. The increase in critical tensile stress of almost 5% for the randomly assigned LE case can be attributed to the effect of single axle being more sensitive to local stiffness changes in the soil. The frequency distribution of k-values, shown in Figure 94, reports that R-LE121 has higher cluster of k-values near the mean relative to R-RE121. The magnitude of tensile stresses between R-LE 121 and R-RE121 is approximately the same at the mid-slab because of the similar k-values as seen in Figure 94.

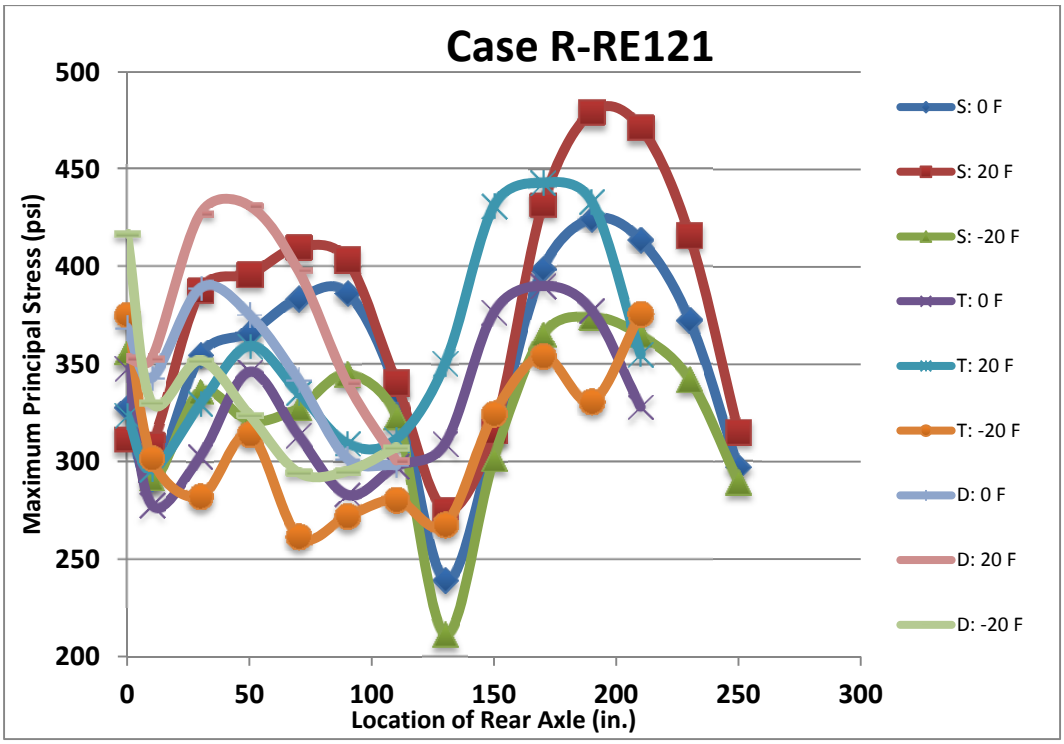

Figure 92. Maximum principal (tensile) stress for Case R-RE121 versus axle position.

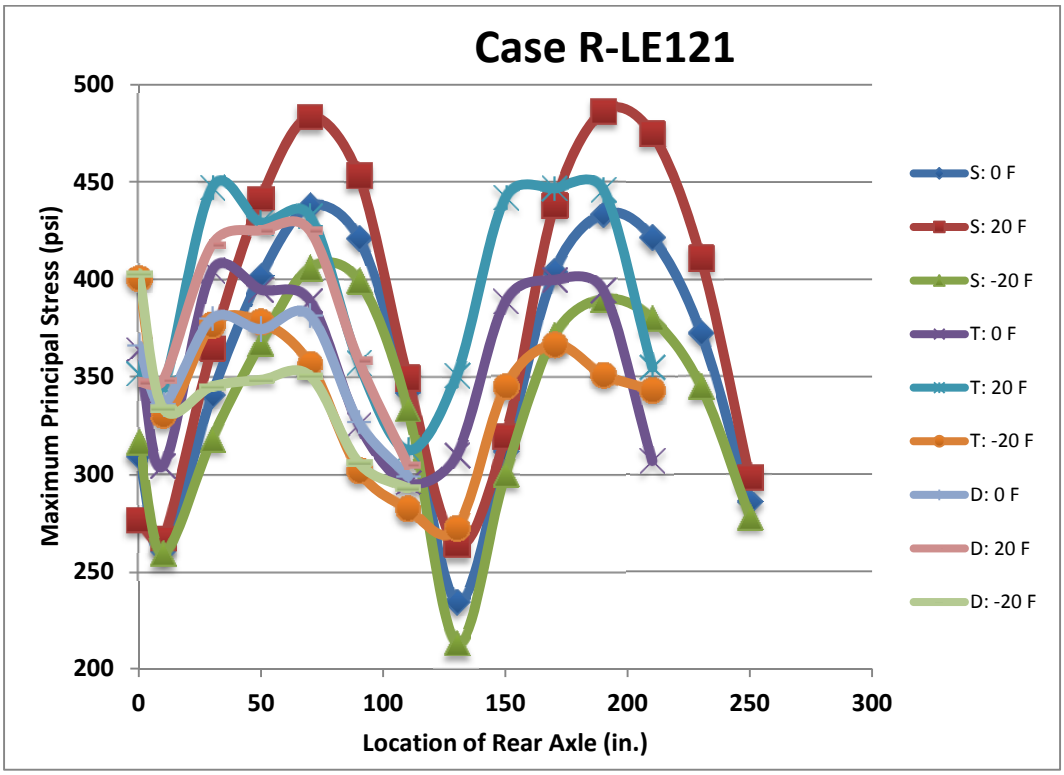

Figure 93. Maximum principal (tensile) stress for Case R-LE121 versus axle position.

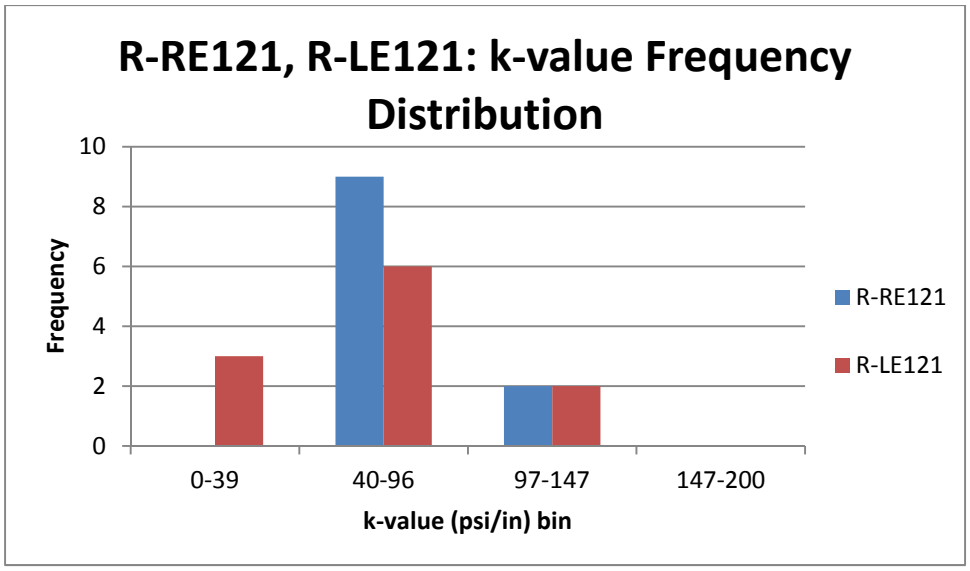

Figure 94. The k-value distributions for case R-LE121 and R-RE121 for MI I-94 roadway.

For the critical 36 k-value random assignment subcase (Case R-RE, option IV), the results are presented in Figure 95. The tensile stresses are much higher between locations 30 in and 70 in, which correspond to large variations in adjacent k-values along the edge loading path as seen in Figure 91 (i.e., 1 to 67 and 12 to 81 psi/in). All three axle types with daytime curling produced high tensile stresses for this nonuniform support condition. The critical stresses in this area were 50% greater than the adjacent slab which has the same geometry but different randomly assigned k-values. The 1 psi/in support area could represent loosely graded base material, saturated soil, or loss of support/contact with the slab. Clearly, these tensile stress magnitudes are high enough to create premature cracking distress in the concrete pavement. From Figure 96 it can be seen that there is 32% percent increase in the average peak tensile stress between the nonuniform Case R-RE36 and R-RE121 uniform support case which was partially caused by the increase in the predefined stiffness area from 0.7 x 0.7 m^2 to 1.16 x 1.16 m^2. The increase in average peak tensile stress was also 37% when going from the uniform support assumption to the random assignment with 36 k-values. The difference between the overall peak tensile stress for cases RE121 (478 psi) and R-RE36 (608 psi) was 27%. Therefore, the combination of soft localized support at the mid-slab edge of case R-RE36 of a certain size was critical to magnitude of the tensile stress change. The critical tensile stress for RE is 608 psi, which occurs at (x,y = 0,83 in) on the bottom of the slab.

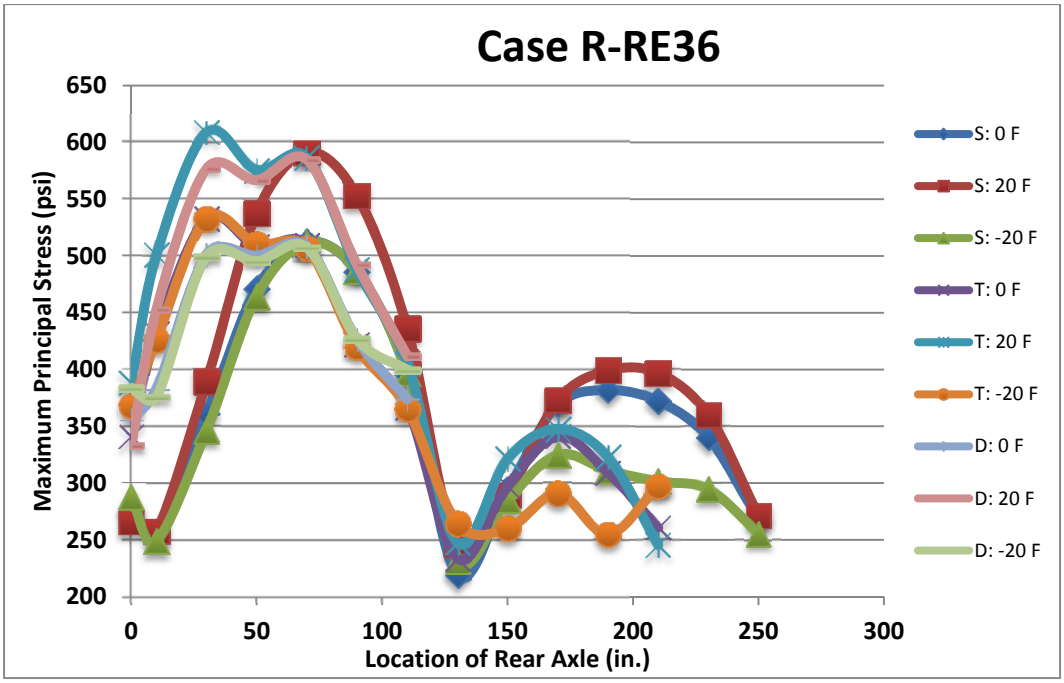

Figure 95. Maximum principal (tensile) stress for Case R-RE36 (Option IV) versus axle position.

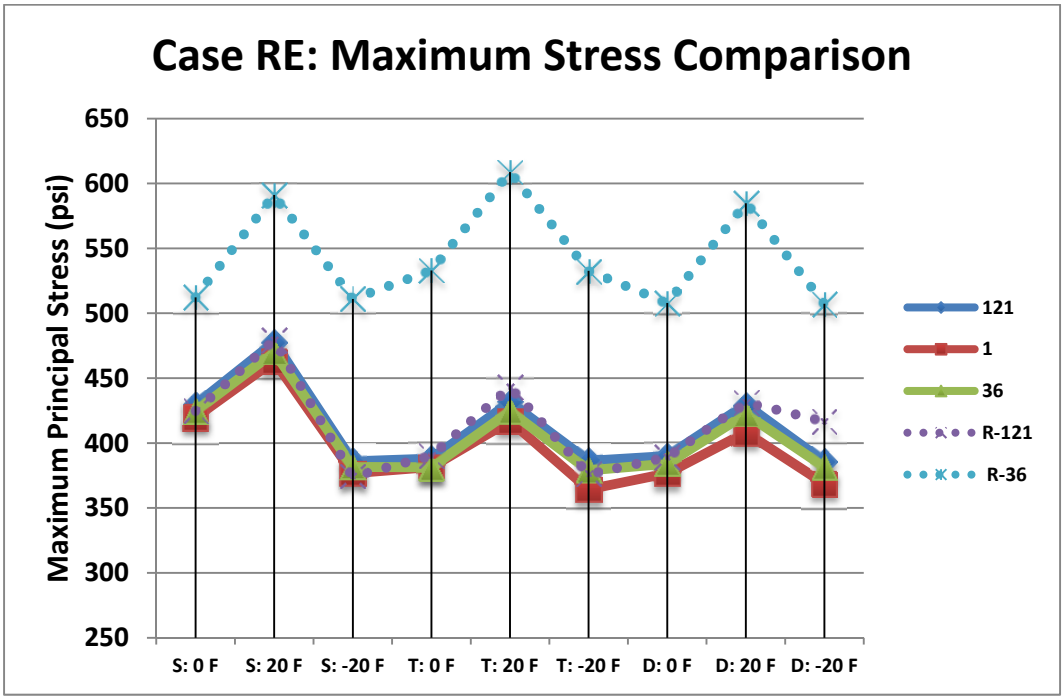

Figure 96. Comparison of the peak tensile stresses for Case RE for each input factor level and the five nonuniform support distributions.

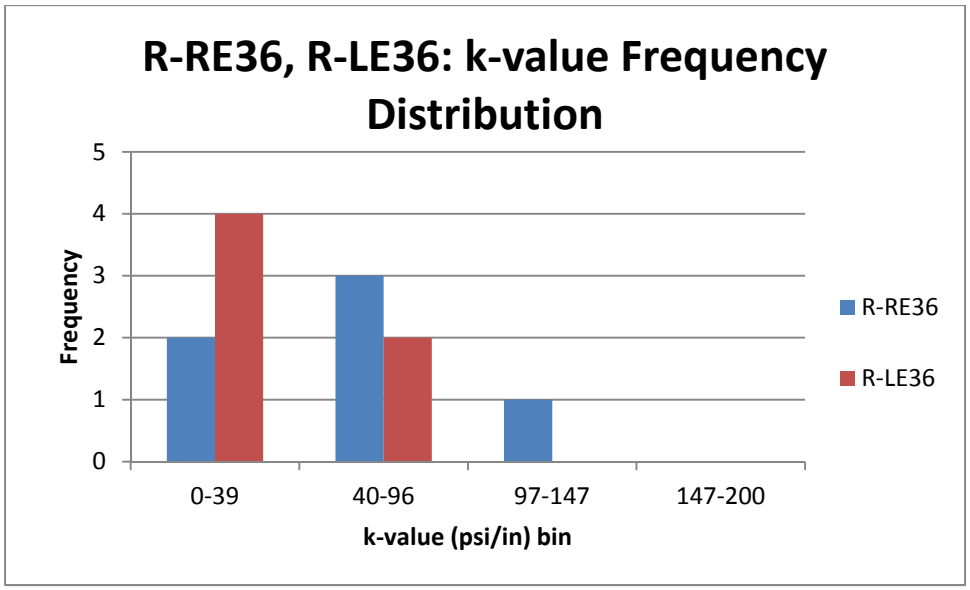

Figure 97. The k-values for Cases R-LE36 and R-RE36 of MI I-94 roadway.

Figure 98 shows the results of the maximum tensile stresses recorded at each longitudinal position along the left edge (Case R-LE36). There is a clear difference with Case R-RE36 in Figure 95, which is linked to the local support conditions under each axle position. The critical stresses near the mid-slab edge of the two slabs corresponded to the higher variations in adjacent k-value areas as seen in Figure 90d. The peak tensile stress was 8% lower than Case R-RE36 as the variations in nonuniformity in stiffness were not as extreme at the mid-slab edge as seen in Figure 91. This is substantiated by Case R-RE36 having a mean of 53 psi/in. and high standard deviation 40.9 psi/in and range of 1 to 111 psi/in along its loading path, whereas Case R-LE36 had a lower mean of 37 psi/in but a lower standard deviation of 20.1 psi/in and range of 7 to 69 psi/in along the left edge loading path. Figure 97 also shows this point by plotting the frequency distribution of support stiffness between R-RE and R-LE.

There was an increase of 20% in the average peak tensile stress from Case R-LE121 with a grid size of 0.7 x 0.7 m^2 to Case R-LE36 with a grid size of 1.16 x 1.16 m^2 in Figure 99. The peak tensile stresses also occurred at the bottom of the slab during daytime curling. For the left and right edges, single and tandem axles produced similar magnitudes for maximum tensile stresses (i.e., within 1%).

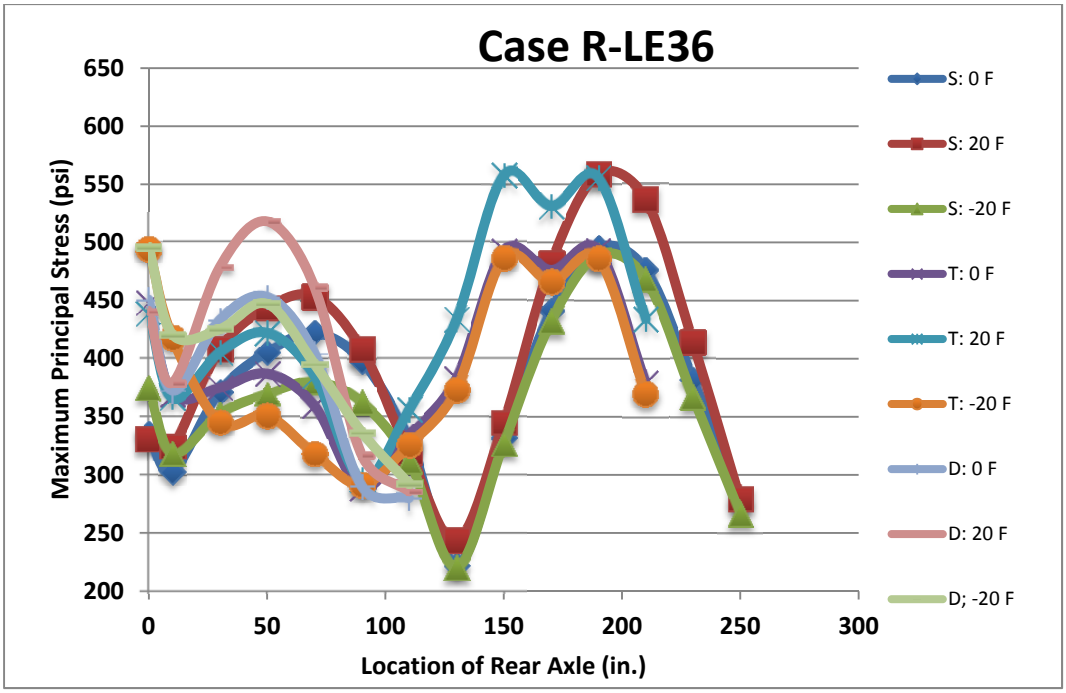

Figure 98. Maximum principal (tensile) stress for Case R-LE36 (Option IV) versus axle position.

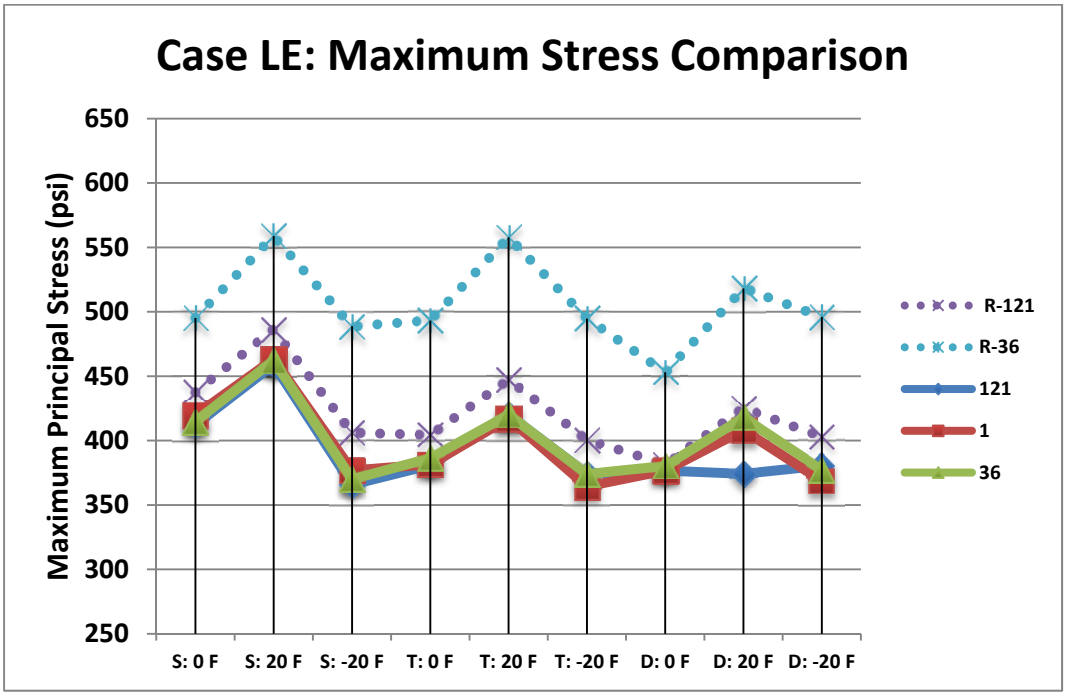

Figure 99. Comparison of the peak tensile stresses for Case LE for each input factor level and the five nonuniform support distributions.

5.1.2 Stress Analysis of Randomly Assigned Support Stiffness for Middle of Lane (R-M) Cases

Figure 100 shows the maximum tensile stresses recorded for Case R-M121 at the each longitudinal position. Random assignment of the 121 k-values increased the average peak

tensile stress by 4% compared to M121. Since the middle of the lane with 36 k-values was a critical case, the maximum tensile stresses at each longitudinal position for Case R-M36 were presented only in Appendix B. As expected, the tensile stresses away from the transverse edge load positions for Case R-M are much lower than the edge load paths. The size of the nonuniform stiffness areas for this loading path was not as critical as the edge loading paths. The middle of the lane k-values (R-M) was calculated similarly to Case M where all the k-values areas under the wheel are taken into consideration, as shown in Figure 102, which reports the majority of the k-values (i.e., 69%) in the 40-96 psi/in bin. The R-M121 case k-values had a standard deviation of 26.8 psi/in and mean of 62 psi/in, which is essentially similar to the uniform k-value of 63 psi/in. Hence, from Figure 102 it can be interpreted that majority of the k-values were within one standard deviation. Overall, Case R-M121 produced the highest tensile stresses for the middle loading path, but the change was only a 3% increase in the overall peak tensile stress moving from Case M1 to R-M121. The maximum tensile stress occurred at the bottom of the slab during daytime curling. The tandem and the steer-drive axles were critical for this case with similar magnitude of tensile stresses. All critical stresses are at the transverse edge which can be expected to be significantly reduced in the presence of a dowelled contraction joint.

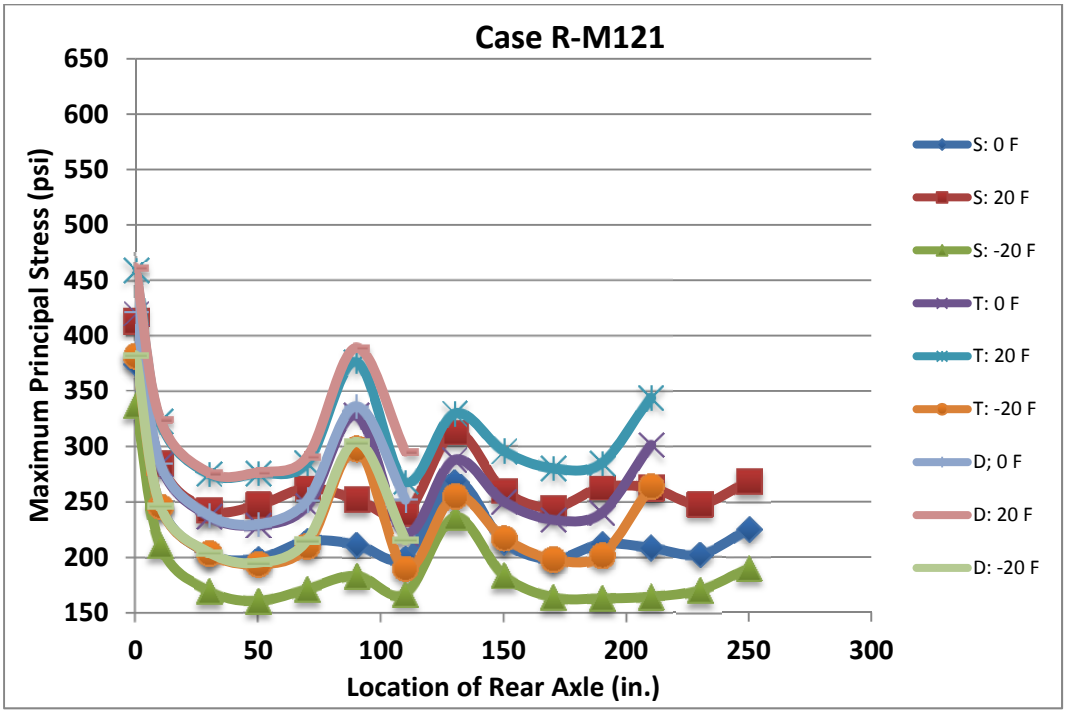

Figure 100. Maximum principal (tensile) stress for Case R-M121 versus axle position.

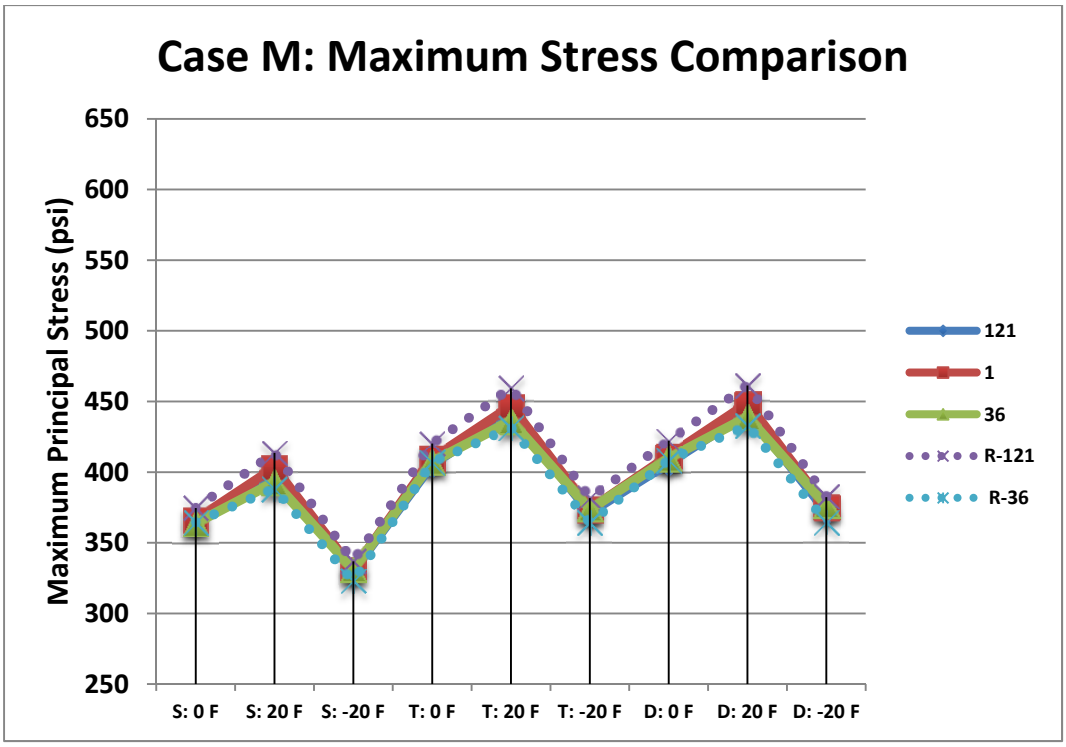

Figure 101. Comparison of the peak tensile stresses for Case M for each input factor level and the five nonuniform support distributions.

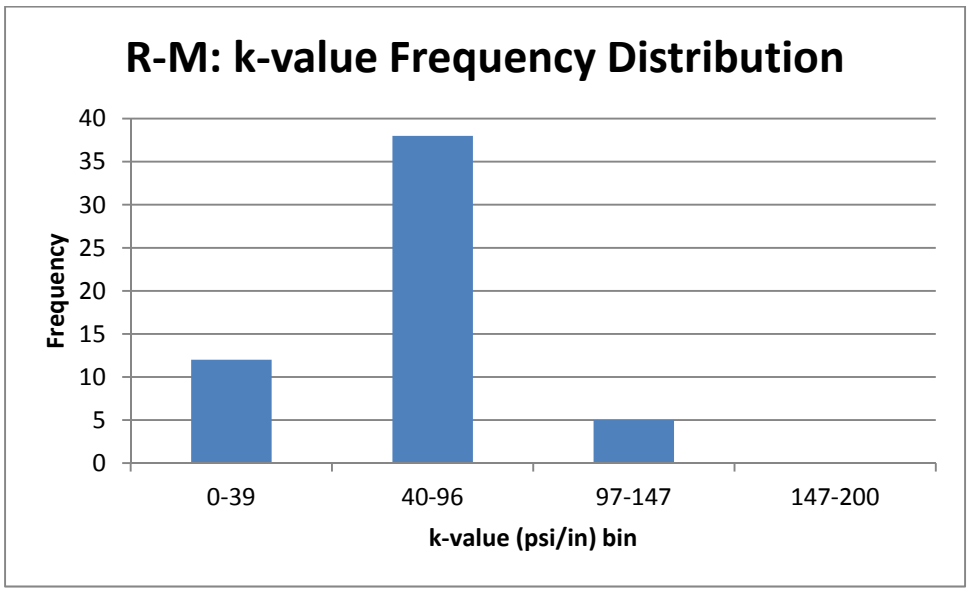

Figure 102. The k-values for Case R-M121 from MI I-94 roadway.

5.1.3 Stress Analysis of Randomly Assigned Support Stiffness for Right Wheelpath (R-RW) and Left Wheelpath (R-LW) Cases

Figure 103 and Figure 104 represent loading path cases RW and LW, respectively, along the right and left wheel path. As expected, the magnitude of tensile stresses recorded at the each longitudinal position for Cases R-RW36 and R-LW36 are lower than the free edge

cases (R-RE36 and R-LE36). The maximum tensile stresses along the right and left wheel path occur on different slabs. However, the three axle types produced similar maximum stresses (i.e., within 5 to 7%) for both wheel paths, as seen in Figure 105 and Figure 106. The peak tensile stress occurred at the bottom of the slab during daytime curling for the right wheel path. However, for the left wheel path, the maximum stress occurs at the top of the slab during nighttime curling but at the initial loading position (transverse free edge condition). The maximum tensile stresses at each longitudinal position for Cases R-RW121 and R-LW121 are included in Appendix B. As seen in Figure 105 and Figure 106, the random assignment of 36 k-values significantly increased the maximum tensile stresses relative to the randomly assigned 121 k-values (i.e., 14% increase in the average peak tensile stress for both R-RW and R-LW cases).

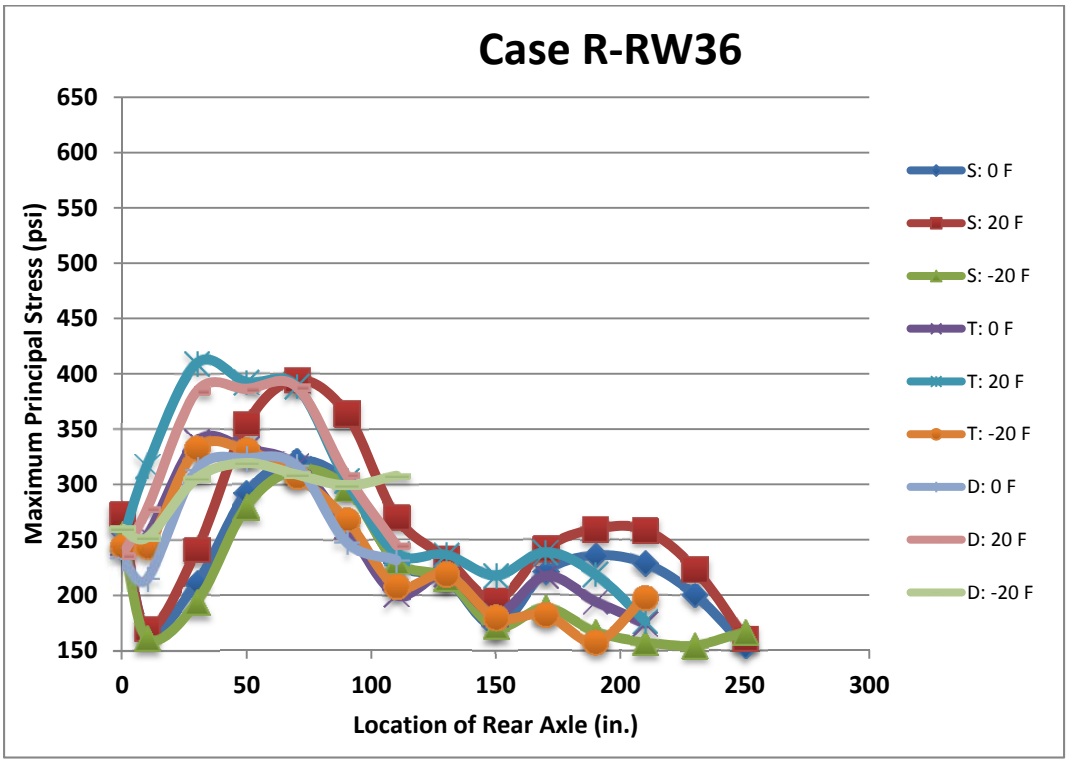

Figure 103. Maximum principal (tensile) stress for Case R-RW36 versus axle position.

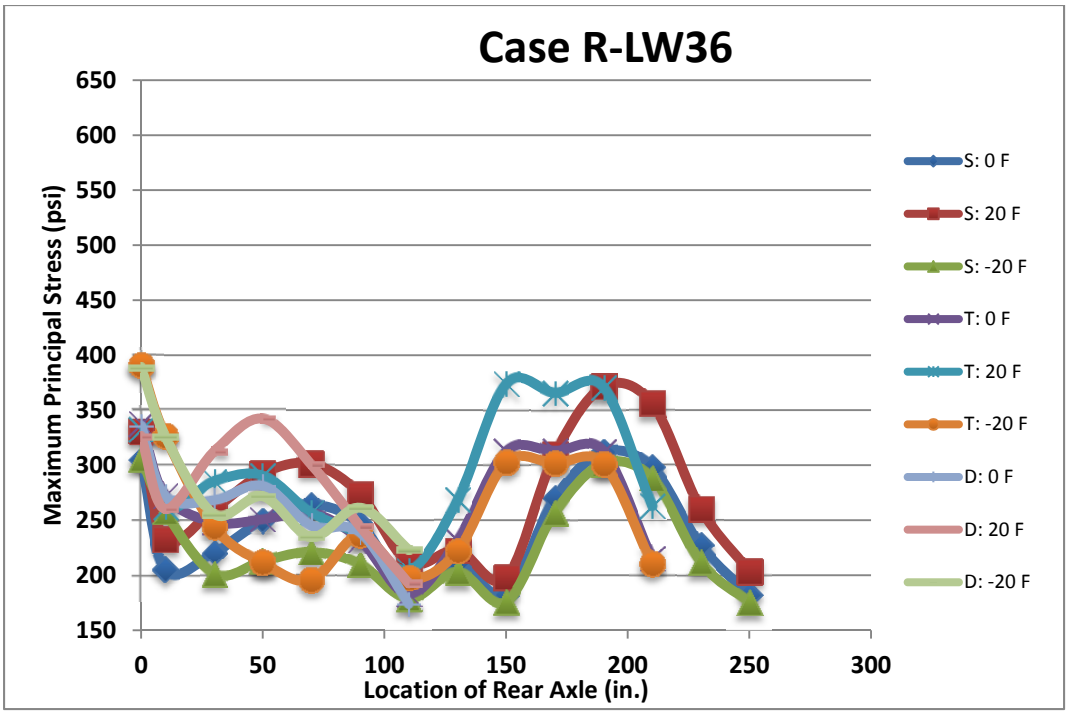

Figure 104. Maximum principal (tensile) stress for Case R-LW36 versus axle position.

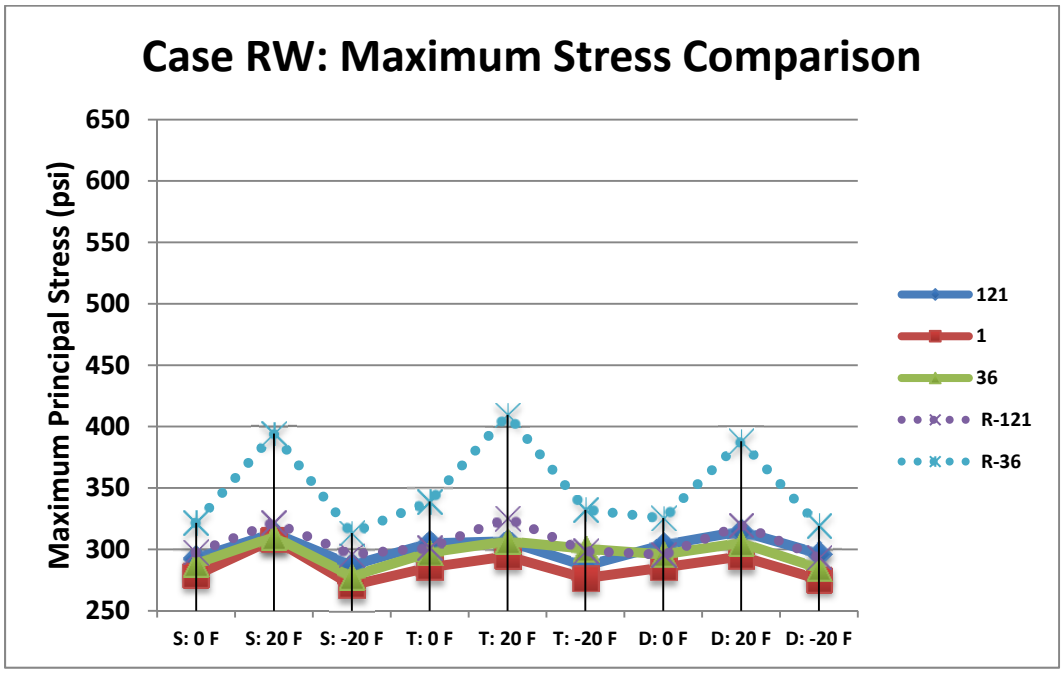

Figure 105. Comparison of the peak tensile stresses for Case RW for each input factor level and the five nonuniform support distributions.

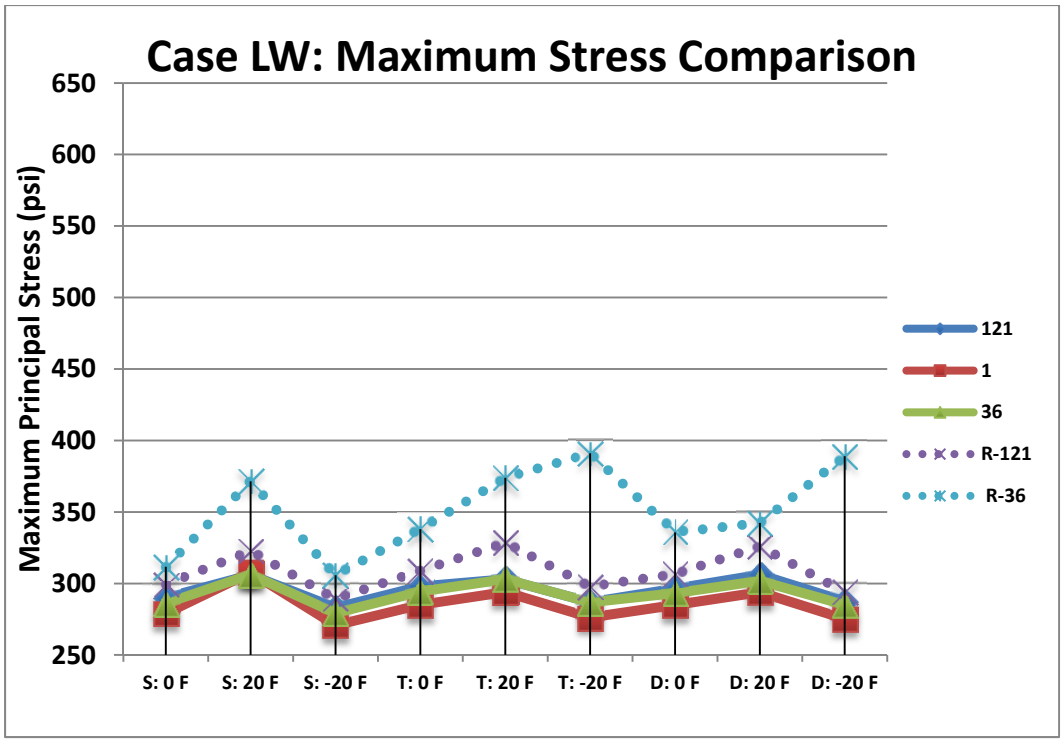

Figure 106. Comparison of the peak tensile stresses for Case LW for each input factor level and the five nonuniform support distributions.

Clearly, random assignment of the expected distribution of k-values produced greater tensile stresses in the slab, as seen in Figure 107, compared to the deterministic analysis which assigned k-value based on the spatially collected field data. With random assignment of the support stiffness, the individual size of uniform areas of stiffness affected the peak tensile stress in the concrete slab. As seen in Figure 107, larger areas of nonuniform stiffness (i.e., 36 k-values sized 1.16 x 1.16 m^2) generated substantially higher tensile stresses as compared to smaller areas (i.e., 121 k-values sized 0.7 x 0.7 m^2) or even a uniform area (single k-value) support condition. The defined area size of uniform k-value was especially sensitive for the longitudinal edge loading paths with the right edge producing the greatest tensile stress for the randomly assigned 36 k-value option IV. Comparing Table 17, Case R-RE36 had a 37% increase in the average peak tensile stress compared to the loading on a uniform support and 31% increase in the overall peak tensile. Although there was a 33% increase in overall peak tensile stress between R-RW36 compared to uniform support, the magnitude of tensile stresses 409 psi (R-RE36) and 308 psi (RE1) were not critical. For the middle of the lane loading path, the area size of predefined subgrade stiffness was not a factor in the peak tensile stresses.

Daytime curling conditions combined with axle loading produced the greatest tensile stresses in the slab except for Case R-LW36, which occurred at the first loading position. As shown in Table 18, the peak tensile stresses were at the bottom of the slab for all the cases except for R-LW36. As in the deterministic analysis of the measured field data, the longitudinal edges produced the most critical loading locations. With respect to the axle configurations, there was not one axle that always produced the highest tensile stress which was significantly greater than the other two axles. The frequency distribution for Cases R-121 and R-36, shown in Figure

108, resembles a normal distribution for both the cases. The important thing to note in Figure 108 is that R-36 has 7% more k-values in the bin range of 0-40 psi/in with some values as low as 1 psi/in as reported earlier suggesting the presence of more softer areas than R-121. Case R-121 had a mean of 65 psi/in and a standard deviation 27.4 psi/in with a coefficient of variation of 42%, and Case R-36 had a mean of 61 psi/in, a standard deviation of 29.3 psi/in, and coefficient of variation of 48%. The combination of lower k-value magnitudes along the free edges coupled with the larger area size with 36 independent k-values led to Case R-36RE producing the most critical tensile stress (608 psi).

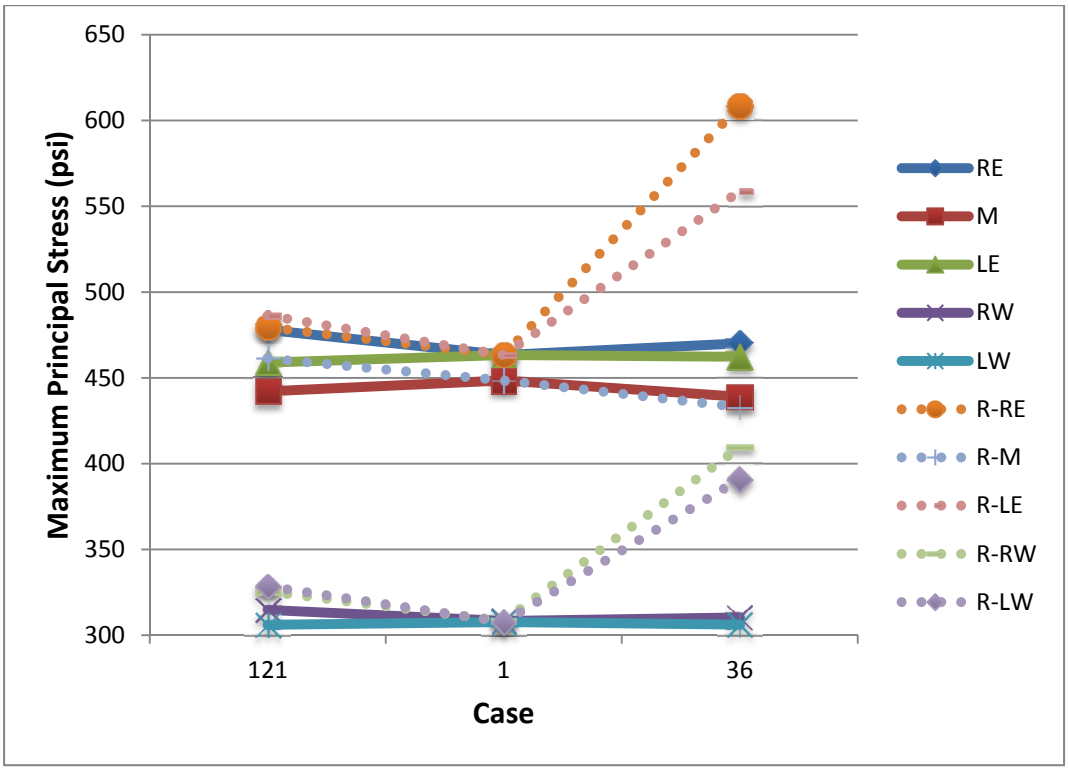

Figure 107. Comparison of overall peak tensile stress for each load location with different nonuniform subgrade support conditions for roadway MI I-94.

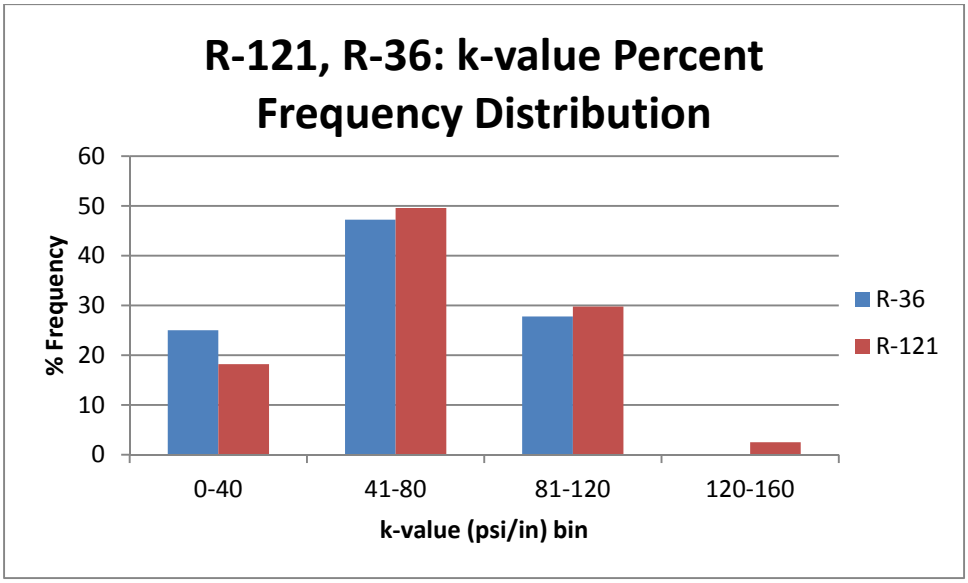

Figure 108. Percent frequency distribution of k-values for Case R-121.

Table 17: Summary of the Percent Change in Overall and Average Peak Tensile Stress from Random Assignment of 36 k-Value Areas Relative to Uniform Subgrade for Each Loading Path

Loading Path	Change in Overall Peak Tensile Stress (%)	Change in Average Peak Tensile Stress (%)
Case RE (Right Lane Edge)	+31	+37
Case M (Middle of Lane)	-3	-2
Case LE (Left Lane Edge)	+21	+28
Case RW (Right Lane Wheelpath)	+33	+22
Case LW (Left Lane Wheelpath)	+27	+23

Table 18. Location and Magnitude of Critical Tensile Stress for Each Factor Level Analyzed on MI I-94 Randomly Generated Support Stiffness

Case	Single Axle			Tandem Axle			Steer-Drive Axle		
	0 F	20 F	- 20 F	0 F	20 F	- 20 F	0 F	20 F	- 20 F
R-RE121	425 (0,195,b)	479 (0,195,b)	374 (0,195,b)	390 (0,223,b)	443 (0,223,t)	376 (49,275,t)	389 (0,179,b)	431 (0,199,b)	416 (0,79,t)
R-RE36	512 (0,75,b)	591 (0,75,b)	510 (0,75,b)	532 (0,83,b)	608 (0,83,b)	532 (0,83,b)	507 (0,75,b)	584 (0,75,b)	507 (0,75b)
R-LE121	437 (275,75,b)	486 (275,195,b)	406 (275,75,b)	404 (275,83,b)	447 (275, 83,b)	400 (227,0,t)	381 (275,75,b)	425 (275,199,b)	403 (227,0,t)
R-LE36	495 (275,195,b)	558 (275,195,b)	488 (275,195,b)	493 (275,195,b)	557 (275,203,b)	494 (219,0t)	453 (275,199,b)	518 (275,199,b)	496 (219,0,t)
R-M121	374 (185,0,b)	413 (185,0,b)	336 (185, 0,b)	420 (185, 0,b)	459 (185,0,b)	381 (185, 0,b)	422 (185,0,b)	461 (185, 0,b)	382 (185,0,b)
R M36	364 (89,0,b)	388 (89,0,b)	323 (89,0,b)	406 (89,0,b)	431 (89,0,b)	364 (89,0,b)	408 (89,0,b)	432 (89,0,b)	364 (89,0,b)
R-RW121	297 (22,0,b)	321 (22,0,b)	295 (22,0,b)	301 (22,0,b)	325 (22,0,b)	298 (22,0,b)b	295 (22,0,b)	319 (22,0,b)	293 (0,83.7t)
R-RW36	321 (20,75,b)	394 (20,75,b)	313 (20,75,b)	339 (20,81,b)	409 (20,81,b)	332 (20,81,b)	323 (20, 55,b)	388 (20,75,b)	319 (20,101,b)
R-LW121	299 (157,0,b)	322 (255,75,b)	289 (157,0,b)	308 (157,0,b)	328 (157,0,b)	297 (157,0,b)	306 (157,0,b)	326 (157,0,b)	294 (157,0,b)
R-LW36	311 (255,195,b)	371 (255,195,b)	305 (211,0,b)	337 (211,0,t)	373 (255,203,b)	391 (209,0,t)	335 (211,0,t)	342 (255,199,b)	388 (209,0,t)
RE1/LE1	419 (0,195,b)	463 (0,175,b)	376.7 (0,195,b)	381 (0,175,b)	417 (0,55,b)	364.3 (42,0,t)	376.7 (0,179,b)	408.0 (0,179,b)	368.7 (44,0,t)
M1	366 (89,0,b)	403 (89,0,b)	330 (89,0,b)	409 (89,0,b)	446 (89,0,b)	373 (89,0,b)	411 (89,0,b)	448 (89,0,b)	374 (89,0,b)
RW1/LW1	279 (117,0,b)	308 (20,75,b)	270 (117,0,b)	285 (117,0,b)	294 (117,0,b)	276 (117,0,b)	285 (117,0,b)	294 (117,0,b)	275 (117,0,b)

b: Bottom; t: Top

5.2 MI I-94: Random Assignment of Support Condition by a Beta Distribution to Arbitrary Predefined Discrete Areas

The results of the analysis of the nonuniform subgrade support with random assignment of k-values showed that extremely weak areas (i.e., k-values of 1 psi/in) are linked to large tensile stress changes in the slab. Based on the normal distribution assumption and field data, the likelihood of such a low k-value is in the 1 percentile range. In order to limit the probability of unrealistic k-values (i.e., less than 0 psi/in) a beta distribution function was to provide a lower limit boundary. The probability density function of the beta distribution is described by the following equation (Evans et al. 2000), where α and β are shape parameters and $B(\alpha,\beta)$ is the beta function with domain [0,1] and a and b are continuous boundary parameters ($a<b$).

$$f(x) = \frac{1}{B(\alpha,\beta)} \frac{(x-a)^{\alpha-1}(b-x)^{\beta-1}}{(b-a)^{\alpha+\beta-1}} \tag{5.1}$$

The lower limit k-value (a) was set at 20 psi/in, which was within two standard deviations of the mean of the field data set, and the upper limit (b) was 202 psi/in which was the highest k-value obtained from MI I-94 field data. By knowing the mean (μ) and variance (σ^2) of the deterministic field data, the shape factors can be determined (α=1.9 and β=6) by solving the Equations 5.2

and 5.3 below (Evans et al. 2000). Figure 109 shows the beta distribution selected for the field-correlated k-values.

$$\mu = \frac{\alpha}{\alpha + \beta} \tag{5.2}$$

$$\sigma^2 = \frac{\alpha\beta}{(\alpha + \beta)^2 + (\alpha + \beta + 1)} \tag{5.3}$$

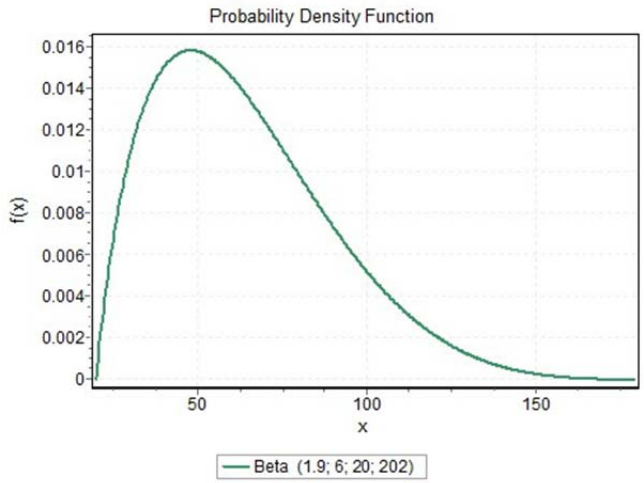

Figure 109. Beta distribution of field-correlated k-values.

The conclusions from Chapter 4 and Section 5.1 showed that the right and left edge loading paths were critical and, thus, the wheelpath and middle of lane cases were not analyzed with the beta distribution k-value assignment. The analysis did include the three different axle configurations and temperature differentials. A random number generator was used to assign k-values to 36 discretized areas of 1.16 x 1.16 m^2, as shown in Figure 110, using the beta distribution previously discussed. Five different distributions of k-value were generated and only the distribution deemed to give the higher tensile stresses was kept for further analysis. For nomenclature, a prefix of "B" is added to the subcases to distinguish from the original deterministic and random assignment of k-value despite the beta distribution assignment also being "random."

Case B-RE36 involved the movement of the vehicle along the right lane edge. Figure 111 shows the results of the tensile stresses recorded at each longitudinal position for Case B-RE36 with the magnitude of stresses being similar to the original field data (i.e., Case RE36), as seen in Figure 112. This is due to the change in adjacent stiffness areas that was not as drastic (i.e., around a factor of 2) as compared with the random assignment with the normal distribution shown previously in Figure 91. The mean k-value of B-RE36 was 85 psi/in with a standard deviation of 33.9 psi/in, which was similar to Case RE121 (mean of 86 psi/in and standard deviation of 50 psi/in). The relatively similar peak tensile stress behavior suggested that a small change between adjacent k-value areas (i.e., factor of 2 in Figure 110) causes small stress variations but fails to produce the same tensile stress increase of 31% as in Case R-RE36. For the random assignment with the beta distribution, the peak tensile stress was at the bottom of

the slab during daytime curling. The single axle caused the highest stress for this case with the tandem and steer-drive axle behaving similar in magnitude (i.e., 10% less than the single axle).

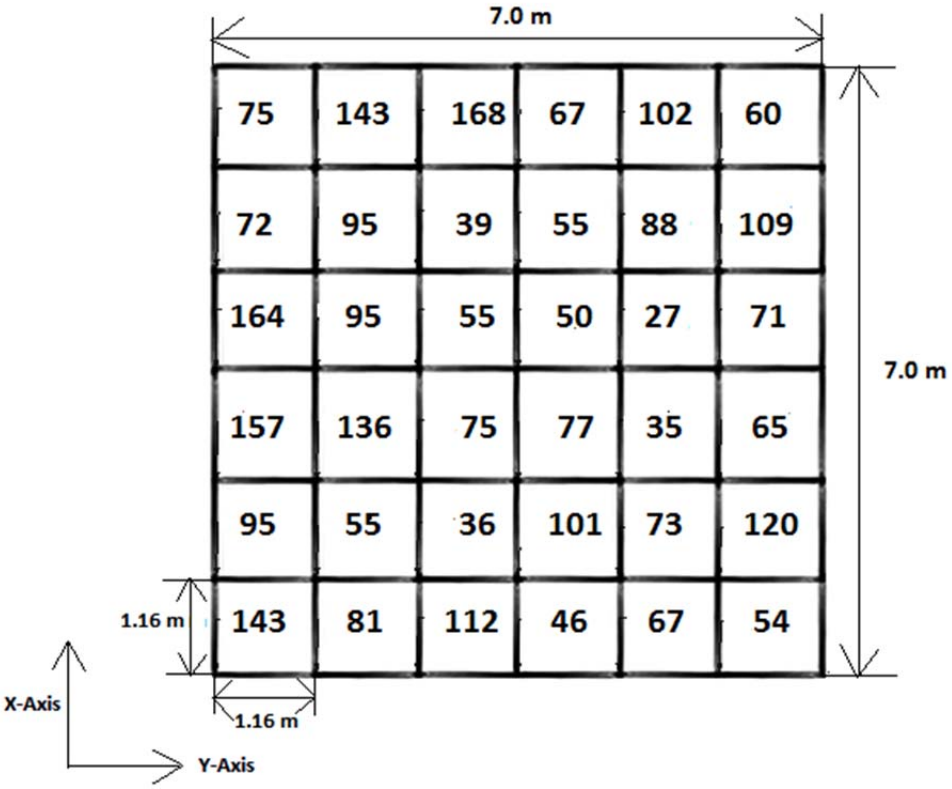

Figure 110. Case B-36 with 36 discretized k-value areas.

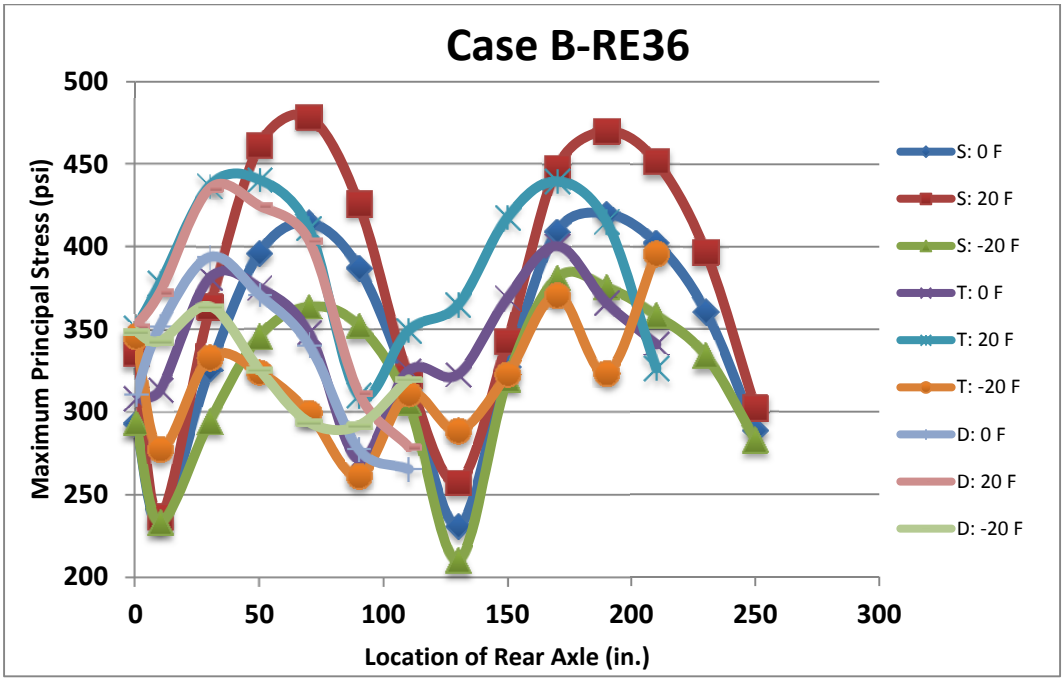

Figure 111. Maximum principal (tensile) stress for Case B-RE121 versus axle position.

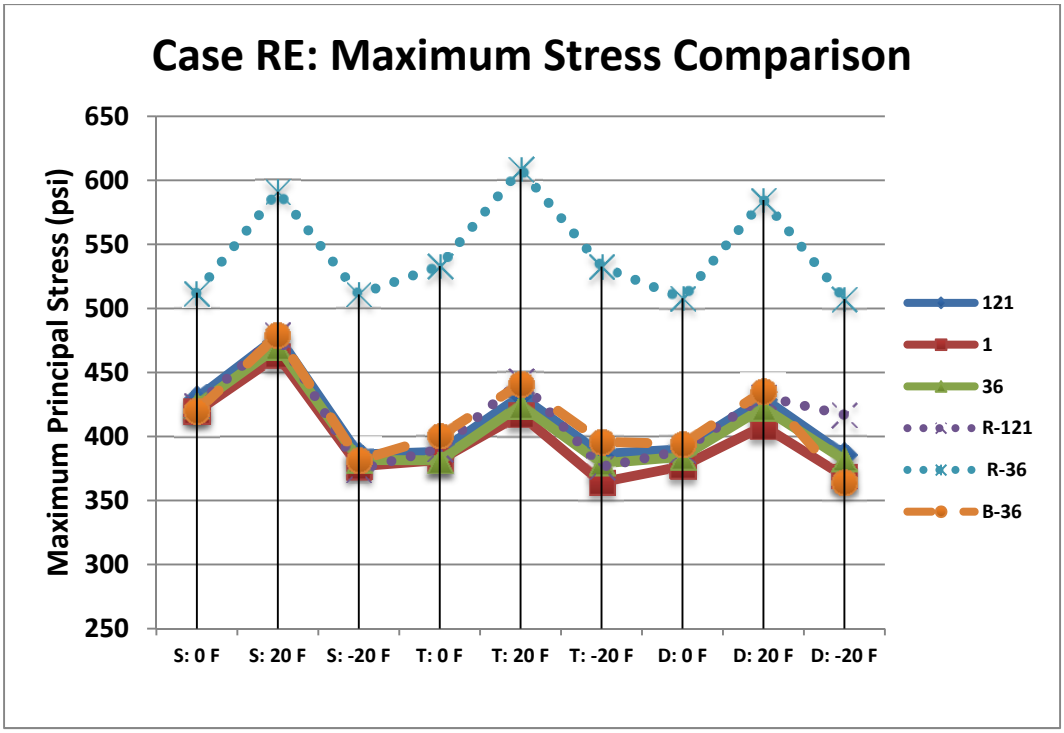

Figure 112. Comparison of the peak tensile stresses for Case RE for each input factor level and the six levels of nonuniform support.

Case B-LE36 represents the longitudinal movement of the vehicle along the left edge of the slab. Figure 113 shows that the results of the maximum tensile stresses recorded at each longitudinal position were slightly lower in magnitude than Case B-RE36. The peak tensile stresses of B-RE36 were 8% higher than B-LE36, as seen in Table 19. Figure 115 shows that the k-value for both edges does not show a uniquely different pattern and confirms why the tensile stresses for the two loading paths were similar. Case B-LE had a slightly higher mean of 103 psi/in than B-RE with 84 psi/in. The effect of a higher standard deviation of 40.3 psi/in for B-LE was negated by its larger mean. The magnitudes of the peak tensile stresses were similar to corresponding field data Case LE-36, as seen in Figure 114. The behavior of the all the axle configurations was similar with single axle causing slightly higher peak tensile stress. The critical tensile stress occurred at the bottom of the slab during day time curling. Although there were adjacent areas with relatively high variation in k-value (i.e., 168 to 39 psi/in), the tensile stress changes were not as great as with very low support stiffness at the critical load location with adjacent stiffer support.

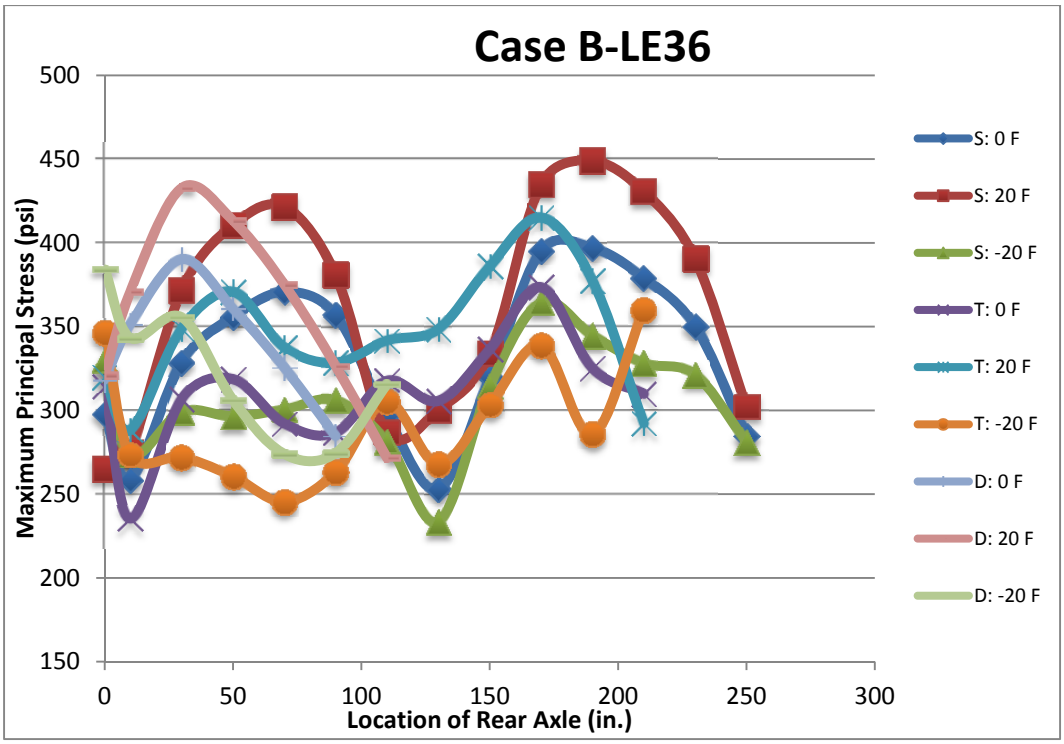

Figure 113. Maximum principal (tensile) stress for Case B-LE121 versus axle position.

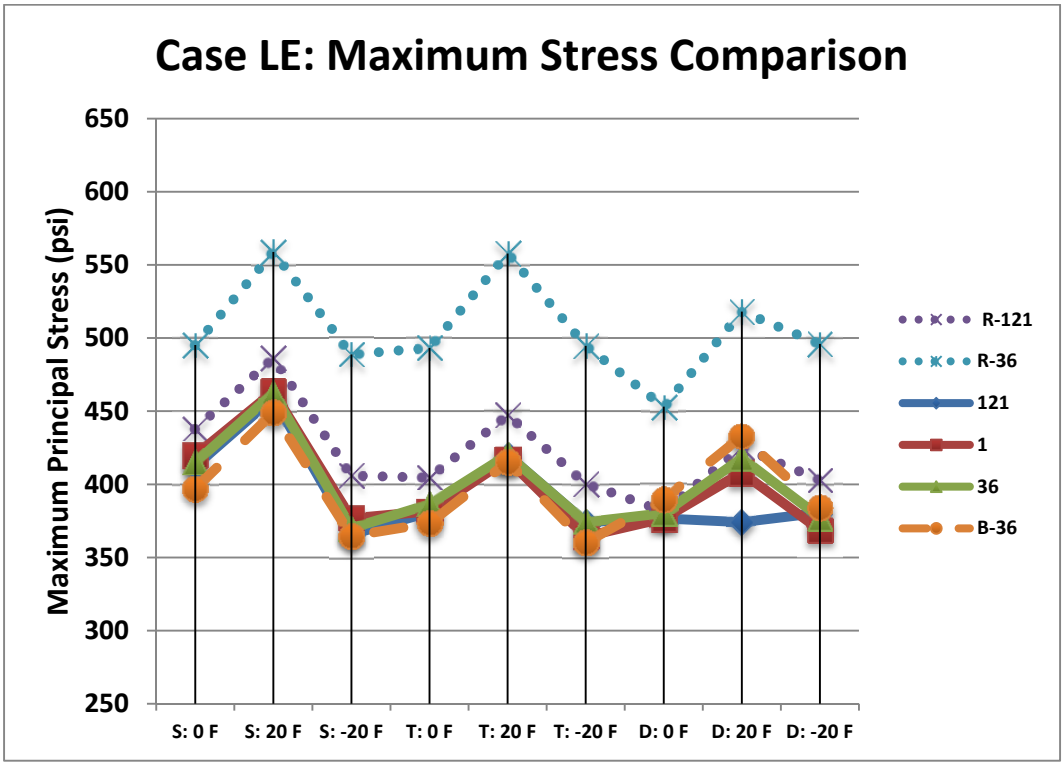

Figure 114. Comparison of the peak tensile stresses for Case LE for each input factor level and the six levels of nonuniform support.

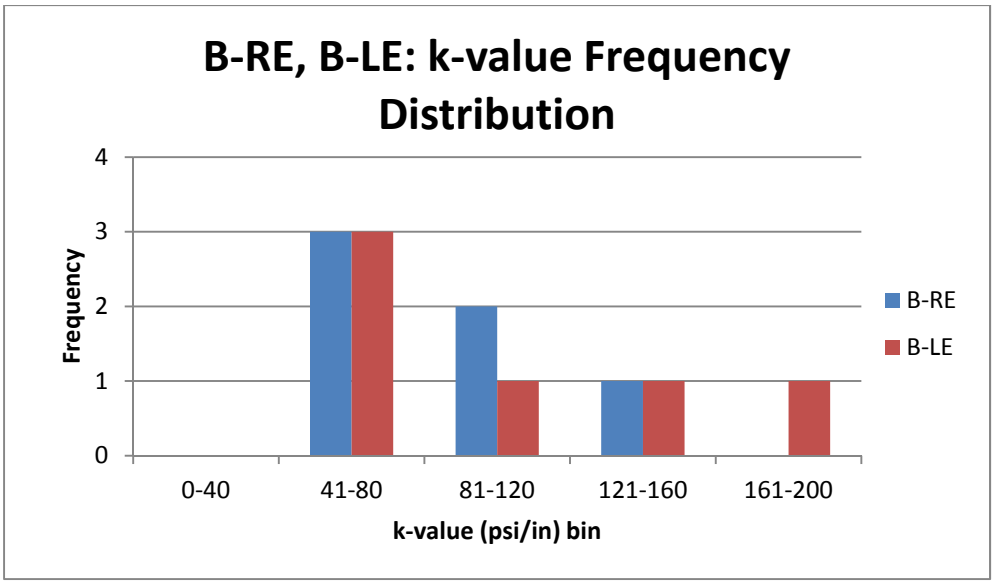

Figure 115. The k-values for Cases B-RE and B-LE for MI I-94 roadway.

Table 19. Location of Peak Tensile Stresses for Randomly Assigned k-Value with Beta Distribution for MI I-94

Case	Single Axle			Tandem Axle			Steer-Drive Axle		
	0 F	20 F	- 20 F	0 F	20 F	- 20 F	0 F	20 F	- 20 F
B-RE36	420 (0,195,b)	479 (0,75,b)	381 (0,175,b)	400 (0,175,b)	440 (0,55,b)	395 (51,275,t)	394 (0,179,b)	435 (0,180,b)	363 (0,179,t)
B-LE36	397 (275,195,b)	448 (275,195,b)	364 (275,75,b)	373 (275,175,b)	415 (275,175b)	360 (223,275,t)	389 (275,179,b)	432 275,79,b)	384 (275,79,t)
b=Bottom of slab; t=Top of slab									

The result of carrying out a beta distribution assignment proved that having extremely soft spots (i.e., k-value of 1 psi/in as in Case R-RE36) were detrimental to the concrete slab in the presence of an adjacent higher k-value area. Increasing the k-value along the edge lowered the magnitude of peak tensile stresses even with adjacent nonuniform stiffness. Because of the low probability of occurrence of low k-values, the beta distribution showed that minimum stiffness values for the support conditions can avoid future high tensile stress concentrations.

5.3 MI I-96: Random Assignment of Support Condition by a Normal Distribution to Arbitrary Predefined Discrete Areas

A random number generator using the mean and the standard deviation of the field data for MI I-96 (Case 81) was carried out to analyze if a random assignment of the k-value following the measured field data distribution (normality assumed) would produce significantly greater tensile stresses than just the uniform support assumption. This analysis was similar to MI I-94 (Section 5.1) except for the k-values were much greater for MI I-96. Figure 116 shows the spatial plot developed through random generation of k-values in an unbiased manner. The frequency distribution of Case R-81 is shown in Figure 117 having more k-values in the lowest stiffness bin of 100-240 psi/in compared to Case 81. Case R-81 had a mean of 390, a standard

deviation of 112.6, a coefficient of variation of 29%, and a range of 132-647 psi/in. The analysis matrix for different axle types and temperature differentials remained the same as previous sections with the loading path at the right lane edge, left lane edge, and middle of the slab only.

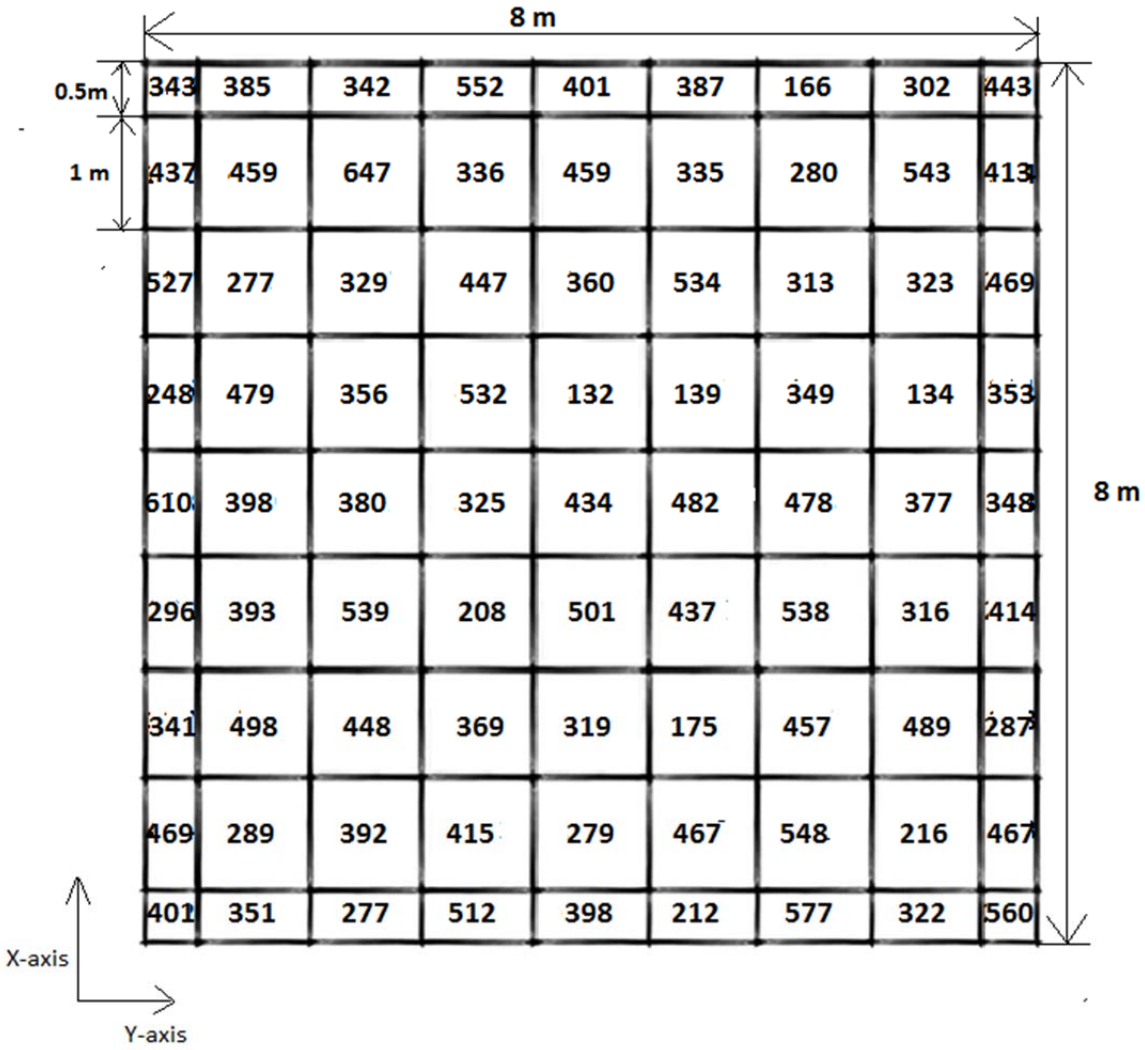

Figure 116. Case R-81 with 81 discretized k-value areas randomly assigned from MI I-96 data.

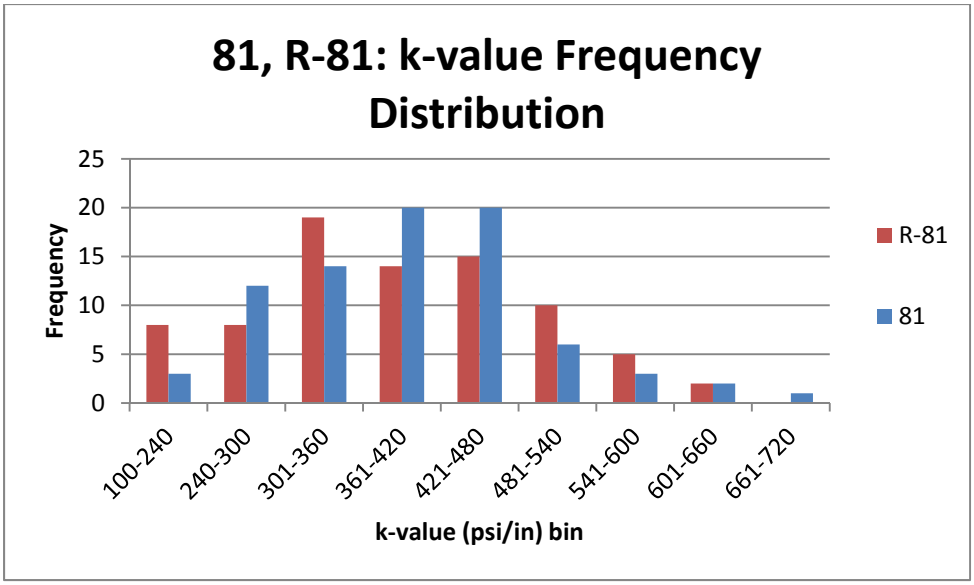

Figure 117. Frequency distribution of k-values for Case R-81.

5.3.1 Stress Analysis of Randomly Assigned Support Condition for Right Edge (R-RE) and Left Edge (R-LE) Cases on MI I-96 Roadway Section

The results of Case R-RE81 in Figure 118 show the maximum tensile stresses recorded at each longitudinal position. Case R-RE81 had slightly higher overall peak tensile stress (approximately 8%) compared to Case RE-81. In Figure 119, a similar pattern with previous runs was observed with respect to the magnitudes of the critical stresses caused by each axle type (i.e., the single axle with daytime curling was the critical set of input factors). From Figure 119, the random assignment of the k-values did not have a significant impact in terms of the increase in tensile stress between Case R-81 and Case A1 (uniform) for a particular combination of axle type and temperature differential. The peak tensile stresses occurred at the mid-slab position of the first slab, as seen in Figure 120, at location of lower k-value (277 psi/in) adjacent to a higher stiffness area of 512 psi/in, albeit only a factor of 2. The overall and average peak stress change from uniform to nonuniform (R-RE81) increased 5%, which was much less than the increases found with the MI I-94 analysis with random assignment with lower support stiffness.

The difference between the critical daytime curling stresses compared to the nighttime curling and loading case was again significant. A 47% increase in average peak tensile stress between the no temperature differential and positive temperature differential case and a 37% increase in average peak tensile stress between negative temperature differential and positive temperature differential cases was observed in Figure 119. The critical tensile stresses were located at the bottom of the slab, as listed in Table 20.

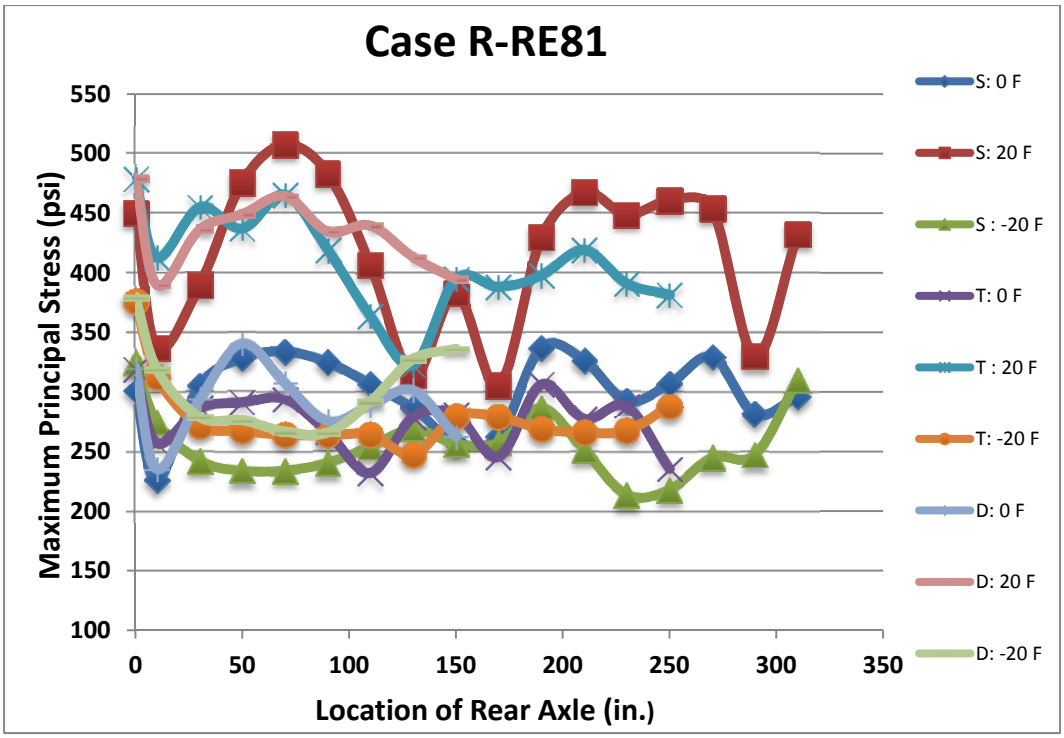

Figure 118. Maximum principal (tensile) stress for Case R-RE81 versus axle position.

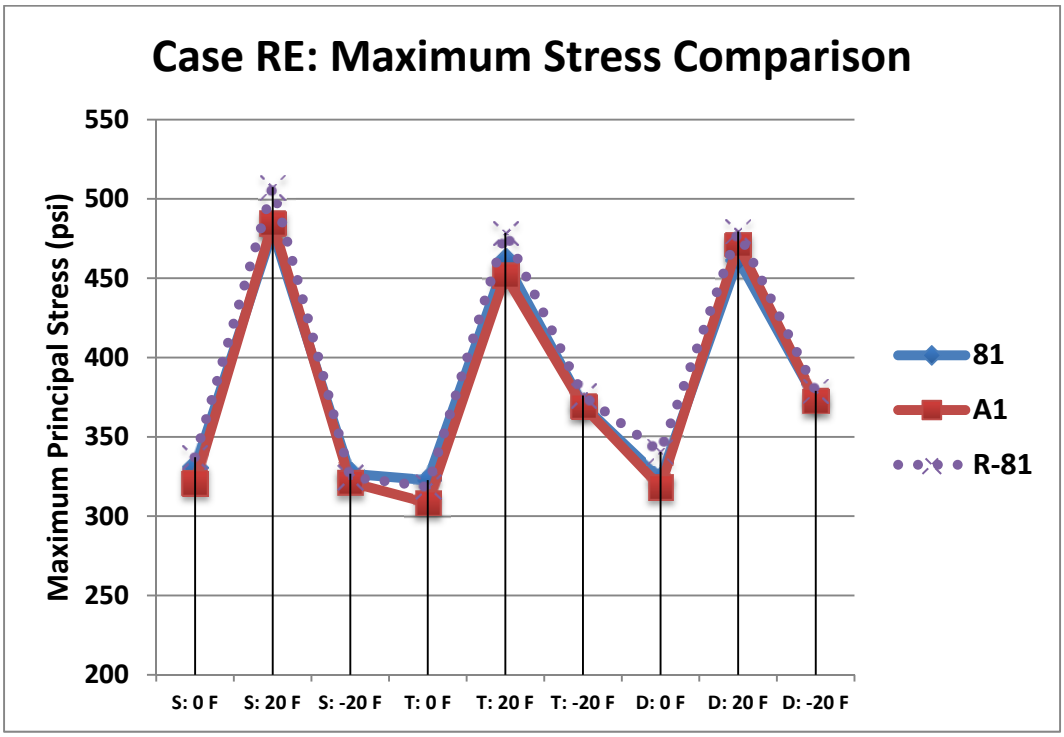

Figure 119. Comparison of the peak tensile stresses for Case RE of MI-I-96 roadway for each input factor level and the three levels of nonuniform support.

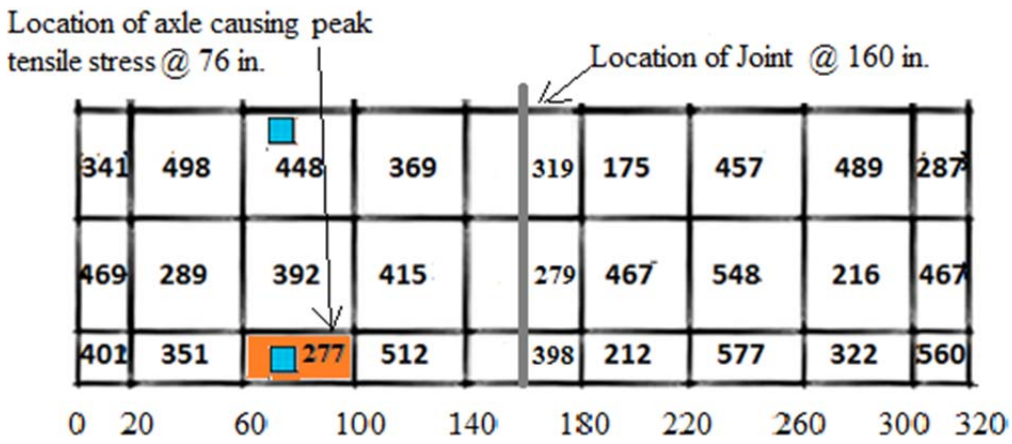

Figure 120. Local variation in k-values along right hand edge of the slab for Case R-RE81.

The maximum tensile stresses for the left edge loading path (Case R-LE81) in Figure 122 showed greater overall peak tensile stress than case R-RE81. In fact, the overall and average peak tensile stress changes from R-RE81 to R-LE81 were 7% and 3%, respectively. The reason for this behavior was the lowest k-value of R-LE81 was 166 psi/in, which occurred near the mid-slab load location, as seen in Figure 121. Figure 124 does not support the difference in peak tensile stresses since the frequency distribution between R-LE and R-RE were approximately the same despite R-LE81 having a slightly lower mean of 369 psi/in, compared to 401 psi/in for R-RE81. However, the k-value near the critical load location for R-RE81 was 277 psi/in, which supports the conclusion that the nonuniformity spatial position and magnitude are important factors in generating high tensile stresses in the slab.

The overall peak stress change from uniform (Case A1) to nonuniform (Case R-LE81) increased 11% with an increase in the average peak tensile stress of 8%. A 53% increase in average peak tensile stress between the no temperature differential and positive temperature differential case and a 43% increase in average peak tensile stress between negative temperature differential and positive temperature differential cases was observed, as seen in Figure 123. The overall peak tensile stress was produced by the single axle and was located at the bottom of the slab.

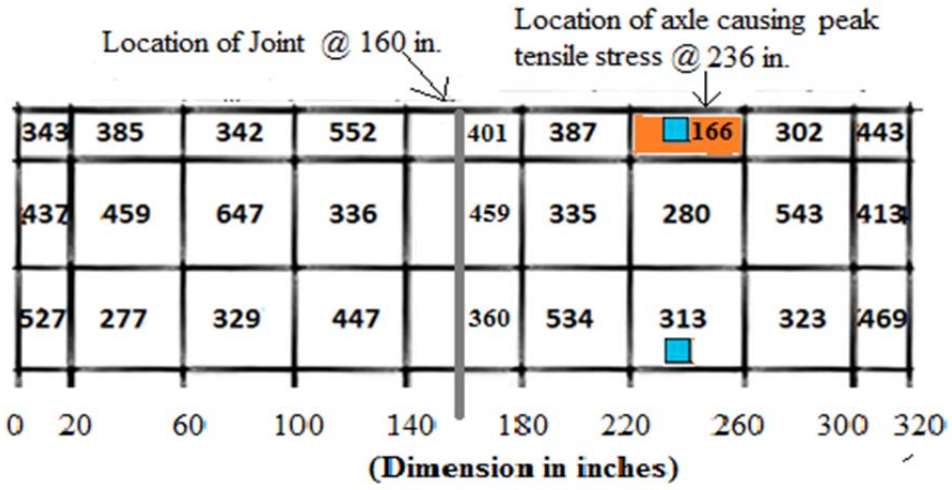

Figure 121. Local variation in k-values along left hand edge of the slab for Case R-LE81.

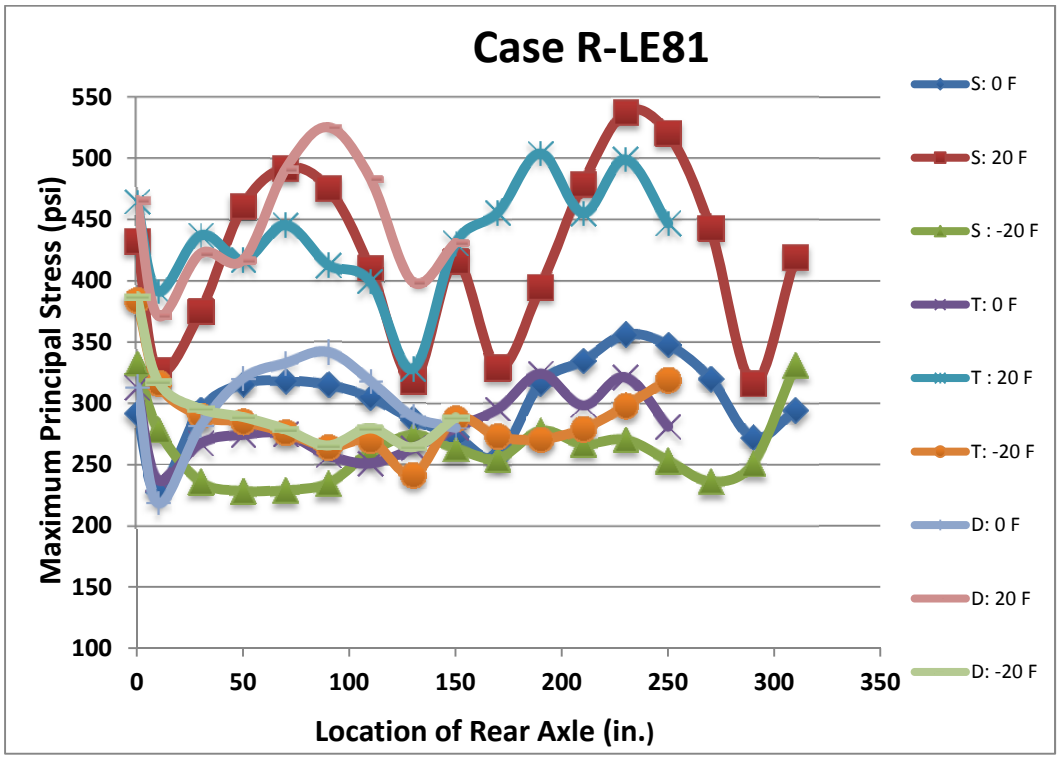

Figure 122. Maximum principal (tensile) stress for Case R-LE81 versus axle position.

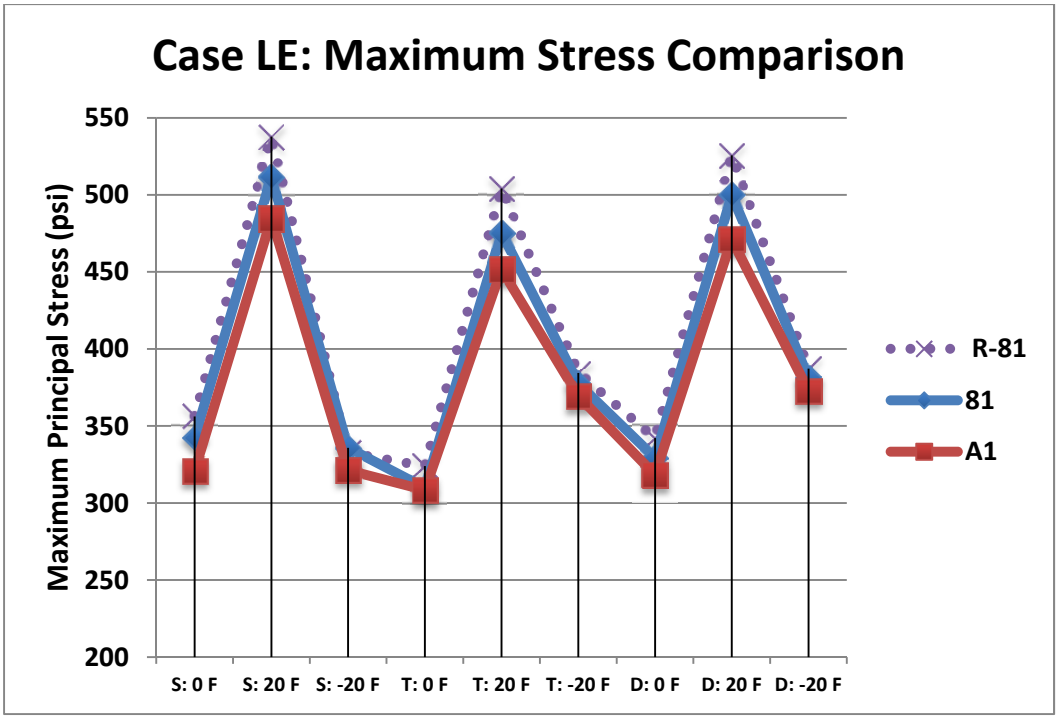

Figure 123. Comparison of the peak tensile stresses for Case LE of MI-I-96 roadway for each input factor level and the three levels of nonuniform support.

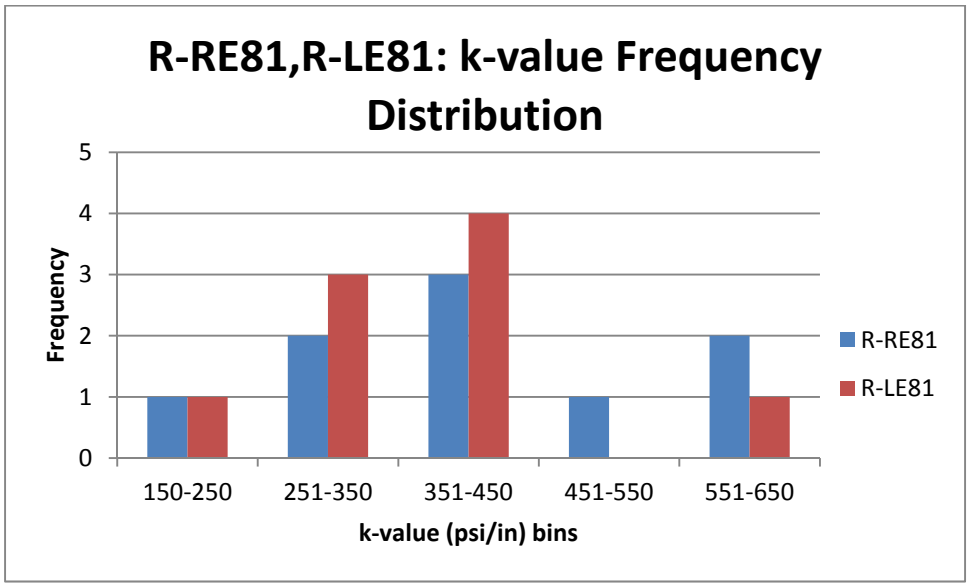

Figure 124. The k-values for Cases R-RE81 and R-LE81 on MI I-96 roadway.

5.3.2 Stress Analysis of Randomly Assigned Support Condition for Middle of Lane (R-M) Case on MI I-96 Roadway Section

Figure 127 shows the results of the maximum tensile stresses recorded at the each longitudinal position of the axle for Case R-M81. The maximum tensile stress for the middle of the slab loading path occurred at the bottom of the slab at the transverse edge. Peaks in the tensile stresses are observed because of a significant drop in support stiffness from 532 to 132

psi/in at 110 in from the initial loading location. The frequency distribution of R-M81 (Figure 126) shows that the k-values for the lowest stiffness bin of 100-250 psi/in were higher than M81, which did not have a single k-value in this bin. A 5% increase in overall peak tensile stress was realized from Case M-81 to R-M81 because of the presence of softer stiffness areas especially at the transverse edge and joint position as seen in Figure 125. The overall peak stress change from uniform to nonuniform (R-M81) increased 8% with an average increase in peak tensile stress of 6%. In Figure 128, a 39% increase in average peak stress between the no temperature differential and positive temperature differential case and an 88% increase in average peak stress between negative temperature differential and positive temperature differential cases was observed.

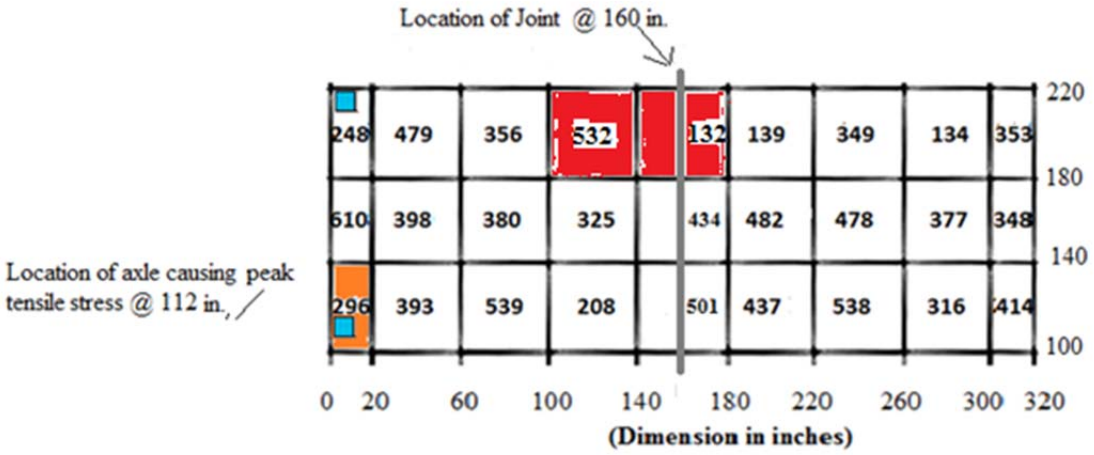

Figure 125. Local variation in k-values along middle of slab for Case R-M81.

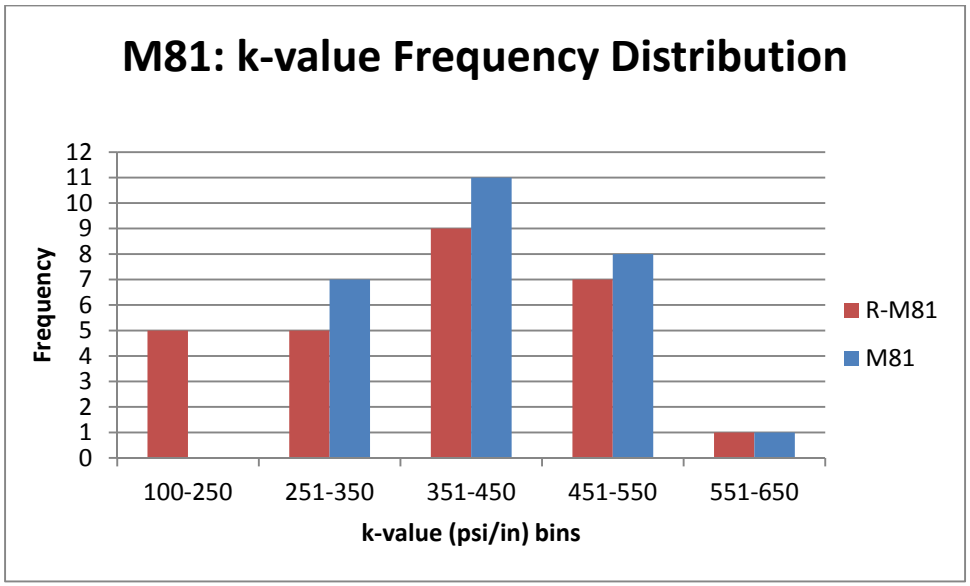

Figure 126. The k-values for Case R-M81 on MI I-96 roadway.

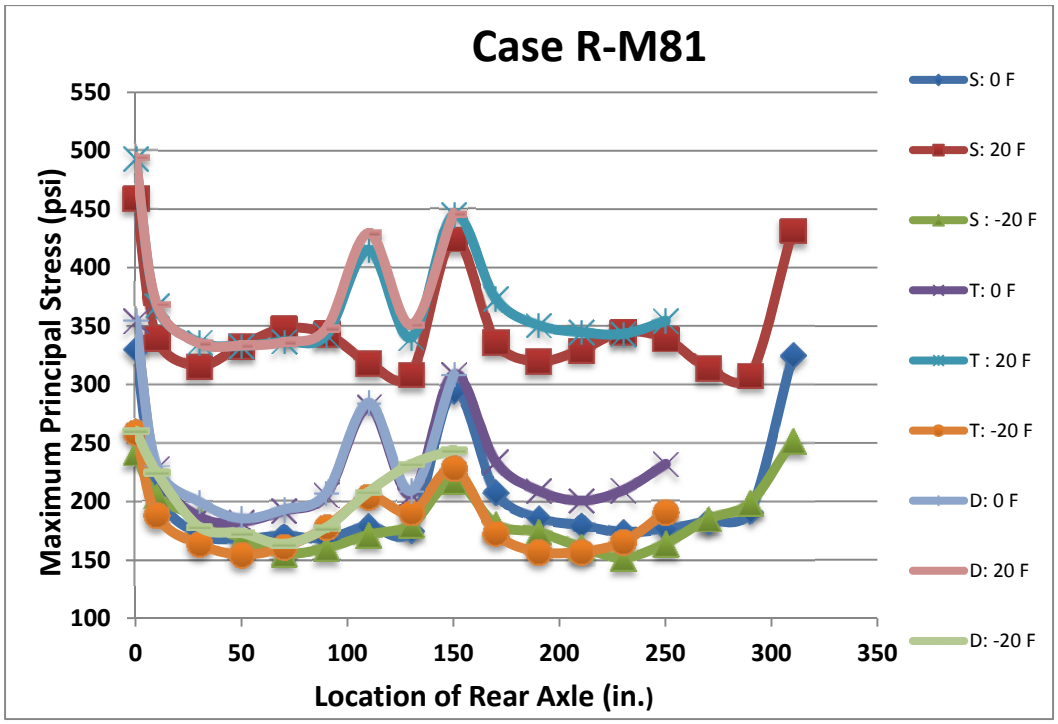

Figure 127. Maximum principal (tensile) stress for Case R-M81 versus axle position.

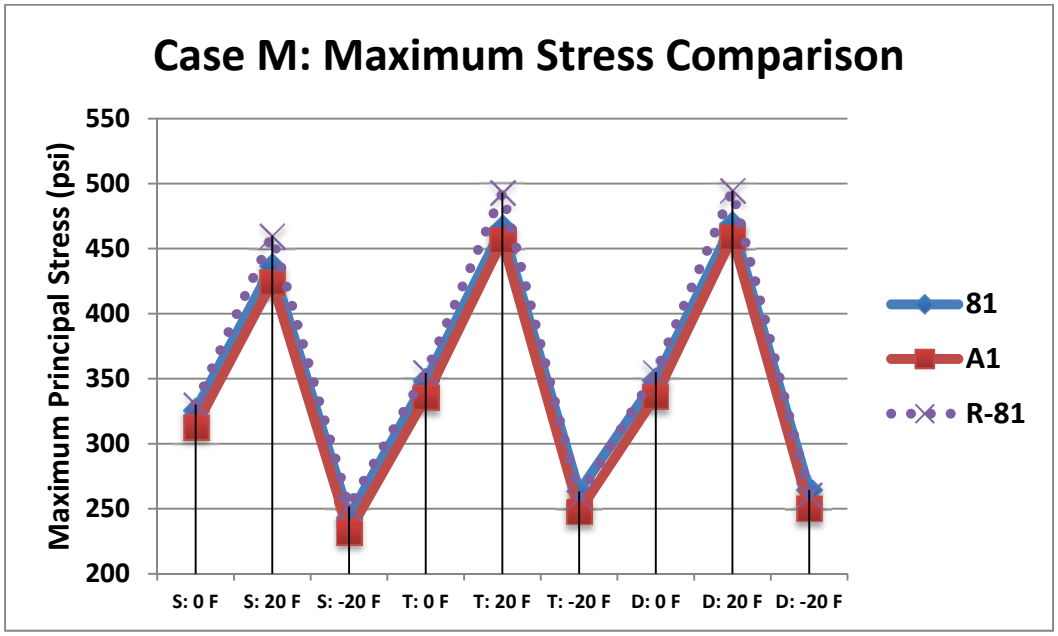

Figure 128. Comparison of the peak tensile stresses for Case M of MI-I-96 roadway for each input factor level and the three levels of nonuniform support.

Table 20 shows the location and magnitude of the peak tensile stresses for the different sets of inputs analyzed. Nighttime curling along the longitudinal free edges caused maximum tensile stresses at the top of the slab whereas for the rest of the subcases the maximum tensile stresses were at the bottom of the slab.

Table 20. Location and Magnitude of Peak Tensile Stresses for Randomly Assigned k-Value Support Conditions for MI I-96 Roadway

Case	Single Axle			Tandem Axle			Steer-Drive Axle		
	0 F	20 F	- 20 F	0 F	20 F	- 20 F	0 F	20 F	- 20 F
R-RE81	337 (0,196,b)	507 (0,76,b)	324 (46,0,t)	318 (102,0,b)	478 (102,0,b)	376 (46,0,t)	340 (0,200,b)	479 (102,0,b)	378 (46,0,t)
R-LE81	356 (320,236,b)	537 (320,236,b)	332 (276,0,t)	323 (320,244, b)	504 (320,244, b)	384 (276,0,t)	342 (320,240, b)	525 (320,240,b)	387 (276,0,t)
RE/LE A1	321 (102,0,b)	484 (102,0,b)	321 (46,0,t)	308 (102,0,b)	451 (102,0,b)	369 (46,0,t)	318 (0,200,b)	471 (0,240,b)	372 (44,0,t)
R-M81	330 (112,0,b)	459 (112,0,b)	251 (208,320,b)	354 (112,0,b)	493 (112,0,b)	258 (208, 0,b)	355 (112,0,b)	494 (112,0,b)	260 (112,0,b)
MA1	313 (208,0,b)	424 (208,0,b)	232 (112,0,b)	335 (208,0,b)	456 (112,0,b)	247 (112,0,b)	336 (208,0,b)	458 (112,0,b)	250 (112,0,b)

B: Bottom of slab; t: Top of slab

Comparing the overall peak tensile stresses between the critical cases of MI I-94 and MI I-96 (deterministic and randomly assigned data set), there was a 13% increase from case R-LE81 to R-RE36. Also, the average peak tensile stress increased by 36% between these critical cases. Based on the stress analysis carried for the MI I-96 roadway for the measure spatial stiffness, the overall and average peak tensile stresses were not as sensitive to difference between adjacent k-values as MI I-94 because of the relatively stiff subgrade support magnitude, as seen in Table 21 and Table 22. The deterministically assigned support values only increased the overall and average peak tensile stress by 6% and 4%, respectively, when moving from uniform and nonuniform support condition. Random assignment of the k-values on the field spatial plot lead to 11% increase in overall peak tensile stress between a uniform support and a nonuniform support condition and an 8% increase in average peak tensile stress. The stiffer support was more sensitive to changes in temperature curling conditions, as expected. The overall peak tensile stresses produced by the three axle types along the different loading locations on account of a nonuniform stiff subgrade support were still relatively high between 450-525 psi/in during the daytime curling for the slab, loading, and material inputs assumed. Furthermore, daytime curling compared to the other temperature differential condition in Figure 129 and Table 23 produced significant increases in peak tensile stresses for all input cases.

Table 21. Summary of the Percent Change in Overall and Average Peak Tensile Stress from Uniform Support Relative to Deterministically Assigned Field Nonuniform Support (81 k-Values)

Loading Path	Change in Overall Peak Tensile Stress (%)	Change in Average Peak Tensile Stress (%)
Case RE (Right Lane Edge)	-1	+1
Case LE (Left Lane Edge)	+6	+4
Case M (Middle of Lane)	+2	+4

Table 22. Summary of the Percent Change in Overall and Average Peak Tensile Stress from Uniform Subgrade Relative to Random Assignment of 81 k-Value Areas Each Loading Path

Loading Path	Change in Overall Peak Tensile Stress (%)	Change in Average Peak Tensile Stress (%)
Case RE (Right Lane Edge)	+5	+5%
Case LE (Left Lane Edge)	+11	+8%
Case M (Middle of Lane)	+8	+6%

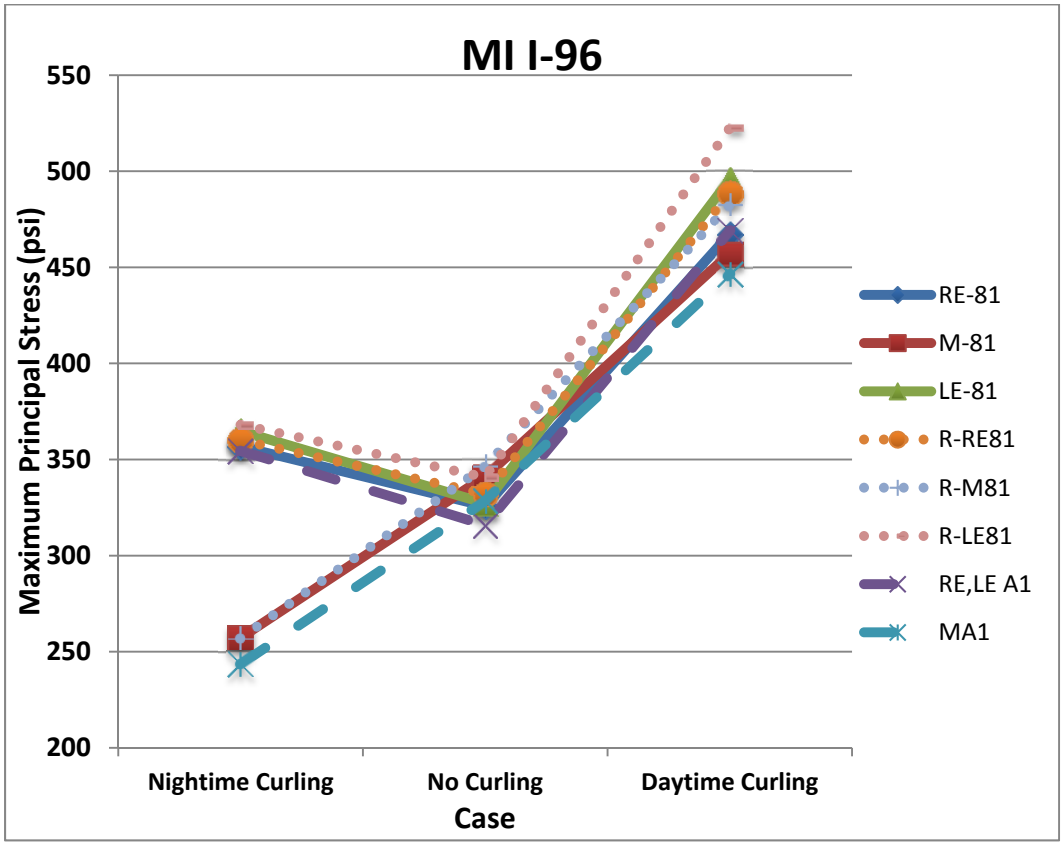

Figure 129. Comparison of effect of temperature differential on the nonuniform subgrade support cases of MI I-96 roadway.

Table 23. Percentage Difference between the Average Peak Tensile Stresses of the Temperature Differential Cases for a Given Loading Path and Subgrade Type Combination

Case	No temperature to Positive Temperature Differential (%)	Negative temperature to Positive Temperature Differential (%)
RE81	+43	+32
R-RE81	+47	+37
M81	+34	+78
R-M81	+39	+88
LE81	+52	+36
R-LE81	+53	+43

5.4 Chapter 5 Summary and Conclusions

In this chapter the field-correlated k-values from I-94 and I-96 were reassigned to the discrete areas using several statistical distributions. Both I-94 and I-96 were reassigned k-values by a normal distribution, and the I-94 data was additional reassigned with a beta distribution. Once the nonuniform support was distributed, a two-dimensional finite element analysis was performed using the ISLAB2000 program following the same analysis factorial as previously described in Chapter 4.

The I-94 k-values were normally distributed for the 36 and 121 discrete area cases, with the mean value being assigned to the uniform support condition. The maximum tensile stresses were greatly increased (up to 30%) by the normally distributed 36 k-values while the normally distributed 121 k-values and uniform condition were marginally affected. The edge-loaded and wheelpath-loaded cases were the most influenced by the normally distributed 36 k-values.

A beta distribution was used on the I-94 data to reduce the probability of low (soft) k-values. The results indicated that the beta-distributed tensile stresses were less than the normally distributed tensile stresses in the support condition with 36 independent, uniform areas. This was due to the fact that there were less soft areas adjacent to stiff areas along the edges. The tensile stress behavior and magnitude caused by the beta-distributed nonuniform support was more on the order of the field-correlated nonuniform support analysis.

The I-96 was also normally distributed for the 81 discrete areas. The resultant tensile stresses were only marginally increased relative to the field-correlated results. The stress results from the loading along the left edge were the most affected by the normally distributed nonuniform areas.

CHAPTER 6 SUMMARY AND CONCLUSIONS

Intelligent compaction (IC) technologies are gaining attention for their ability to both spatially characterize the compaction effort of a given pavement layer as well as help provide a more uniform layer compaction. One of the significant advantages to IC is that areas of nonuniform compaction can be located. This report aims to answer some of the questions concerning the effects of these nonuniform support areas on the stresses and deflections in a concrete slab. Previous studies at the University of Illinois (Barenberg et al. 1976) and Iowa State University (White et al. 2005) demonstrated that a nonuniform support of a concrete slab can have significant detrimental effects such as increased tensile stresses.

This study was divided into several sections. The initial study (Chapter 2) evaluated the effects of various (10) predetermined nonuniform supports with support (k-values) differing between 50 and 500 psi/in in addition to two uniformly supported slabs. The pavement was modeled as a single concrete slab over a given uniform or nonuniform support using the two-dimensional (2D) finite element software ISLAB2000. Combined with severe temperature curling and typical loading scenarios with single, tandem, and steer-drive axles, it was found that certain nonuniform support conditions could greatly increase the maximum slab tensile stresses relative to a uniform support. The overall highest peak tensile stress was 676 psi, which was due to a "random" support condition where 20 predefined areas were assigned a soft or stiff k-value. The second worse support condition consisted of a stiff k-value with soft longitudinal edges, which resulted in a maximum tensile stress of 637 psi. Assuming a typical concrete flexural strength of 650 psi, it is evident that the tensile stresses are significant enough to result in potential premature failure.

Based on the critical predetermined support conditions, a three-dimensional (3D) finite element analysis was conducted in which slabs with preexisting cracks were evaluated for crack propagation potential due to the nonuniform support (Chapter 3). Partial-depth (quarter-elliptical) and full-length (rectangular) cracks were inserted on both the top and bottom of the slab at the transverse and longitudinal edge, respectively, where the peak tensile stresses in the slab were produced. Four subgrade conditions were chosen to support the concrete slab: uniform stiff, uniform soft, nonuniform soft edges, and nonuniform stiff edges. The 3D analysis showed significantly higher mode I stress intensity factor (K_I) values for surface-initiated cracks (maximum of 2.0 MPa-$m^{1/2}$) rather than bottom-initiated cracks (maximum of 1.22 MPa-$m^{1/2}$), given the same slab and crack geometry, support conditions, and load configuration. The nonuniform soft subgrade support with surface cracks resulted in a 50% increase in the K_I values compared with the uniform soft support condition. For the bottom-initiated cracks, the uniform soft support produced the highest K_I values for the longitudinal edge loading cases, but these values were still 38% less than the maximum K_I value for surface-initiated cracks. For many of the cases analyzed, the maximum K_I values were high enough to cause unstable crack propagation based on concrete critical stress intensity factors (K_{IC}). Preexisting cracks coupled with nonuniform support were shown to produce conditions that could cause unstable crack propagation whereas the same slabs without cracks and nonuniform support produced high tensile stresses but not sufficiently high to produce immediate slab failure.

The final part of this research used in situ testing carried out on two roadway segments, MI I-94 and MI I-96, in order to gather field data on the spatial variation in soil stiffness. Dynamic cone penetrometer (DCP) tests were conducted on top of the subbase material for both sections that were used to correlate to California bearing ratio (CBR) values. Plate load tests (PLT) conducted on one test section (MI I-94) were correlated to the CBR data to develop an empirical relationship that was used to correlate CBR to k-value on both test sections. These measured stiffness variations over a small area were defined as support nonuniformities. Pavement stress analysis was completed using the 2D finite element analysis (ISLAB2000), which utilized the spatially derived k-values as an input support parameter. These k-values were either deterministically or randomly assigned to a predefined support area size. Multiple nonuniform support cases were developed to theoretically analyze the effects of the support condition, based on defining the size of each individual area of uniform k-value (i.e., Case 121 would represent a 121 individual k-value areas of 0.7 x 0.7 m^2). A total of four nonuniform support conditions were analyzed for each set of inputs: single k-value, 36 k-values of 1.16 x 1.16 m^2, 81 k-values of 1 x 1 m^2, and 121 k-values of 0.7 x 0.7 m^2. These nonuniform support conditions were analyzed for three different axle configurations (single, tandem, and steer-drive axle), three temperature differential (+20°F, 0°F, -20°F), and loading paths (left/right edge, middle of the lane, and left/right wheelpath). All analysis was completed on a four-slab assembly with a single slab thickness. The axles were traversed across the slabs in the various loading paths to determine the peak tensile stress for a given set of inputs.

The results of the finite element analysis on the MI I-94 test for the two sets of deterministically assigned nonuniform support conditions (121 and 36 k-values and single mean k-value) showed that there was little difference between the nonuniform support with 121 k-values and using the mean k-value of 63 psi/in to characterize the support. Even though the measured k-value range was 31 to 202 psi/in or a factor of almost 7 difference for Case 121, the overall peak tensile stresses were only 3.2% different than the uniform case with the average peak tensile stress increasing only 3.6% for each set of inputs. For the highest case (Case 121), the peak tensile stress occurred for the single axle along the right edge loading path.

In order to further determine the critical size of the nonuniform support area, a random assignment of the k-values using a normal distribution with the mean and standard deviation of the field data for two cases, 121 and 36 k-values, was completed. For MI I-94 the mean k-value was 63 psi/in (standard deviation = 25.6 psi/in) and for the randomly generated k-values less than zero, a value of 1 psi/in was assigned. When the same analysis was run with the 2D finite element program, the nonuniform support condition with randomly assigned k-values into 36 predefined areas (case R-36) produced a range of 22% to 37% increase in average peak tensile stress for the edges and wheelpath cases. More importantly, an increase of 31% in overall peak tensile stress was determined when going from a nonuniform subgrade support condition (case R-RE36) to an uniform subgrade support condition with edge loading and random assignment of k-values. For this critical case, the overall peak tensile stress in the slab was 608 psi and was produced by a single axle and daytime curling conditions at the bottom of the mid-slab edge. This level of tensile stress increase over a uniform support case (478 psi) can easily lead to premature cracking since many agencies use a design flexural strength of the concrete of 650 psi.

The size of the nonuniformity also affected the tensile stress increase over uniform support. With random assignment for the MI I-94 project, moving from a 0.7 x 0.7 m^2 to 1.16 x 1.16 m^2 increased the peak tensile stress by 27%. Another key finding from this analysis demonstrated that the nonuniformity was the most critical, especially in the presence of very low support conditions (<20 psi/in) found beneath the location of expected maximum tensile stress. The middle of the lane loading path was not significantly impacted by large differences in spatial support distribution assuming there was adequate load transfer across the joints.

A random assignment using a beta distribution of the same field data was done in order to provide an upper and lower boundary on the values for expected field k-values (i.e., minimum and maximum k-values of 20 and 202 psi/in). By introducing a lower boundary for k-value, the tensile stresses were very similar for all predefined support area sizes and loading paths including the uniform k-value case. The primary reason for this finding with the beta distribution was a lack of very low stiffness areas in the region of expected maximum tensile stress, as seen in the random assignment with normal distribution assumption.

The MI I-96 section was analyzed in a similar manner to MI I-94. The axle configurations and the temperature differentials remained the same; however, the wheelpath loading cases were not run based on their lack of sensitivity to support changes found during the MI I-94 analysis. The subgrade support on MI I-96 was significantly stiffer (mean k-value = 397 psi/in) compared to the MI I-94 section (mean k-value = 63 psi/in). The greatest increase in peak tensile stress from uniform to nonuniform subgrade conditions was 6% (increase of 4% for average peak tensile stress) for the left edge loading path with 81 k-values (1 x 1 m^2 area) deterministically assigned and single axle configuration. The k-value ranged from 235-713 psi/in representing a difference of 478 psi/in, but the ratio from minimum to maximum was around 3, which was less than MI I-94 field data k-values which had a factor of almost 7 difference.

Random assignment of the support stiffness using a normal distribution with the mean and standard deviation defined from the field data (81 k-values) did not provide the same critical results as obtained by loading paths along the edges for case R-36 of MI I-94. The left loading path with 81 k-values randomly assigned in predefined spatial areas produced an 11% increase in overall peak tensile stress over uniform support with the average peak tensile stress increasing for this support case by 8%. This 11% is in comparison to a 31% increase in tensile stress for the MI I-94 field section with significantly lower k-values. The overall peak tensile stress for the MI I-96 section occurred at the bottom of the slab at the mid-slab edge region with the peak tensile stresses during daytime curling significantly higher than nighttime and no curling conditions.

For the field data study, nonuniformity in the subgrade stiffness did not produce significant increases in peak tensile stresses compared to uniform support when deterministically assigned, but when the field data distribution was randomly assigned to predefined areas, the peak tensile stresses did increase significantly. For the softer soil section, MI I-94, the tensile stress increases with subgrade nonuniformity was higher than the stiffer section (MI I-96). Furthermore, for the slab geometry, axle configurations, and temperature conditions, the size of the predefined area of uniform support which produced the largest tensile stress increases was approximately 1.3 m^2. Extremely soft areas with less than 20 psi/in affected the local slab stresses, especially when they were located near areas of expected maximum tensile stress. In all cases analyzed, the free edge loading paths produced the most

critical fatigue damage locations, which should be areas where the foundation stiffness and variability be monitored closely.

The theoretical analysis and the comparison of the two roadway sections in terms of subgrade stiffness variability confirms that nonuniform subgrade support is a complex interaction between the k-value range, the magnitude of k-values, the distribution of the support stiffness relative to the critical loading location, and the size of the predefined area. The field data suggested the presence of changing soil stiffness changes even over a small area (i.e., 1.16 x 1.16 m^2) can produce significant tensile stresses. The presence of surface- or bottom-initiated cracks will exasperate the local stress intensity under nonuniform support conditions. The findings from this research suggest that IC detection of very low stiffness zones near the edge loading path is crucial and that avoiding early-age surface cracks is equally important. The next research step must be to spatially map a concrete pavement foundation layer with the variability level presented in this study and then utilize accelerated load testing until failure in order to link slab failures with changes in the spatial foundation stiffness.

REFERENCES

AASHTO. (1993). *AASHTO Guide for Design of Pavement Structures*. Washington D.C.

ASTM D6951. (2010). "Standard Test Method for use of the Dynamic Cone Penetrometer in Shallow Pavement Applications," ASTM International, West Conshohocken.

Barenberg, E.J., P.F. Wilbur, and S.D. Tayabji. (1976). "Mathematical Analysis of Pavements with Nonuniform Paving Materials," *Transportation Research Record*, 575, 27-38.

Bažant, Z.P. and J. Planas. (1998). *Fracture and Size Effect in Concrete and Other Quasibrittle Materials*. CRC Press: Boca Raton.

Darter, M.I., K.T. Hall, and C.M. Kuo. (1994). *Support under Concrete Pavements*, National Cooperative Highway Research Program 1-30, Transportation Research Board, Washington D.C.

Departments of the Army and the Air Force. (1966). *Rigid Airfield Pavements*. TM 5-888-9/AFM 88-6, Washington D.C.

Duarte, C.A., L.G. Reno, and A. Simone. (2007). "High-Order Generalized FEM for Through-the-Thickness Branched Cracks," *International Journal for Numerical Methods in Engineering*, 72 (3), 325-351.

Duarte, C.A. and D.J. Kim. (2008). "Analysis and Applications of a Generalized Finite Element Method with Global-Local Enrichment Functions," *Computer Methods in Applied Mechanics and Engineering*, 197 (6-8), 487–504.

Evangelista, F., Jr. and J. Roesler. (2009). "Top-Down Cracking Predictions for Airfield Rigid Pavements," *Transportation Research Record*, 2095, 13-23.

Evans, M., N. Hastings, and I.A. Stegun. (2000). *Statistical Distributions*, Wiley: New York.

Facas, N.W., M.A. Mooney, and R. Furrer. (2010). "Anisotropy in the Spatial Distribution of Roller-Measured Soil Stiffness," *International Journal of Geomechanics*, 10 (4), 129-135.

Federal Aviation Administration. (2009). "Airport Pavement Design and Evaluation," Advisory Circular No. 150/5320-6E, U.S. Department of Transportation, Washington D.C.

Federal Highway Administration. (2011). *Onboard Technology Makes Compaction More Accurate* [online]. FHWA. Available from: http://www.fhwa.dot.gov/hfl/innovations/intelligentcompaction.cfm [Accessed October 2011].

Hossain, M., J. Mulandi, L. Keach, M. Hunt, and S. Romanoschi. (2006). “Intelligent Compaction Control,” *Proceedings of the 2006 Airfield and Highway Pavements Specialty Conference*, Atlanta, Georgia, April 30-May 3, 304-316.

Hudson, W.R. and H. Matlock. (1966). “Analysis of Discontinuous Orthotropic Pavement Slabs Subjected to Combined Loads,” *Highway Research Record*, 131, 1-48.

Leonards, G.A., and M.E. Harr. (1959). “Analysis of Concrete Slabs on Ground,” *Journal of the Soil Mechanics and Foundation Divisions*, 85 (SM3), 35-58.

Levey, J.R. (1968). *A Method for Determining the Effects of Random Variation in Material Properties on the Behavior of Layered Systems*, Ph.D. Thesis, University of Illinois at Urbana-Champaign, Urbana, Illinois.

Levey, J.R. and E.J. Barenberg. (1970). “A Procedure for Evaluating Pavements with Nonuniform Paving Materials,” *Highway Research Record*, 337, 55-69.

Lysmer, J. and J.M. Duncan. (1969). *Stresses and Deflections in Foundations and Pavements*. 4th Edition, University of California at Berkeley: Berkeley.

Mindess, S., J.F. Young, and D. Darwin. (2003). *Concrete*. 2nd Edition, Prentice Hall: Upper Saddle River.

Mooney, M.A., and R.V. Rinehart. (2007). “Field Monitoring of Roller Vibration During Compaction of Subgrade Soil,” *Journal of Geotechnical and Geoenvironmental Engineering*, 133 (3), 257-265.

Mooney, M.A., R.V. Rinehart, N.W. Facas, O.M. Musimbi, D.J. White, and P.K.R. Vennapusa. (2010). *Intelligent Soil Compaction Systems*, NCHRP Report 676, Transportation Research Board, Washington D.C.

Pereira, J.P., C.A. Duarte, and X. Jiao. (2010). “Three-Dimensional Crack Growth with Hp-Generalized Finite Element and Face Offsetting Methods,” *Computational Mechanics*, 46 (3), 431-453.

Petersen, D.L. (2005). *Continuous Compaction Control MnROAD Demonstration*, Final Report No. MN/RC-2005-07, CNA Consulting Engineers, Minnesota Department of Transportation, Maplewood, Minnesota.

Petersen, L. and R. Peterson. (2006). *Intelligent Compaction and In-Situ Testing at Mn/DOT TH53*, Final Report No. MN/RC-2006-13, CNA Consulting Engineers, Minnesota Department of Transportation, St. Paul, Minnesota.

Richart, F.E., Jr. and P. Zia. (1962). “Effect of Local Loss of Support on Foundation Design,” *Journal of the Soil Mechanics and Foundation Divisions*, 88 (SM1), 1-27.

Sebesta, S., W. Liu, and T. Scullion. (2009). “Instrumented Rollers to Assess Construction Quality on Texas Projects,” *Transportation Research Record*, 2116, 1-7.

Shah, S., S.E. Swartz, and C. Ouyang. (1995). *Fracture Mechanics of Concrete.* Wiley: New York.

Szabó, B. and I. Babuška. (1991). *Finite Element Analysis*, Wiley-Interscience: New York.

Terzaghi, K. and R.B. Peck. (1967). *Soil Mechanics in Engineering Practice*, 2nd Edition, John Wiley & Sons: New York.

Van Hampton, T. (2009). “Intelligent compaction is on a roll,” *Engineering News-Record*, 263 (2), 54-57.

White, D.J., D. Harrington, H. Ceylan, and T. Rupnow. (2005). *Fly Ash Stabilization for Non-Uniform Subgrade Soils, Volume II: Influence of Subgrade Non-Uniformity on PCC Pavement Performance*, Final Report No. IHRB Project TR-461; FHWA Project 4, Center for Transportation Research and Education, Federal Highway Administration, Washington, D.C.

White, D.J., M.J. Thompson, K. Jovaag, E.J. Jaselskis, V.R. Schaefer, and E.T. Cackler. (2006). *Field Evaluation of Compaction Monitoring Technology: Phase II*, Report No. CTRE Project 04-171, Center for Transportation Research and Education, Iowa Department of Transportation, Ames, Iowa.

White, D., M. Thompson, and P. Vennapusa. (2007). *Field Validation of Intelligent Compaction Monitoring Technology for Unbound Materials*, Final Report No. MN/RC 2007-10, Iowa State University, Minnesota Department of Transportation, St. Paul, Minnesota.

White, D.J., P.K.R. Vennapusa, H.H. Gieselman, A.J. Wolfe, S. Douglas, and J. Li. (2011). *Pavement Foundation Layer Reconstruction Project- Michigan I-94 Field Study*, Report No. ER 11-03, Center for Earthworks Engineering Research.

APPENDIX A FIELD CBR TO K-VALUE CORRELATIONS FOR MI I-94 AND MI I-96

Table A1. Field CBR to k-Value for MI I-94 Roadway (121 Data Points)

Field CBR	k-Value (Eq. 4.8)	Field CBR	k-Value (Eq. 4.8)	Field CBR	k-Value (Eq. 4.8)	Field CBR	k-Value (Eq. 4.8)
3.0	55	2.2	43	3.3	60	1.7	36
2.5	48	1.8	37	5.7	91	4.8	80
7.6	114	6.0	95	3.3	60	2.4	47
2.9	54	6.0	95	2.8	52	2.7	51
3.2	58	2.1	42	2.4	47	3.9	68
3.7	65	7.5	113	7.2	109	3.9	68
1.7	36	3.3	60	5.8	92	3.5	62
5.4	87	1.8	37	3.0	55	6.0	95
6.2	97	5.7	91	3.3	60	6.9	106
2.4	47	5.1	84	2.2	43	1.4	31
3.0	55	1.9	39	3.0	55	2.8	52
3.1	57	4.9	81	2.6	50	3.1	57
4.5	76	2.9	54	6.3	99	4.0	69
3.8	67	5.5	89	3.3	60	2.0	40
4.8	80	5.2	85	3.7	65	1.5	32
1.4	31	3.2	58	1.7	36	3.8	67
2.5	48	2.2	43	6.3	99	4.1	71
2.8	52	6.2	97	4.1	71	6.1	96
2.4	47	2.1	42	3.7	65	3.3	60
1.6	34	5.1	84	5.8	92		
2.2	43	4.8	80	2.7	51		
2.7	51	7.6	114	3.4	61		
10.6	148	1.7	36	3.1	57		
4.1	71	3.0	55	7.4	112		
3.7	65	4.2	72	4.6	77		
1.9	39	4.1	71	4.2	72		
2.9	54	2.5	48	1.4	31		
2.0	40	2.2	43	3.1	57		
3.3	60	3.0	55	3.3	60		
3.1	57	2.5	48	3.5	62		
2.3	45	4.8	80	4.4	75		
4.0	69	2.0	40	2.2	43		
2.4	47	5.4	87	1.7	36		
15.8	202	2.5	48	2.6	55		

Table A2: Field CBR to k-Value for MI I-96 Roadway

Field CBR	k-Value (Eq. 4.8)	Field CBR	k-Value (Eq. 4.8)	Field CBR	k-Value (Eq. 4.8)
33	356	35	371	42	433
20	243	30	336	44	452
31	342	21	253	42	433
36	382	40	419	40	414
46	464	47	472	42	432
52	507	30	337	40	415
20	240	39	407	51	502
19	235	36	383	30	333
25	284	37	393	65	609
30	334	46	465	37	395
41	421	25	293	80	713
24	279	26	299		
38	403	42	433		
38	397	58	556		
31	341	55	530		
44	449	51	504		
38	403	45	453		
22	262	38	400		
22	257	32	351		
33	357	26	301		
36	387	38	397		
31	345	21	256		
40	414	44	445		
43	440	48	481		
30	335	59	564		
37	391	36	380		
19	235	46	463		
22	261	31	338		
45	457	23	268		
49	487	31	343		
42	430	42	433		
47	468	72	655		
35	373	42	433		
35	372	57	550		

APPENDIX B ADDITIONAL MAXIMUM PRINCIPAL STRESS PLOTS FOR MI I-94 AND MI I-96

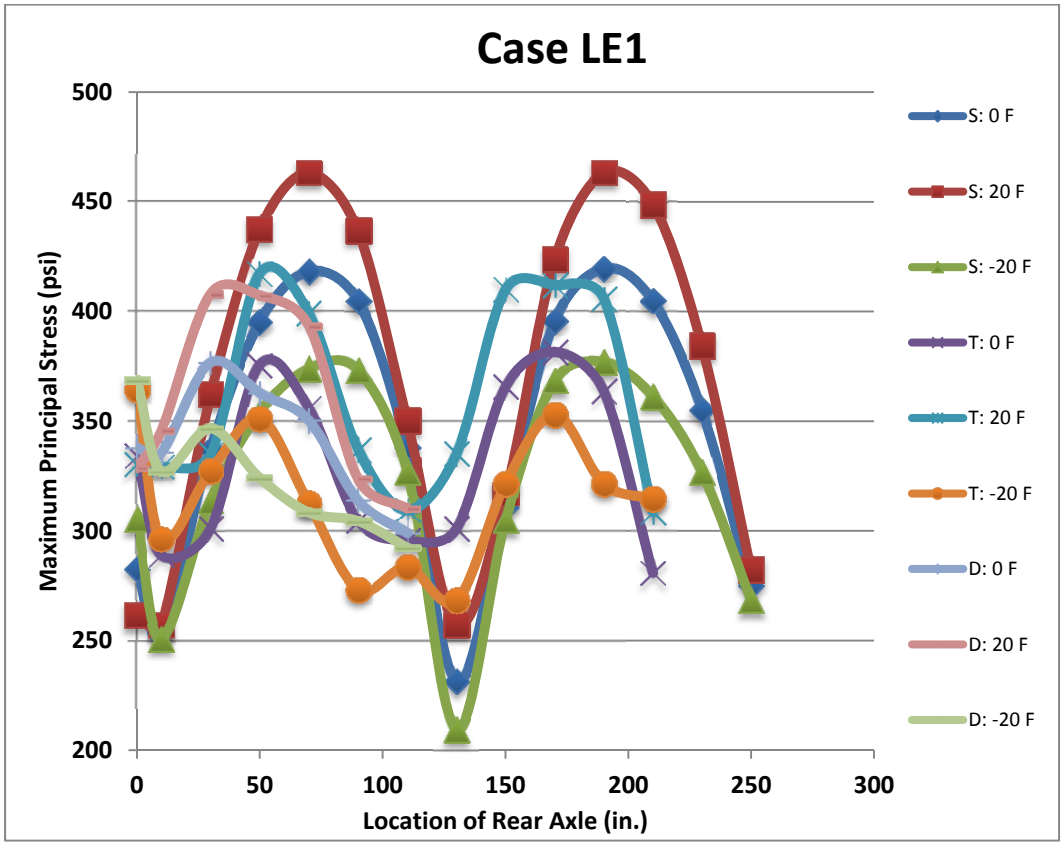

Figure B1. Maximum principal (tensile) stress for Case LE1 versus axle position.

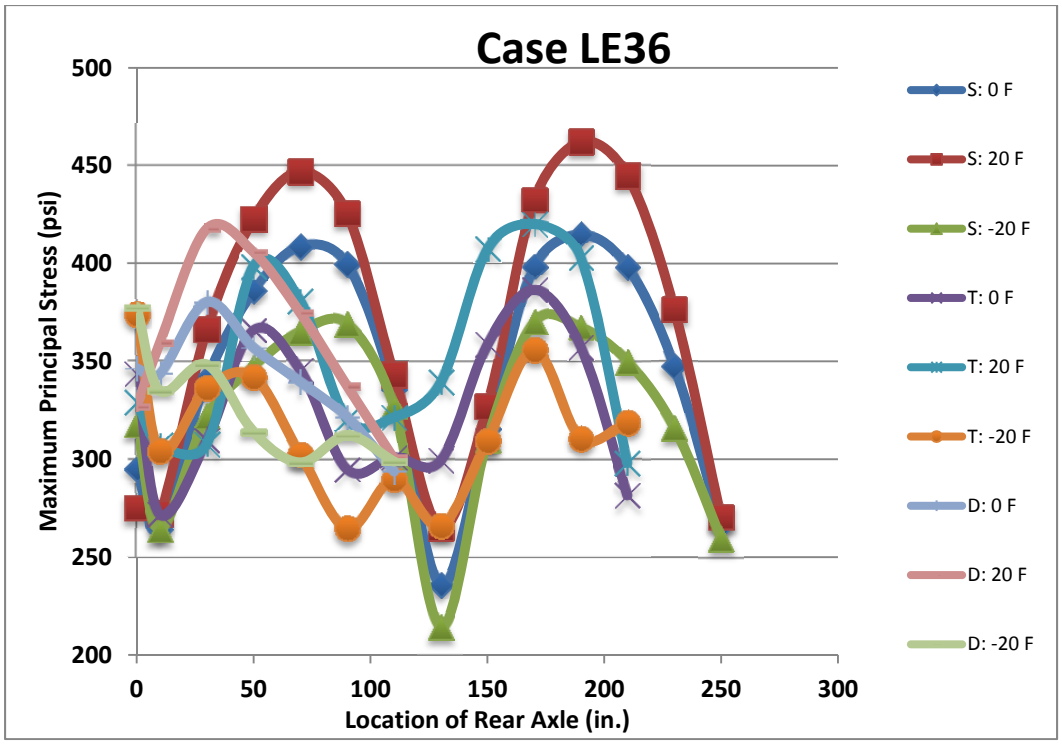

Figure B2. Maximum principal (tensile) stress for Case LE36 versus axle position.

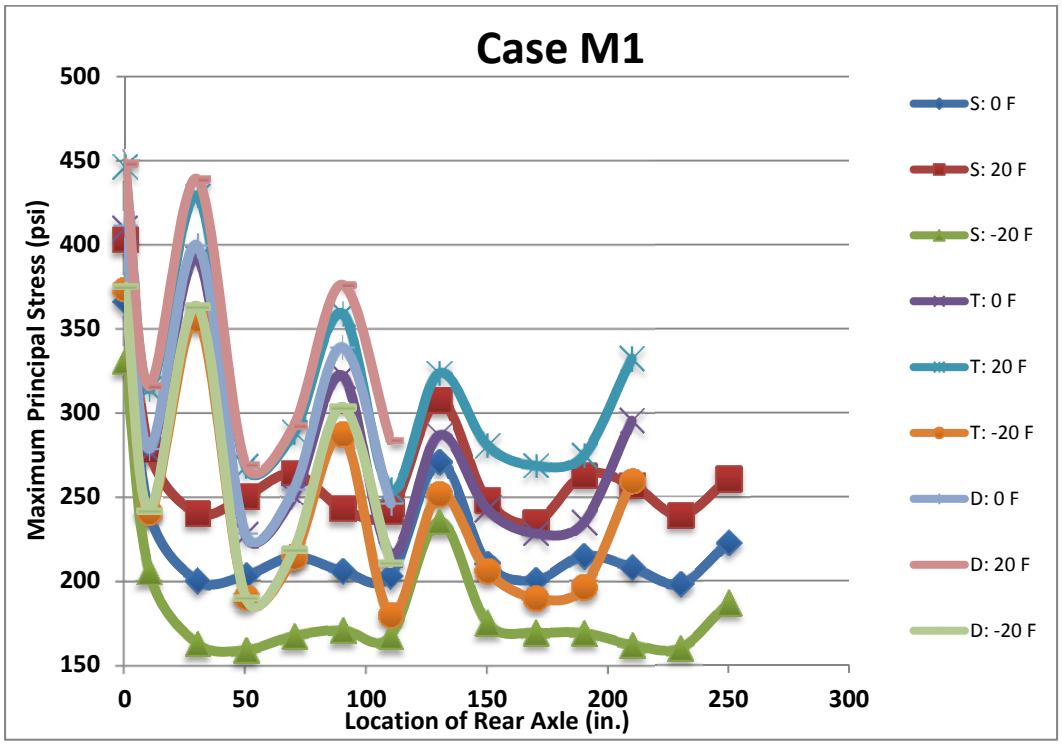

Figure B3. Maximum principal (tensile) stress for Case M1 versus axle position.

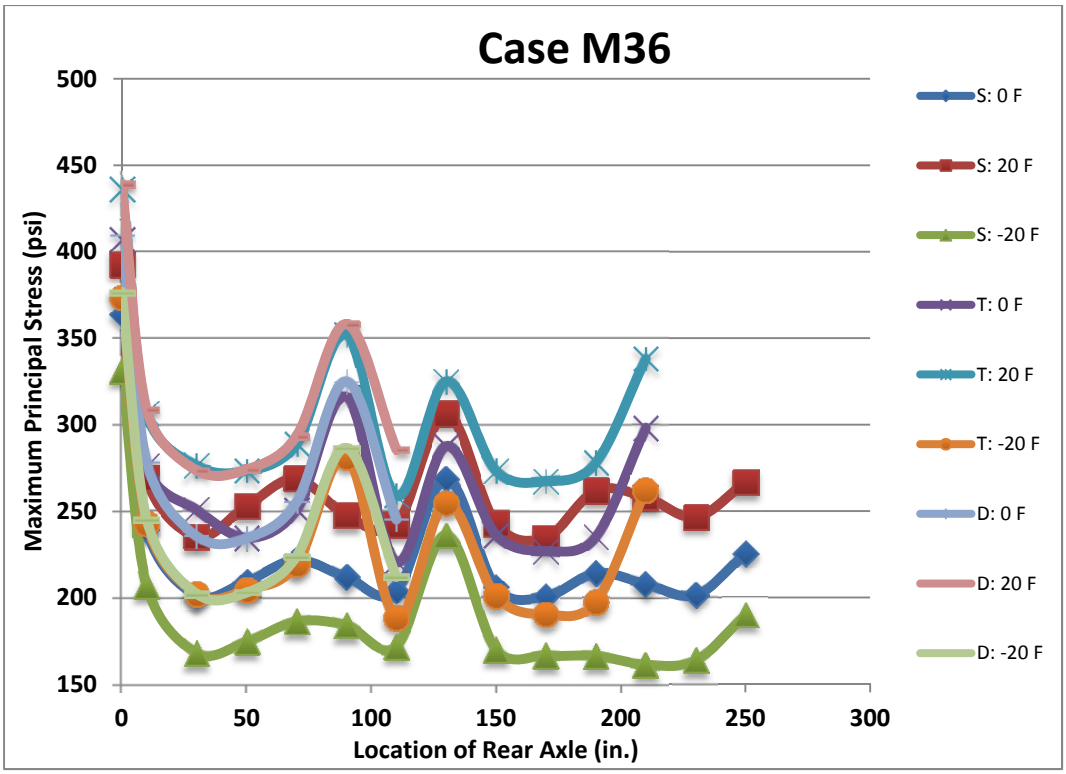

Figure B4. Maximum principal (tensile) stress for Case M36 versus axle position.

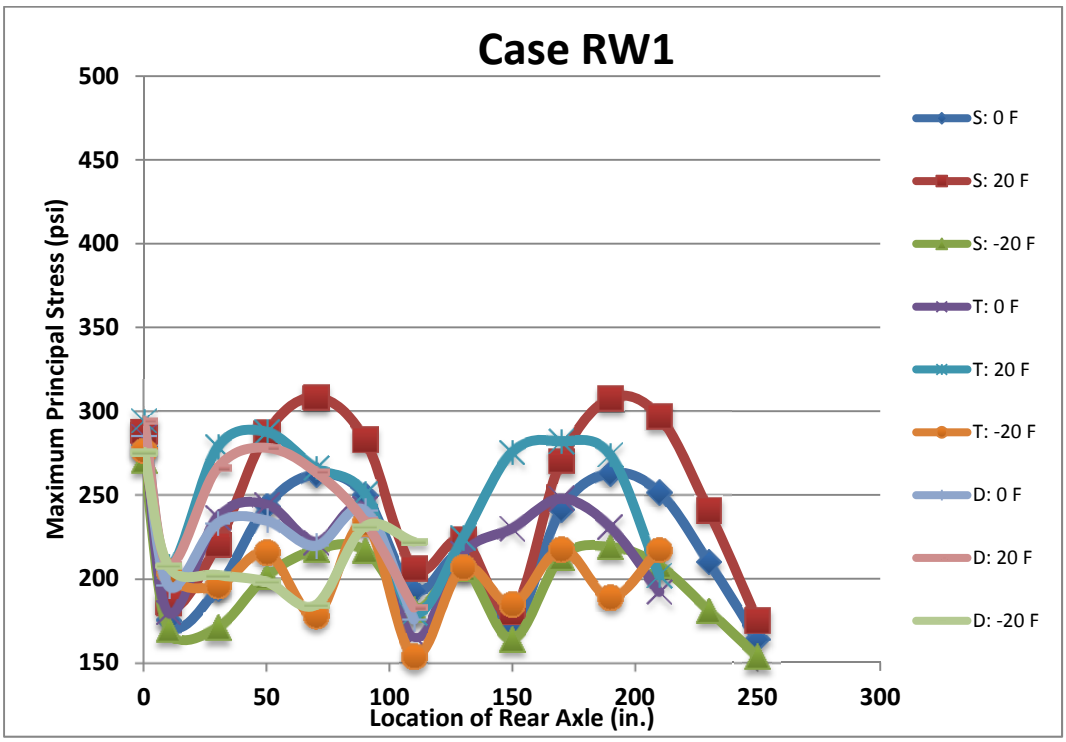

Figure B5. Maximum principal (tensile) stress for Case RW1 versus axle position.

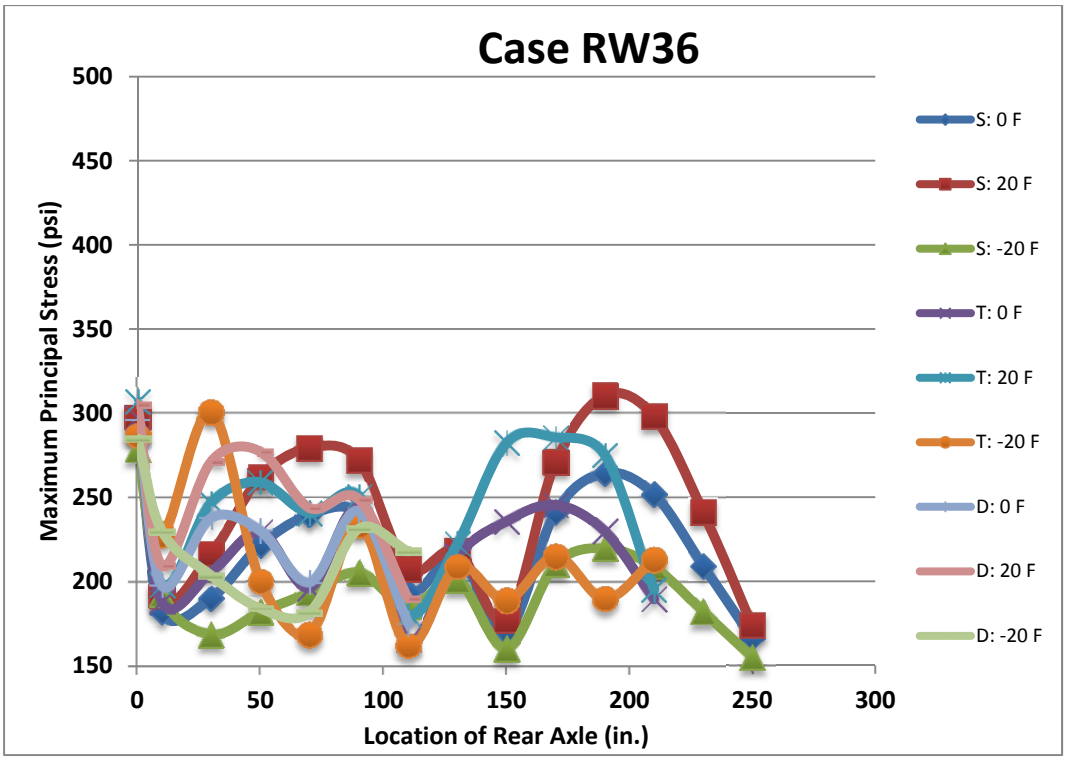

Figure B6. Maximum principal (tensile) stress for Case RW36 versus axle position.

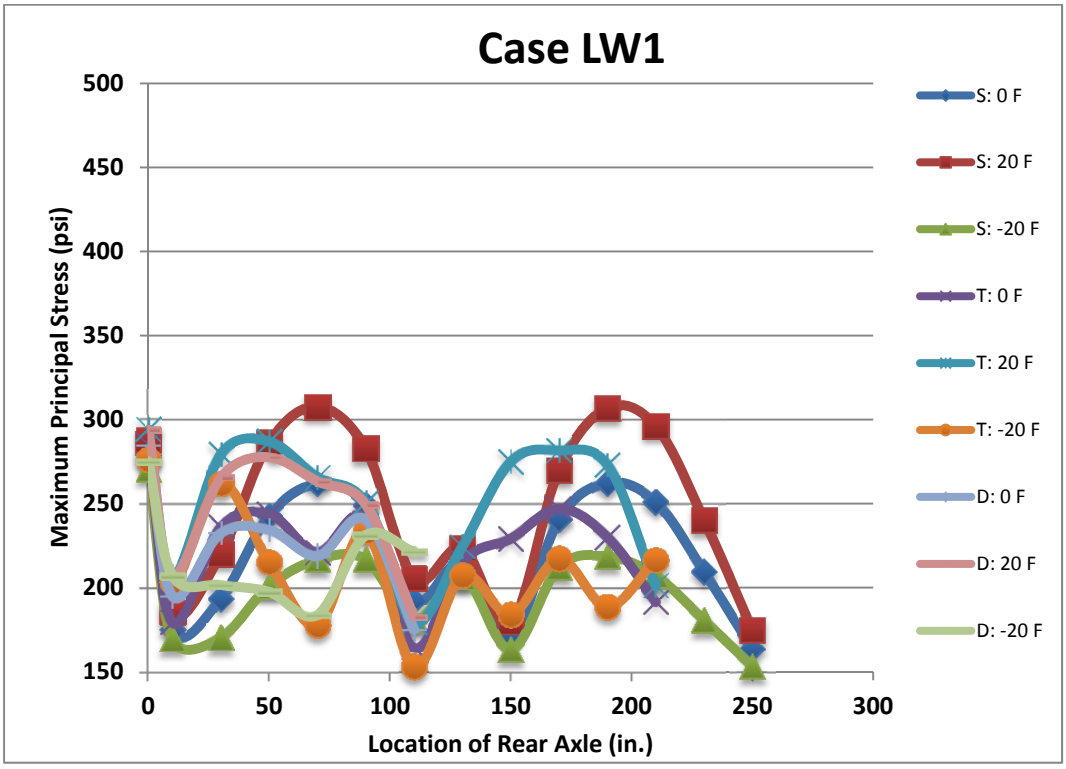

Figure B7. Maximum principal (tensile) stress for Case LW1 versus axle position.

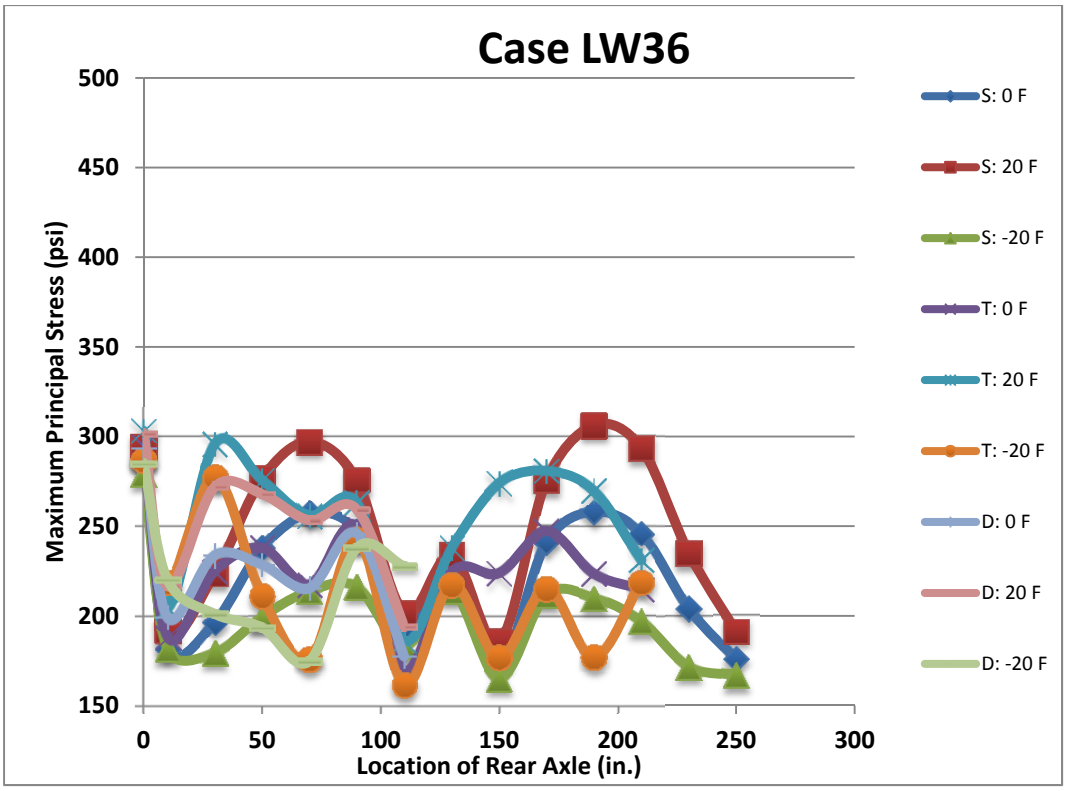

Figure B8. Maximum principal (tensile) stress for Case LW36 versus axle position.

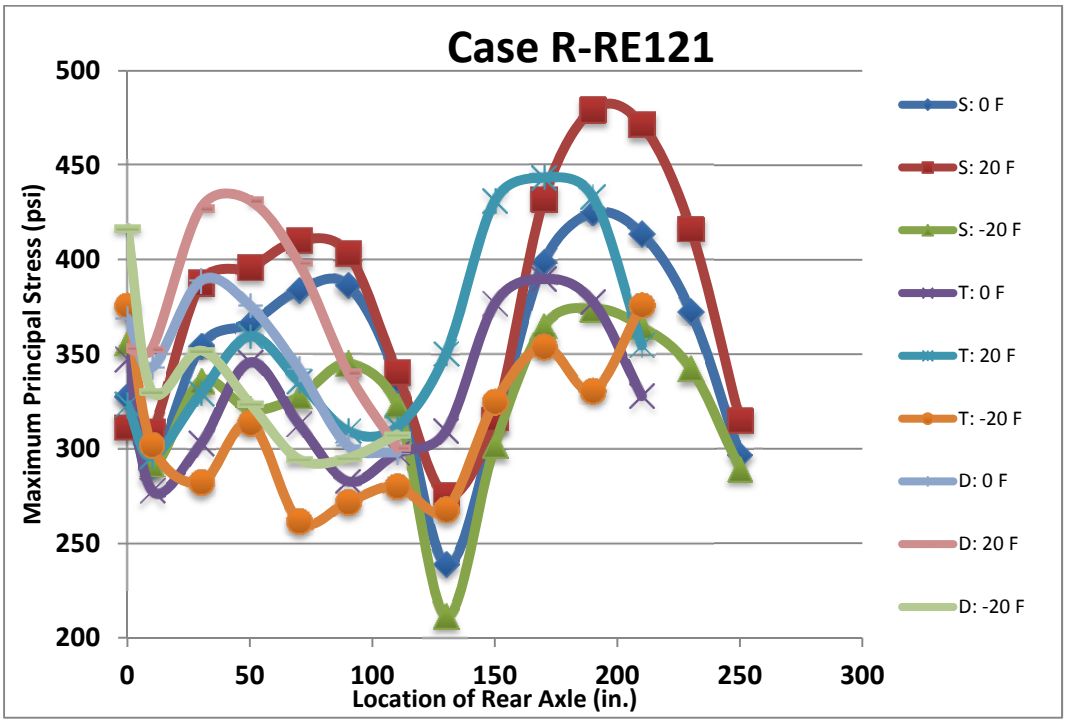

Figure B9. Maximum principal (tensile) stress for Case R-RE121 versus axle position.

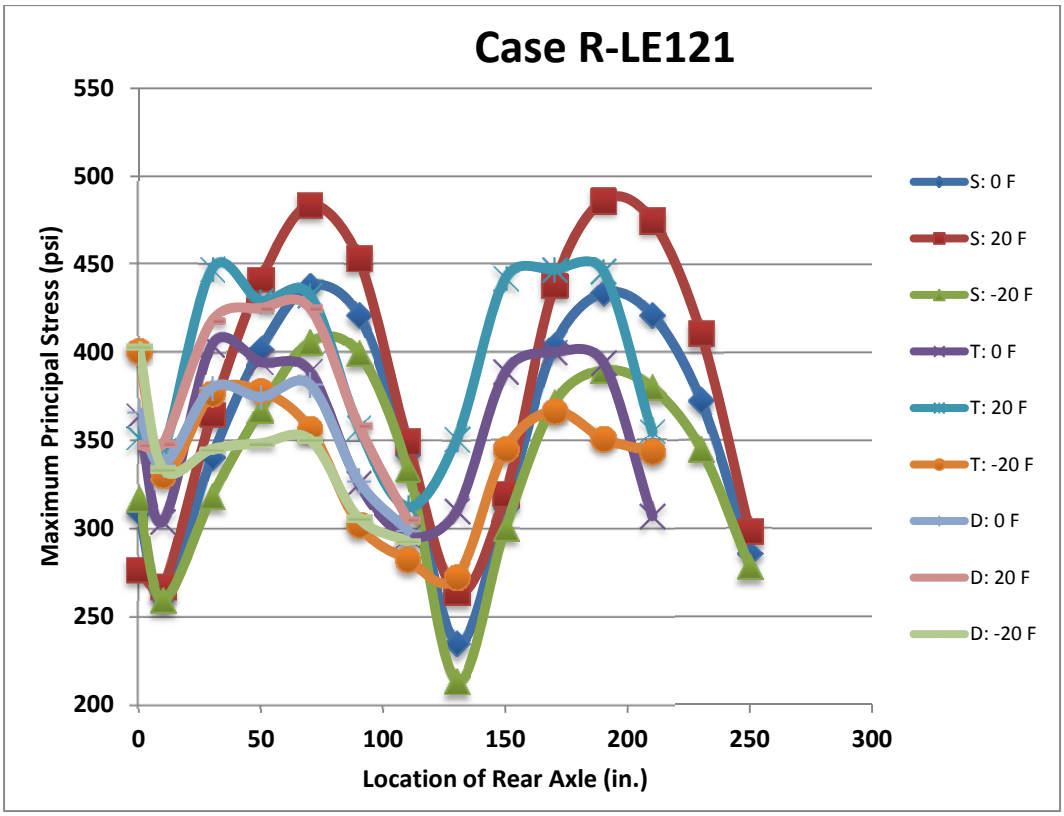

Figure B10. Maximum principal (tensile) stress for Case R-LE121 versus axle position.

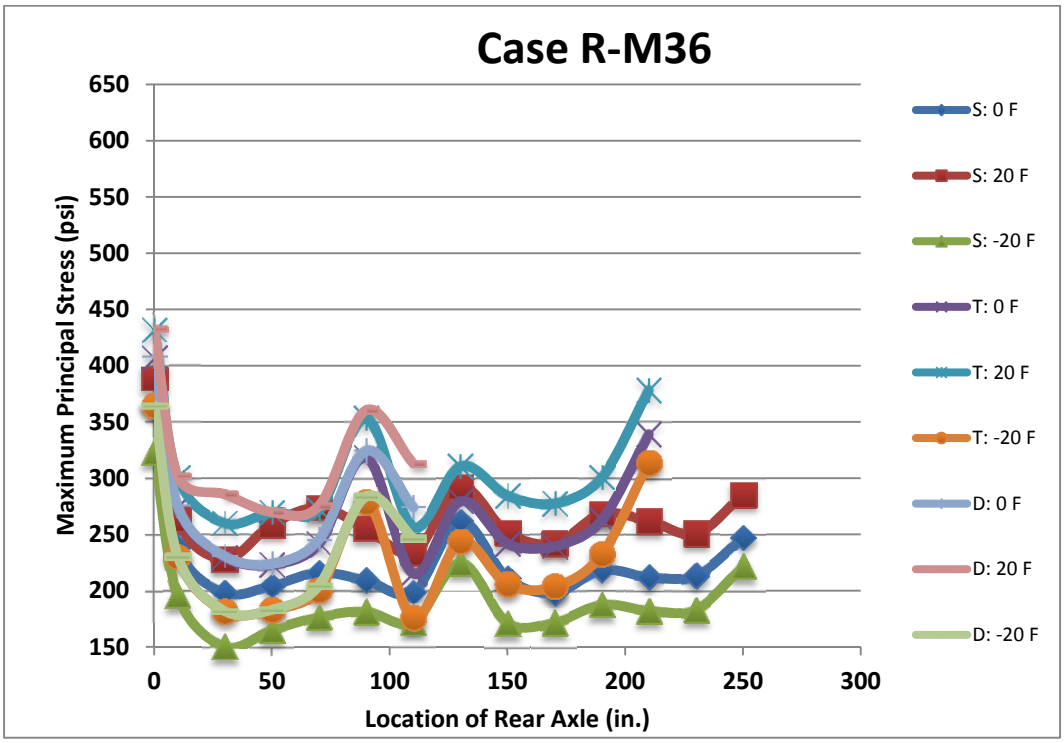

Figure B11. Maximum principal (tensile) stress for Case R-M36 versus axle position.

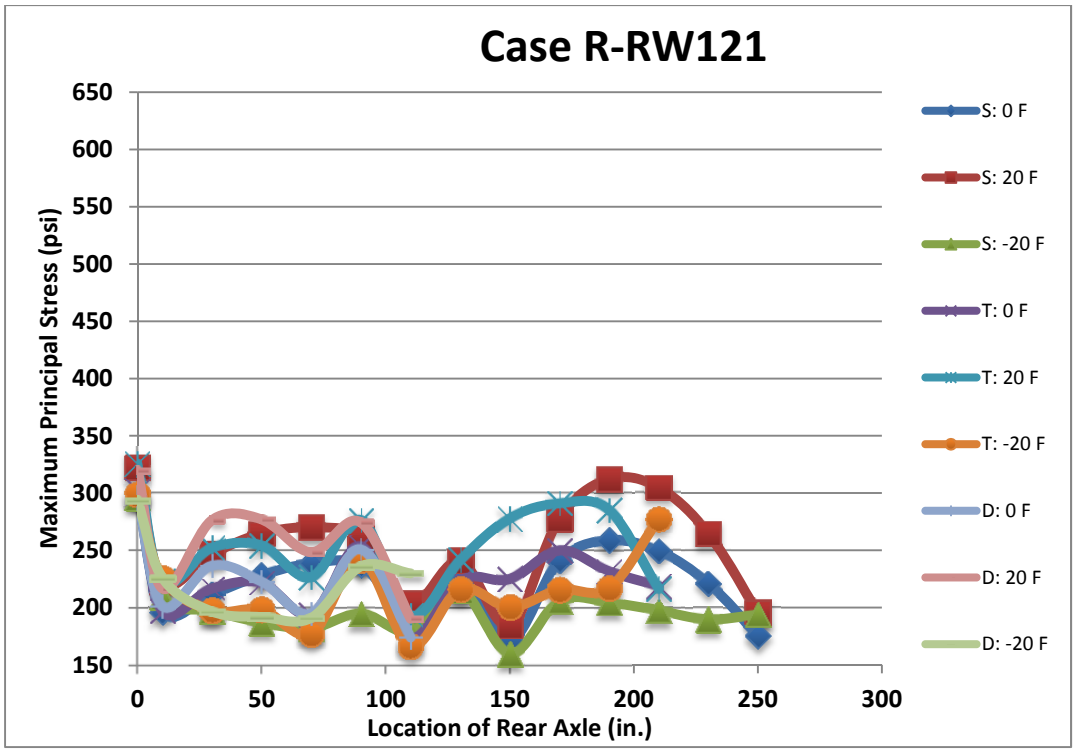

Figure B12. Maximum principal (tensile) stress for Case R-RW121 versus axle position.

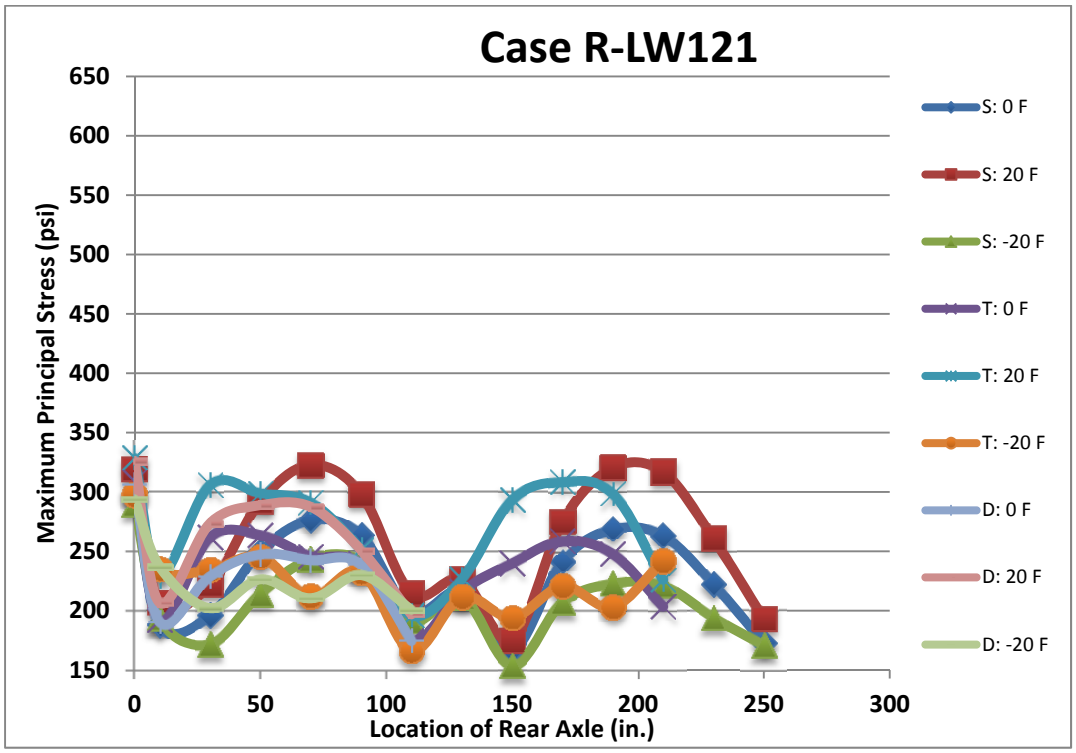

Figure B13. Maximum principal (tensile) stress for Case R-LW121 versus axle position.

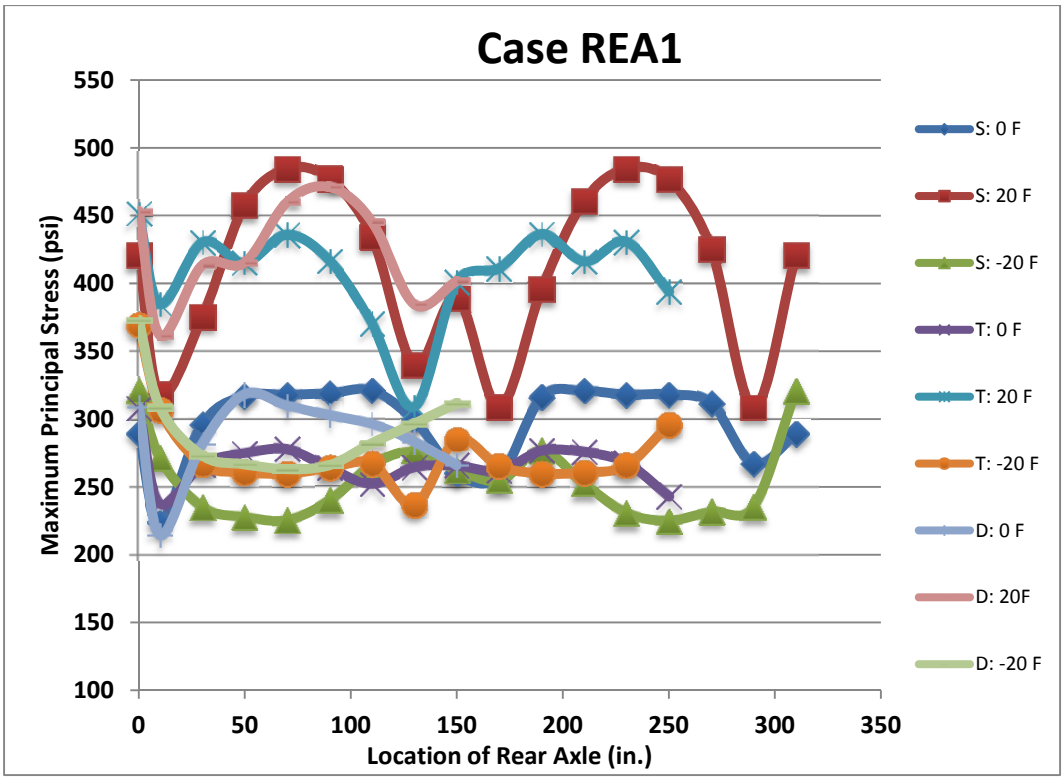

Figure B14. Maximum principal (tensile) stress for Case REA1 versus axle Position.

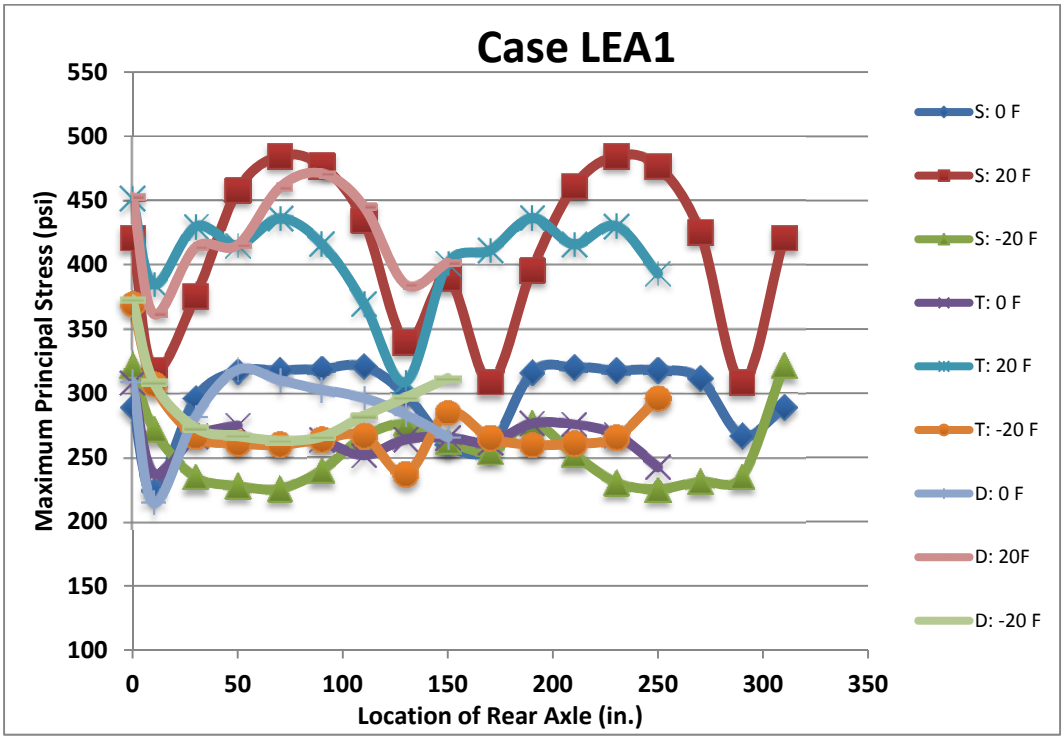

Figure B15. Maximum principal (tensile) stress for Case LEA1 versus axle Position.

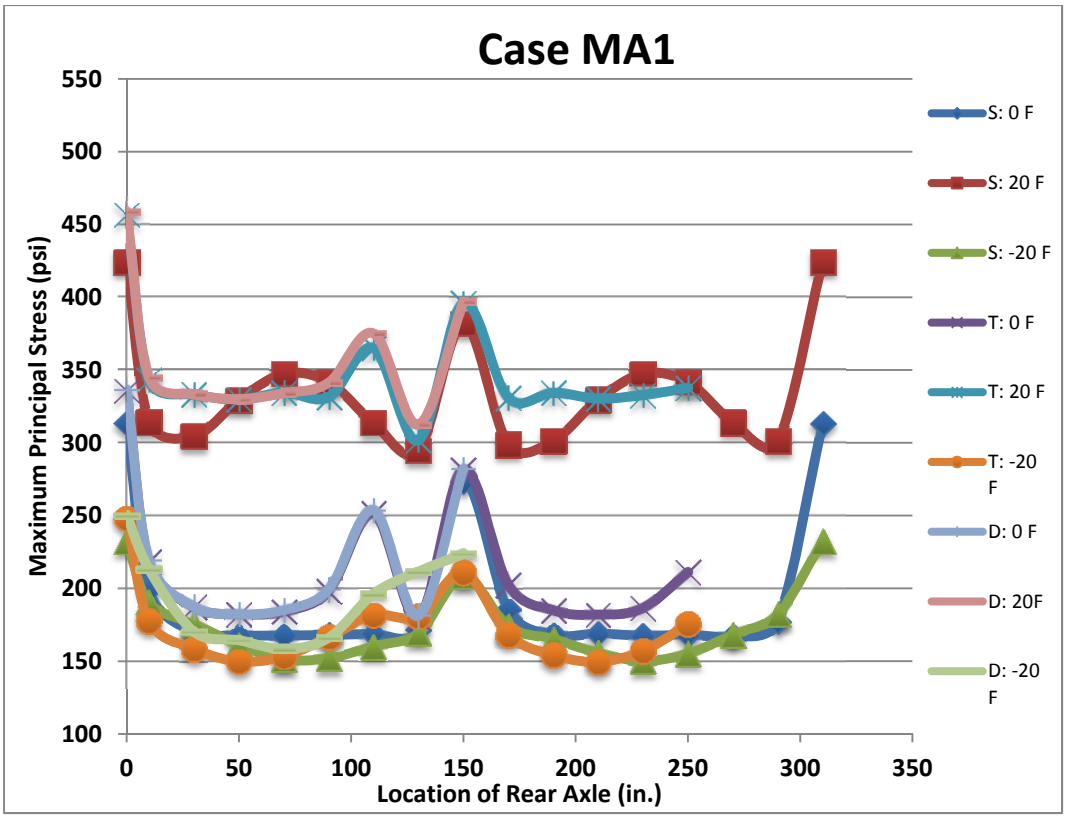

Figure B16. Maximum principal (tensile) stress for Case MA1 versus axle position.


ILLINOIS
UNIVERSITY OF ILLINOIS AT URBANA-CHAMPAIGN